ABUNDANCE PATTERNS OF OLD OPEN CLUSTERS AS TRACERS OF GALACTIC CHEMICAL EVOLUTION

A thesis
submitted for the degree of

Doctor of Philosophy

To
The Department of Physics
School of Physical, Chemical & Applied Sciences
Pondicherry University
Puducherry - 605 014, INDIA

By

A. Bala Sudhakara Reddy

Indian Institute of Astrophysics
Bangalore - 560 034, India

June - 2014

Declaration

I hearby declare that the thesis titled **"Abundance Patterns of Old Open Clusters as Tracers of Galactic Chemical Evolution"** is the result of the investigations carried out by me at the Indian Institute of Astrophysics, Bangalore under the guidance and supervision of Prof. Sunetra Giridhar. The results reported in this thesis are new, and orginal, to the best of my knowledge, have not been submitted in whole or part for the award of any degree, diploma, associateship, fellowship, etc. of any university or other institutes.

In keeping with the general practice of reporting scientific observations, due acknowledgment has been made whenever the work described is based on the findings of other investigators. Any omission which might have occurred by oversight or error in judgment is regretted.

Bangalore
June – 2014

Bala Sudhakara Reddy
(PhD Candidate)

Certificate

This is to certify that the thesis entitled **"Abundance Patterns of Old Open Clusters as Tracers of Galactic Chemical Evolution"** submitted to the Pondicherry University by Mr. Bala Sudhakara Reddy for the award of the degree of Doctor of Philosophy in the faculty of science, is based on the results of the investigations carried out by him under my supervision and guidance, at the Indian Institute of Astrophysics. This thesis has not been submitted in whole or part for the award of any degree, diploma, associateship, fellowship, etc., of any university or institute.

Bangalore
June – 2014

Prof. Sunetra Giridhar
(Thesis Supervisor)

Dedicated to,

My Parents and My Sister

Acknowledgements

First and foremost, I wish to pay obeisance to God Almighty for his blessings and for having given me this opportunity to pursue the important goal of my life.

I gratefully acknowledge the immense help of my thesis supervisor Professor Sunetra Giridhar, without whom it would have been impossible for me to reach the end of my PhD. Her invaluable guidance, enormous faith in my abilities, her patience and encouragement made it possible to achieve this important goal of life. I am very thankful to her for all she has done for me throughout my PhD career showing her affection, anger, also her emotional support, care and above all by being a very strong supporting pillar so that I could get every kind of academic and personal support from her. I have never felt being alone. I have seen not only my guide inside her but also a mother, a friend, a well wisher and a very good teacher. I cannot forget the important part of my life I spent with her during my PhD. I am also very thankful to her family for their love and affection. I am indeed lucky to have had such a great person as my thesis supervisor.

It was indeed a boon for me to come in touch with one of the experts in the field of observations and analysis of stellar photospheres and the chemical evolution of the universe, Professor David L. Lambert, without whom I could not have dreamt of finishing my PhD work. I am eternally grateful to him for obtaining the high resolution spectra of my program stars at our request and for his valuable comments and suggestions during my PhD which immensely helped in enriching my knowledge and understanding of the subject. His constant encouragement, consistent help whenever I needed, affection and friendly attitude played a very profound role in my success.

I would like to thank the former Directors Prof. S. S. Hasan and Prof. Bhanu Pratap Das (Acting) and the present Director Prof. P. Sreekumar for giving me the opportunity to work in this Institute and providing all the support and facilities for completing my research work. I also thank our former Dean (Academic), Prof. Harish Bhatt, and the present Dean, Prof. Tushar Purushottam Prabhu, for helping me on many occasions when I needed. I am thankful to all the members of Board of Graduate studies for their help and support. I also thank all the members of the IIA-PhD selection committee for welcoming me into their community. It is my sincere thanks to Prof S. K. Saha (former Chair, BGS) and Dr. Annapurni Subramaniam (present Chair, BGS) for their help, encouragements and wishes. I would like thank all the members of my Doctoral committee: Prof. N. Satyanarayana (Pondicherry Univerisity (PU)), Dr. Eswar Reddy (IIA) and Dr. Gajendra Pandey (IIA) for their valuable suggestions *throughout my PhD. I would like to acknowledge the support extended by Dr. B. A. Varghese, Dr. Dipankar Banerjee and IIA support team. I would also like to thank Ms. Christina Birdie, Mohan B. S., Prabhahar and the other library staff for their help with the library facilities. I would also like to thank Mr. K. Shankaranarayanan, Dr. P. Kumaresan, Mr. A. Narasimharaju, Mr. Narasimhamurthy, Mr. S. Rajendran, B. Mohan, Mr. Valsalan and Mr. S. B. Ramesh in particular and all the other staff members of the administration department.*

I am indebted to Prof. G. Chandrasekaran (HOD, Department of Physics) and Prof. N. Satyanarayana (Dean, Department of Physics) of PU for arranging and giving their valuable comments and suggestions during my pre-PhD submission Colloquium at PU campus. I would also like to thank Dr. P. Muralidassan (Assistance Registrar) of PU, for being extremely helpful and co-operative in all the formalities related to my Ph.D work.

I am thankful to all the members of the VBO observing support team: Mr. G. Selvakumar, Mr. V. Moorthy, Mr. M. Appakutty and Mr. C. Velu and Engineer in charge P.Anbazhagan for teaching me “hands on“ observational astronomy.

I am indebted to my uncle Raveendra Reddy (IMSc, Chennai) and aunt Sharmila and researchers from IMSc: Dr. Srinivas, Dr. Suryanarayana, Professor M. V. N. Murthy, Dr. Indumathi for their blessings, encouragement for selecting this path of life, their help when I needed and also their valuable advice which guided me to reach the completion of my PhD thesis. I would like to extend my gratitude to my roommates Rama krishna, Mangala pandi and Subhakar.

The first year of my PhD was very much exciting and interesting with all my batchmates. It is difficult to forget the days when we had spent doing our homework. I wish to thank my batchmates: Hema B. P., Ramya P., Indu, Sindhuja, Drisya, Arya, Prashanth, Dinesh, Rathna Kumar, Pradeep, Smitha, Samyaday who have been helpful during my days at IIA. It is my privilege to thank all my friends of IIA: Sumangala Rao, Bharat Kumar, Ramya S., Chandrasekhar, Krishna Prasad, Sasikumar Raja K., Kishore, Uday, Abhay, Amit Sukla, Anantha, Blesson Mathew, Sreeja, Smitha Subramanian, Nagraj, Nataraj, Veeresh, Vigeesh. Their company gave me many important things to learn in life which I was lacking in some sense. I can not forget the hostel life and the food that I had at the canteen with them. I would like to extend my thanks to all the cooks at IIA, in particular to Subramani and Narayana Samy.

Bala Sudhakara Reddy

List of Publications

Following is the list of refereed publications till date. It is written in the format; title, authors, year of publication, journal, volume number, page number.

1. *Comprehensive abundance analysis of red giants in the open clusters NGC 752, 1817, 2360 and 2506*, **Arumalla B. S. Reddy**, Sunetra Giridhar & David L. Lambert, 2012, MNRAS, 419, 1350.

2. *Comprehensive abundance analysis of red giants in the open clusters NGC 2527, 2682, 2482, 2539, 2335, 2251 and 2266*, **Arumalla B. S. Reddy**, Sunetra Giridhar & David L. Lambert, 2013, MNRAS, 431, 3338

In preparation:

1. *Comprehensive abundance analysis of red giants in the open clusters NGC 1342, 1662, 2447, 2354, 1912, 2548 and Collinder 350* by **Arumalla B. S. Reddy**, Sunetra Giridhar & David L. Lambert

2. Chemical inhomogeneties in the Galactic disk by **Arumalla B. S. Reddy**, Sunetra Giridhar & Muneer S.

Conference Proceedings

1. *'Comprehensive abundance studies of four open clusters'*, **Bala Sudhakara Reddy, Arumalla**, Sunetra Giridhar & David L. Lambert, 2011, ASInc, 3, 133, Editors: Pushpa Khare & C. H. Ishwara-Chandra in ASI Conference Series (ASICS) Volume 3.

2. *'The chemical abundances of open clusters: NGC 752, NGC 1817, NGC 2360 and NGC 2506'*, **Arumalla B. S. Reddy**, Sunetra Giridhar & David L. Lambert, 2012, ASInc, 4, 197, in *Recent Advances in Star Formation: Observations and Theory*, Editors: Subramanian A. & Sumedh Anathpindika (ASICS Volume 4).

3. *'Abundance analysis of an extended sample of open clusters: a search for chemical inhomogeneities'* **Arumalla B. S. Reddy**, Sunetra Giridhar & David L. Lambert, 2013, 2013, ASInC, 9, 77, Editors: Pushpa Khare & C. H. Ishwara-Chandra (ASICS Volume 9).

Abstract

We have initiated a program to explore the presence of chemical inhomogeneities in the Galactic disk using the open clusters (OCs) as ideal probes. We have obtained high S/N - ratio and high- dispersion echelle spectra (R $\geq$ 55,000) of red giant members for eighteen OCs using the 2.7-m Harlan J. Smith telescope at the McDonald observatory and measured abundances for many elements representing different production mechanisms (α- and r- process, Fe- peak, and s-process) and sites (i.e. Type II SN, Type Ia SN, and AGB star environments). The membership to the cluster has been confirmed through their radial velocities and proper motions. The spread in temperatures and gravities being very small among the red giants, nearly the same stellar lines were employed thereby reducing the random errors. The errors of average abundance for the cluster were generally in 0.02 to 0.08 dex range. Synthetic spectra were computed for species affected by hyperfine and isotopic splitting or affected by blends.

Our sample of eighteen OCs supports the view that both the field and OCs giants of near-solar metallicity have very similar, if not identical, compositions (within the errors of measurements) for alpha, Fe-peak and r-process elements. We have noticed a small but significant enrichment in [s-process/Fe] abundance ratios among young OCs, suggesting that the Galaxy has received significant contribution from low mass AGB stars. We find intracluster abundance variations for some s-process elements, for example Zr and Ba.

We merged our sample of OCs with the available high-quality results in the literature and a suitable normalization has been done with extreme care to place all the results on a common abundance scale. We recalculated the R_{gc} value for each of these clusters to bring them to a common distance scale to study the metallicity gradient(s) in the Galactic disk. We derived membership probabilities and assigned all these OCs to either the thin disk, thick disk or halo stellar populations to know their kinematic origin. We also studied the dynamics of these OCs using a multicomponent galactic gravitational potential model and derived birthplaces and other orbital parameters.

The connection between the observed gradients in the Galactic disk and the spiral density waves is explored. The modulation of smooth metallicity distribution with R_{gc} and the spread in metallicity near 8-9 kpc and 11-12 kpc is well explained by the resonance interaction of disk material with spiral density waves and hence the subsequent exchange of metal rich gas and OCs near corotation. We argue that orbital migration of old OCs born in the inner regions is responsible for the flat abundance gradient in the outer disk.

The ratio of alpha-elements to Fe of the sample does not vary appreciably with the Rgc, which reveals an homogeneous history of star formation. Future studies of significantly extended sample of OCs allowing the study of radial as well as azimuthal variations of metallicity for a range of elements analysed identically and on homogeneous scale is required to test these results and to enhance our knowledge on the chemical evolution of the Galactic disk. We emphasize that all these studies eventually would provide insight on the evolution of disks in galaxies in time and space.

Contents

List of Figures

List of Tables

Chapter 1

Introduction

The chemical compositions of stars and galaxies provide a unique insight into the evolution of the Universe. Nucleosynthetic processes describe the sequence of reactions involved in combining light atomic nuclei to form heavier ones. Stars are superb astrophysical laboratories providing ideal environment needed for nucleosynthesis to occur. As the stars evolve, a significant fraction of the processed material is brought to surface through mixing processes and ejected into the interstellar medium (ISM) via mass-loss thereby enriching it. Thus all the elements heavier than helium in the cosmos have been created and recycled through various nuclear burning processes in stars. Therefore, the newer stars are born from a gas cloud already enriched with many heavy elements. As the cosmic clock runs, this has the effect of creating distinctly different stellar populations with markedly different chemical composition.

As the composition of stars holds the key to the chemical evolution of the Universe, stellar astronomers seek an understanding of how the elements and isotopes are synthesized and then mixed within stars. The theory that the stellar interiors have high enough temperatures to make up the elements heavier than helium was first proposed by **B**urbidge, **B**urbidge, **F**owler and **H**oyle (**B^{2}FH**, 1957). B^{2}FH proposed eight nucleosynthesis processes and their likely environments that accounted for most of the elements in the periodic table. Their theory predicts that stars of different masses have very different internal temperatures, and hence synthesize very different elements and heavy isotopes at different stages of evolution. Several subsequent review papers have updated B^{2}FH accordingly (Wallerstein et al. 1997; Gratton et al. 2004 and Sneden et al. 2008). Numerous astrophysical books are available to provide a comprehensive summary of the stellar nucleosynthesis and nuclear physics in detail (see for example Iliadis, 2007 for a recent review). In the following sections we give a brief introduction to the stellar structure and evolution, the time scales over which the ISM will be enriched with certain group of elements which in turn is related to initial mass of the star and their connection to the evolutionary history of the Milky Way.

1.0.1 The abundances of elements

In astrophysics the elements heavier than hydrogen and helium are called metals. The abundance, a parameter related to the number density of all elements, is customarily referred to hydrogen, the dominant species in the Universe, whose abundance is set to 10^{12}. It is convenient to express abundance on a logarithmic scale[1]. Figure 1.1 displays the abundances of the elements in the solar system material against their atomic number Z.

The noticeable feature is a overall decline with a sawtoothed pattern. This is because the two most abundant elements, hydrogen and helium, are produced at the birth of the universe while the heavier elements are synthesized in stellar interiors. The valley at Li, Be and B occurs as these elements are destroyed in stars. The odd-even effect is more clear where the elements with even Z are more abundant than the neighbouring odd atomic elements. This is because the elements with even Z have more isotopes and are more stable over odd Z elements as the nucleons in them are paired up.

The elements heavier than boron (B) but lighter that Fe are produced in charged particle reactions during thermonuclear burning in stars. The innate charge of these elements is sufficiently low, hence the nuclear force, which is effective at short distances, overcome the Coulomb repulsion and the nuclei can capture charge particles such as protons and alpha particles. The elements beyond Fe have sufficiently high charges that extreme energies are required for the interacting protons to overcome the Coulomb barrier. In stellar interiors the temperatures are not high enough for heavy elements to be formed via proton-capture. Instead, they formed via feeding the seed nuclei such as Fe or Ni with neutral particles, neutrons, as there is no Coulomb repulsion to overcome in interactions between neutrons and heavy elements (Sneden et al. 2008). Thus a sequential thermonuclear burning within stellar cores and neutron capture reactions ultimately results in building up the elements in the Universe (Iliadis, 2007).

---

[1] The abundance of an element X is denoted as $\log\epsilon(\mathrm{X}) = \log(\mathrm{N}_X/\mathrm{N}_H) + 12.0$, where N_X and N_H are the number densities of element X and hydrogen atoms in the stellar atmosphere. This relation is normalized to solar abundance on a logarithmic scale as $[\mathrm{X/H}] = \log(\mathrm{N}_X/\mathrm{N}_H)_{star}$ - $\log(\mathrm{N}_X/\mathrm{N}_{H Sun}$

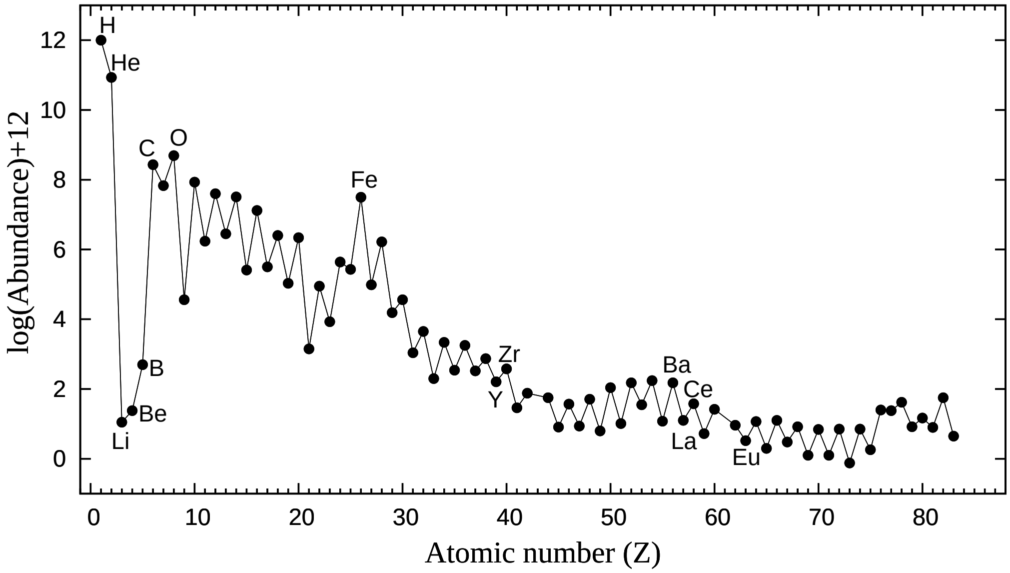

Figure 1.1: The present-day solar photospheric elemental abundances as a function of atomic number with abundances taken from Asplund et al. (2009).

1.1 Nucleosynthesis and the stellar evolution

All stars follow through the same basic evolutionary phases: protostar, pre-main sequence, main sequence and post-main sequence. The lifespan of star in each phase and the types of chemical elements it will synthesize depends on its initial mass. Higher the mass of the star, the shorter its life time. The changes in the evolutionary phase of a star are accompanied by corresponding changes in effective temperature (T_{eff}), surface gravity ($\log\ g$) and its chemical compositions. All the phases during the lifespan of a star are conveniently displayed on a diagram of luminosity versus T_{eff} which is the well known **HR** diagram (**H**ertzsprung **R**ussel diagram), as shown in figure 1.2, named after two famous astronomers Ejnar Hertzsprung and Henry Norris Russel.

1.1.1 Pre-main sequence

Stars are initially formed from the fragmentation of giant molecular clouds of gas and dust which are generally cool and dense. The high density of these clouds ensures the self-gravity to become stronger and overcome the effects of thermal pressure, turbulence, magnetic fields etc. This increased gravitational attraction favours collapse so that an isothermal cloud of certain mass and temperature begins to collapse under

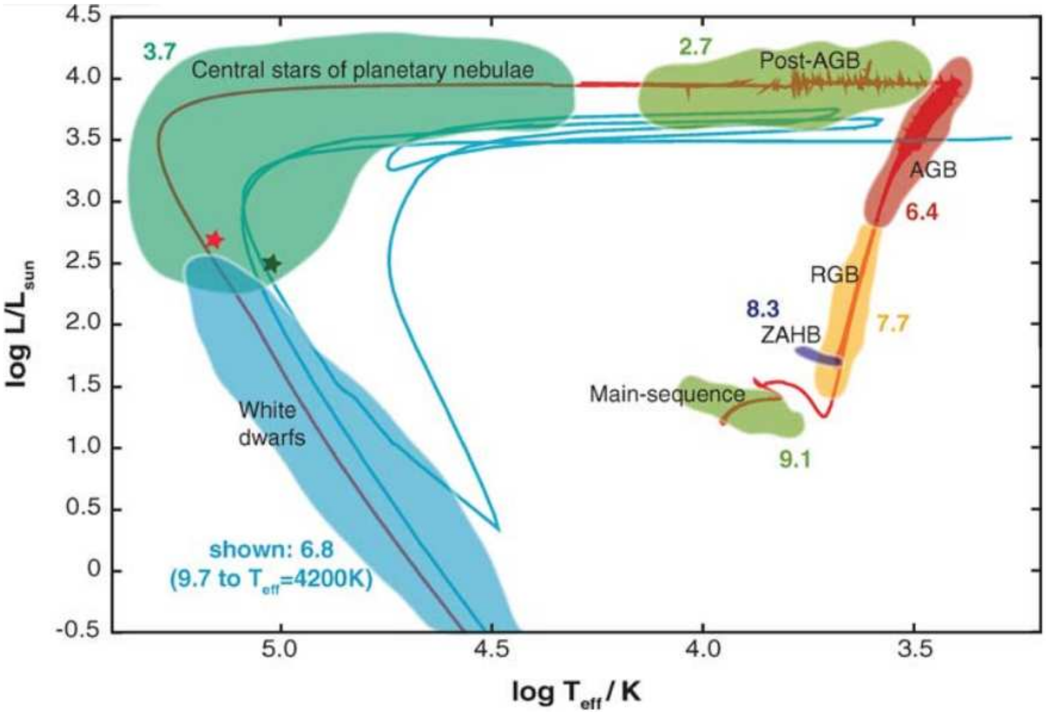

Figure 1.2: Various phases in the evolution of a 2 $M_\odot$ star is shown in H-R diagram. Courtesy: Herwig (2005)

its own weight. The contracting cloud fragment converts its gravitational potential energy into thermal and radiative energies. As nearly half of the energy is radiated away from the surface layers, the cloud contracts further leading to a rapid rise in central temperature. This heats up the core to the ignition temperature at which the hydrogen fusion reactions begin to occur. The contracting cloud fragment before reaching hydrostatic equilibrium is called a protostar. As the equilibrium establishes, but before the ignition of core fusion reactions, the star is undergoing its pre-main sequence evolutionary phase.

Afetr the onset of fusion reactions, the star is so hot that a temperature gradient builds up from the centre to the outer boundary of the gaseous blob. The atmosphere is in hydrostatic equilibrium such that at any radial point r, the inward gravitational attraction exactly balances the outward total pressure.

$$\frac{dP}{dr} = \frac{-G\,M(r)\,\rho(r)}{r^2} \tag{1.1}$$

where M(r) and ρ(r) are the cumulative mass and density inside the shell at a radial distance r.

1.1.2 Main sequence

The main sequence phase, during which the star converts hydrogen into helium, is a longest stage in a star's life and can take from 10^6 years for a massive star ($\approx$ 25 $M_\odot$)[2] to 10^{10} yr for a low mass star (Wallerstein et al., 1997). On the HR diagram, the main sequence is the most populated and appears as a band of stars. The width of this band indicates the difference in chemical composition and mass of stars. The star spends 80% of its lifetime on the main sequence burning hydrogen quietly in its core where the temperature is the highest. The structure of the star is characterized by a radiative interior with a convective outer envelope. Depending on the mass, the hydrogen burning occurs via one of two processes: the PP chain or the CNO cycle (Rolfs & Rodney, 1988).

PP chain

The PP chain essentially converts four protons into one helium atom while also releasing energy in the form of a gamma rays (γ) and a neutrino (ν). There are three distinct sets of reactions referred collectively as PP chains. At the core temperatures $T \sim 1 \times 10^7$ K, once two protons fused together to form a deuteron atom further reactions follow quickly. Depending on the temperature and relative importance, the initial reactions:

$$\begin{aligned} \mathrm{H}^1 + \mathrm{H}^1 &\rightarrow \mathrm{D}^2 + \mathrm{e}^+ + \nu \\ \mathrm{D}^2 + \mathrm{H}^1 &\rightarrow \mathrm{He}^3 + \gamma \end{aligned}$$

have three possible endings. For temperatures in the range $T \sim 1$ - 1.4×10^7 K, PPI reaction occurs.

$$\text{PPI:} \qquad \mathrm{He}^3 + \mathrm{He}^3 \rightarrow \mathrm{He}^4 + 2\,\mathrm{H}^1$$

For $T \sim 1.4$ - 2.3×10^7 K and if some He^4 is present, PPII reaction is favoured over PPI.

$$\begin{aligned} \text{PPII:} \quad \mathrm{He}^3 + \mathrm{He}^4 &\rightarrow \mathrm{Be}^7 + \gamma \\ \mathrm{Be}^7 + \mathrm{e}^{-1} &\rightarrow \mathrm{Li}^7 + \nu \\ \mathrm{Li}^7 + \mathrm{H}^1 &\rightarrow 2\,\mathrm{He}^4 \end{aligned}$$

For $T > 2.3 \times 10^7$ K, a less efficient reaction, PPIII chain, proceeds as

---

[2] $M_\odot$ = 1 solar mass = 1.99×10^{30} kg

$$\mathrm{Be}^7+\mathrm{H}^1 \rightarrow \mathrm{B}^8+\gamma$$
$$\mathrm{B}^8 \rightarrow \mathrm{Be}^8+\mathrm{e}^++\nu$$
$$\mathrm{Be}^8 \rightarrow 2\,\mathrm{He}^4$$

The first generation stars whose composition is essentially hydrogen and helium, the PPI chain is the dominant hydrogen burning process. The subsequent generation of stars formed from the debris of the first generation stars will contain heavy metals such as carbon (C), nitrogen (N), oxygen (O). The presence of C, N and O in the stars permits an alternate hydrogen burning process, CNO cycle, to occur. However the core temperature required for CNO cycle is much higher than that required for the PP chain. Therefore low mass stars ($M \leq 1\ M_\odot$) follow PPI chain for energy generation while the higher mass stars whose internal temperatures $> 2.5 \times 10^7$ follow CNO cycle for hydrogen burning. However the exact temperature where the CNO cycle dominates over PPI chain depends not only on the mass but also on the metallicity of the star as a high mass star with low metallicity would have insufficient amounts of heavy elements for the CNO cycle to proceed. (Iliadis, 2007).

The complete CNO cycle occurs in two paths, one which turns C to N, the CN cycle, and the other one which turns O to N, the ON cycle. The relative occurance of these reactions is about 10^4:4.

Along the reaction paths the relative abundances of seed nuclei (C, N, O) vary but the total abundance of the seed nuclei is conserved. This chemical signature is used to distinguish between the types of nuclear burning processes a star has undergone. The outcome of CNO cycle is the same as that of PP chain where four protons combined into a single helium atom. Theoretically these hydrogen core-burning stars have no mechanism that mixes the processed material in the core to the surface of the star (Cannon et al. 1998). Hence the spectrum of a main sequence star is an exact template to the chemical composition of the gas cloud from which the star was formed.

1.1.3 Post-main sequence

When the core hydrogen has been exhausted and helium is all that remains in the core, the thermonuclear reactions cease in the core but continue in a shell around the core where hydrogen still exists. The star has turned off the main sequence track in the HR diagram and migrated onto the red giant branch (see figure 1.2). The core shrinks and liberates gravitational potential energy causing the helium core and surrounding hydrogen-burning shell to increase in temperature. Then the envelope expands and the star's outer radius increases but the surface temperature drops. This fall in the temperature causes a steep temperature gradient and increases opacity in the envelope so that convection carries most of the energy outward. Now the structure of the star is as that shown in figure 1.3, with a small, dense, degenerate He core and a large convective envelope.

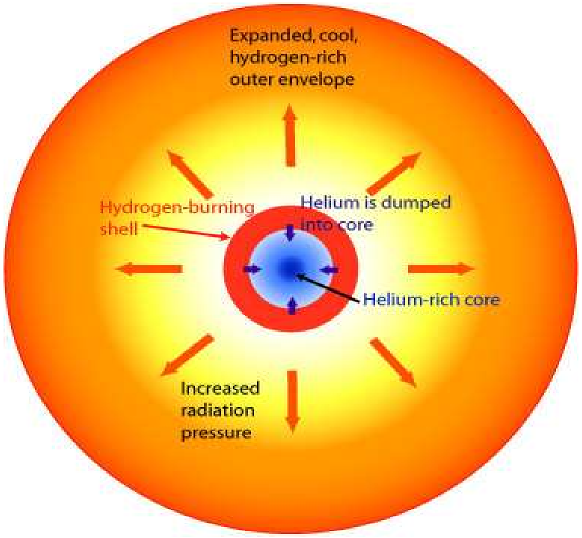

Figure 1.3: A schematic illustration of the structure of a red giant branch star, showing the degenerate He core, H-burning shell and a convective envelope.

The convective zone deepens reaching all the way down to the stellar core and pulls up the elements that have been synthesized during hydrogen burning. At the base of the convective zone carbon can be converted to nitrogen and the convection exposes this freshly processed material to the surface. As a result photospheric chemical composition will be altered with reduced C^{12}, increased N^{14}, He and C^{13}. This phenomenon which occurs in a star when it becomes a red giant is called the first dredge-up. Following this the luminosity increases gradually and the star climbs up the red giant branch on the HR diagram, as shown in figure 1.2.

When the temperature of the core, which has been steadily increasing due to contraction, reaches $T \sim 10^8$, helium burning starts via the triple-alpha process.

The triple-alpha process

As the name suggest, this process combines three alpha particles to form one carbon atom.

$$\mathrm{He}^4 + \mathrm{He}^4 \rightarrow \mathrm{Be}^8$$
$$\mathrm{Be}^8 + \mathrm{He}^4 \rightarrow \mathrm{C}^{12} + 2\,\gamma$$

For low mass stars (M $<$ 2.3 $M_\odot$), the electrons in the hydrogen-exhausted helium core becomes degenerate (Iben 1968; Bertelli et al. 2008). As the ashes of the hydrogen burning shell continues to deposit on the helium core, the core density grows thereby increasing the temperature. However as the gas is degenerate, the temperature continues to increase which in turn increases the energy generation rate. Eventually tremendous amount of energy is released that the electron degeneracy will be lifted in run away process, known as helium core flash. After helium core flash, the radius and luminosity decreases with a slight increase in surface temperature and the star appears on the Horizontal Branch (HB) (Herwig, 2005) where it quietly burns helium in a convective core and hydrogen in a shell. But the stars of mass M $>$ 2.3 $M_\odot$ do not experience the He-core flash as the core remains non-degenerate and burns He quiescently. The structure of the star on the HB is a core that is burning helium into carbon and oxygen, surrounded by a hydrogen burning shell.

The carbon produced in the triple-alpha reaction then captues another alpha particle to produce oxygen as follows:

$$C^{12}+He^{4} \rightarrow O^{16}+\gamma$$

As this process occurs at a slower rate, only a small fraction of carbon is processed into oxygen (Iliadis, 2007).

1.1.4 AGB phase

Once the core helium supply has been exhausted, the helium burning eventually ceases leaving a CO stellar core. As there is no radiation pressure to balance the self-gravity, the core contracts until the CO becomes degenerate. The increasing temperature ignites the helium in a shell around the CO core and the star becomes a highly luminous red giant, but this time ascending the Asymptotic Giant Branch (AGB) (figure 1.2). Not all HB stars reach this stage as low mass stars depending on chemical composition and heavy mass loss during the red giant branch end up as hot extreme HB stars (Möhler, 2004). At the onset of the AGB phase, the star has a structure as shown in figure 1.4: an inactive CO degenerate core, a He fusing shell, a He-rich inter-shell region, a H fusing shell and a H-rich convective envelope (Herwig, 2005).

It is often claimed that all the low to intermediate mass stars (M $\sim$ 0.8 to 8 $M_\odot$) evolve through AGB phase. During the early AGB phase, where the star spends 90% of the total AGB lifespan, the AGB star burns He quietly in a narrow shell surrounding the electron degenerate CO core. The high energy output from the He-burning shell causes the star to expand and pushes the H-burning shell further out to

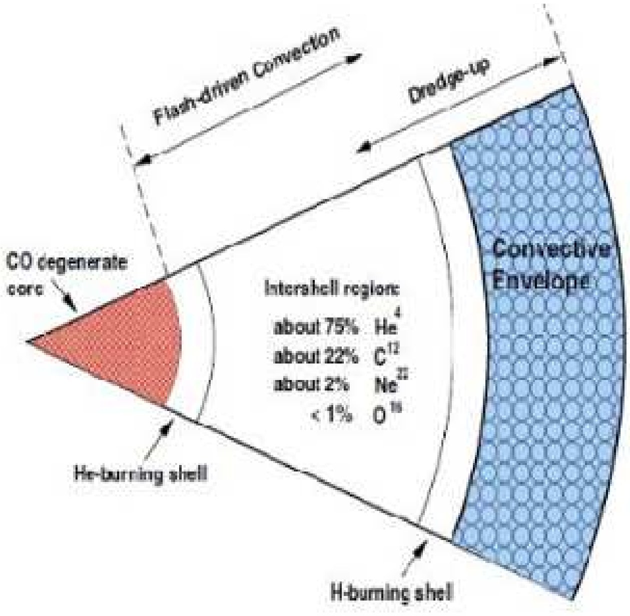

Figure 1.4: A schematic illustration of the structure of an AGB star by Lattanzio and Boothroyd (1997).

large radii which provides most of the luminosity. In the case of high mass stars with M $\gtrsim$ 4 M$_\odot$ the H-burning shell is pushed out so far that it is completely extinguished. This is called the second dredge-up.

Stars of mass M $\lesssim$ 4 M$_\odot$ do not experience second dredge-up and the H-burning shell is not extinguished while the He-burning shell moves closer to the H-burning shell (Iliadis, 2007). This leads to another stage in a star's evolution called the thermally pulsing AGB (TP-AGB). Though it is a very short stage of stellar evolution, the complex nucleosynthetic processes that occurs during this phase is of great consequence in the understanding of s-process element formation and recycling in the cosmos.

The H-burning shell deposits He continuously in the inter-shell region until it reaches a density beyond which the He-burning shell cannot sustain equilibrium. The star ignites the built-up helium thereby sending a flash of energy, thermal pulse, through the inter-shell region to the H-burning shell (Herwig, 2005). Although the initial pulse has no effect on the H-burning shell, the subsequent pulses that are of increasing energy eventually pushes the H-burning shell to the extent that it will be extinguished. At this stage convective envelope penetrate through the area of the H-burning shell down into the inter-shell region and pulls the material from this region and modifies the surface composition. This is known as the third dredge-up (TDU)

(Herwig, 2005).

Once the helium flash has been dissolved the star resettles into equilibrium, re-forming both the H-burning shell, although it has moved further outward, and the inter-shell region. The protons move from the hydrogen rich envelope into the helium zone in low mass AGB stars (1.5-3 $M_\odot$), due to semiconvective mixing. Subsequently, these protons interact with carbon (and nitrogen) in the inter-shell region forming a layer enriched in C^{13} (and N^{14}), called the C^{13} (and N^{14}) pocket.

$$\begin{aligned} C^{12}+H^{1} &\rightarrow N^{13}+\gamma \\ N^{13}+\beta^{+} &\rightarrow C^{13}+\nu \\ C^{13}+H^{1} &\rightarrow N^{14}+\gamma \end{aligned}$$

During the next thermal pulse, the C^{13} is then engulfed by the high density helium of the inter-shell region, releasing neutrons via the $C^{13}(\alpha,n)O^{16}$ reaction. The s-process occurs at low neutron densities ($N_n \approx 10^8$ cm^{-3}) where the time scale for successive neutron captures is very large, typically $\gtrsim$ 10 yr, so that the seed nuclei have enough time to acquire stability over β-decay before capturing another neutron and so the gradual build up of s-process elements and their stable isotopes which fall in the atomic mass number range $90 < A < 208$ (e.g., Ba, La, Ce, Nd etc.)

During the earlier thermal pulses the light s-process elements such as Sr, Y and Zr dominate. For the s-process to progress to the heavy elements (Ba, La, Ce, Nd etc.) the neutron flux must be sufficiently high, or there must be a small reservoir of seed nuclei. Thus, heavy s-process elements are produced predominantly at low metallicity as the neutron exposure per seed nuclei is greater than those at high metallicity. The s-processed material is mixed up to the surface when the H-burning shell is extinguished.

When the helium rich inter-shell in the intermediate mass stars ($5 \leq M_* / M_\odot \leq 8$) reaches a temperature of T $\geq 3.5 \times 10^8$, N^{14} act as a secondary source of s-processing.

$$\begin{aligned} N^{14}+He^{4} &\rightarrow F^{18}+\gamma \\ F^{18}+\beta^{+} &\rightarrow O^{18}+\nu \\ O^{18}+He^{4} &\rightarrow Ne^{22}+\gamma \end{aligned}$$

This Ne isotope is then engulfed by the high density helium, releasing neutrons via the $Ne^{22}(\alpha,n)Mg^{25}$ reaction which is not as efficient as C^{13} process for producing free neutrons. At the tip of the AGB phase the outer envelope has been blown off due to increased luminosity. Thus AGBs are the major contributors of C, N, F and s-process elements to the ISM.

1.1.5 Post-AGB evolution

The increased mass loss from the AGB stars lead to the ejection of the convective envelope and when the mass of the envelope becomes smaller than 0.05 $M_{\odot}$, the stellar effective temperature increases and the mass loss rate decreases and the star begins its post-AGB phase (or) proto planetary nebulae phase, as shown in figure 1.2. They evolve horizontally on the HR diagram with increasing temperature and constant luminosity. The post-AGB phase is a very short phase, about 10^3 to 10^4 yr, and hence identifying them is very difficult. As they have relatively stable atmospheres they are excellent probes to study the AGB nucleoesynthesis and mass loss rates. The dust envelope that was created during AGB phase of low mass stars keep on moving away from the central star and dissolves slowly into ISM. In relatively high mass stars the surface temperature rises fast enough and ionize the dust shell which appears as a nebula around a central star.

All the low to intermediate mass stars ($M \sim 0.8$ to 8 $M_{\odot}$) evolve through the planetary nebula phase before finally ending their lives as white dwarfs (see Herwig 2005, for a recent review). This gaseous nebulae is the remnant of the deep convective envelope that once surrounded the core, which is now exposed as the central star of the planetary nebula. Thus the composition of the nebula should reveal information about the chemical processing that took place during the AGB phase, and more precisely, information about the final thermal pulses (Karakas et al. 2007). At temperatures of the central star ($\sim 10^4$ K) the nebular material gets ionized and visible in optical. The nebula expands to a great extent that it dissolve slowly into the ISM and enrich it with s-process elements that have been synthesized inside the stars during AGB phase. Hence the planetary nebulae play a vital role in the Galactic chemical evolution studies.

All the stars with mass $M < 4$ $M_{\odot}$ are fated to end their lives as white dwarfs which present the densest form of matter, surpassed only by neutron stars and black holes, supported by degenerate electron pressure. These are very hot with central temperature as high as 10^5 K. As there is no fuel to power them, they dissipate thermal energy into space and fades away slowly. All the stars with mass $M > 4$ $M_{\odot}$ evolve through various stages and end their lives as a neutron star or black holes, as shown in figure 1.2.

1.1.6 Supernova: r- process

Stars with initial masses exceeding 11 $M_{\odot}$ are capable of igniting successive burning stages in their cores using the ashes of the previous core burning stage as fuel.

The burning stages follow hydrogen burning, helium burning, carbon burning, neon burning, oxygen burning, silicon burning and eventually forming into burning shells surrounding an iron core, as shown in the figure 1.5.

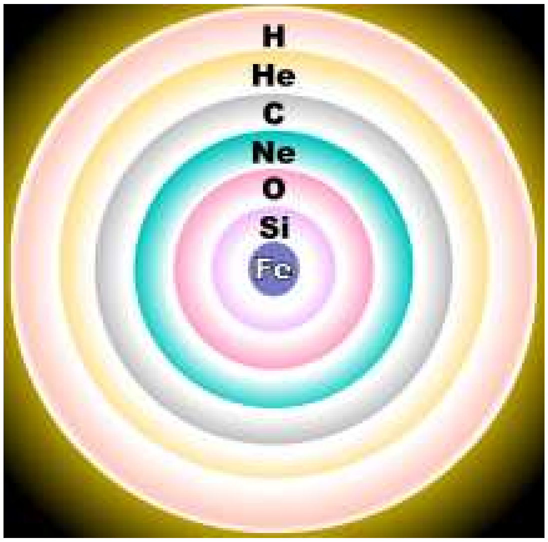

Figure 1.5: The onion skin like structure of a massive evolved star just before core collapse.

As iron has the highest binding energy per nucleon of all the elements, no further fusion reactions occur and hence the iron core keeps on growing due to the ashes of the shell burning. When the core's mass, initially supported by electron degeneracy pressure, surpass the Chandrasekhar mass limit ($\approx 1.4\ \mathrm{M}_{\odot}$), it will no longer be able to support itself by electron degeneracy pressure and a catastrophic collapse begins. During the core-collapse the rapidly shrinking core heats up, producing high-energy γ-rays that photodisintegrate the iron nuclei into helium and free neutrons.

$$\mathrm{Fe}^{56}+\gamma \rightarrow 13\,\mathrm{He}^{4}+4\,\mathrm{n}$$

which in turn split helium nuclei into protons and neutrons, the basic building blocks of elements, via photodisintegration.

$$\mathrm{He}^{4}+\gamma \rightarrow 2\,\mathrm{p}+2\,\mathrm{n}$$

The r-process begins at these high neutron fluxes ($\mathrm{N}_n \approx 10^{21}\ \mathrm{cm}^{-3}$) where the time scale for successive neutron captures is very less, typically $\lesssim 10^{-4}$ s, so that the the seed nuclei (Fe or Ni) does not have time to acquire β-stability and so the gradual build up of r-process elements and their stable isotopes (Iliadis, 2007). Eventually the instability forces the nuclei to decay into stable isotopes after the recession of the neutron flux.

The massive stars (8-9 $M_\odot < M \leq 100\ M_\odot$) are destined to end their life as a core-collapse supernova ejecta (SNe), which can be either type II SNe or type Ib/c SNe. The type Ib/c SNe arise either in binary systems or Wolf-Rayet stars, whereas type II SNe originate in massive stars in the lower mass range (Calura & Matteucci 2006). All these stars explode violently either after electron captures in their O-Ne-Mg core (8-9 $M_\odot < M \leq 11\ M_\odot$) or after Fe-core collapse ($M \geq 11\ M_\odot$) while leaving a neutron star (NS) or a black hole (BH) as a residue (Prantzos 2008). The mass of the remnant depends on the initial mass of the star and on the mass left to it before the explosion. The mass of the neutron stars are well constrained by the observations of pulsars in binary systems (Thorsett & Chakrabarty 1999) as

$$M_{NS} = 1.35 M_\odot \qquad 9 < \mathrm{M}/\mathrm{M}_\odot < 25 \tag{1.2}$$

Though the mass of the BH is not known observationally as a function of the progenitor mass, theoretical models (Woosley & Heger 2007) predict that as a result of high mass losses for $M \geq 25\ M_\odot$, the average black hole mass of 3 $M_\odot$. Type II SNe is responsible for the production of α-elements, such as O, Mg, Si, S, Si and Ti (Edvardsson et al. 1993) and r-process elements (Sneden et al. 2008) such as Sm, Eu along with very small quantities of Fe-peak elements.

1.1.7 Supernova: Fe-peak elements

A substantial amounts of Fe ($\sim 0.6\ M_\odot$ per event) and Fe-peak elements are mainly synthesized in Type Ia SN with none or little contribution of the α-elements. Stars in the mass range ($M \sim 0.8$ to 8 $M_\odot$) when evolve through C-O white dwarf phase act as a progenitors of type Ia SNe if they have a binary companion, such as a main sequence star, a (super) giant, or a He star, whose outer layers are accreted onto the surface of white dwarf through intense winds. When the mass of the accreting C-O white dwarf surpass the Chandrasekhar mass limit ($\approx 1.4\ M_\odot$), electron degeneracy pressure no longer supports its weight. This leads to raise in core temperature thereby igniting carbon fusion. As the degeneracy pressure is independent of temperature, the white dwarf is unable to regulate the burning process like normal stars (i.e., expand and cool in order to counterbalance an increase in thermal energy), so it is vulnerable to catastrophic fusion reactions. As there is no excess production of neutrons in this process, no r-process elements are formed.

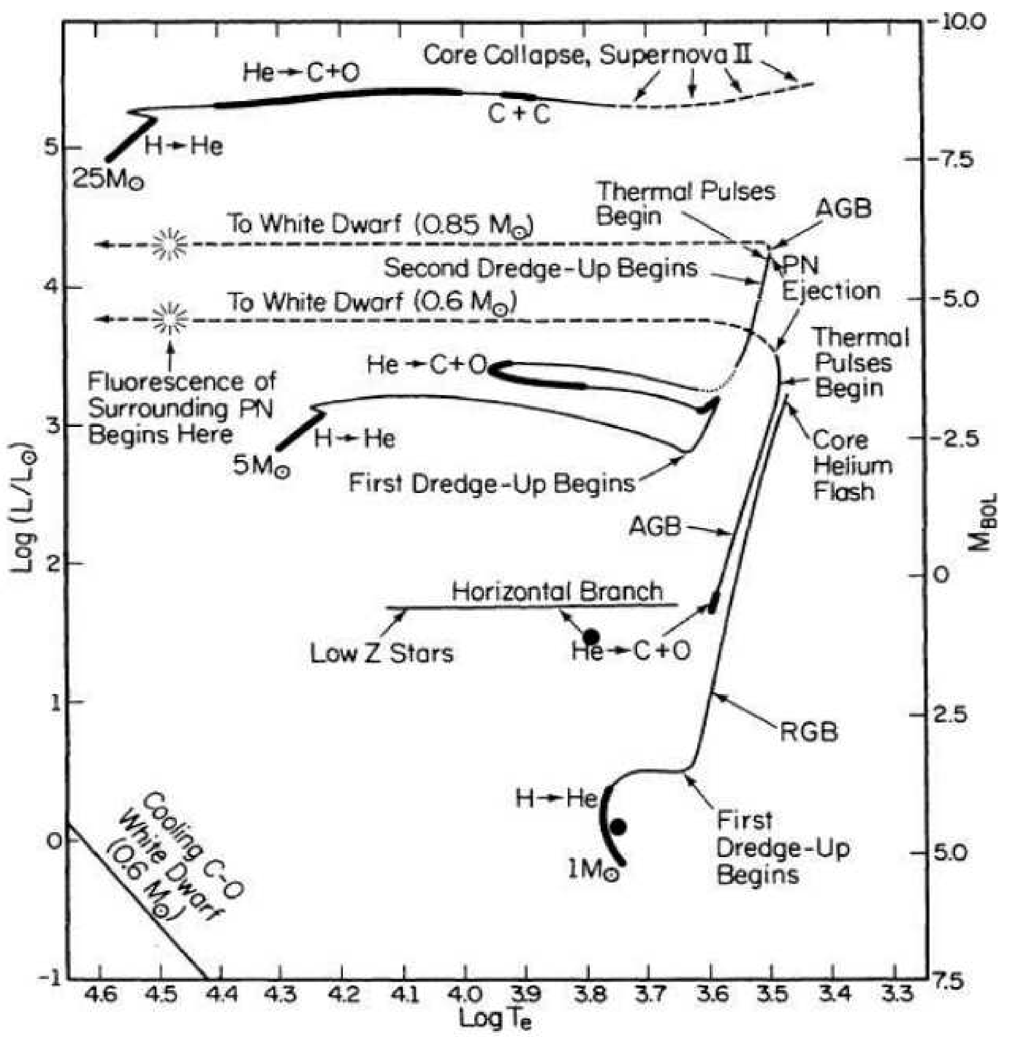

Figure 1.6: The HR diagram showing main phases of one, five and twenty five solar mass stars. Thick lines indicate the events of nuclear processing. Courtesy: Iben (1985).

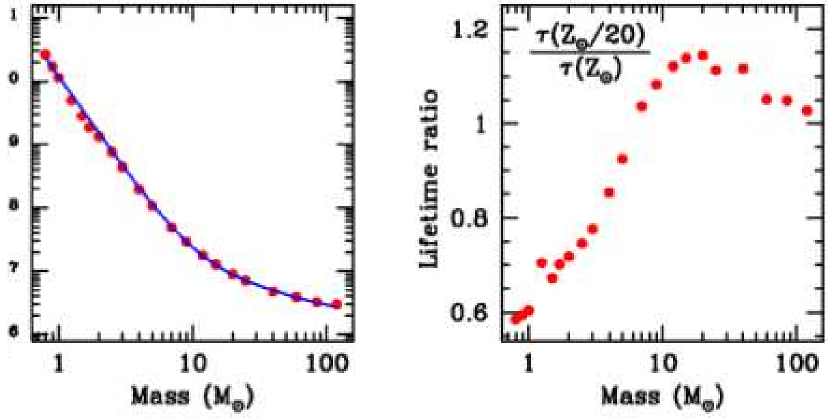

Figure 1.7: Left: The lifetimes of stars of solar metallicity Z$_\odot$. Right: the ratios of stellar lifetimes at different initial metallicities of Z$_\odot$/20 and Z$_\odot$. Courtesy: Prantzos et al. (2008)

The contributions from Type II and Type Ia SNe to the chemical enrichment of the galaxy can be traced by the enrichment of the ISM first with α and r-process elements released in Type II supernova events and then with Fe-peak elements ejected from Type Ia supernova. The main phases and possible end products in the evolution of one, five and twenty five solar mass stars are shown in the figure 1.6. The lifetime of stars of various initial masses and metallicities (or) the time scales over which the ISM will be enriched with certain elements from progenitors of different initial masses are shown in the figure 1.7.

1.2 Galactic structure

The Milky Way has an elegant structure that shows both order and complexity. The current understanding of our Galaxy is that it is a large spiral galaxy whose luminous part hosting multiple stellar populations can be divided into three components: a boxy/peanut shaped bulge, a dual disk system and a dual stellar halo. An artistic impression of the Milky Way galaxy is shown in figure 1.8 (top view) and in figure 1.9 (side view). Furthermore, stellar overdensities and structures are seen in velocity space (Antoja et al. 2012) as well as in three dimensional space (Belokurov et al. 2006). As explained below, each of these stellar subsystems present its own chemical and dynamical properties, most probably holding the clues to different formation mechanisms. Therefore, by investigating their properties it is possible to unravel the formation and evolutionary history of our Galaxy.

1.2.1 Bulge

The bulge occupies the central portion of our Galaxy containing a total mass of $\sim 2 \times 10^{10}$ $M_\odot$ (Sofue, Honma & Omodaka, 2009). It has an elongated boxy structure, well established as a bar (Dwek et al. 1995) as suggested by de Vaucouleurs (1964), with a scale length of approximately 1.5 kpc (Zoccali 2010). The bulk of its stellar population is older than 10 Gyr (Zoccali et al. 2003; Clarkson et al. 2008) and has a multi-modal metallicity distribution, with peaks at [Fe/H] $\approx$ -0.6 dex, -0.2 dex and +0.4 dex (Bensby et al. 2013), in the range $-1.5 \lesssim$ [Fe/H] $\lesssim 0.5$ dex, with a mean value of ≈ -0.25 dex. The bulge shows cylindrical rotation (Kunder et al. 2012) with a peak velocity of ~ 75 km s^{-1} and has a large velocity dispersion of 120 km s^{-1}, that decreases out with Galactocentric radius, R_{gc}, (Minniti & Zoccali 2008). Though the formation history of the bulge is not well understood, most observational evidence indicates that the bulge could be the result of two formation processes: an old spheroid with a rapid star formation history (i.e. showing enhanced [α/Fe] ratios

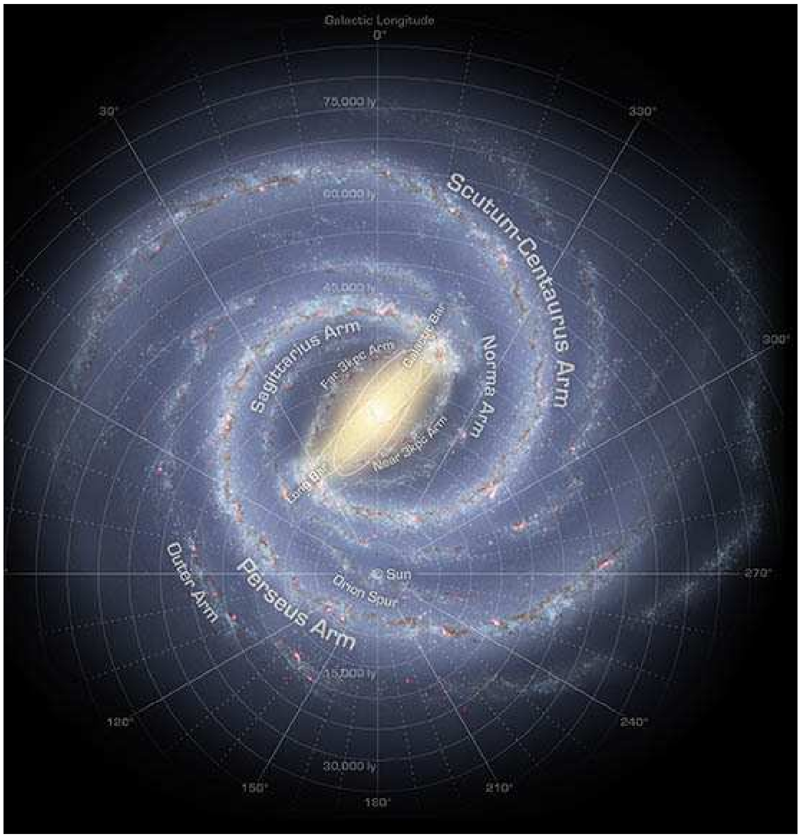

Figure 1.8: An artistic impression of the top view of the Milky Way galaxy. Credit: NASA Spitzer Space Telescope.

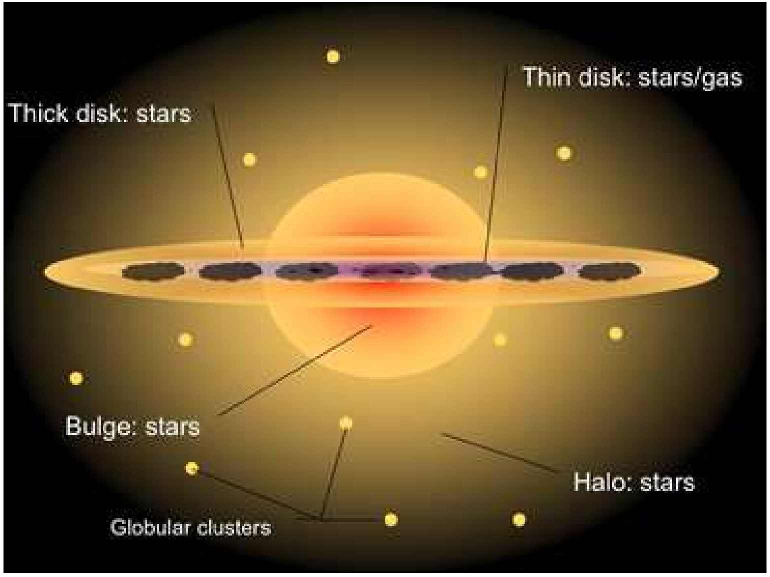

Figure 1.9: An artistic impression of the side view of the Milky Way galaxy.

over other Galactic populations) and a significant fraction of young and intermediate stars formed over a long time scale via the dissipational collapse (Melendez et al. 2008; Hill et al. 2011). The present understanding is that bulge is the central region of the Milky Way where other Galactic stellar populations meet and overlap (Bensby et al. 2013).

1.2.2 The disk

The spiral disk of our Galaxy is a rotationally supported and highly flattened structure with a total mass of approximately 6×10^{10} $M_\odot$ (Sofue, Honma & Omodaka, 2009) locked in gas, dust and stars/open clustes. Based on star counts towards the Galactic North Pole, Gilmore & Reid (1983) found that the Galactic disk has two distinct overlapping components: the thin disk and the thick disk. The thin disk has a radial extent of up to $\sim$ 15 kpc (Ruphy et al. 1996) and follows a double exponential density distribution with a scale length of 3.4 kpc (Cheng et al. 2012) and a scale height of 0.3 kpc (Jurić et al. 2008). This is the youngest component of our Galaxy with no stars older than $\sim$ 9 Gyr, covering a range of metallicity of $-1.0 \lesssim$ [Fe/H] $\lesssim +0.4$ dex which peaks at [Fe/H] ≈ -0.2 dex (Nordström et al. 2004). The average metallicity of thin disk at the position of the Sun is $\sim -0.06\pm0.22$ while at 11 kpc it drops to -0.48 ±0.12. This signifies that the thin disk shows a strong abundance gradient (Bensby et al. 2011). The circular velocity of the thin disk sample lags by $\sim$ 9 km s^{-1} from the LSR velocity of 220 km s^{-1} and has velocity dispersion of (39±2, 20±2, 20±1) on space velocity components(U, V, W) (Soubiran et al. 2003). Instead, the thick disk component host very old and metal poor stars with a range of $\sim$ 8 - 13 Gyr in ages (Fuhrmann 1998; Reddy, Lambert & Allende Prieto 2006) and $-2.2 \lesssim$ [Fe/H] $\lesssim 0.0$ dex in metallicity (Bensby et al. 2007). The stellar density profile of thick disk is well fitted with a double exponential function with a scale length of 1.8 kpc (Cheng et al. 2011) and a scale height of 1.35 kpc (Binney & Merrifield 1998, Reddy & Lambert 2008). Typical thick disk stars have generally lower net orbital rotational velocities with larger velocity dispersions (Soubiran et al. 2003; Wyse et al. 2006) and exhibit higher [α/Fe] ratios over thin disk sample and show no sign of radial metallicity gradient (Bensby et al. 2011).

The run of [α/Fe] versus [Fe/H] diverge at [Fe/H] ~ -1.0, with the thin disk [α/Fe] declining towards higher [Fe/H] while the thick disk [α/Fe] stays constant upto -0.4 dex from where it begins to decline towards solar metallicity (see figure 1.10). The α-elements are mainly synthesized during type II SN explosions of massive stars on a relatively short time scale ($\sim 10^7$ yr), whereas iron is produced by type Ia SNe on a much longer time scale ($\sim 10^9$ yr). Hence, [α/Fe] can act as a clock to probe the star formation history of a Galactic component. The [α/Fe] enrichment time scales coupled with the observed ages of stars in the thin and thick disk suggest that the thick disk has formed on short time scales but much earlier than the thin disk. The observational evidence is available from the studies of solar neighbourhood field dwarfs that the thick disk has evolved to solar metallicities probably within $\sim$ 3 Gyr and experienced strong enrichment from both SNe II and SNe Ia during this period before ending star formation about $\sim$ 8-9 Gyr ago in the history of Galaxy formation (Bensby et al. 2007).

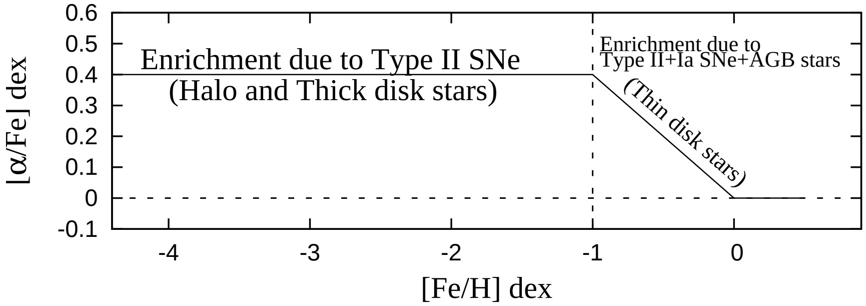

Figure 1.10: A schematic representation of variation of [α/Fe] with metallicity.

Whereas the thin disk formation has been well explained by the dissipational collapse of gas clouds, the formation of the thick disk is now well understood. Various formation mechanisms have been proposed for thick disk component based on violent relaxation and secular evolution. Among the models involving violent origin are (i) the heating scenario (Quinn et al. 1993; Kazantzidis et al. 2008), where the thick disk has originated from the dynamical heating of pre-existing thin disk by satellite mergers. (ii) the accretion origin (Abadi et al. 2003) that invokes that the thick stars were formed in dwarf galaxies and then absorbed into Milky Way disk from orbits that reached near the Galactic disk plane. (iii) in-situ mechanism, where the thick disk stars formed through chaotic mergers of gas rich systems, prompting simultaneous early star formation before and during the mergers, and that thin-disk component formed after the merger events settled down (Lee et al. 2011). The secular evolution involves the resonant scattering of stars with the spiral arms or non-resonant scattering by molecular clouds (Rŏsker et al. 2008; Schönrich & Bineey 2009) and the Galactic bar (Minchev & Famaey 2010). The scattering of stars increases the velocity dispersion for old population and also cause them to move radially from the inner (outer) to the outer (inner) regions.

1.2.3 The halo

The halo is a spheroidal Galactic structure supported by pressure and surrounds the disk and bulge components occupying a total mass of 2×10^9 $M_\odot$. The bulk of the halo consists of dark matter: an invisible material of unknown composition, whose presence is deduced by its gravitational influence. The halo has stellar component consisting of a spheroidal collection of stars, known as globular clusters, whose presence make it as a oldest remnant (age $\sim$ 10-15 Gyr) of our Galaxy. Several surveys carried out over the past few decades have shown that stellar halo, indeed, is divisible into two globally overlapping stellar components (Carollo et al. 2007, 2010). The first component, or inner halo, dominates the population of halo stars found up to 10-15 kpc from the Galactic center whose stellar density can be parametrised as a power law, $\rho_{in} \sim \mathrm{r}^{-\alpha}$ with $2 \lesssim \alpha \lesssim 3$ (Bell et al. 2008). It has a modestly flattened distribution of stars with a major to minor axis ratio of $\sim$ 0.6 and a mean metallicity of [Fe/H] $\sim$ -1.6 dex. The kinematics of the stars are characterized by a zero to slightly prograde mean rotational velocity of 7±4 km s^{-1} with large velocity dispersions of (σV_R, σV_ϕ, σV_z) = (150±2, 95±2, 85±1) km s^{-1} (Carollo et al. 2010). In contrast, the second component, or outer halo dominates beyond 15-20 kpc and exhibit a more spherical stellar density distribution, $\rho_{out} \sim \mathrm{r}^{-\alpha}$ with $3 \lesssim \alpha \lesssim 4$ (Bell et al. 2008) with an axis ratio of 0.9 (Carollo et al. 2007). The metallicity distribution of its stars peaks at [Fe/H] $\sim$ -2.2 dex, and exhibit a clear retrograde circle rotation of -80±13 km s^{-1} with velocity dispersions of (159±4, 165±9, 116±3) km s^{-1}.

Recent surveys such as SDSS/SEGUE suggest that the stellar halo contains a number of substructures in spatial distribution (Jurić et al. 2008) or kinematics (Schlaufman et al. 2009) of constituent stars. Now it is believed that a fraction of halo was formed out of tidal debris of accreted satellite galaxies (Cooper et al. 2010), even though in-situ star formation has played a role (Helmi 2008; Zolotov et al. 2009).

1.3 Galactic archaeology

From the discussion above, we know that various luminous components of the Galaxy have assembled at different epochs, as inferred by their ages, and each one of them has evolved with a distinct chemistry and dynamics. This must be related to the different formation mechanisms and enrichment levels that each component has experienced. According to the first galactic formation models, the Milky Way began as one spherical cloud of gas–the protoGalaxy–that was poor in metals and contracting rapidly towards its center of gravity (Eggen, Lynden-Bell & Sandage 1962, hereafter ELS).

As the cloud condenses to smaller radii, some of its energy would be lost to heat in a dissipative collapse. The energy dissipation coupled with the increasing rotational speed deduced from the conservation of angular momentum induce the cloud to collapse anisotropically along its rotational axis, so that it would be quickly deformed to progressively flatter configurations until finally, the central component would be surrounded by a fast spinning thin disk of gas supported by rotational equilibrium. During the collapse phase, the cloud would be forming clusters and stars. As the initial gas was metal poor and so were the stars formed out of it. As the clusters and stars are dissipationless systems, they would inherit and preserve not only the velocity of the gas in which they formed but also the metallicity at their time of birth. These first stars would inject metals into the remaining gas on different time scales, as stars of various masses have different lifetimes to pollute the Galactic chemical inventory (see figure 1.7). Thus the present observed spatial, kinematics and chemical properties of stars and clusters would unravel the major phases of Galaxy's formation and evolution.

In contrast, evidence has accumulated over the past few decades that mergers had played an important role in the formation process, particularly of the stellar halos where one can see wealth of substructures (Helmi 2008; Klement 2010, Nissen 2010). While studying the globular clusters in the Galactic halo, Searle & Zinn (1978) have noticed that some clusters are significantly older than others. The spread in the age suggests that they have not been formed in a rapid, dissipational collapse as proposed by ELS. Recent detections of the accretion of dwarf galaxies show that merger is a continuing way for the survival of Galaxy (Ibata et al. 1997; Yanny et al. 2003). The collective evidence now suggest the low angular momentum material has formed the stellar halo and the bulge on a short time scale as suggested by ELS and mergers with dwarf galaxies also contributed to the halo, but most of them happened before the formation of the thin disk.

Theoretical ideas about mergers in the usual ΛCDM[3] universe predict that the rate of mergers was much higher in the past with a marked decline in the rate at about 8 Gyr ago. The history of mergers when coupled with the formation of thick disk stars explains why the Galactic thick disk stars are old (Reddy et al. 2006). But the lack of cosmic scatter in chemical composition of solar neighbourhood thick disk stars suggest that they may not have come from variety of satellite galaxies. Moreover, the abundance analyses of stars in dwarf spheroidal galaxies and the Magellanic Clouds

---

[3] The ΛCDM or Lambda-CDM model is the standard model of Big Bang cosmology, where Λ is cosmological constant associated with dark energy and CDM stands for cold dark matter.

(Shetrone et al. 2003; Hill 2004) show a variety of abundance patterns, each unlike those of the thick disk. However, it is possible that the dwarfs galaxies that had merged long back may have abundance patterns distinct from those of the surviving dwarf spheroidal and irregular galaxies.

The chemical composition analyses of dwarfs in the solar neighbourhood (Bensby et al. 2005; Reddy et al. 2006) suggest that a part of the thin disk has evolved rapidly to [Fe/H] $\sim$ -0.3, prior to the disruption of the gas by merger events. After the merger, the star formation would have ceased and the thick might have originated from the dynamical heating of the former thin disk due to frequent encounters with the satellite galaxies. During the pause in the star formation, the remaining gas of the former thin disk and the metal poor gas of the satellite galaxies accumulates in the Galactic plane, forming a new thin disk. Once enough material has been collected, the star formation is triggered in the new thin disk. In the hiatus before the reconstitution of the thin disk, the gas is contaminated by the ejecta from SNe Ia, which will cause [α/Fe] ratios low for the thin disk over the thick disk. A recent study on the age distribution of open clusters (OCs) in the Milky Way disk also supports that the Galaxy has undergone episodic period of enhanced star formation each lasting about 0.2 Gyr with production of larger clusters (de la Fuente Marcos & de la Fuente Marcos 2004). These authors have ruled out continuous star formation history over the entire Galactic disk. They suggest that the cyclic behaviour of star formation with a period of 0.4±0.1 Gyr could be the result of density waves perturbations and/or interactions with satellite galaxies. There is an impeccable observational evidence that has been manifested in the form of radial metallicity gradient(Janes 1979) suggest that the thin disk did not form all at once, so that the inner regions of the disk are older than the outer parts i.e. favouring the inside-out formation scenario.

When two satellite galaxies, whose formation histories have been imprinted in the chemical and dynamical properties of stellar populations, merge with each other, the outcome will be a large galaxy that will contain detailed information about the formation history of its progenitors. Consequently, by tagging the stars/clusters using their chemistry and dynamics, it may be possible to identify and assign the stars/clusters to each individual satellite galaxy. However, a large galaxy such as the Milky Way may have undergone multiple merger events at different epochs. Hence it is a stiff challenge to identify the remnants of these events, particularly if the star formation histories of the building blocks are not significantly different.

1.3.1 Suitability of OCs for Galactic archaeology

Since the disk is the defining stellar component for any disk galaxy, understanding it formation and evolution is the heart of the galaxy formation theory. The goal of Galactic archaeology is to use the present day spatial distribution, kinematics, ages and chemical abundances of remnants/stellar aggregates to reconstruct the sequence of events involved in the formation and evolution of the Galaxy. The fact that stars numbering hundreds to thousands are born in rich aggregates – stellar associations and OCs – is supported by observations in optical, infrared, millimeter and radio wavelengths (Carpenter et al. 2000; Lada & Lada 2003). The existence of stellar aggregates at earlier epochs are also observed in the form of old OCs, stellar associations and moving groups (De Silva et al. 2009). In addition the theoretical hydrodynamical simulations indicate that the star formation occurs in groups, where a giant molecular cloud undergo fragmentation preventing collapse onto a single star (Jappsen et al. 2005). A typical example of a Galactic open cluster and its color-magnitude diagram (equivalent of HR diagram) are shwon in figure 1.11 and figure 1.12.

Evolution and properties of OCs

The structure of most OCs is divided into two subsystems: the dense core and the sparse halo (corona). All the stellar content of an OC presumably formed at the same time from the same parent interstellar gas cloud, thus sharing similar initial conditions (Bonatto & Bica 2005). Stellar and dynamical evolution coupled with frequent interactions with Galactic structures changes the morphology and the internal mass distribution of clusters (Bergond et al. 2001). In the process of dynamical relaxation, the inner core of the cluster contracts and transfer energy effectively to the outer halo, resulting in its expansion. As a result of mass segregation high mass sink towards the cluster centre while low-mass stars are transferred to the halo. Theoretically, the interior contraction further leads to a catastrophic rise in central density (Lynden-Bell & Wood 1968). This runaway is halted when hard binaries[4] form near the centre and release energy through three-body encounters (Hills 1975). OCs dissolve over time thanks to tidal forces and feed stars into the field. The vast majority of field stars that we observe today sample a complex mixture of stellar populations with different ages and metallicities. The youngest OCs may be intact. The oldest OCs (or the less-massive ones) may be totally disrupted. Thus, the field stars do not fully sample

---

[4] A binary star having a binding energy greater than the mean kinetic energy of the stars in the binary system

Figure 1.11: A typical example of a OC (NGC 2682) in our Galaxy where a single giant molecular cloud fragments into a large number of stars. Depending on the initial mass, each star evolve through the phases as mentioned in previous Section 1.1.

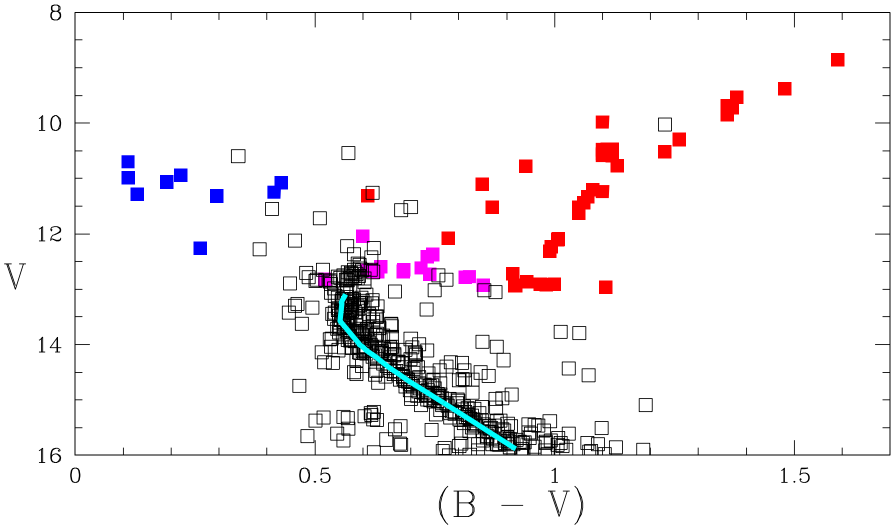

Figure 1.12: A color-magnitude diagram (CMD) of above open cluster: The cyan line indicates the main sequence, the blue filled squares are the high mass stars, magenta filled squares represent the sub giant branch and the red filled squares corresponds to stars on red giant branch. The scattered open squares represent the field star contamination to the CMD.

the age distribution of OCs and, in particular, the youngest stellar generations are under-represented by field stars.

If star-forming aggregates have, as commonly expected, unique chemical signatures, then it should be possible to tag samples of stars with precise chemical compositions to common star forming events. Therefore a detailed chemical abundance patterns, when sufficiently different in one or more elements, offer the possibility to reconstruct now dispersed stellar aggregates of the protogalactic disk and so improve our basic understanding of the disk formation process (Bland-Hawthorn & Freeman 2004). The presence of chemical homogeneity among cluster members has been shown by the study of OCs, see, for example, spectroscopic analyses of the Hyades (Paulson et al. 2003; De Silva et al. 2006) and Collinder 261 (Carretta et al. 2005; De Silva et al. 2007). This observed chemical homogeneity among cluster members signifies that the proto-cloud is well mixed, and hence, the abundance pattern of a cluster bears the signature of chemical evolution of the natal cloud. Theoretically, the high levels of supersonic turbulence is associated with star formation in giant molecular clouds (McKee & Tan 2002), which would result in a well mixed gas cloud. Hence, the chemical abundance patterns OCs can be regarded as "fossil record" of the history of the disk's stellar content.

The abundance variation of chemical elements with R_{gc} i.e., the radial metallicity gradient along (and across) the disk and the gradient's temporal variation over the disk's lifetime put constraints on Galactic chemical evolution models which are controlled, in large part, by variations of quantities as the initial mass function (IMF), the star formation rate (SFR), gas flows in and out of the disk as well as through the disk. Particularly informative diagnostics are the spatial and temporal variations of relative abundances which are traditionally referenced to the iron abundance, i.e., ratios such as O/Fe which primarily samples the relative rates of Type II and Type Ia supernovae and Ba/Fe where Ba measures heavy element synthesis by AGB stars.

Abundance variations across the Galaxy, particularly measurements of the radial gradient, have been measured using a wide variety of objects including H II regions, hot young stars, Cepheid variables, planetary nebulae, red giants, and OCs. Various disagreements and inconsistencies remain - see, for example, Magrini et al. (2010). The actual shape and the gradient of the radial abundance distribution requires derivation of accurate distances and homogeneous abundance measurements. The abundance gradients based on H II regions and planetary nebulae suffer from large uncertainties in distance measurements. In addition, their abundance estimates are uncertain because of large inaccuracies in constraining the electron temperatures in those regions. Moreover, they provide abundance estimates for [O/H], [N/H], [Ne/H], [P/H] and [S/H]-ratios instead of [Fe/H], traditionally referred as a metallicity indicator. Though the Cepheids are good distance indicators and at certain phase are stable enough to analyze their photospheres, because of their youth they represent the current state of the ISM.

As most OCs contain coeval groups of stars bearing the same chemical composition and are at the same distance, basic stellar parameters like age, distance, and metallicity can be determined more accurately than for field stars. Moreover OCs either through high dispersion spectroscopy of their red giants or cooler main sequence stars provide abundance estimates for many elements, essentially, elements sampling all the major processes of stellar nucleosynthesis (i.e. SN II, SNIa and AGB environments). As the ages of clusters range from very young where stars are still forming to nearly 10 Gyr (Dias et al. 2002), by studying clusters of different ages one can map the structure, kinematics, and chemistry of the Galactic disk with respect to Galactic coordinates and time. It is also possible to estimate the birthplace of the OC from its space motion and employing a contemporary model of the Galactic gravitational potential.

1.4 Aim of the thesis

Addressing abundance variations across the Galactic disk and applying chemical tagging requires homogeneous and accurate abundance analysis of as large a sample of OCs as possible. Several recent attempts have been made to construct a homogeneous sets of spectroscopic OC metallicities (e.g., Friel et al. 2010, Heiter et al. 2014) using the existing literature data. But all of them noted that it is hard to quantify systematic errors for individual studies and for individual elements. In spite of astrophysical significance, not many clusters are subjected to high-resolution spectroscopy and most of them lack heavy element abundance measurements. We, therefore continued our modest efforts in this regard and analysed a sample of eighteen OCs using high-dispersion echelle spectroscopy to

1) derive abundances for many elements including the s- and r-process elements for which the measurements are often lacking in the literature (Chapter 4).

2) study the kinematics and membership probabilities of OCs to infer their kinematic origin i.e. whether they belong to either thin, thick or halo stellar populations. We will discuss the evolution of [α/Fe], [s/Fe] and [r/Fe] ratios as a function of metallicity and cluster's age (Chapter 5).

3) study the dynamics of OCs to trace their birth-sites in the Galactic disk and to investigate the radial abundance variations along the Galactic plane by compiling and homogenizing the high resolution data from literature to establish a common distance and abundance scale, and then interpret the results (Chapter 6).

1.5 Outline of the Thesis

Chapter 1 provides a brief introduction to the stellar evolution and nucleosynthesis and its connection to unravel the fossil record of the Galactic disk.
Chapter 2 describes the high resolution observational facilities, data reduction and extraction techniques involved in the analysis of the spectra.
Chapter 3 provides theoretical background, on the formation of spectral lines in stellar atmospheres, required for interpreting the stellar spectra. We also describe model atmosphere grid, radiative transfer code and atomic data used to extract a wealth of information from the stellar spectra.
Chapter 4 provides spectroscopic abundance analysis techniques employed for the derivation stellar atmospheric parameters and chemical composition of the OCs under study. We also briefly review each of the studied clusters and include a summary of available photometry and metallicity results. For relatively explored clusters, we also offer a brief comparison of our derived abundances with those from literature.
In **Chapter 5**, we discuss our results and compare them with the abundances derived from samples of field thin and thick disk stars and finally with the available OC data in the literature. This chapter explains the technique used to prepare a homogeneous set of data while making comparison with literature OCs. We will also discuss the kinematics and membership probabilities of this extended sample of OCs (i.e. our OCs and literature sample). We also investigate the evolution of cluster abundances with metallicity and age and its connection to chemical evolution of the Galaxy.
Chapter 6, deals with the abundance variations along the Galactic disk. We also explore the possible connection between the observed gradients in the Galactic disk with the spiral density waves .
Chapter 7 provides summary and conclusion of the thesis highlighting important results. Here, we also indicate our plan for further studies in this direction.

Chapter 2

Observations and data reduction

2.1 Introduction

This thesis work has made an extensive usage of optical spectra of our program stars obtained with the available astronomical facilities. We devote this chapter to describe the observational facilities providing high spectral resolution, data reduction and extraction techniques involved in the analysis of the spectra.

Each stellar spectrum, a unique fingerprint of that object, is a collection of photons of all wavelengths or frequencies with a superimposition of spectral features (i.e. absorption lines) resulting from the removal of photons at discrete wavelengths representative of characteristic transitions by the atoms, ions and molecules present in the outer layers of stellar atmosphere. These spectral features when resolved distinctly provide a wealth of information on the physical state and turbulence in the stellar atmosphere, chemical composition, radial and rotational velocities and evolutionary status of the star. The spectra of stars are obtained with a dedicated instrumental set up comprising a telescope, spectrograph and a detector. A brief description of each component of the set up is given below.

2.2 Telescope

The primary purpose of an astronomical telescope for studies of stellar photospheres is to collect enough light from distant objects to build a spectra with good signal, required for spectral line analysis. Since, the light gathering capacity of a telescope varies as the square of the diameter of the primary mirror with allowance for the shadowing of the secondary mirror, the faint limit can be extended using a telescope of larger diameter. For a given telescope the faint limit is lower for higher resolutions, as the stellar light is stretched over a larger span.

2.3 Spectrograph

The main function of the spectrograph is the decomposition of incoming polychromatic light beam into its constituent wavelengths or frequencies. This basic components of the spectrograph are an entrance slit, collimator, dispersing elements (prism, grating etc.,), a camera and a detector.

2.3.1 Entrance slit

An Entrance slit (aperture) is placed at the focus of the telescope, and usually has an adjustable width which must be smaller than the full width at half maximum (generally called diameter) of the seeing disc. As a result the slit allows only a fine pencil of telescope beam through it and prevents all unwanted light from the sky and other nearby sources entering the spectrograph.

As the slit width is optimized, it sets a reference point to achieve the best possible angular resolution ($\theta = \frac{\lambda}{d}$, where θ is in radians, λ is the wavelength of the light and d is the diameter of the telescope beam) with a negligible beam divergence for a given telescope under ideal sky conditions. The formula implies that the resolution can be increased by narrowing the slit width, but that also decreases the throughtput and eventually affecting the quality of the spectrum. This problem is even severe for the observation of faint stars. Hence, there is an eternal trade-off between the resolution and the faintness of the stars.

2.3.2 Collimator

The purpose of the collimator is to make the divergent telescope beam coming from the slit into parallel and redirects it towards the dispersing elements in the spectrograph. It is usually an off-axis paraboloid placed such that the light from the slit just fills the collimator, the distance between the slit and collimator is called the focal length of the collimator (f_{coll}). The focal ratio of the collimator (focal length divided by its diameter) must match the effective focal ratio of the telescope to avoid light loss. Hence, the collimator diameter limts the diameter of the light beam in the spectrograph and finally defines the size of the slit image on the detector.

2.3.3 Dispersing element

Dispersing elements such as prism and grating separate the polychromatic light beam into a continuum of monochromatic wavelengths. Prism disperses the light by refraction whose dispersive power depends on the refractive index of the material of the prism that varies with wavelength of light. Since, its dispersion is non linear in wavelength, prisms are often used in low resolution spectrographs or as cross-dispersers in high resolution spectroscopy. Gratings work on the principle of diffraction and produce multiple spectra in integer order direction with equally spaced fringes in each order. Since, its dispersion is almost linear it is widely used in low and medium resolution spectroscopy. To achieve high spectral resolution, a specially designed grating, called **echelle grating**, is used almost universally in astromnomical spectrographs.

2.3.4 Camera

A camera receives the monochromatic beams from the grating or prism and renders them into parallel and finally focuses onto a detector placed at the focus of the camera. The distance between the camera and the focused spectrum is called the focal length of the camera (f_{cam}). The spectrograph used for our observations uses a transmission camera.

Transmission cameras use a system of lenses to correct for chromatic and other optical aberrations and focus the image onto a detector. Lenses are placed generally on-axis with no central obstruction. A wide wavelength coverage requires mutiple elements which will eventually affect contrast in the image as each lens material absorb certain fraction of light, especially in the blue and ultra-violet regions.

2.4 Detector

A detector converts the dispersed stellar spectra that come from the spectrograph into a recordable signal. Common examples are photographic plates, infrared arrays and Charge coupled devices (CCDs). Due to high quantum efficiency and dynamic range CCDs are preferred for astronomical observations.

A CCD chip consists of a regular array of light sensitive metal oxide semiconductor capacitors (each capacitor is equivalent to a pixel) that emit electrons when exposed to light. A typical CCD chip is shown in the figure 2.1. CCDs are typically fabricated by growing a thin region of n-type silicon material over a highly doped thick p-type silicon semiconductor substrate. This structure is identical to a p-n junction diode that has a buried channel between n- and p-type materials. Again a thin layer of silicon dioxide is grown on top of the n-type region to provide thermal and electrical insulation. The capacitor is finished off by placing metal electrodes, generally a heavily doped polycrystalline silicon conducting layers, on top of the silicon dioxide layer. The channel stops, to define the columns, are formed by doping high concentration

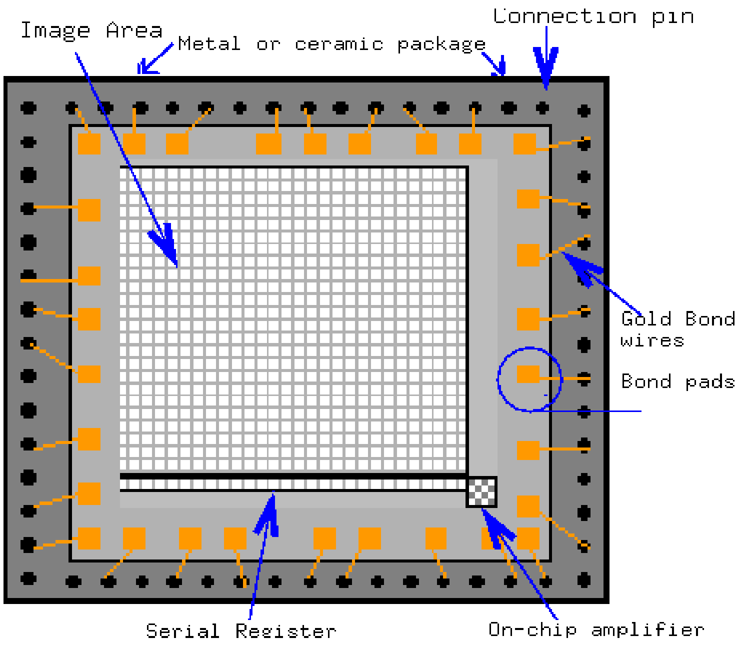

Figure 2.1: The structure of the CCD: The charges collected in the image are transferred, one pixel at a time, via a serial register to the on-chip amplifier. The electrical connections are made of a series of bond pads and thin gold wires.

of boron in the silicon. The detector rows, defined by the horizontal electrodes, are used in charge transfer during readout.

CCDs work on the principle of photoelectric effect that generate electrons whenever the CCD surface is exposed to a stream of photons. Each absorbed photon leaves behind an electron-hole pair and the electrons are accumulated in n-region during the integration time. A positive electric field is applied to the electrodes to sweep the electrons apart and prevent recombination. In the absence of electric field, the thicker p-type substrate cause almost immediate recombination of any photo-generated charge. This reversible character of the CCDs make them highly preferable for astromnomical observations. Once the exposure is completed, the charges from each pixel in a row are shifted sequentially to its edge, where the charges are converted to voltage levels, buffered, and sent out as an analog signal. This signal is then amplified and digitized using an analog-to-digital A/D converter and then fed to a computer where further manipulation and analysis are being done. Once all the pixel voltages in a row have been measured, the charges of subsequent rows are forced to migrate towards their edges and digitized. Millions of pixels are ditized in few seconds by this process of charge transfer.

To make qualitative observations and study the spectra in great details, the observer must be aware of the basic detector parameters:

(i) Quantum efficiency: It is measured as the probability of a photon with wavelength λ causing a recordable event and is written as

$$q(\lambda) = \frac{\text{number of photons detected}}{\text{number of photons incident}} \tag{2.1}$$

Silicon based diodes have high quantum efficiency well into the red wavelengths, whereas photographic detectors usually peak in blue and typically have much less q(λ) ($\sim$ 10%). These diodes become transparent and insensitive to UV photons, whose energy falls below the diode band gap ($<$ 1.26 eV, equivalent to optical band). Hence, the front illuminated silicon based detectors are preferable to work in visible wavelengths.

(ii) Linearity: It is a measure of how consitently the CCD responds to the amount of incident radiation. This means that the ratio of the outputs from two measurements is equal to the ratio of the number incident photons. If a detector is linear, it is convenient to specify a spectral line profile directly as the detector output as a function of wavelength across the profile. Secondly, linearity must be maintained at each step during the charge transfer across the diodes, through electrical switches to output lines, as well as amplification and digitization of the signal. Many CCDs used in modern astronomy are linear over the range of their full well capacity.

(iii) Full well capacity: It is a measure of the maximum number of electrons accumulated in a pixel before the leakage occurs into neighbouring pixels. The typical full well depth of a CCD range from 40,000 to 2,00,000 electons and depend on the size of the pixel whose typical size range from 9 μm to 27 μm depending on the manufacturer.

(iv) Gain: It is a measure of how many electrons of charge are represented by a single A/D conversion unit (ADU), often expressed as electons/ADU. There is also a maximum number of gray levels available in an A/D converter. For example, a 16-bit converter can have a maximum of 2^{16}=65,536 levels. If a CCD has a full well capacity of 85,000 electons, usage of a 16-bit amplifier with a gain of 1.0 can digitize only 65,536 electons out of 85,000. But, the same amplifier reduce the digization noise at the expence of well depth. Hence, the amplifiers are pre-selected as a balance between the digitization levels, digitization noise and full well depth for a proper digitization.

(v) Readout noise: During digitization, CCD amplifiers and the camera controlling electronic devices inject unwanted random signals which ends up getting digitized along with the pixel charge. In addition, every A/D converter show a spread about an ideal conversion value when the same charge from the same pixel was digitized. Thus, there is an uncertainty about the true digitized counts and is referred as readout noise, specified in electrons (e^-).

Readout noise can be decreased by controlling the readout rate. The readout rate is defined as the rate at which the charges from a whole CCD are readout by issuing a square-wave clock signals from an amplifier. The usage of multiple amplifiers speed up the readout rate and is expressed as

$$\text{Readout time (seconds)} = \frac{\text{Number of pixels}}{\text{(Readout rate (Hz)*No. of ports)}} \tag{2.2}$$

Readout rates of 20 kHz to 1 MHz ($2\text{x}10^4$ to $1\text{x}10^6$ pixels) are typical. At 250 kHz, a 2048 x 2048 CCD with two ports can be readout in 8.4 sec.

(vi) Dark noise: All detectors generate charge in each pixel on its own in the absence of illumination, known as dark current, that builds up with time and increment in temperature. Since it is a repeatable phenomenon, it can be handled easily by subtracting dark frames from all the images. But, there is a noise component of it, known as dark noise, defines as

$$\text{Dark noise} = \sqrt{\text{Dark current}} \tag{2.3}$$

which will spoil the image quality if not treated carefully. As the thermal leakage of electrons falls exponentially with temperature, it is a universal practice to cool the CCDs down to $\sim -30°\text{C}$ to $-150°\text{C}$ using dry ice or liquid nitrogen as a refrigerant. As a result, the full well depth of each pixel is optimized by reducing the dark current which in turn minimizes the dark noise.

(vii) Photon noise: As the detection of photons on the CCD chip is a statistical process, the photon noise (shot noise) arises from the irregular times of arrival of the photons (from star and sky background) incident on the CCD at a given location. The fluctuations in photon rate follow the well known Poisson distribution and varies as a function of square root of the number of detected photons.

Obsevers often use the word S/N, the signal-to-noise ratio, to measure the quality of observations. Let N be the total detected photon flux (photons/pixel/second) on a CCD with a quantum efficiency of q(λ) over an integration time of t (seconds). Among these, L number of photons comes from the star and B come from the equipment, sky, and other background sources. Assuming a dark current value of D (electrons/pixel/second) and readout noise of N_r (electrons rms/pixel), the S/N can be expressed as

$$\frac{S}{N} = \frac{Lq(\lambda)t}{\sqrt{((N+B)q(\lambda)t + Dt + N_r^2)}} \tag{2.4}$$

The asymptotic region of interest where the S/N approaches that of an ideal detector is the photon-noise dominated regime in which the background counts are negligible (i.e. B<<L). Then for negligible dark current and readout noise, the precision attainable per exposure is given by equation 2.4 as

$$\frac{S}{N} = (Lq(\lambda)t)^{\frac{1}{2}} \tag{2.5}$$

For example, a full well capacity of 10^4 photons would limit the precision of S/N $<$ 100 per exposure. But in reality, observers should not work very close to the limit of full well depth as the saturated well gives a useless signal. Instead, they add together many exposures to build a desired S/N.

The worst situation stands in the regime where there is a weak signal on top of a large background (i.e. L<<B). Now from equation 2.4

$$\frac{S}{N} = \frac{Lq(\lambda)t}{\sqrt{(2Bq(\lambda)t)}} \tag{2.6}$$

In this domain, the observer should strive to increase the S/N either by increasing L, using a large telescope and a detector with higher quantum efficiency, or decreasing B i.e., by observing in a dark night.

When working in low light levels, the readout noise exceeds photon noise and the noise penalty is equal to the square root of the number of readouts. So, the integration time should be increased until photon noise exceeds the readout noise to improve the quality of the data.

(viii) Dynamic range: It is the ratio of the smallest resolvable signal to the full range, generally a full well depth, over which the signal can run. It is often expressed in dB as

$$\begin{aligned}\text{Dynamic range} &= 20\ \log_{10}\left(\frac{\text{Full well depth}}{\sqrt{\text{read noise}^2 + \text{dark noise}^2}}\right)\\ &\simeq 20\ \log_{10}\left(\frac{\text{Full well depth}}{\text{read noise}}\right)\ (\text{for dark noise} \simeq 0)\quad (2.7)\end{aligned}$$

Higher the dynamic range the better the detector can work over a substantial range of source brightness. This ratio is also an indication of the number of digitization levels appropriate for a given sensor. For example, a detector with a well depth of 60,000 electons and with 10 electrons of read noise would yield a dynamic range of 60,000/10=6000 or 75 dB, or just over 12 bits. Hence, a 14-bit A/D converter with 16384 gray levels is more than adequate for digitization.

2.5 Diffraction grating

A typical plane diffraction grating consists of a series of equally spaced parallel grooves (space between each groove act as a slit) ruled on a highly polished flat glass substrate coated with a thin layer of aluminium or gold.

Consider a plane reflection grating with a series of N slits, each of width b and with centres separated by d, fill an aperture of width W as shown in the figure 2.2. A plane wave of wavelength λ is incident on the grating surface at an angle α and the diffracted light is observed a long distance away along a set of angles β_m relative to the grating normal. The diffracted angle β can have the same sign as α when it is on the same side of the grating normal. In general, positive angles are measured to the left of the grating normal and negative angles to the right.

The total intensity at any arbitrary angle β is given by the square of the amplitude of the resultant wave at that point (Gray, 1992)

$$I_{tot}(\theta) = (|A_{tot}|)^2 = I(0)\left(\frac{sin[\pi(b/\lambda)\theta]}{\pi(b/\lambda)\theta}.\frac{sin[\pi N(d/\lambda)\theta]}{N sin[\pi(d/\lambda)\theta]}\right)^2 = I_1(\theta).I_2(\theta) \qquad (2.8)$$

where $\theta = \sin\alpha$ - $\sin(\pm\beta)$. The first factor is a diffraction term due to a single slit of width b, and the second one represent the inteference of diffracted light due to N-thin slits. Since Nd > b (as d > b), the second factor oscillates much faster than the first. The resultant amplitude turns out to be a nice interference pattern with a series of narrow peaks modulated by a single slit diffraction envelope set by the slit width b. Figure 2.3 shows the interference and diffraction pattern for $N = 2$ and slit width of

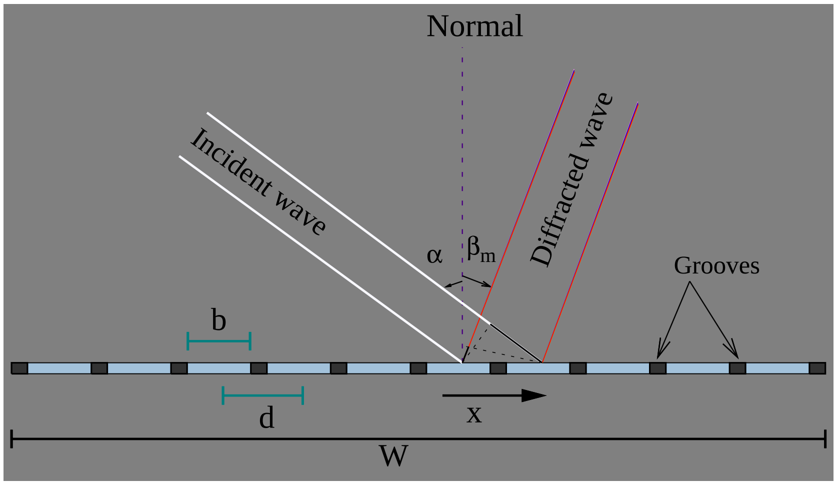

Figure 2.2: A side view of the plane reflection grating of slit width b and slit spacing d as shown. The linear coordinate x runs across the rulings. Plane wave is incident at angle α and β_m is the set of diffraction angles for different wavelengths.

d/5. The zeros of the interference maxima are equally spaced in θ from the center of the maximum and the width of maxima defines the angular resolution of the grating by

$$\Delta\theta = \lambda/Nd$$

or

$$cos\beta\ \Delta\beta = \lambda/Nd \tag{2.9}$$

The maxima of the interference peaks occur every time the denominator of $I_2(\theta)$ becomes zero - i.e. when,

$$\begin{aligned} \pi(d/\lambda)\theta &= m\pi \\ sin\ \alpha + sin\ \beta &= \theta = m\lambda/d\ \ (for\ m = 0, \pm1, \pm2, \ldots) \end{aligned} \tag{2.10}$$

This is the famous grating equation with each interference maxima corresponds to an order integer m. It has defined implicitly through the grating equation that at a given θ, the overlap of wavelengths from different orders occurs for all combinations of mλ having the same value- i.e. one could detect 6000 Å light from first order and 3000 Å light from second order at the same time. This problem is solved by placing a filter into the diffracted light beam so as to exclude light from unwanted orders.

2.5.1 Spectroscopic properties of gratings

(i) **Angular resolution**: For a given m, the collection of maxima for diffrent wave-

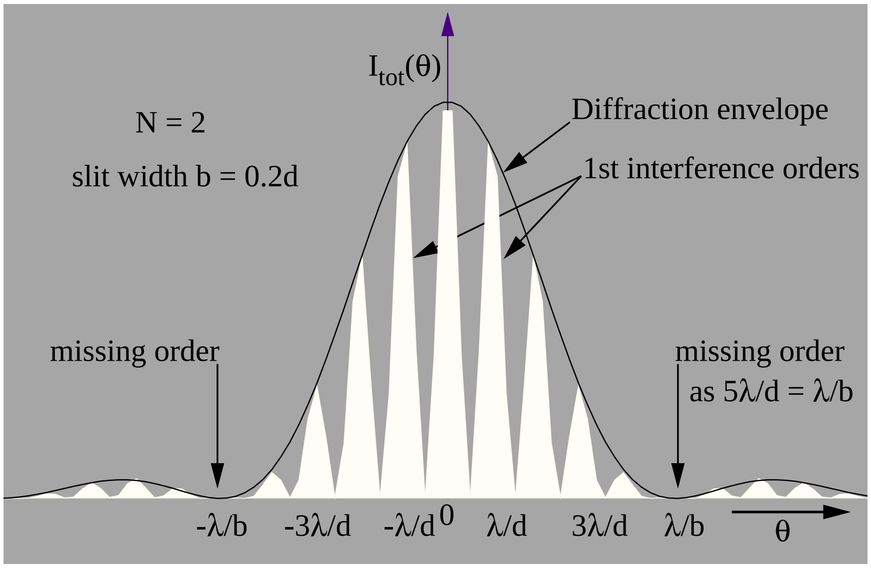

Figure 2.3: The intensity distribution of the light of wavelength λ after interacting with a grating having slit width b and slit distance d. Some of the interference peaks are suppressed whenever the diffraction minima coincides with interference maxima and appear as missing orders.

lengths directed at different angular positions (β) define the mth-order spectrum. The angular spread $d\beta$ of the mth-order spectrum across the wavelength range λ to $\lambda+d\lambda$ can be obtained by differentiating the grating equation. Thus, the change in diffraction angle per unit wavelength is

$$\frac{d\beta}{d\lambda} = \frac{m}{d\cos\beta} \tag{2.11}$$

Therefore the angular resolution can be increased by moving to higher orders or by selection of a grating having high ruling densities.

(ii) **Free spectral range**: The largest wavelength coverage for a given spectral order that does not overlap with light from neighboring orders is called free spectral range. If the wavelengths of light λ_1 and λ_2 in (m+1)th and mth orders overlap with each other (both lie at the same angle β), then

$$\begin{aligned}(m+1)\lambda_1 &= m\lambda_2 \\ \lambda_2 - \lambda_1 &= \frac{\lambda_1}{m} \quad (\text{for } \lambda_1 < \lambda_2)\end{aligned} \tag{2.12}$$

For example, when observing in first order with wavelengths greater than or equal to 350 nm, wavelengths upto 700 nm are free from overlapping. Then, the range from 350 to 700 nm is called the free spectral range for that order.

(iii) **Chromatic resolution**: An expression for the chromatic resolution (wavelength resolution) implicit in the grating of width W (=Nd) working in the mth order is obtained by combining angular resolution given by equation 2.9 with the angular dispersion from equation 2.11. It can be written as

$$\Delta\lambda = \frac{\lambda}{W}\frac{d}{m} = \lambda/Nm \tag{2.13}$$

(iv) **Resolving power**: The resolving power of a grating is generally expressed as a dimensionless number R, that is a measure of ability to separate adjacent spectral lines of average wavelength λ. It a usual practice to denote R as

$$R = \frac{\lambda}{\Delta\lambda} = \frac{mW}{d} = Nm \tag{2.14}$$

Therefore, a grating operated in higher orders with large groove density produce high spectral resolution, but at the expense of free spectral range which decreases as the order number increases (see equation 2.12).

2.5.2 Echelle gratings

The diffraction envelope $I_1(\theta)$ has its largest maxima at $\theta = 0$, corresponds to zeroth order spectrum, which gives zero chromatic resolution. As we move to higher orders to gain resolution, we can see that the light intensity falls to low levels beacuse a large part of the light is lost to zeroth order located at $\theta = 0$ (see figure 2.3). Alternatively, one can observe in higher orders by shifting the diffraction profile relative to the inteference pattern to those θ values where who want to work. This can be accomplished by ruling the grating with groove structure where each groove facet is tilted at an angle ϕ with the grating normal. This would shift the diffraction envelope by angle ϕ while leaving the interference pattern unchanged because the grooves would still have same separation and oriented along the same plane. When this is done the grating is said to be blazed. Then a large part of the light is concentrated in higher orders which eventually results in high chromatic resolution. This is the way the echelle gratings are designed to work, with typically tanϕ = 2 (R2 echelle) or greater.

A ray diagram of the blazed reflection grating is shown in the figure 2.4. Since, the reflection facet is tilted through the angle ϕ the reflected wave changes its phase such that α is replaced by α-ϕ and β by β-ϕ. The real reflection gratings have both

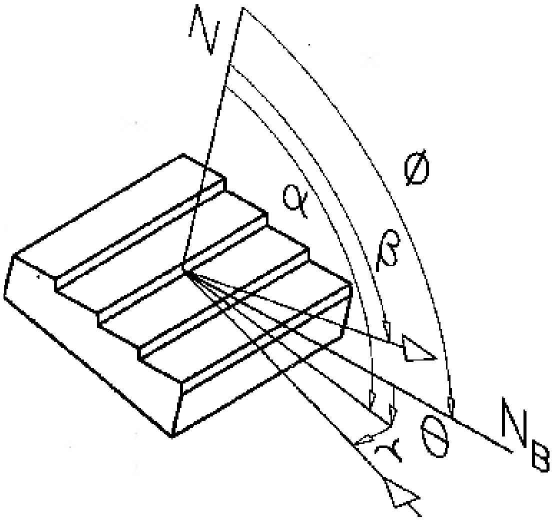

Figure 2.4: Geometry of the blazed grating: α and β are the angles of incidence and reflection, the incident ray makes an angle θ with the normal to the groove face and γ with the plane of grating, and the grating is blazed at ϕ (Courtesy: Tull et al. 1995).

the slit width and slit separation identical (i.e. b ≈ d) therby making the interruling space sufficiently small. But for echelles, ϕ is very large, e.g., 60°-75°, and the effective slit width is reduced to b = d $\cos^2\phi$, as the front and back sides of the groove facet are usually at right angles. As a result the width of the diffraction envelope is broadened and reduces the light intensity in the zeroth order, as it lost to neighboring orders. The efficiency curve (blaze distribution) of the diffraction grating in this case becomes (as given in Gray, 1992)

$$I(\beta) = (|A_1(\theta)|)^2 = \left(b\frac{sin(n\pi\, b/d)\{cos\phi - [sin\phi/tan\frac{1}{2}(\alpha+\beta)]\}}{(n\pi\, b/d)\{cos\phi - [sin\phi/tan\frac{1}{2}(\alpha+\beta)]\}} \right)^2 \tag{2.15}$$

The efficiency curve reaches its maxima at α+β=2 ϕ, that corresponds to the specular reflection (α=β) off the facet surface.

2.5.3 Blaze wavelength

The blaze wavelength for a given diffraction order m is defined as that wavelength for which the blaze distribution reaches its maxima. A grating blazed at 6000 Å in first order is also equally blazed at 3000 Å in second order and so on.

The blaze angle of the echelles is optimized to achieve maximum efficiency such that the incident and diffraction angles are identical (i.e. $\alpha = \beta = \phi$). This is the so called Littrow configuration where a large fraction of incident light is concentrated in the desired diffraction order while reducing the intensity in other orders. For this configuration the blaze wavelength λ_b of the grating is expressed as

$$m\,\lambda_b = 2\,d\,sin\,\phi \tag{2.16}$$

Departures from Littrow condition will shift the true blaze to appear at different wavelength (λ_p) such that

$$\lambda_p/\lambda_b = \frac{sin\,\alpha + sin\,\beta_p}{2\,sin\,\frac{1}{2}(\alpha+\beta_p)} = cos\,\frac{1}{2}(\alpha-\beta_p) \tag{2.17}$$

If $(\alpha-\beta_p) = 40°$ (i.e. the departure from the Littrow condition is 40°), then a grating that is said to be blazed at 6000 Å (λ_b) will actually have its blaze at 5638 Å (λ_p).

2.6 Spectrograph resolution

The final resolving power of the whole spectrograph is always much less than the resolution provided by its grating. The main instruments that makeup echelle spectrograph are the entrance slit, collimator, echelle grating and a camera with CCD detector. A converging beam of light from the telescope that enters the spectrograph through the slit of width w is made parallel by a collimator of focal length f_{coll}, diffracted by the grating and finally focused onto the detector by camera with focal length f_{cam}. The angular size of the entrance slit as seen by the grating or collimator is $\tan\delta \simeq \delta = w/\mathrm{f}_{coll}$. A shift in the ray's original direction by the amount w will change the incident angle on the grating from α to $\alpha+d\alpha$. As a result $d\alpha = \delta$. The angular size $d\beta$ of the monochromatic slit image behind the grating, which is projected by the camera onto the CCD detector, is obtained by differentiating the grating equation 2.10. Therefore, we have

$$d\beta = -\frac{cos\alpha}{cos\beta}d\alpha = -\frac{cos\alpha}{cos\beta}\frac{w}{f_{coll}} \tag{2.18}$$

An infinitesimal variation in the linear size of the spectral image on the detector is

$$dx = f_{cam}d\beta = -\frac{cos\alpha}{cos\beta}\frac{f_{cam}}{f_{coll}}w \tag{2.19}$$

If w' is the total linear size of the slit image, then w'/w is the image magnification in the dispersion direction (or the magnification of the width) of the entrance slit and f_{cam}/f_{coll} is along the slit.

Therefore, the wavelength interval recorded on the detector is

$$\Delta\lambda = d\beta f_{cam} d\lambda/dx \tag{2.20}$$

The factor $d\lambda/dx$ is obtained by combining the equation 2.19 with the grating equation as follows:

$$\frac{d\lambda}{dx} = \frac{d\lambda}{d\beta}\frac{d\beta}{dx} = \frac{1}{f_{cam}}\frac{d\,cos\beta}{m} \tag{2.21}$$

Therefore the wavelength interval $\Delta\lambda$ imaged on the focal plane of the detector for an angular image size of $d\beta$ is

$$\Delta\lambda = -cos\alpha\frac{w}{f_{coll}}\frac{d}{m} \tag{2.22}$$

With this definition, the resolution of the spectrograph reads:

$$R = \frac{\lambda}{|\Delta\lambda|} = \frac{sin\alpha + sin(2\phi - \alpha)}{cos\alpha}\frac{f_{coll}}{w} \tag{2.23}$$

To attain a good chromatic resolution $\Delta\lambda$, one can choose a grating with high ruling density or one blazed to send a large part of light to higher orders. Since the blazed gratings have steep facet angle with deep grooves, it is difficult to manufacture high ruling densities. The resolution also increases by making the slit width w small, but that effects the throughtput of the spectrograph. Alternatively, one can gain high spectral resolution by increasing f_{coll}. This is the reason why coude spectrographs are large in size.

2.7 Observations

High-resolution optical spectra of our program stars were obtained with the Robert G. Tull echelle coudé spectrograph (Tull et al. 1995) on the 2.7-m Harlan J. Smith telescope (HJST) at the McDonald observatory using TK3, a thin, grade 1, Tektronix 2048x2048, 24 μm pixel, backside illuminated, anti-reflection coated CCD as a detector. The two-pixel resolving power obtained using an echelle with 52.67 gr/mm is 60,000 and offer a minimum inter-order separation of 10.5 arcsec. At this resolution the spectrograph provides a wavelength coverage from 3400 to 10,900 Å, covered in 69 echelle orders.

Though a detailed discussion of the instrument and its design is available elsewhere, this thesis work presents a brief description of the TS2. The optical layout of the 2dcoudé echelle spectrograph is shown in the figure 2.5. The star light hits the

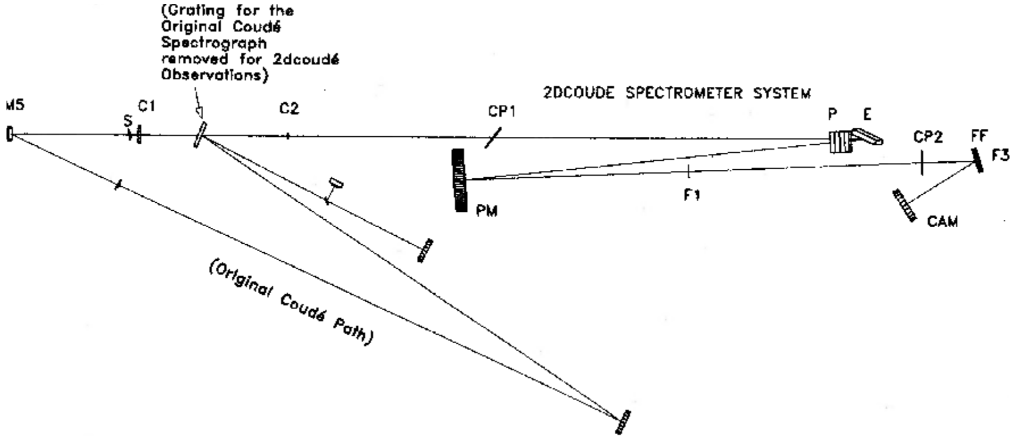

Figure 2.5: Optical layout of 2dcoudé system. S is a field mirror and slit, C1 and C2 are collimator primary and secondary mirrors, CP1 and CP2 are aspheric corrector plates. P indicate the position of prisms, E for echelle grating, PM for pupil mirror F1 corresponds to R=250,000 focus and F3 for R = 60,000 focus. FF is camera folding flat and CAM is the camera primary mirror (Courtesy: Tull et al. 1995).

primary mirror (2.72-m), then the secondary, and then it is diverted, with the help of two flat mirrors, down the axis to the coudé room. This f/32.5 beam then enters the slit S and collimated into a 19.0 cm beam by an off-axis parabolic collimator C1C2, that maintain high throughput in the design. Then the light beam falls on a R2 echelle ($\phi = 65.3°$) grating through a correcting lens CP1 and pre-dispersed by a pair of 30° prisms P, formed by optically contacting two pairs of 15° wedges, each having a thickness of 72 mm. The plate CP1 correct for the off-axis errors introduced by the collimator. The echelle with ruled area up to 204×408 mm, and 52.67 gr/mm from Milton Roy Inc. is used in plane ($\gamma = 0°$) with $\theta = 3°$ (the angle between the incident ray and the normal to the groove face). The prisms are of Corning quality 1A fused silica, selected and supplied by Glass Fab Inc. Prisms with this material were selected over gratings since they provide high ultrviolet transparency, homogeneity, high throughput, lack of blaze fall-off, and excellent dispersion with uniform order separation. TS2 is designed with minimum order separation, thus resulting in maximum spectral coverage per exposure. Both the prisms and echelle are mounted on a cradle which serves to tilt prisms and echelle for selection of the wavelength region to be centered on the CCD.

Pupil mirror PM, with its center of curvature near the echelle, receives the light dispersed horizontally by grating and cross dispersed vertically by prisms and produces a large scale cross dispersed spectral format at the highest resolution focus

F1. After diverging through F1 and passing through the Schmidt corrector CP2, the final focal surface F3 is flattened by a lens in front of dewar window. The CCD in its dewar cooled down to about -105° is mounted at F3 to form an exquisitely detailed spectrum in its entirety from 3400 to 10,900 Å at resolution of R = 60,000.

2.8 Data reduction and extraction techniques

2.8.1 Data preparation

It is a usual practice to open the dome around sunset, well before the actual observing run, to bring the entire telescope to the same temperature as the surroundings. The quality of the image and the observational set up are checked every evening by taking the spectra of twilight or uniform source of light. In general, every observing run not only includes spectra of program stars, known as science frames, but also many exposures of bias, dark, flatfield, comparison spectra, and hot star(s). They are necessary to correct and edit the science frames to guarantee an optimal extraction process.

(i) Bias and dark frames: Bias frames are acquired by taking short exposures before and after each night of observation with the shutter closed, so that the detector is not exposed to any light. This is done to read the counts from each pixel in a raw CCD in the absence of light. Since the bias level is almost spatially uniform across the chip it must be subtracted from all other images where it also exists. Typically several exposures are taken and averaged to supress the read-out noise. A typical bias image is presented in the top panel of figure 2.6.

Dark frames are also obtained with the shutter closed, but with exposures of comparable length to that of program stars. Since, this signal is generated thermally, CCD detectors have to be cooled down and maintained at constant temperature to prevent thermal leakage of electons in each pixel. Since the TK3 CCD used for our observations has exceptionally low dark current we skipped taking dark exposures.

(ii) Flatfield images: Due to manufacturing limitations not all the pixels in a CCD chip responds equally to light of all wavelengths. This effect of sensitivity is quite random for each pixel and independent of its position on the CCD grid. The science frames has to be corrected for relative sensitivity of pixels by averaging few exposures of flatfield calibrations. Flat frames are acquired by illuminating the CCD with a uniform source of light, for example twilight, tungsten or halogen lamps, to get a featureless spectra. Flatfield correction also minimizes the effect of errors in the optics, dust on CCD chip, aberrations, stray light due to optical elements and surfaces, and vignetting caused by various out of focus objects, such as support for the secondary mirror.

(iii) Comparison lamp frames are the spectra of a lamp (Th-Ar, Fe-Ar etc.) with well known features covering the whole extent of program star spectra to map the pixel number on the CCD to wavelength scale. Since the whole instrumental set up is fixed firmly and does not change during the observing run, the pixel numbers of the comparison spectrum match with those of the science frames. Now it is easier to convert the science frames from pixel coordinates to a wavelength scale.

(iv) Hot star spectra are taken with an early type stars having rotational velocities of the order of 100−300 km/sec. Because of rapid rotation the photospheric lines are smeared out into a continuum and their spectra contains only the absorption lines from the Earth's atmosphere. They allow the removal of telluric contamination from our program star spectra.

2.8.2 Data reduction

The raw spectra registered on a CCD chip are digitized and stored in the digital file format, called FITS (Flexible Image Transport System). Currently used CCD sensors in Astronomy can handle data upto 16-bits, that can store a binary file with 2^{16} bytes of information. The spectra taken from HJST are stored in USHORT format where the digitized data is stored as an unsigned 16-bit/pixel (2 bytes) integers in the range 0 to 65,535.

The data reduction process to produce a good quality spectra requires certain instrument and exposure information, including the orientation of the echelle format, usuable portion of the CCD, read noise, gain, and exposure time. These values can be assigned manually in the reduction script before processing of the data. We have used the standard spectral reduction software IRAF[1] that offers various packages to execute tasks and analyze the raw data files.

The basic data reduction procedure using IRAF is described below. (i) Most of the spectroscopic data does not occupy the whole CCD frame and contain the regions that are unexposed to light. These are overscan regions, located at the edges, and need to be trimmed off from all images before processing the data. This is achieved with the task *ccdproc* in IRAF. (ii) The bias frames were median combined, that operation effectively removes the cosmic ray counts, to form a master bias using the task *zerocombine*. The master bias is subtracted from all flatfields and science frames to correct for any spatial structure using *ccdproc*. (iii) The bias subtracted flatfield

---

[1] IRAF is a general purpose software system for the reduction and analysis of astronomical data distributed by NOAO, which is operated by the Association of Universities for Research in Astronomy, Inc. under cooperative agreement with the National Science Foundation.

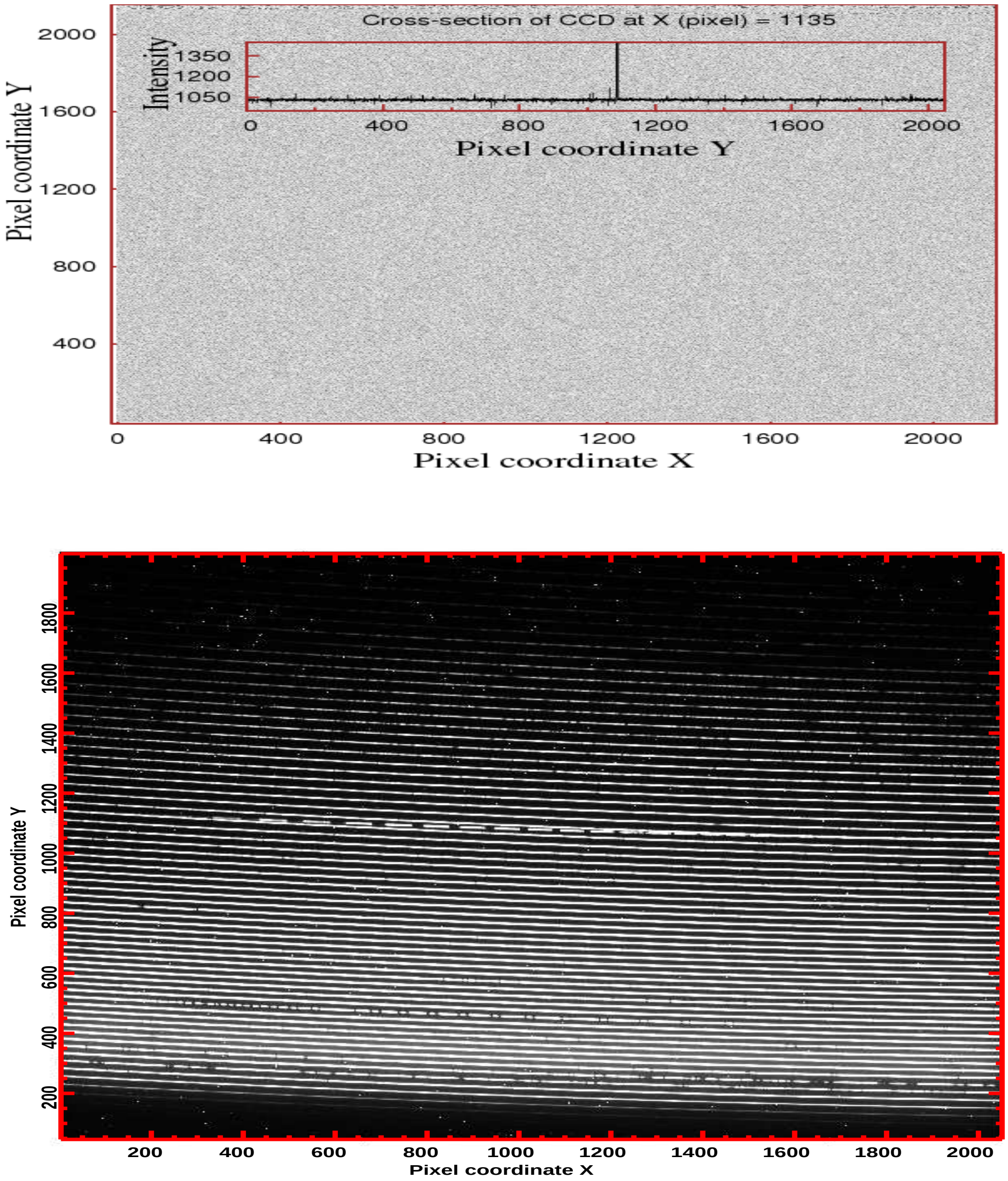

Figure 2.6: (a) Top panel: A bias frame overplotted with a cross-section of the image at X (pixel) = 1135 is shown. The typical structure clearly shows no strong features other than certain noise level around a CCD and temperature specific mean value of intensity (≈ 1020 in arbitrary units). The frame also shows a cosmic ray (emission lines with very high flux) whose number increases with exposure time. (b) Bottom panel: A science exposure frame with various spectral orders is shown. The typical structure is apparent - spectral orders running as thin curved stripes from the left of the image to the right.

frames are median combined to form master flat using the task *flatcombine*. (iv) The next step is to subtract the scattered light from the master flat and science frames. In order to do that one has to trace the location and shape of each spectral order, and the choice of background region on the two-dimensional CCD image. Each spectral order is a two-dimensional intensity profile built from a series of one dimensional monochromatic slit images. Since they appear as parallel stripes on the CCD frame, it is easy to identify and mark their positions. At first, we have identified the apertures for a hot star and used them as a reference to mark the apertures in master flat and science frames. An example of a science frame is shown in the bottom panel of figure 2.6. Once the position of the orders is known, their width and shape has to be defined. The deposited orders on the CCD are curved, mainly beacuse of the cross-dispersing action of the prism while the curvature due to grating is unimportant, and they don't align either with the CCD rows or columns. As a result assigning a constant width to all the orders, or even for the entire length of a single order is not sufficient. To tackle this problem, we have defined the profile center and width for each of the orders such

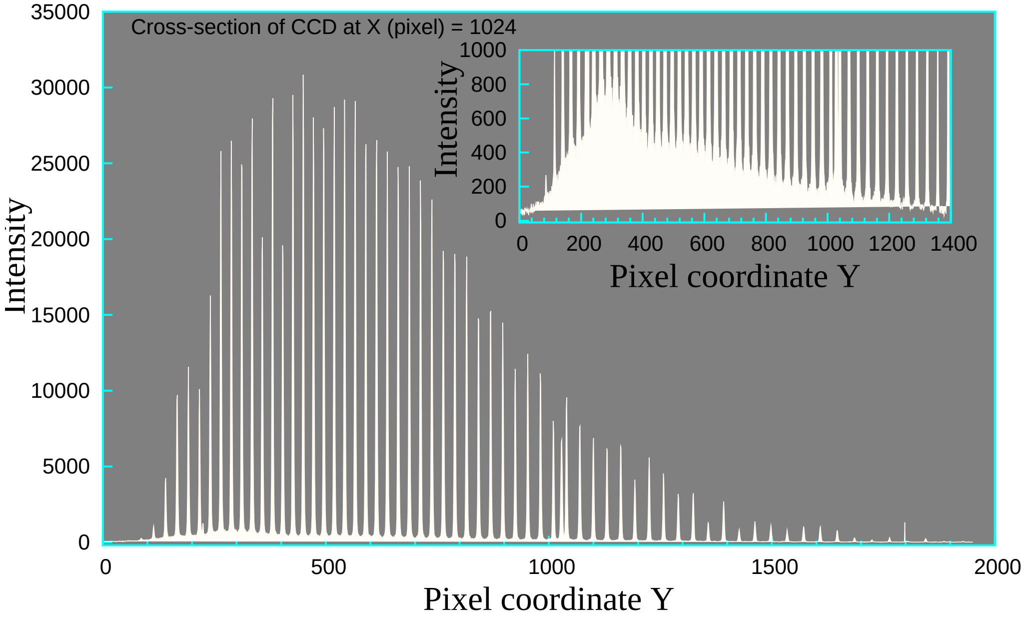

Figure 2.7: The intensity distribution in the cross-dispersion direction (along pixel coordinate Y in the bottom panel of figure 2.6) for a cross-section of X = 1024 over almost the entire Y range is shown. It is clear that the orders around Y = 400 are much more intense than others. The inter-order regions does not show zero intensity but background intensity with a specific shape as shown in the overplotted area at the right. It should be noted that this scattered light is very high for intense orders and has to be fitted and substracted to retrieve the spectral information in those orders.

that the region between the successive orders automatically defines the background level.

The maximum intensity on the CCD for each spectral order varies in the cross-dispersion (spatial) direction such that the central orders have very high intensities, and the orders on either side barely emerge from the background level. This situation is much worse if the background is dominated by scattered light that masks and contaminate the spectral information located in the orders. A typical light intensity in spectral orders at a cross-section X (pixel) = 1024 and the scattered light beneath each order of a science frame is presented in the figure 2.7. It is important to subtract this residual intensity from the data before the extraction of orders. We have modeled and subtracted the scattered light in the dispersion and spatial direction from master flat and science exposures by fitting polynomials (chebyshev and legendre) of lower order that pass through the inter-order regions without intervening with the intensity in any order. Scattered light correction was carried out with the task *apscatter*.

(v) The master flat is normalised using the task *apnorm* and the science exposures were divided by normalised flat to account for the pixel-to-pixel variations, blaze distribution and other systematic errors mentioned earlier. Flatfield divison was accomplished within the task *ccdproc*. Here, the basic idea is to preserve ADU values in the object spectra when dividing them by the flats.

2.8.3 Extraction of echelle spectra

As of now we have a two-dimensional science exposure frames, subtracted for the bias and scattered light and divided by the normalised flatfield, with a knowledge of the order location and its shape. The science frames are extracted to one-dimensional spectrum, which means that summing up the counts along cross-dispersion direction (along pixel coordinate Y in the bottom panel of figure 2.6) from all pixels lying inside the area of a defined order, subtracting the sky, and then follow the path of each order in the dispersion direction by fitting a lower order Legendre polynomial to straighten the echelle orders. Now the extracted spectra read out with their flux (photons counts) on y-axis over each pixel number (x-axis). The shape of the flux distribution along each order follows the blaze function of that order which varies enormously along the dispersion direction because the pixels at the center receive more intensity than those at the borders. The extraction procedure is handled with IRAF task *apall* by treating all the pixels equivalent.

In the next step we have used the comparison lamp frames to translate the pixel coordinates to wavelength scale. Comparison spectrum orders in our case is the emission line specrum of Th-Ar arc extracted similarly as the science spectra. This lamp provides sharp narrow lines over the full spectral range. The dispersion relation between pixel coordinates and wavelength is arrived using the task *ecidentify* with a list (thar.dat) of lab wavelengths available in IRAF directory as a input. We have marked several emission lines from each order, typically 10, and entered their wavelengths manually while referring to the atlas of Th-Ar laboratory spectrum by D'Odorico et al. (1987). We fit a relation between pixel coordinates and the entered wavelength using the Legendre polynomial of the order 3 along each echelle order. Now we prompted the *ecidentify* task to identify few more features from the input list and mark their positions automatically. Again, a fit is performed and after manipulation, we have arrived the dispersion solution with an accuracy of about 5% per pixel. Accurate wavelength calibration is necessary to measure accurate equivalent width of spectral lines and radial velocity of the star which will be discussed in the next chapter.

We used the above wavelength calibrated arc spectrum as a reference to all the extracted stellar spectra observed on the same night using the task *refspec*. Then, the dispersion correction is applied to all science spectra to transform them to wavelength scale using the task *dispcor*. The resulting output is a spectrum with incident photon counts against their wavelengths. The spectra are corrected carefully for cosmic ray hits, easily identifiable as emission line spread over a narrow wavelength (or pixel) range. The spectrum is normalised to unity interactively using the cursor commands available in *splot* task by marking continuum regions, those regions which are uneffected by the presence of spectral lines, on each aperture which were then fitted by a slowly varying function such as cubic spline of appropriate order for better normalisation.

Chapter 3

Analysis and Interpretation of stellar spectra

3.1 Basic concepts

The spectra of normal stars are dominated by absorption lines. Photons produced in the deeper layers of a star are repeatedly absorbed, reemitted and frequently scattered in random directions by the overlaying stellar material. But, the presence of temperature gradient enables the photons to works its way out to the visible surface which is outer part of the gaseous atmosphere called the photosphere. When there are nearly as many photons moving into the star as there are moving out, then the material is close to Thermodynamic Equilibrium (TE) and the radiation is described by the laws of black body.

According to Kirchhoff's law a continuum is formed by the hotter, high pressure gas at the bottom of the stellar photosphere. The geometrical thickness of the photosphere varies inversely with the surface gravity and also depends upon opacity of the gases comprising the photosphere. At the higher layers the leakage of photons become more significant and the TE is only applicable locally, hence the name Local TE (LTE), to relatively small volumes of the photosphere - volumes with dimensions of unit optical depth. Then the photosphere is characterized by one physical temperature at each depth.

Some of the continuum energy photons moving out are absorbed by the atoms in cool and low density gases of these outer layers. The net result is the formation of absorption lines superimposed on the bright continuum. The cooler photospheric region in which the major portion of visible stellar spectrum originates is called the reversing layer. The schematics of the formation of spectral line in the stellar photosphere is shown in the figure 3.1. In the limit of low pressure, the perfect gas law holds good and the total gas pressure is sum of the partial pressures of each species in the atmosphere i.e.

$$P_g = k\,T \sum_j N_j \tag{3.1}$$

where k is the Boltzmann constant, T is the temperature and N_j is the number of particles of a given species per unit volume. The partial pressure due to the free electons (P_e) in the ionized gas of the photosphere is then

$$P_e = N_e\,kT_{ion} \tag{3.2}$$

where N_e is the number of electons per unit volume and T_{ion} is ionization temperature of the gas.

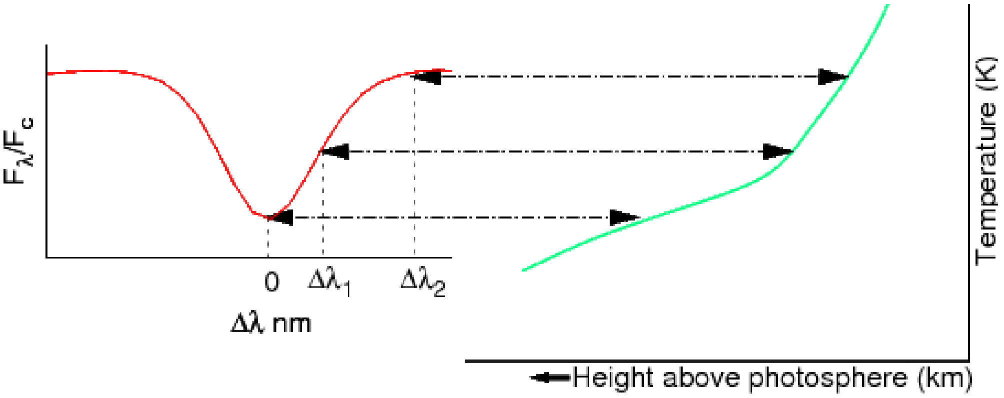

Figure 3.1: The dependence of formation of absorption line on the temperature and hence the height above the photosphere. It is the decline of the temperature, hence the source function, outward through the photosphere that produces the absorption lines.

3.2 Local Thermodynamic Equilibrium

The LTE implies that the components of a gas (atoms, molecules, electrons, photons) interact well enough and distribute the energy equally among all possible forms, like kinetic, radiation, excitation, ionization etc. Then the physical processes in the photosphere are governed by the following principles:

1. When the particles in a hot photospheric gas interact sufficiently they spread the available energy around and equilibrium distribution evolves such that speed of the partciles follow *Maxwell-Boltzmann* distribution. Then, the fraction of the

particles in the speed interval (v,v+dv) is

$$\frac{dN(v)}{N_{total}} = \left(\frac{m}{2\pi kT_k}\right)^{\frac{3}{2}} exp\left(-\frac{mv^2}{2kT_k}\right) 4\pi v^2 dv \tag{3.3}$$

where T_k is the kinetic temperature of the gas.

2. The photon energies are distributed in accordance with the *Planck radiation law* which depends only on the frequency of radiation and the temperature of the material. That is the Planck function

$$B_\nu(T) = \frac{2h\nu^3}{c^2}\frac{1}{exp(h\nu/kT) - 1} \tag{3.4}$$

with its maximum at $h\nu/kT = 2.8214$ or $\lambda_m T = 0.50995$ cm-K, where λ_m is the wavelength of the maxima. A fit to the shape of the stellar continuum with Planck function gives the color temperature of the star.

3. When collisions dominate over radiative processes the relative population of various excitation levels of an atom in equilibrium can be expressed as the excitation or *Boltzmann* equation. It gives the number of atoms per unit volume in a level n as a fraction of all atoms of the same species as

$$\frac{N_n}{N_{total}} = \frac{g_n}{u(T_{exc})} exp\left(-\frac{\chi_n}{kT_{exc}}\right) \tag{3.5}$$

where g_n and χ_n are the statistical weight and excitation potential of the n^{th} level, T_{exc} is the excitation temperature and $u(T_{exc}) = \sum g_i \, exp(-\frac{\chi_i}{kT_{exc}})$, called the partition function.

4. The relative population of various ionization levels of a collision dominated gas in equilibrium is driven by the *Saha-Boltzmann* equation which gives the fraction of the atoms in a ionization level n to neutral as

$$log\left(\frac{N_1}{N_0}P_e\right) = 2.5\, log(T_{ion}) - \frac{5040}{T_{ion}}I_1 + log\left(\frac{u_1}{u_0}\right) - 0.1762 \tag{3.6}$$

Where N_1/N_0 is the ratio of the ions to neutrals, u_1/u_0 is the ratio of ionic to neutral partition functions, and I_1 the first ionization potential of the species. Where P_e drives the equilibrium to neutral state if the electon density is high and towards ionized state when it is low. This means the partial pressure of electons in the stellar atmosphere changes the absorption line strength. For a simple gas in LTE the color temperature, T_k, T_{exc} and T_{ion} are the same.

3.3 Opacity

As the major mode of energy transport through the stellar photosphere is by radiation, a thorough understanding of the processes controlling the energy flow in these outer layers allow us to interpret and extract information from the spectrum we ultimately see and measure. The two important physical processes that dictates many observable features on the stellar spectrum are the continuous absorption coefficient (or continuum opacity) and the line opacity, which occurs at discrete wavelengths.

3.3.1 Continuum opacity

The wavelength dependence of continuum opacity shapes the continuum spectrum emitted by a star. The detailed calculation of continuous opacity is often tough in astrophysics as it involves the computation of cross-sections for all sorts of atoms, molecules and even dust grains as a function of frequency in the stellar atmosphere. The physical processes of bound-free and free-free absorption and electon scattering are referred collectively as the sources of continuous opacity.

Bound-free absorption ($\kappa_{\lambda,bf}$) occurs when a photon has sufficient energy to ionize an atom. Since these transition takes place from any level to the continuum, the freed electon can have a range of energies and thus contributes to continuum opacity. Free-free absorption ($\kappa_{\lambda,ff}$) occurs for a range of λ where a free electon absorbs photon upon passing close to another charge, causing the speed of the electon to increase. A single free electron in isolation cannot absorb a passing photon, but scatter the photons of all wavelengths with the same efficiency defined as

$$\kappa(e) = \frac{8\pi}{3}\left(\frac{e^2}{mc^2}\right)^2 = 6.648\ \times 10^{-25} cm^2/electron \tag{3.7}$$

This is called the electon scattering which is a very inefficient process and dominates only at very high temperatures, where other sources of opacity tend to decrease. When there are many overlapped and crowded spectral lines, even a bound-bound absorption ($\kappa_{\lambda,bb}$) adds to the continuum opacity by creating a line blanket to the flow of photons in the upper photospheres.

The primary source of continuum opacity in most stellar atmospheres (A, F, G and K stars) is the photoionization of H^- ions along with the scattering of photons by hydrogen atoms and molecules. All photons with wavelength $\lambda < 16444$ Å have sufficient energy to ionize the H^- back to the neutral hydrogen atom and a free electon. The extra electons needed to form H^- ion are supplied by the ionized metals. At high temperatures, for A and B stars, H^- is over-ionized, and then the bound-free and free-free absorption of neutral hydrogen become dominant. For very cool stars H^- ceases to be a strong absorber because of the lack of free electons. For O type stars, the primary source is electon scattering with a secondary contribution from the photoionization of He atoms. Several molecules such as CN, C_2, MgH, TiO, CO, H_2O and CH_4 and their ions survive in very cool stars (M, L and T type). All these molecules can absorb not only in electron transitions but also in vibrational and rotational modes thereby creating bands of absorption which can provide efficient impediment to the flow of photons and reduce the flux over major portions of the spectrum. The metals such as carbon, silicon, aluminum, magnesium and iron play a role in contributing bound-free opacity to the continuum which is important in the ultraviolet.

The total continuum opacity per square centimeter due to all forms of opacity can be expressed as

$$\kappa_\lambda = \kappa_{\lambda,bf} + \kappa_{\lambda,ff} + \kappa_e + \kappa_{\lambda,bf}(metals) \tag{3.8}$$

where the bound-free and free-free opacities can be derived using Kramer's formula (Gray, 1992) and the physical state of the gas is represented by the Boltzmann and Saha relations.

3.3.2 Line opacity

The absorption lines in stellar spectra adjust their shape and strength in accordance with the physical state and composition of the star's photosphere and thus reflects the existing conditions at a range of heights in the stellar atmosphere, as the surface flux at any point in a line profile comes from a considerable range in optical depth. Hence, the study of varied line profiles and line strengths provide us tools to interpret and measure the effective temperature, surface gravity, chemical composition and velocity fields in the stellar atmosphere.

The line opacity or line absorption coefficient, resulting from several different physical processes operating in the stellar atmosphere, plays a fundamental role in shaping the spectral lines. The major processes responsible for the variation of line strength as a function wavelength across the line profile are:

1. **Natural atomic absorption**: The spectral line of an atom is formed by a transition of electon between two bound states, whose energy difference yields the frequency of the line by the relation E$_u$ - E$_1$ = hν_{lu}, where E$_u$ and E$_l$ are the upper and lower energy levels. The excited levels of an isolated atom have a finite lifetime because of the probability of emission of photons due to its interaction with self-electromagnetic field. According to the uncertainty principle the excited energy levels acquire a finite small width so that the spectral lines are not infinitely sharp but extends over a certain wavelength band. The shorter the lifetimes of the excited levels involved in a transition, the broader the corresponding spectral lines. This is called natural broadening and the resulting absorption coefficient per atom takes the form

$$\kappa(\text{natural}) = \frac{\pi\, e^2}{mc} \frac{\gamma_{nat}}{(\Delta\omega)^2 + (\gamma_{nat}/2)^2} f \tag{3.9}$$

where $\Delta\omega = \omega - \omega_0$ is the offset from the central frequency ω_0 $(= 2\pi\, \nu_0)$, γ_{nat} is the damping constant and is calculated, according to the classical electrodynamics, as

$$\gamma_{nat} = \frac{2e^2\omega_0^2}{3mc^2} = \frac{0.22}{\lambda_0^2} \tag{3.10}$$

where e = 1.602$\times$10^{-19} C and m = 9.1094$\times$10^{-28} g are the charge and mass of the electon, c = 2.998$\times$10^{10} cm-sec^{-1} is the speed of light and λ_0 is the central wavelength of the spectral line in centimeters. The oscillator strength f, is different for each atomic level and is related to the Einstein atomic absorption probability B$_{lu}$. Equation 3.9 gives the damping profile or Lorentzian profile with a FWHM of γ_{nat}= 2$\Delta\omega$

2. **Pressure broadening**: It occurs due to the collisional interaction of light absorbing atoms with the ions, electons, or atoms of the same type as the absorbers or another type, and molecules. These collisions shortens the lifetime of the excited state and increases the natural width of energy level. The energy change induced by the collision is a function of R, the separation between the absorber and the perturbing particle, often approximated by a power law of the form

$$\Delta E = C_n/R^n \tag{3.11}$$

where C$_n$ is the interaction constant and the integer n depends on the type of perturbation. If the interaction is with an electric field, then

$$n = \begin{cases} 2 & \text{for linear Stark broadening} \\ 4 & \text{for quadratic Stark broadening} \end{cases}$$

If the coupling is between the pair of atoms of same kind then the resonance broadening arises for which the perturbation energy is proportional to R^{-3}, making $n = 3$ for this interaction. The Van der waals broadening occurs when the perturber is of a different species for which the perturbation energy is proportional to R^{-6}, so $n = 6$.

The pressure broadening of the lines result in a absorption profile similar to that for natural damping with a damping constant γ_n, which depends on the pressure and temperature in the stellar photosphere. The net result of all the absorbers along a spectral line through the stellar photosphere is a line shift, an asymmetry, and/or a line broadening.

3. **Thermal Doppler broadening**: The light absorbing atoms in the photosphere are not at rest but have a component of velocity (v_0) along our line of sight to the star due to their thermal motion. These atomic motions follow Maxwell-Boltzmann distribution and introduces Doppler shift of the line absorbed by the atom following

$$\frac{\Delta\lambda_D}{\lambda} = \frac{\Delta\nu_D}{\nu} = \frac{v_0}{c} = \left(\frac{2kT}{mc^2}\right)^{\frac{1}{2}} \tag{3.12}$$

where v_0 is the most probable velocity of the thermal distribution, λ_D and ν_D are the Doppler shifted wavelength and frequency. The distribution of $\Delta\lambda$ ($= \lambda - \lambda_0$) give the shape of the thermally broadened absorption profile as

$$\kappa(\text{thermal}) = \frac{\sqrt{\pi}\, e^2}{mc^2} f \frac{\lambda^2}{\Delta\lambda_D}\, exp\left[-\left(\frac{\Delta\lambda}{\Delta\lambda_D}\right)^2\right] \tag{3.13}$$

The total line broadening coefficient is the convolution of the natural, Stark, van der Waals and thermal broadening. i.e.

$$\kappa_{l,a}(\text{total}) = \kappa(\text{natural}) * \kappa(\text{pressure}) * \kappa(\text{thermal}) \tag{3.14}$$

The first two coefficients can be written as a single Lorentzian profile with a damping parameter γ defined as

$$\gamma = \gamma_{nat} + \gamma_4 + \gamma_6 \tag{3.15}$$

The convolution of the Lorentzian and Doppler profile is called Voigt function. The resulting atomic absorption coefficient

$$\kappa_{l,a}(\text{total}) = \frac{\sqrt{\pi}\, e^2}{mc} \frac{f}{\Delta\lambda_D} \frac{\lambda^2}{c} H(u,a) \tag{3.16}$$

can be calculated using the tabulated H-function values for a given u ($= \Delta\lambda/\Delta\lambda_D$) and damping parameter a ($= \lambda^2\,\gamma/4\pi\,\Delta\lambda_D\,c$) (Gray, 1992). This final distribution is a combination of Doppler core with the damping wings: the damping profile is negligible near the line center as the Doppler width is large, but in the wings the Doppler profile falls off rapidly while the damping wings fall slowly as $1/\Delta\lambda^2$ curve. A comparison of the Doppler and Lorentzian profiles for equal widths and strengths is shown in the figure 3.2.

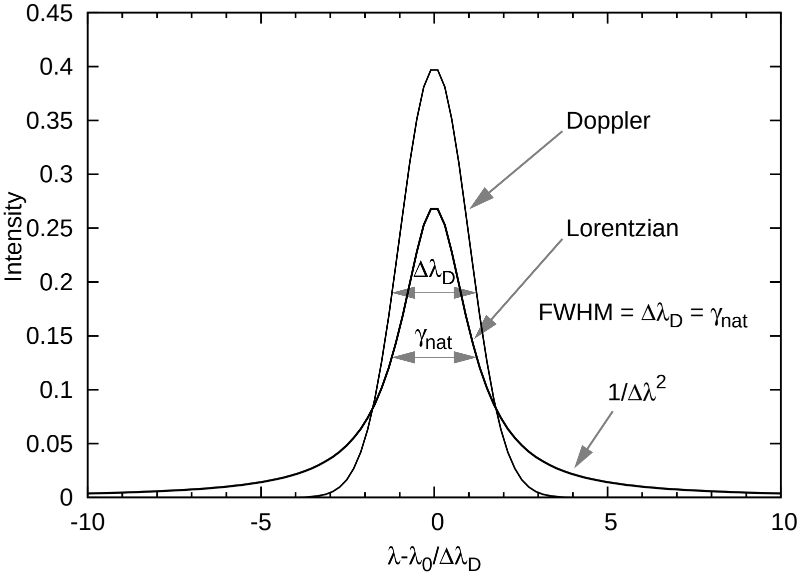

Figure 3.2: Comparison of Doppler and Lorentzian line shapes having equal FWHM and strengths.

The mass absorption coefficient, expressed in area per unit mass, used in numerical calculations is obtained by multiplying the equation 3.16 with the number of absorbers per unit mass (N/ρ). Again the excitation and ionization equations 3.5 and 3.6 are used to calculate the population of species in a given excitation and ionization levels. The dominant absorbers that contribute effectively to the line opacity in the atmospheres of stars of various spectral types are shown in the figure 3.3.

On the other hand, the geometry of the photospheric gases introduce additional broadening on the microscopic and macroscopic scales. If the size of the turbulence

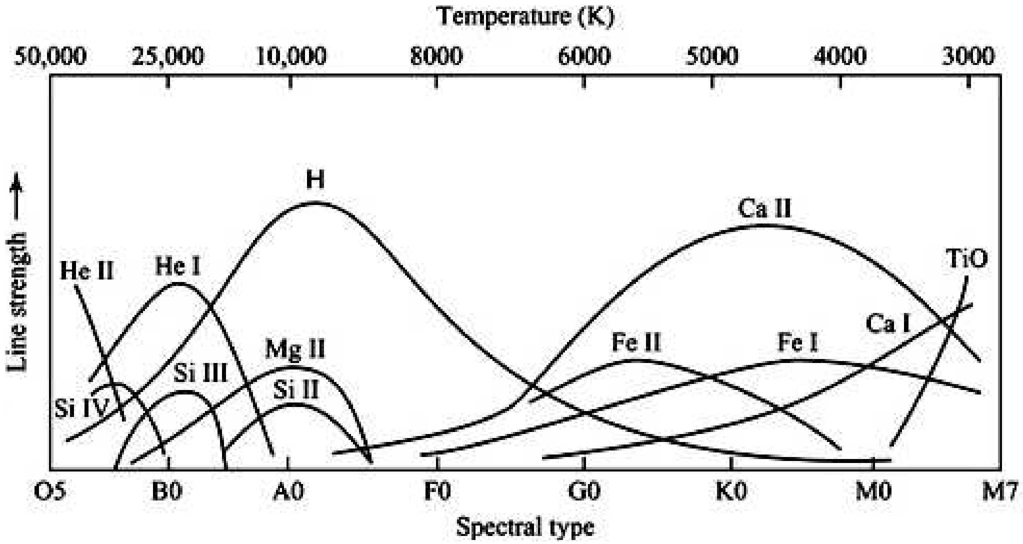

Figure 3.3: Dependence of line strength on the surface temperature

cell is smaller than the mean free path of the photon, we have the case for a non-thermal velocity field known as microturbulence, whose profile is similar to thermal profile and desaturates the core since it introduces extra broadening thereby increasing the line strength. Other broadening mechanisms that fall into this category are Zeeman splitting and hyperfine structure.

Macroturbulence prevails in the photosphere when the size of turbulence elements is large enough to confine the photons to them from the time they are created until they escape from the star. Since all stars rotate, it also introduces an additional broadening. Both these large scale motions have the effect of smearing out the spectral line without changing the line strength.

3.3.3 Contribution function

We know that the lines observed in a stellar spectrum are not all formed at the same geometrical depth in the atmosphere. For efficient probing, the average depth of formation of spectral lines is essential to study the depth dependence of certain atmospheric variables, such as the temperature, the atmospheric turbulence etc. In the centre of a strong line, where the line opacity is so high and there is no contribution from the continuum forming layers (as we can not see deep enough), the majority of the photons emerge from the cool outer layers. This makes the radiation flux lower in core of the spectral line than in the surrounding continuum. If we move toward the line wings, where the opacity becomes smaller, we can see relatively deep into the stellar atmosphere; then we can receive the radiation due to the line and also from the continuum. In the continuum forming layers the opacity is relatively low, as only continuum processes contribute. As a result we can see much deeper into the atmosphere at those wavelengths to relatively hot layers and thus the observed radiation is dominated by the continuous radiation.

Contribution function quantitatively describes the relative contribution of various atmospheric layers to the observed line depression, and is calculated for several wavelength distances $\Delta\lambda$ relative to the line centre. This function is also useful to evaluate the sensitivity of the derived abundances to changes in atmospheric parameters.

Numerous attempts have been made to derive the contribution function to the spectral line depression in a stellar atmosphere. MOOG uses the formal-solution method, as discussed in Edmonds (1969), which involves straight forward evaluation of formal solutions for both the minimum residual flux in the line and continuum flux. The relative line depression at some frequency in a stellar atmosphere is defined by

$$R(0) = \frac{[F_c(0) - F_l(0)]}{F_c(0)} \tag{3.17}$$

where $\mathrm{F}_c(0)$ and $\mathrm{F}_l(0)$ are the line and continuous flux at the same frequency.

The surface flux at some frequency is given by

$$F(0) = 2\pi \int_0^\infty S(\tau[x]) E_2(\tau[x])\, d\tau(x) \tag{3.18}$$

where

$$E_2(\tau_\nu[x]) = \int_1^\infty \frac{exp[-\tau(x)w]}{w^n} dw \qquad \text{where } w = \sec\theta$$

and $\mathrm{S}(\tau[x])$ is the total source function at an optical depth $\tau(x)$ and x is the geometrical depth.

In stellar atmospheres, it is more convenient to work in the $\log\tau_{ref}$ scale, τ_{ref} being the optical depth at a reference wavelength λ_{ref}. In LTE, $\mathrm{S}(\tau[x]) = \mathrm{B}(\mathrm{T}[\mathrm{x}])$, where $\mathrm{B}(T[x])$ is the Planck function and the optical depth scales are related by

$$\begin{aligned} dx = \frac{d\tau}{\kappa\,\rho} \quad &= \quad \frac{d\tau_{ref}}{\kappa_{ref}\,\rho} \\ d\tau = \frac{\kappa}{\kappa_{ref}} d\tau_{ref} \quad &= \quad \frac{\kappa}{\kappa_{ref}} \frac{\tau_{ref}}{ln\, e}\, d\, log\, \tau_{ref} \end{aligned} \tag{3.19}$$

Replacing the quantities in the numerator of equation 3.17 by their expressions of the form in equation 3.18, we obtain

$$R(0) = \int_0^\infty C_D(\Delta\lambda, x)\, d\, log\, \tau_{ref} \tag{3.20}$$

Thus, the contribution function, $C_D(\Delta\lambda, x)$, to the line depression within a spectral line with a opacity κ_{ref} and optical depth τ_{ref} at a reference wavelength λ_{ref} is given by

$$C_D(\Delta\lambda, x) = \frac{2\,\tau_{ref}}{0.4343}\frac{\kappa_c(x)}{\kappa_{ref}}\frac{B(T[x])}{F_c(0)}\left[E_2(\tau_c[x]) - \left(1 + \frac{\kappa_l(x)}{\kappa_c(x)}\right) E_2(\tau_c[x] + \tau_l[x])\right] \tag{3.21}$$

where the subscript c is associated with the continuum which is assumed to be constant over the width of the line. The subscript l referes to the discrete (line) components which varies over the line and hence a function of $\Delta\lambda$. Following this κ_c and τ_c represent the continuum opacity and optical depth at the wavelength of the line; and κ_l and τ_l are the line opacity and associated optical depth. $F_c(0)$ is the emerging continuum flux.

3.4 Analysis

A detailed analysis of the spectral line profiles and their relative strengths allow us to extract information on many important stellar parameters such as the star's radial and rotational velocities, the effective temperature (T_{eff}), surface gravity (log g), microturbulence (ξ_t), and the chemical composition of the stellar atmosphere. Stellar profiles of certain lines such as H_α exhibiting P-Cygni profile have also been used to estimate mass-loss. In the following sections we describe the determination of the parameters relevant to our study from the analysis of our program star spectra.

3.4.1 Radial velocity

The first thing that can be measured easily using the absorption lines in the stellar spectra is the radial (or line-of-sight) velocity of the star. It is calculated by means of the Doppler shift in central wavelength of the spectral lines relative to their laboratory values. We used Rowland's preliminary table of solar spectrum wavelengths (Moore et al. 1966) and the Arcturus spectrum (Hinkle et al. 2000) to identify clean, unblended, unsaturated and isolated spectral lines due to both the atomic and ionic species. The central wavelength of these lines is calibrated by fitting a gaussian profile to their line core using the routines available in *splot* task of IRAF. The radial motion of the star changes the effective wavelength of the light received by an observer on the Earth by $\Delta\lambda$ ($= [\lambda_o - \lambda_c]$) such that

$$\frac{v_{rad}}{c} = \frac{\Delta\lambda}{\lambda_c} \qquad (\text{for v}_{rad} << \text{c}) \tag{3.22}$$

where λ_o and λ_c are the observed and rest wavelengths. c is the speed of light and v_{rad} is the radial velocity of the star. Next, the observed spectrum is corrcted for the Doppler shift using the routine *dopcor* available in IRAF. The accuracy of the radial velocities depends upon to the S/N ratio, accurate dispersion solution, spectral resolution and stability of the instrumental set up during observation.

Due to the orbital motion of the Earth around the Sun, the measured radial velocity of the star keep varying over the year. The heliocentric radial velocity of a star is measured by correcting the observed radial velocity for the Earth's rotation, lunar motion and annual motion using the task *rvcorrect*. In addition to proper motions, radial velocity of stars is essential to confirm their membership to OC.

3.4.2 Equivalent width

The principle goal of current study is the determination of chemical composition of the stars preserved in their photospheres in the form of absorption lines. In abundance studies the strength of the profile is termed as equivalent width (EW) and measured in units of Å or mÅ. The EW of a spectral line is defined as the width of a dark rectangular profile whose area is equivalent to integrated area of that line on a normalised spectrum (see figure 3.4). EW quantifies the amount of electromagnetic flux removed by the line from the adjacent continuum and is expressed as

$$W_\lambda = \int_{line} \left(1 - \frac{F_\lambda}{F_c}\right) d\lambda \tag{3.23}$$

Where F_λ and F_c are the line and continuum fluxes respectively.

The selection of stellar lines which are free from blends is very crucial for deriving accurate elemental abundances. The EW for a given species is measured manually using the routine *splot* contained in IRAF by fitting often a Gaussian profile, for a few lines a direct integration was preferred as a best measure of EW.

3.4.3 Concept of Curve of growth

Theroretical stellar models follow the curve-of-growth (cog) concept for the computation of abundance of the species in the stellar atmosphere. The cog describes the

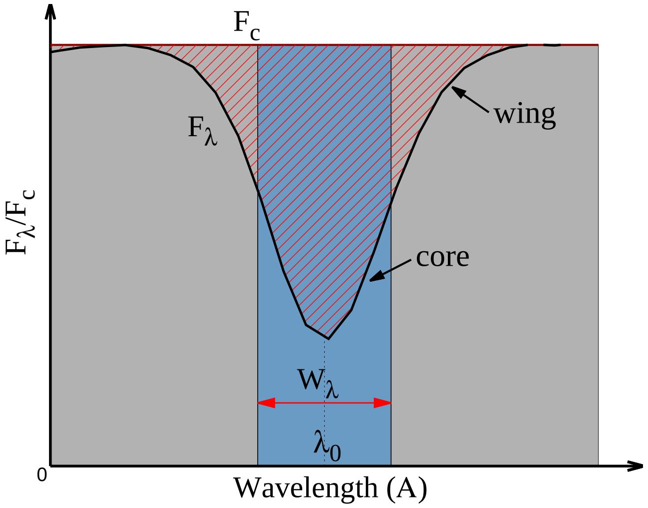

Figure 3.4: The equivalent width (W_λ) of a spectal line with central wavelength λ_0.

dependence of equivalent width on the effective number of absorbing atoms or ions. It allows a simultaneous measurement of the stellar atmospheric parameters (T_{eff}, log g, ξ_t) and chemical composition of the star.

A basic cog constructed using the measured solar EWs of Fe I lines from the solar integrated disk spectrum (Kurucz et al. 1984) is shown in the figure 3.5. A cog can be formed by plotting reduced equivalent, $\log{(W_\lambda/\lambda)}$ against abundance or log gf-$\chi\Theta_{exe}$, where gf is the statistical weight of the lower energy state multipled by oscillator strength, χ the excitation potential and Θ_{exe} is the excitation temperature, given by 5040/T_{eff}.

There are three regions on the cog characteristic of spectral lines of various strength.

- For smaller effective number of absorbing atoms (Nf), lines are weak. The line strength varies linearly with Nf (i.e., $W_\lambda \propto$ Nf), and is called the linear part of the cog. This means that if the number of absorbers are doubled, twice as much of flux is removed and the spectral line doubles in strength.

- For intermediate values of Nf, the Doppler core of the line becomes optically thick and saturates. The presence of microturbulence causes the saturation at relatively higher Nf. But, the line wings are still optically thin and deepen very slowly with the number of absorbers and produces a plateau in the cog, known as flat part of the cog, where $W_\lambda \propto (\ln \mathrm{Nf})^{\frac{1}{2}}$. Since the equivalent width of lines on this part is affected by ξ_t in addition to abundance, moderately strong lines are useful for abundance analysis only when accurate ξ_t is available.

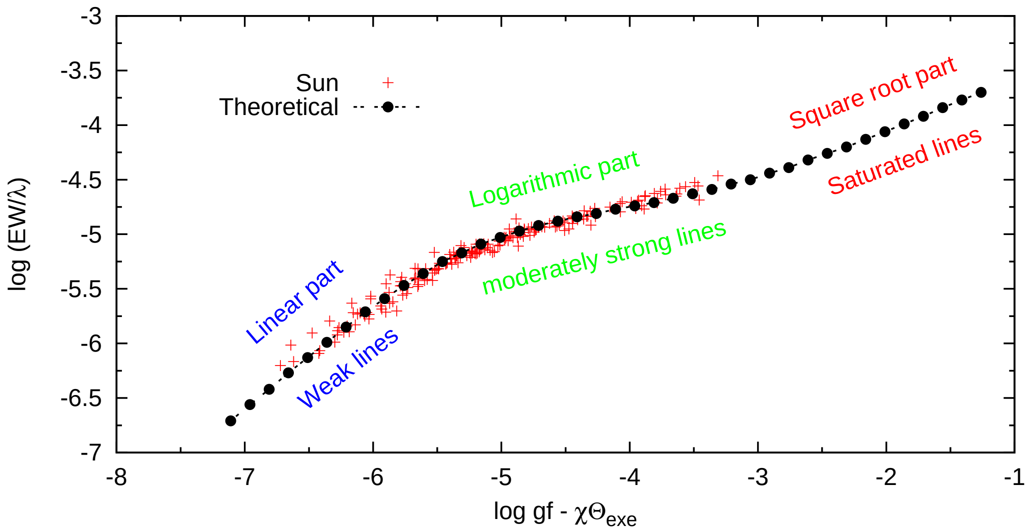

Figure 3.5: An example of a curve-of-growth constructed using Fe I lines from the Sun with measured EWs (plus signs) along with a theoretical one (dot-dashed line) generated for a solar atmospheric model with T_{eff}= 5777 K, log g=4.44 cm s^{-2} and ξ_t = 0.95 km s^{-1}

- For very large values of Nf, the core saturates and the equivalent width is dominated by the line wings, which can no longer be fitted with a gaussian profile. Thus the measured equivalent widths are uncertain for the strong lines and this region is not useful for abundance analysis. This portion is called the damping or the square root part of the cog for which $W_\lambda \propto (N\gamma f)^{\frac{1}{2}}$, where γ is the damping factor.

We have employed only those lines for abundance analysis which lay mainly on the linear and logarithmic parts of the curve-of-growth due to their sensitivity to the number of absorbers.

The observed cog, resulted from the EWs and selected stellar atmosphere model, is compared to the theoretical cog in order to determine an abundance for each spectral line. The equation that connects the observed EW and stellar model atmosphere parameters with the abundance and atmoic details of the element is given by (chapter 14, Gray 1992)

$$\log\left(\frac{W_\lambda}{\lambda}\right) = log(C) + log\left(\frac{N_r/N_E}{u(T)}\right) + log\,A + log(gf\lambda) - \left(\frac{5040}{T_{exc}}\right)\chi - log\,\kappa_\lambda \quad (3.24)$$

Where C is a constant. λ and W_λ are the central wavelength and EW of a given spectral feature which are measured from the spectra. gf and χ are respectively the oscillator strength and lower excitation potential (LEP), atomic details, of a given species. u(T) and κ_λ are the partition function and opacity distribution functions. T_{exe} is the excitation temperature/effective temperature of the star and the abundance defined as $A = N_E/N_H$ is the ratio of number of atoms of the element E to that of hydrogen atmos (N_H). Finally, N_r/N_E, defined as the fraction of the element E in the r^{th} ionization state, is given by the Saha ionization equation as

$$log\left(\frac{N_1}{N_0}P_e\right) = 2.5\,log(T_{ion}) - \frac{5040}{T_{ion}}I + log\left(\frac{u_1}{u_0}\right) - 0.1762 \qquad (3.25)$$

Where N_1/N_0 is the ratio of the ions to neutrals, u_1/u_0 is the ratio of ionic to neutral partition functions, I and T_{ion} are the ionic potential and ionization temperature of the species, and P_e ($=N_e kT_{ion}$) is the partial pressure due to the number of free electons (N_e) in the ionized atmosphere. P_e is proportional to surface gravity, and varies as $g^{0.30-0.45}$ when going from deep to shallow layers of the cool stars.

Presently available radiative transfer codes solve these equations more rigourously, using input atomic data and a detailed depth-independent theoretical model atmospheres, while assuming the stellar atmosphere is in Local Thermodynamical Equilibrium (LTE). A brief description of these details is given below.

3.4.4 Atomic data

The important inputs for abundance analysis are high quality atomic data: central wavelengths, LEPs, and oscillator strengths (or) atomic transition probabilities (or) log gf-values. Of these, the accuracy of the derived abundances to a great extent depend on the quality of the gf-values. Experimental log gf-values of high accuracy (5 to 10%) are available for a large fraction of iron lines (neutral and singly ionized) from the literature: Führ & Wiese (2006), NIST database[1] etc. This gave us a freedom to select a large sample of absorption lines due to iron thanks to the availability of numerous number of iron lines in the optical spectra. As the overall goal is to have the best possible abundance determination, for other elements due to their scarcity in the optical region, we have identified a set of self-consistent absorption lines that have high-quality relative gf-values. The details of the selected spectral lines used for the abundance analysis will be discussed elsewhere in this thesis work.

---

[1] `http://physics.nist.gov/PhysRefData/ASD/lines_form.html`

3.4.5 Model atmospheres

Extracting information about the chemical composition of the stars requires realistic models of the stellar photosphere and the line-formation processes. The stellar photosphere is defined as the deepest region of a star, transparent to photons of certain wavelengths and the cooler region above it, where the absorption lines are formed is called the reversing layer of the star. Stellar models are constructed to closely mimic the physical conditions in the stellar atmosphere by characterising each layer with a temperature, gas pressure, electon density, mean opacity etc. The most widely used theoretical model atmospheres in the solar and stellar abundance studies are the Kurucz (1993) and MARCS (Gustafsson et al. 2008) grids of models. The main assumptions and limitations of these classical models are:

1. The atmosphere is plane parallel as the geometrical depth of the photosphere is much smaller than the radius of the star, and hence the gravity is a constant through out the photosphere. The optical depth (τ_λ) varies from infinity in the deeper layers to 0 at the surface of the photosphere. The plane-parallel approximation is adequate for main sequence and giant stars employed in present work, but breaks down for low surface gravity stars with extended envelopes (for example, supergiants).

2. The atmosphere is homogeneous, ignores fine structures like granulation and starspots, so that the physical quantities vary only with depth.

3. The atmosphere is in hydrostatic equilibrium i.e. there is no net acceleration of the atmospheric layers in the normal direction. Hence the total pressure at every geometrical depth exactly balances the gravitational attraction.

   $$\frac{dP}{d\tau_\lambda} = \frac{g}{\overline{\kappa}_\lambda} \tag{3.26}$$

   where τ_λ is the optical depth, g the surface gravity, P the total pressure, and $\overline{\kappa}_\lambda$ the mean mass absorption coefficient of the stellar substance.

4. As there are no sources of energy within the atmosphere, the total energy flux remains constant with depth and the energy is carried by radiation alone. This makes the atmosphere in radiative equilibrium, neglecting convective transport and hydrodynamical effects.

The model atmospheres developed with these assumptions are called LTE models. In LTE, every transition is exactly balanced by its inverse transition due to collisions among the absorbers and the radiation field is unimportant in govering level populations. The velocity distribution of particles is Maxwellian, and the level populations are calculated from the Saha and Boltzmann equations and depend only on local temperature and electron number density. LTE is valid approximation in the deep layers of a stellar photosphere where the densities are high enough for the collisions to dominate over radiative processes. In this condition, the intensity and flux become more isotropic and the material radiates at a local temperature as a black body radiator. At the higher layers the assumption of LTE breaks down as the leakage of photons become more significant that the intensity of radiation is far from being in thermal equilibrium.

LTE is not a good approximation for photospheres of stars having too hot or extended atmospheres (supergiants). Then the equations of statistical equilibrium need to be solved to obtain the correct population numbers. Since our program stars are all low-mass giants, some of the elemental abundances might be affected by non-LTE effects, eventhough the affect is not severe. But the use of non-LTE models is constrained by insufficient atomic data like collision strengths and uncertainities in the handling the radaiation field properly. Moreover, in LTE it is relatively easy to handle line blanketing, as one neglects the effect of radiation on atomic population numbers, which saves enormous computing time. Hence only LTE models have been employed for the abundance determination of all our program stars.

We have used the ATLAS9 (Castelli & Kurucz 2003) model atmosphere grid available at the database[2] from which one can interpolate individual model atmospheres. The grid covers a range of effective temperature between $3500 \leq \mathrm{T}_{eff} \leq 50000$ K at steps of 250 K and surface gravities between $0.0 \leq \log\ g \leq 5.0$ dex at steps of 0.5 dex, where larger temperatures only have high gravities. All models were calculated with a constant microturbulent velocity of 2 km/sec. For each model 72 individual layers are calculated, making it the highest resolution grid available. Each layer in Kurucz model is characterised by its mass density per unit volume (ρ_x), Temperature (T), gas pressure (P_g), electon number density (N_e), Rosseland mean opacity (κ_{Ross}). Most of the outer layers have meager impact on the abundance analysis because only few layers near $\tau = 1$ significantly contribute to the absorption profile.

All these models were computed using the standard solar metallicity opacity distribution functions (ODFs) and the abundance of each element is explicitly set to solar values in each of the models. The overall difference between the models

---

[2] `http://kurucz.harvard.edu/grids.html`

calculated at [M/H] = 0 dex versus other metallicities is not significant to make any difference in the abundance analysis.

3.4.6 Radiative transfer code

Following the measurement of EWs, the next step in the analysis is the determination of element abundances for each of the selected spectral lines. Chemical composition studies involve both the fine analysis and spectrum synthesis methods depending on the need and quality of the spectra. The measured EWs from the spectra are converted to abundances in fine analysis while in the spectrum synthesis the observed spectra are directly compared with the synthetic spectra until a good match is found.

For the abundance analysis of our program stars we have used the latest version (2010) of the LTE line analysis and spectrum synthesis code MOOG which was developed by Chris Sneden and originally described in Sneden (1973)[3] for his PhD thesis. The coding is in various subroutines that are called from a few driver routines; these routines are written in standard FORTRAN. Much of the MOOG code follows other radiative transfer codes such as WIDTH and SYNTHE of R. L. Kurucz[4]. MOOG supports the graphics package Supermongo (SM), chosen for its ease of implementation in FORTRAN codes, to do online plotting. We briefly describe the above two methods of abundance analysis using MOOG.

Fine analysis

This method of analysis consists of matching the EW of a line predicted for a given model atmosphere and the input line data to the measured EW. The line data comprises of the central wavelength of the line, ionic state of the element, LEP, oscillator strengths (or) log gf-values and the measured EWs.

MOOG follows the formal solution method (refer to section 3.3.3) and compute the abundance of a given species by minimizing the difference between the observed and theoretical cogs. The shape of the cog is the same for the lines of different elements in the same star, but varie from star to star. Hence, the same cog is used to derive abundance of other elements in the stellar atmosphere.

As a final step, the derived abundances from the individual lines of a particular element are averaged and the MOOG produces three graphs: abundance against reduced equivalent width, abundance against LEP, and abundance against wavelength of the lines due to same element. These graphs offer a possibility to select a suitable

---

[3] `http://www.as.utexas.edu/~chris/moog.html`

[4] `http://kurucz.harvard.edu/`

model atmosphere from the grid for which the observed absorption lines in the spectra are readily reproduced.

Selection of model atmosphere: We have performed abundance analysis by running the MOOG in *abfind* mode while satisfying the below three constraints:

1. **Microturbulence**: The microturbulence assumed to be isotropic and depth independent is determined from Fe II lines by the requirement that the abundance be independent of a line's EW i.e. both the weak and strong lines must yield a same abundance for a chosen ξ_t value. This approach is born out of consideration that weak lines are unaffected by ξ_t while moderately strong lines are affected by ξ_t. Fe II lines are preferred as they cover a small range in LEP so that the derived abundance is free from non-LTE effects, and cover a large range in equivalent widths, that will include both weak and strong lines. Further, the derived ξ_t value is verified using the Sc I, Ti I, Ti II, V I, Cr I, and Cr II lines, details will follow in the next chapters.
2. **Effective temperature**: The effective temperature is estimated by imposing the requirement that the Fe abundance from Fe I lines (as they provide large number of lines with a good range in LEP: 0.0 to 5.0 eV) be independent of a line's LEP. This is because the predicted population of various excitation levels is a function of the temperature of the stellar atmosphere. If we have the temperature right, all the Fe I lines of different LEPs yield the same abundance that match well the observed absorption.
3. **Surface gravity**: The surface gravity is estimated by requiring that Fe I and Fe II lines give the same Fe abundance, i.e. maintaining the ionization equilibrium between neutral and ionized species, for the derived effective temperature and microturbulence. A check on this condition is performed by Sc, Ti, V, and Cr lines also as they provide both neutral and ionized lines.

Finally, the best model for each of the program stars is selected through successive iterations until all three constraints are satisfied simultaneously.

Spectrum synthesis

We compared the stellar spectra to the synthetic spectra to derive abundances for the lines affected by blends, hyperfine structure and isotopic shifts. Spectrum synthesis was done by adopting the various smoothing parameters such as instrumental, rotational, microturbulence broadening, and limb darkening with a fine tuned macroturbulence to adjust the resolution of the synthetic spectra and to match the overall width of the spectral lines. The instrumental broadening is better represented by a guassian profile, which has the same FWHM as the instrumental profile, measured by the FWHM of Th I lines in comparison spectra, convolved with the observed spectrum. The rotational broadening, not significant for red giants, enters into the synthesis by intergrating the Doppler shifted, due to rotation of the star, intensity measurements coming from the different parts of the stellar disc to obtain the flux. The microturbulence velocity is same as that obtained in fine analysis. In order to account for the decrease in the emergent intensity from the center of the disc to the limb a limb darkening value is calculated from the available empirical relations. Finally, the large scale structures in the stellar atmospheres, macroturbulence, are simulated by a gaussian and convolved with observed specta.

The inputs to the *synth* driver for spectrum synthesis are as follows: stellar atmospheric model used for the fine analysis along with a reference abundance for relevant elements, synthesis limits, step size in Å smoothing parameter values, and a well organized linelist similar to the one used in fine analysis but without measured EWs. The linelist includes both atomic and molecular features (C_2, CN, MgH etc.) near the line whose abundance has to be determined, and multiple components and isotopic shifts for the case of the lines affected by hyperfine structure, that desaturates and smears out the single stellar line to appear as a broad line, thereby resulting spurious abundances for species if the calculations are based on EW measurements. The atomic and molecular data required for the spectrum synthesis are available at the Kurucz database.

The user has a control to change the abundance of individual elements and isotopes, and also the smoothing parameters to speed up the process of converging on the best fit. For a given input MOOG driver calculates the continuum and line flux at each point separated by a step size.

Chapter 4

Chemical compositions of the sample Open Clusters

4.1 Introduction

We have used high quality (S/N) and high-dispersion echelle spectra ($R \geq 55,000$) of red giant members for a sample of eighteen OCs obtained using the 2.7-m Harlan J. Smith telescope at the McDonald observatory to measure abundances for many elements representing different production mechanisms (α- and r- process, Fe- Peak and s-process) and sites (i.e. SNII, SNIa and AGB environments). The basic observation procedures, data reduction and differential abundance analysis techniques relative to the Sun are discussed in our published papers Reddy et al. (2012, 2013).

We maintained the homogeneity throughout the analysis i.e. observing only giants, avoiding spectroscopic binaries, and those with very similar color to narrow down the spread in temperature and gravities, usage of the same linelist/atomic data and model atmosphere grid for abundance analysis to reduce the random errors. Synthetic spectra were computed for species affected by hyperfine and isotopic splitting or affected by blends. We have tested our linelists extensively to reproduce the solar and Arcturus spectra and measured the solar abundances to establish a reference abundance scale.

We devote this chapter to the derivation of abundances for various elements from Na to Eu including the s- and r-process elements for which the measurements are often lacking in the literature.

4.2 Sample selection

We selected the OCs sample, not yet subjected to a comprehensive abundance analysis using high resolution spectroscopy, from the *New catalogue of optically visible open clusters and candidates*[1] (Dias et al. 2002).

Though the spectra of hot main sequence stars are the exact representation of the chemical composition of proto-cluster gas clouds from which the cluster members were formed, they are unsuitable for measuring accurate abundances. The unevolved hot stars generally have low luminosities and their high rotational velocities result in shallower line profiles with low residual intensities. Weak photospheric lines, especially due to s- and r-process elements, in the spectra of these stars become washed away completely in rotationally broadened profile. Moreover, these lines are intrinsically weaker in the spectra of main sequence stars than for giants.

We elected to observe giants, primarily, because of their high luminosity. Selection of giants instead of main sequence stars enables the extension of our observations to more distant OCs for the faint limit of the telescope and spectrometer combination accessible to us. In addition, the spectra of giants are favourable for abundance determination as their lines are sharp and they contain both the weak and strong lines due to various atomic species including the s- and r-process elements for which the measurements are often lacking in the literature.

We have made use of the WEBDA[2] database for the selection of suitable red giant candidates and cross-checked with the SIMBAD[3] astronomical database. Our sample of OCs covers galactocentric distances (R_{gc}) of 7.8 to 11.3 kpc, [Fe/H] of $\sim$ -0.4 dex to solar and an age range of 0.2 to 1.2 Gyr, with an exception of NGC 2682 (M67) with an age of 4.3 Gyr.

4.3 Observations and Data reduction

High-resolution optical spectra of the program stars were obtained during the nights of 1999 February 6-10, 2011 January 12-14 and March 15-18 with the Robert G. Tull echelle coudé spectrograph (Tull et al. 1995) on the 2.7-m Harlan J. Smith telescope at the McDonald observatory using a 2048 x 2048 pixel Tektronix charge-coupled device (CCD) as a detector. The CCD has a gain of 0.584 e^-/ADU and readout noise of 3.06 e^-. All the spectra correspond to a resolving power of $R \gtrsim 55{,}000$ (< 6

---

[1] `http://www.astro.iag.usp.br/~wilton/`

[2] `http://www.univie.ac.at/webda/`

[3] `http://simbad.u-strasbg.fr/simbad/`

km s^{-1}) as measured by the FWHM of Th I lines in comparison spectra, except for the members of NGC 2354 whose spectra was taken at lower resolution of 30,000. The spectral coverage in a single exposure from 4000 Å to 5600 Å across various orders was complete but incomplete from 5600 Å to about 9800 Å, where the inter-order gaps begin to appear. Such a wide wavelength coverage is essential for the chemical abundance studies allowing us to select suitable unblended lines.

The basic observation procedure and the data reduction techniques have already been elaborated in Chapter 2. During each observing run, we have acquired a series of bias and flat frames at several exposure levels chosen to match those of the program stars, and comparison Th-Ar spectra were taken to establish the wavelength scale. We obtained on each night the spectrum of a rapidly-rotating B star to monitor the presence of telluric lines. In order to minimize the effect of cosmic rays and to acquire a good signal-to-noise (S/N) ratio for our program star spectra, two or three exposures were taken each lasting for 20-30 min depending on the magnitude of the star.

Spectroscopic reductions were done with the standard spectral reduction software IRAF[4] containing the *imred* and *echelle* packages, towards bias subtraction, scattered light correction, flat-fielding, order tracing with subsequent extraction, wavelength calibration and continuum fitting.

Multiple exposure frames from each of the stars were median combined to acquire optimal S/N ratio and then trimmed to reduce the edge effects before the continuum fitting. The final extracted spectra have S/N ratio of about 100−190 as measured around 6000 Å region, while at wavelengths shorter than 5000 Å the S/N ratio decreases to 50-80 with decreasing wavelength. The continuum fitting was done interactively by marking continuum regions on each aperture which were then fitted by a cubic spline of appropriate order for proper continuum fitting.

We measured the radial velocity (RV) of each star from its continuum-fitted spectrum using the cores of weak and moderately strong lines (as discussed in Section 3.4.1 of Chapter 3) of various atomic species. Observed radial velocities were converted to heliocentric velocities using the *rvcorrect* routine available in IRAF software. Our radial velocity measurements are in good agreement with the previous radial velocity measurements for the red giants in OCs (Mermilliod et al. 2008). But, for NGC 2266, no radial velocity measurements from high-resolution spectra

---

[4] IRAF is a general purpose software system for the reduction and analysis of astronomical data distributed by NOAO, which is operated by the Association of Universities for Research in Astronomy, Inc. under cooperative agreement with the National Science Foundation.

are available in the literature. Recently, Carrera (2012) analyzed medium-resolution spectra (R $\sim$ 8000) in the infrared CaT region ($\sim$ 8500 Å) for stars in NGC 2266 and derived a mean radial velocity of $\langle$ RV $\rangle = -16\pm15$ km s^{-1} based on four stars. For this cluster, we selected the star with ID 73 whose membership has been confirmed through photometry (Kaluzny & Mazur 1991). Our radial velocity estimate of -29.7 ± 0.2 for this OC would appear to be the first measurement available in the literature with negligible dispersion whereas Carrera's measurement suffers from large uncertainty around the mean. Our radial velocity measurement for this OC differs from the Carrera's value by -10 km s^{-1}, but is well within the quoted uncertainty in Carrera (2012).

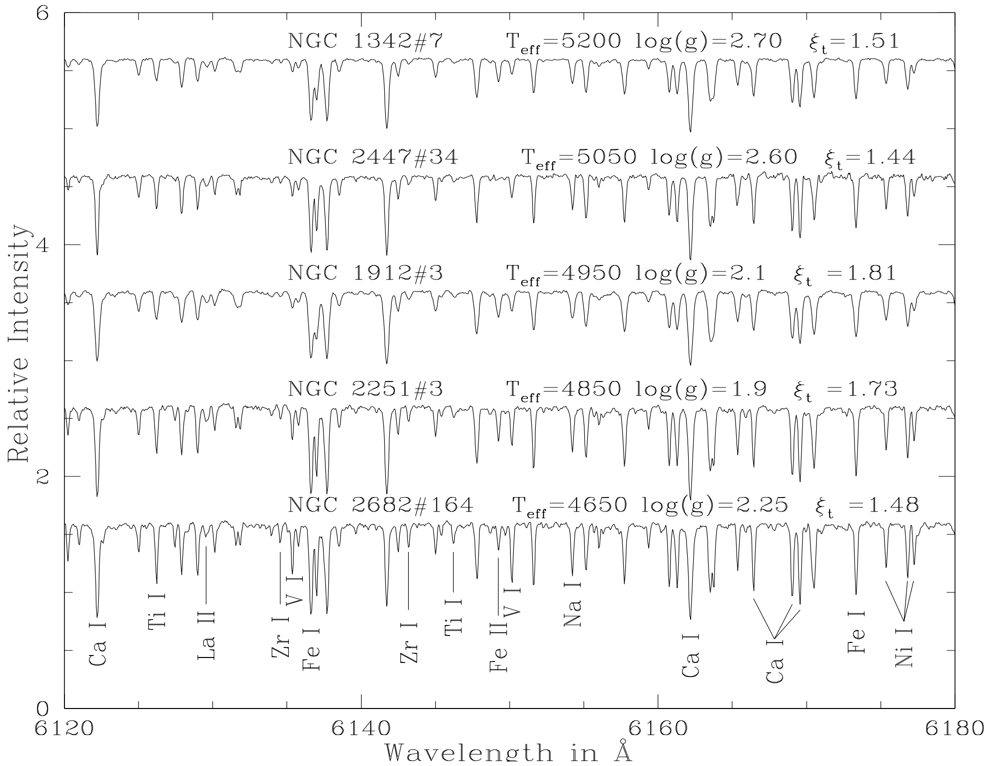

Figure 4.1: Normalized spectra of the red giant members for a sample of five open clusters as described in Table 4.1 are presented in descending order of temperature (top to bottom) in the λ 6120-6180 Å region. All the spectra are on the same scale but have been displaced vertically from each other for clarity.

Table 4.1: The list of stars observed from each of the selected clusters.

Cluster	Star ID	α(2000.0) (hh mm ss)	δ(2000.0) (° ′ ″)	V (mag.)	B-V	V-K$_s$	J-K$_s$	$RV_{\rm helio}$ (km s^{-1})	S/N at 6000 Å	Date of observation
NGC 752	77	01 56 21.60	37 36 08.00	9.35	+1.02	+2.51	+0.64	+6.3±0.2	100	08-02-1999
	137	01 57 03.10	38 08 02.00	8.89	+1.02	+2.35	+0.60	+5.9±0.2	100	07-02-1999
	295	01 58 29.80	37 51 37.00	9.29	+0.96	+2.25	+0.58	+6.3±0.2	120	10-02-1999
	311	01 58 52.90	37 48 57.00	9.04	+1.03	+2.40	+0.63	+6.7±0.2	120	08-02-1999
NGC 1342	4	03 32 11.23	+37 22 55.43	09.26	+1.31	+3.26	+0.78	−10.9±0.2	180	29-11-2012
	6	03 31 26.98	+37 21 28.62	09.65	+1.18	+3.02	+0.66	−10.3±0.2	170	29-11-2012
	7	03 32 02.46	+37 21 21.50	09.98	+1.22	+2.89	+0.64	−10.8±0.2	170	30-11-2012
NGC 1662	1	04 48 29.51	+10 55 48.27	08.34	+1.18	+2.99	+0.71	−13.6±0.2	180	29-11-2012
	2	04 48 32.08	+10 57 59.02	08.87	+1.16	+3.02	+0.69	−12.9±0.2	180	29-11-2012
NGC 1817	8	05 12 19.38	16 40 48.64	12.13	+1.03	+2.80	+0.70	+66.1±0.2	110	09-02-1999
	81	05 12 06.27	16 38 15.34	12.17	+1.12	+2.71	+0.68	+66.6±0.2	90	10-02-1999
	73	05 12 24.65	16 35 48.84	12.04	+1.08	+2.85	+0.74	+66.5±0.2	90	10-02-1999
NGC 1912	3	05 28 44.05	+35 49 52.77	09.85	+1.19	+2.85	+0.66	−0.2±0.2	140	18-11-2011
	70	05 29 08.37	+35 51 29.78	10.04	+1.10	+3.13	+0.66	+0.6±0.2	170	18-11-2011
NGC 2251	3	06 34 51.24	+08 19 31.90	10.39	+1.22	+2.92	+0.72	+26.2±0.2	150	14-01-2011
	33	06 34 37.07	+08 21 39.50	10.39	+1.21	+2.91	+0.70	+26.3±0.2	150	14-01-2011
NGC 2266	73	06 43 16.69	+26 57 05.19	11.06	+0.99	+2.46	+0.69	−29.7±0.2	100	14-01-2011
NGC 2335	11	07 06 11.42	−09 56 22.70	10.89	+1.13	+2.76	+0.67	−3.21±0.1	160	16-03-2011
NGC 2354	183	07 13 51.93	−25 44 24.30	11.41	+1.25	+2.79	+0.70	+35.6±0.4	100	06-03-2013
	205	07 13 59.21	−25 45 50.31	11.13	+1.20	+2.50	+0.71	+35.0±0.3	110	06-03-2013
NGC 2360	5	07 18 14.13	−15 37 30.49	10.74	+1.04	+1.50	+0.23	+30.4±1.1	77	07-02-1999
	6	07 18 19.08	−15 37 32.62	11.03	+1.04	+1.00	+0.16	+29.1±0.1	95	08-02-1999
	8	07 18 10.84	−15 34 13.30	11.09	+1.01	+1.44	+0.16	+29.2±0.2	80	08-02-1999
	12	07 18 09.58	−15 31 39.80	10.34	+1.16	+2.89	+0.69	+29.5±0.4	75	07-02-1999
NGC 2447	28	07 44 50.25	−23 52 27.14	09.96	+0.82	+2.33	+0.56	+21.1±0.3	100	04-03-2013
	34	07 44 33.67	−23 51 42.20	10.15	+0.90	+2.21	+0.57	+22.7±0.3	110	04-03-2013
	41	07 44 25.73	−23 49 52.95	10.16	+0.89	+2.28	+0.52	+22.2±0.2	110	04-03-2013
NGC 2482	9	07 55 09.09	−24 22 30.25	10.27	+1.11	+2.38	+0.61	+39.00±0.2	190	15-03-2011
NGC 2506	2212	08 00 08.68	−10 46 37.50	11.95	+1.07	+2.58	+0.67	+84.1±0.2	50	09-02-1999
	3231	07 59 55.77	−10 48 22.73	13.12	+0.98	+2.33	+0.60	+84.9±0.4	45	09-02-1999
	4138	08 00 01.49	−10 45 38.50	13.30	+0.91	+2.38	+0.63	+84.9±0.3	60	10-02-1999
NGC 2527	10	08 04 46.97	−28 07 50.04	09.49	+0.95	+2.17	+0.59	+40.7±0.2	170	12-01-2011
	203	08 05 33.91	−28 08 58.44	09.51	+0.98	+2.21	+0.59	+40.4±0.2	180	13-01-2011
NGC 2539	346	08 10 23.02	−12 50 43.25	10.92	+0.99	+2.28	+0.57	+29.7±0.2	130	17-03-2011
	463	08 10 42.87	−12 40 11.80	10.69	+1.03	+2.42	+0.60	+28.7±0.2	135	17-03-2011
NGC 2548	1628	08 14 28.12	−05 42 16.14	09.47	+1.02	+2.39	+0.62	+08.00±0.2	180	17-11-2011
NGC 2682	84	08 51 12.73	+11 52 42.68	10.51	+1.11	+2.53	+0.67	+35.2±0.2	130	13-01-2011
	151	08 51 26.22	+11 53 52.23	10.48	+1.10	+2.52	+0.66	+35.0±0.2	120	12-01-2011
	164	08 51 29.03	+11 50 33.40	10.52	+1.11	+2.56	+0.61	+34.3±0.1	120	13-01-2011
Collinder 350	47	17 48 43.83	+01 09 51.14	8.82	+1.17	+2.97	+0.64	−14.9±0.1	250	12-05-2011

The identification and basic observational data for the stars observed in each of the clusters are given in Table 4.1 along with the (V-K$_s$) and (J-K$_s$) colors from the Two Micron All Sky Survey (2MASS) catalogue[5] (Cutri et al. 2003)[6], computed radial velocity, S/N of each of the spectra extracted at 6000 Å and the date of observation for each of the program stars. Spectra of a representative region are shown in Figure 4.1 for one star each from a sample of the five OCs.

4.4 Abundance analysis

4.4.1 Preparation of linelist

Selection of stellar lines which are free from blends is crucial for deriving accurate elemental abundances. We used Rowland's preliminary table of solar spectrum wavelengths (Moore et al. 1966) and the the Arcturus spectrum (Hinkle et al. 2000) to identify unblended spectral lines. The temperature range of our program stars are well covered by these two well studied objects. We employed strict criteria in the selection of suitable lines. First, in order to avoid the difficulty in defining the continuum due to heavy line crowding in the blue part of the spectrum, we selected lines only within the 4300 to 8850 Å wavelength range. Second, regions containing telluric absorption lines were generally avoided. Third, lines which appear asymmetric were assumed to be blended with unidentified lines and discarded. Fourth, lines with equivalent widths (EWs) below 10 mÅ were rejected because they are too sensitive to noise and the normalization of the continuum, and lines with equivalent widths greater than 230 mÅ were discarded because they are not suitable for abundance determination.

The final linelist includes 300 lines of 24 elements covering the spectral range 4300 $\sim$ 8850 Å. Our selection criteria provides, on average across the sample of 40 stars, a list of 70 Fe I lines with lower excitation potentials (LEPs) ranging from 0.9 to 5.0 eV and EWs of up to 180 mÅ and 15 Fe II lines with LEPs of 2.8 to 3.9 eV and EWs from $\simeq$ 20 to 120 mÅ.

A portion of final linelist with solar EWs is given in Table 8.1 with details about the lines including the log gf's. For each line in the constructed linelist, we provide a gf-value from the literature. In most cases, we located recent experimental determinations or chose values from critical reviews. References to the adopted sources are given in Table 8.1. The equivalent widths (EWs) for each of the selected absorption features were measured manually using the routine *splot* contained in IRAF by fit-

---

[5] `http://irsa.ipac.caltech.edu/applications/Gator`

[6] Originally published in University of Massachusetts and Infrared Processing and Analysis Center (IPAC)/ California Institute of Technology.

Table 4.2: Solar abundances derived by employing the solar model atmosphere from Castelli & Kurucz (2003) compared with the photospheric abundances from Asplund et al. (2009).

Species	log $\epsilon_\odot$ (our study)	log $\epsilon_\odot$ (Asplund)	Species	log $\epsilon_\odot$ (our study)	log $\epsilon_\odot$ (Asplund)
Na I	6.29±0.03(5)	6.24±0.04	Co I	4.86±0.03(5)	4.99±0.07
Mg I	7.55±0.06(2)	7.60±0.04	Ni I	6.24±0.02(14)	6.22±0.04
Al I	6.35±0.06(3)	6.45±0.03	Cu I	**4.18**	4.19±0.04
Si I	7.55±0.05(2)	7.51±0.03	Zn I	4.59±0.00(2)	4.56±0.05
Ca I	6.28±0.05(8)	6.34±0.04	Y II	2.19±0.07(5)	2.21±0.05
Sc I	2.98±0.03(2)	3.15±0.04	Zr I	2.59±0.11(2)	2.58±0.04
Sc II	3.17±0.05(5)		Ba II	**2.13**	2.18±0.09
Ti I	4.88±0.06(10)	4.95±0.05	La II	1.24±0.13(2)	1.10±0.04
Ti II	4.92±0.09(7)		Ce II	**1.56**	1.58±0.04
V I	3.94±0.05(8)	3.93±0.08	Nd II	1.50±0.09(3)	1.42±0.04
Cr I	5.59±0.04(12)	5.64±0.04	Sm II	**1.00**	0.96±0.04
Cr II	5.67±0.05(6)		Eu II	**0.51**	0.52±0.04
Mn I	**5.39**	5.43±0.04			
Fe I	7.54±0.05(36)	7.50±0.04			
Fe II	7.52±0.05(13)				

Note: Numbers in the parentheses indicate the number of lines used for abundance analysis. The abundances calculated by synthesis are presented in bold numbers.

ting often a Gaussian profile. But for lines with significant damping wings a direct integration was preferred as a best measure of EW.

Several lines were close in wavelength to the telluric lines. The EWs for these lines have been measured only when they appear to be Doppler shifted away from the telluric components, as judged by referring to the Arcturus spectrum (Hinkle et al. 2000). For several absorption features, multiple components of a given atomic transition contribute to the feature. In such cases, we computed a synthetic spectrum including all components and occasionally other lines too and matched the synthetic spectrum to the observed spectrum by varying the abundance of the element in question.

As a check on the chosen gf-values, solar EWs were measured off the solar integrated disk spectrum (Kurucz et al. 1984). We derived solar abundances using the ATLAS9 model for T_{eff} = 5777 K, log g=4.44 cgs. A microturbulence of ξ_t = 0.95 km s^{-1} was found from iron lines. The final solar abundances along with those from the recent review by Asplund et al. (2009) are given in Table 4.2. Our abundances for the majority of elements are in good agreement with Asplund et al.'s. Small differences in abundances are inevitable, for example, the linelists are not necessarily identical as to selected lines and/or gf-values and the adopted solar models are different; ours is a classical model but Asplund et al. for many elements use a model representing the solar granulation. For the purposes of determining the stellar abundances, we adopt our solar abundances as a reference scale when computing [X/H] and [X/Fe] in order to minimize the systematic errors, i.e., our analysis is essentially a differential one relative to the Sun.

4.4.2 Determination of atmospheric parameters

(a) Photometry

Initial estimates of effective temperature for each red giant was derived from dereddened[7] B, V, J and K photometry using the empirically calibrated color-temperature relations of Alonso et al. (1999) based on a large sample of field and globular cluster giants of spectral types from F0 to K5. The corresponding errors around the (B-V), (V-K) and (J-K) relations are 167 K, 25 K and 125 K. Before that the 2MASS K_s[8] magnitudes are transformed to standard K magnitude using the relations given in Carpenter (2001). The mean difference between the two magnitudes is K_s= K+(-0.044±0.003). The effective temperature is expressed as

$$T_{\mathrm{eff}_\star}^{(B-V),(V-K),(J-K)} = \frac{5040}{\theta_{\mathrm{eff}_\star}^{(B-V),(V-K),(J-K)}} \tag{4.1}$$

where

$$\begin{aligned}
\theta_{\mathrm{eff}_\star}^{(B-V)} &= 0.5716 + 0.5404\,(B-V)_0 - 6.126\times10^{-2}\,(B-V)_0^2 - 4.862\times10^{-2}\,(B-V)_0\,[Fe/H] \\
&\quad -1.777\times10^{-2}\,[Fe/H] + 7.969\times10^{-3}\,[Fe/H]^2 \qquad (4.2)\\
\theta_{\mathrm{eff}_\star}^{(V-K)} &= 0.3770 + 0.3660\,(V-K)_0 - 3.170\times10^{-2}\,(V-K)_0^2 - 3.074\times10^{-3}\,(V-K)_0\,[Fe/H] \\
&\quad -2.765\times10^{-3}\,[Fe/H] - 2.973\times10^{-3}\,[Fe/H]^2 \qquad (4.3)\\
\theta_{\mathrm{eff}_\star}^{(J-K)} &= 0.5816 + 0.9134\,(J-K)_0 - 0.1443\,(J-K)_0^2 \qquad (4.4)
\end{aligned}$$

The surface gravities were computed by incorporating the known distance to the OCs, effective temperature $T_{\mathrm{eff}_\star}$, bolometric correction BC_V, and the cluster turn-off

---

[7] The adopted interstellar extinctions are (A_V, A_K, E(V-K), E(J-K))= (3.1, 0.28, 2.75, 0.54)*E(B-V), where E(B-V) is taken from WEBDA

[8] The 2MASS survey uses a K-short (K_s) filter whos effective wavelength is centred around 2.16 microns in the near-infrared.

mass $M_\star$ into the relation given by (Allende Prieto et al. 1999)

$$\log(g_\star/g_\odot) \quad = \quad \log(M_\star/M_\odot) + 4\log(T_{\mathrm{eff}_\star}/T_{\mathrm{eff}_\odot}) - log(L_\star/L_\odot) \tag{4.5}$$

with the corresponding luminosity given by

$$log(L_\star/L_\odot) = -[0.4\,(V_0 + BC_V) + 2\,log\;\pi + 0.12] \tag{4.6}$$

where π is the parallax, V_0 is the apparent Johnson V magnitude corrected for reddening. We adopt log $g_\odot$= 4.44 cm s^{-2} and $T_{\mathrm{eff}\,,\odot}$= 5777 K. The bolometric corrections BC_V are derived from estimated effective temperatures and photometric metallicities using the calibration by Alonso et al. (1999):

$$\begin{aligned} BC_V \quad = \quad & \frac{-5.531\mathrm{x}10^{-2}}{\mathrm{X}} - 0.6177 + 4.420\,\mathrm{X} - 2.669\,\mathrm{X}^2 + 0.6943\,\mathrm{X}\,[Fe/H] \\ & -0.1071\,[Fe/H] - 8.612\mathrm{x}10^{-3}\,[Fe/H]^2 \end{aligned} \tag{4.7}$$

where $\mathrm{X} = \log(T_{\mathrm{eff}_\star}) - 3.52$.

The turn-off mass of giants has been estimated from the stellar evolutionary tracks by Marigo et al. (2008): the adopted turn-off masses are 1.5 $M_\odot$ for NGC 752, 3.1 $M_\odot$ for NGC 1342, 2.8 $M_\odot$ for NGC 1662, 2.0 $M_\odot$ for NGC 1817, 3.5 $M_\odot$ for NGC 1912, 3.3 $M_\odot$ for NGC 2251, 2.1 $M_\odot$ for NGC 2266, 3.8 $M_\odot$ for NGC 2335, 3.5 $M_\odot$ for NGC 2354, 1.98 $\mathrm{M}_\odot$ for NGC 2360, 2.85 $M_\odot$ for NGC 2447, 3.0 $M_\odot$ for NGC 2482, 1.69 $M_\odot$ for NGC 2506, 2.8 $M_\odot$ for NGC 2527, 3.1 $M_\odot$ for NGC 2539, 2.6 $M_\odot$ for NGC 2548, and 1.4 $M_\odot$ for NGC 2682 and 2.5 $M_\odot$ for Collinder 350. Red giants are assumed to have the turn-off mass in computing the surface gravity.

Assuming that the various quantities involved in equations (1) & (2) are independent of each other and by introducing an error of 10% in the stellar mass, an uncertainty of 3% in $T_{eff_\star}$, an uncertainty of 5% in photometric V magnitude and the bolometric corrections, and an error of 10% in the distance (i.e., the parallax), we estimate an error of $\simeq$ 0.11 dex in log $g_\star$ with an uncertainty of 0.08 in log $L_\star$.

Spectroscopy

The spectroscopic abundance analysis was executed using the latest version (2010) of the local thermodynamical equilibrium (LTE) line analysis and spectrum synthesis code MOOG developed by Chris Sneden and originally described in Sneden (1973)[9].

---

[9] `http://www.as.utexas.edu/~chris/moog.html`

Model atmospheres were interpolated linearly from the ATLAS9 model atmosphere grid of Castelli & Kurucz (2003)[10]. For this purpose, initially we used a model with photometrically determined atmospheric parameters. These models assume a line-blanketed plane-parallel uniform atmospheres in LTE and hydrostatic equilibrium with flux conservation.

We performed a differential abundance analysis relative to the Sun by running the MOOG in *abfind* mode using the initially estimated stellar parameters (see., Section 4.4.2) and the measured EWs (Tables 8.13 - 8.17). This *abfind* driver force-fits the individual line abundances to match the computed EWs to the observed ones, previously measured using the *splot* routine of IRAF. The key lines are those of Fe I and Fe II for which we take gf-values from Führ & Wiese (2006) and Meléndez & Barbuy (2009). The microturbulence assumed to be isotropic and depth independent is determined from Fe II lines instead of Fe I, since Fe II lines are less affected by the departures from LTE. The ξ_t is determined by the requirement that the abundance from Fe II lines (generally chosen to have small range in LEP, 2.8−3.9 eV, but a good range in their EWs) are independent of line's EW or reduced EW ($\log(W_\lambda/\lambda)$). The T_{eff} is estimated by the requirement that the Fe abundance from Fe I lines is independent of a line's LEP. Finally, the surface gravity, log g, is estimated from the constraint that Fe I and Fe II lines give the same Fe abundance for the derived $T_{\rm eff}$ and ξ_t.

In Figure 4.2, we show a graphical representation of the determination of atmospheric parameters using Fe I line abundances as a function of three variables (line's LEP, line strength, and the wavelength of the lines) for a typical star (NGC 1342#6) together with a linear fit (red) to each distribution. The vertical axis gives the logarithmic iron abundance on the standard scale in which log $\epsilon(\mathrm{H}) = 12$. The thick dashed lines (cyan) represent the mean Fe I abundance, and the thin dashed lines (red) represent linear trends of abundance with the three variables. The lack of significant trends of the iron abundance with LEP (upper panel) and line strength (middle panel) supports the validity of our chosen model temperature and the adopted ξ_t (previously estimated using Fe II lines). The absence of any trend between the derived iron abundance and the wavelength (bottom panel) represents a check on our continuum placement.

A check on the derived microturbulence is provided by lines of species other than Fe I. For example, for the star NGC 752 #311 we show in Figure 4.3 the dispersion of the abundance computed from the Fe I, Fe II, Ti I, Ti II, V I, Cr I and Cr II lines

---

[10] `http://kurucz.harvard.edu/grids.html`

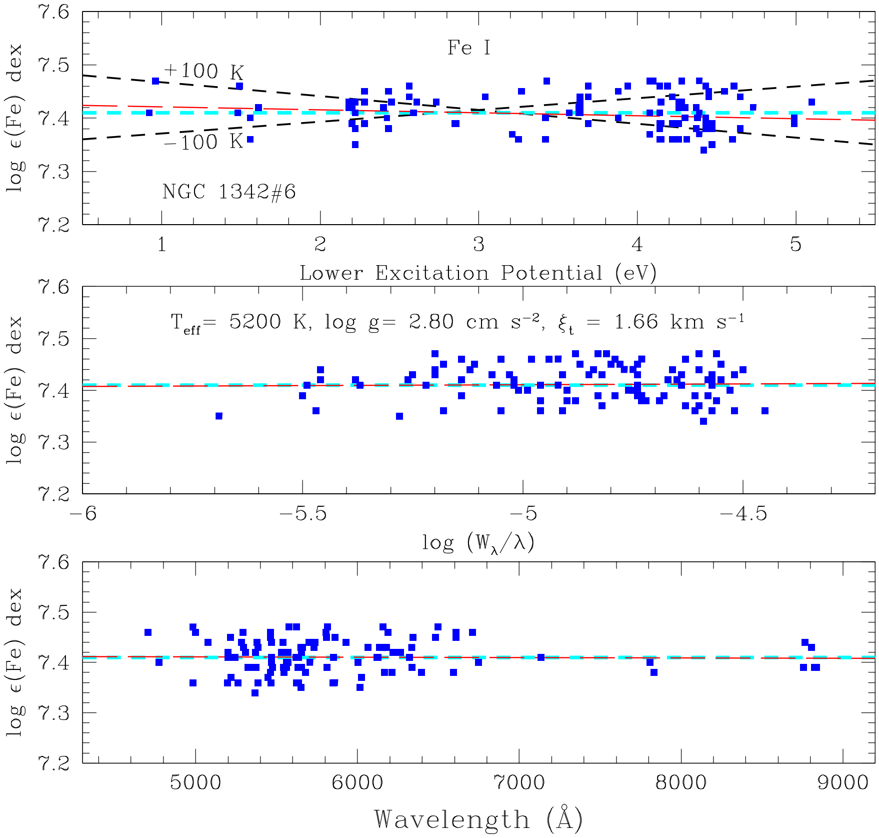

Figure 4.2: The observed plot for the derived abundance from the Fe I lines, [Fe I/H], for the star NGC 1342#6 as a function of LEP (upper panel), reduced equivalent width (middle panel), and the wavelength of each line (lower panel). The dashed lines (black) represent models with increasing or decreasing T_{eff} by ± 100 K (see text for reference).

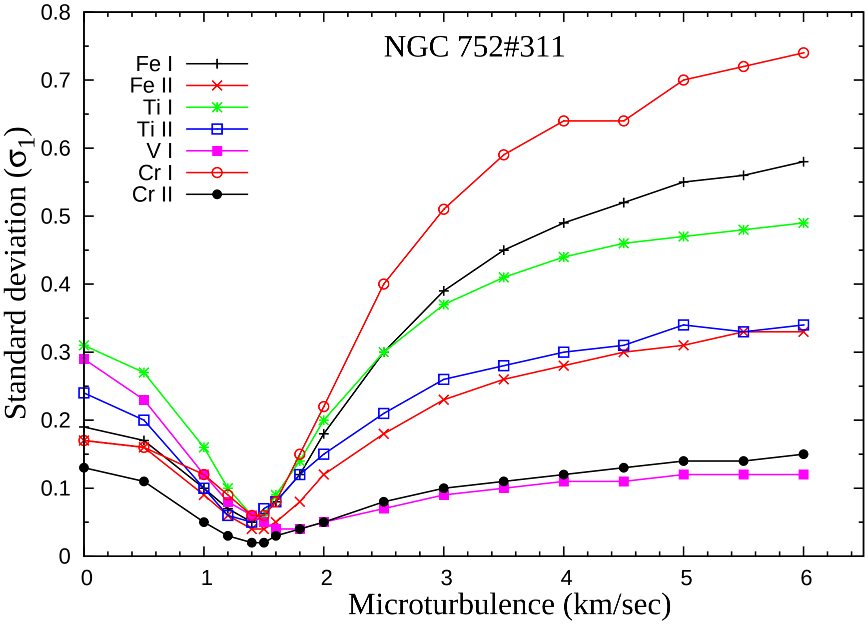

Figure 4.3: The variation of standard deviation about the mean abundances for various species as a function of microturbulence for the star NGC 752 #311.

as the micorturbulence is varied over the range in the microturbulence, ξ_t, from 0 to 6 km s^{-1}. The basic idea is that if both the weak and strong lines of a given species give very similar abundances, that is how ξ_t is determined, the standard deviation about the mean abundance is very less. Inspection of the figure 4.3 shows that the minimum value of dispersion for all species is in the range 1.3-1.6 km s^{-1}. Thus, we adopt a microturbulence of 1.45 km s^{-1} with a conservative uncertainty of 0.20 km s^{-1}.

Several elements other than Fe provide both neutral and ionized lines and so offer a check on the condition of ionization equilibrium of Fe. Consider for example the four giants from NGC 752: the abundance differences [X/H] between neutral and ionized lines of Sc, Ti, V and Cr are on average 0.03, -0.03, -0.01, and -0.05 dex, respectively where ±0.05 dex corresponds to a change of $logg$ by $\mp$ of 0.15. The uncertainty in the T$_{\rm eff}$ is estimated by inspecting the slope of the relation between the Fe I abundance and LEPs of the lines. A perceptible change of slope occurs for variations of temperature by ± 100 K about the adopted model parameter (shown as dashed lines (black) in figure 4.2). Therefore, the typical uncertainties estimated in this analysis are 100 K in $T_{\rm eff}$, 0.25 cm s^{-2} in log g and 0.20 km s^{-1} in ξ_t.

The derived stellar parameters for program stars in each of the cluster are given in Table 4.3: column 1 represents the cluster name, column 2 the star ID, columns 3 & 4 the photometric T$_{eff}$ and log g values, columns 5-7 the spectroscopic T$_{eff}$, log g and ξ_t estimates. Finally, the spectroscopic and photometric luminosities (log(L/L$_\odot$)) are presented in columns 8 & 9. The mean difference in effective temperatures estimated using (B-V) and (V-K) is +36 ± 178 K and using (V-K) and (J-K) is +111 ± 169 K. The corresponding mean differences in T$_{\rm eff}^{(B-V)}$, T$_{\rm eff}^{(V-K)}$ and T$_{\rm eff}^{(J-K)}$ with respect to spectroscopic T$_{\rm eff}^{spec}$'s are -53 ± 131 K, -89 ± 185 K and -200 ± 132 K respectively. Mean differences in log g and log(L/L$_\odot$) across the 40 stars are 0.00 ± 0.36 cm-s^{-2} and $+0.01 \pm 0.29$ erg-s^{-1} respectively.

The photometric T$_{\rm eff}$'s derived from the calibrations based on infrared flux method (Alonso et al. 1999) are sensitive to the adopted colors, reddening estimates and metallicity. When using the (B-V)$-$ T$_{\rm eff}$ calibration an error of 0.03 mag on (B-V) and a conservative uncertainty of 20 % in reddening translates into a temperature uncertainty of 1.1 to 1.3 % each. Equivalently, an error of 0.2 dex in [Fe/H]$_{\rm phot}$ implies a temperature uncertainty of 1.2 %. When using the (V-K)$-$ T$_{\rm eff}$ calibration, we note that an error of 0.03 mag on (V-K) and an uncertainty of 20 % in reddening implies a temperature uncertainty of 0.1 to 0.7 % each and an error of 0.2 dex in [Fe/H]$_{\rm phot}$ implies a temperature uncertainty of 0.1 to 0.9 %. Even though the T$_{\rm eff}$ as a function of (J-K) has no dependence on metallicity, an error of 0.03 mag on (J-K) implies a temperature uncertainty of 2 % while the effect of reddening variation is less. Temperatures derived from (V-K) colour might be least affected by photometric uncertainties and we shall use these values as the photometric $T_{\rm eff}$ estimates of our giant stars.

With few exceptions, our spectroscopic estimates are in good agreement with the photometric ones. The uncertainty affecting latter is subject to the uncertainties in the reddening values. For example, for NGC 2251 the difference in $T_{\rm eff}^{(V-K)}$ and $T_{\rm eff}^{\rm spec}$ is around 200 K using the reddening estimate of E(B-V)= 0.186 as quoted in WEBDA database. If we replace this value with the one (E(B-V)= 0.21±0.03) given in the recent analysis of Parisi et al. (2005), the difference between the two temperatures will be reduced by 50-100 K. Similarly the uncertainties in photometric estimates might be resulting large difference between photometric and spectroscopic measurements of $\log(L/L_{\odot})$ for the OC NGC 2266.

Table 4.3: Basic photometric and spectroscopic atmospheric parameters for the stars in each cluster.

Cluster	Star ID	$T_{\rm eff}^{\rm phot}$ (K)			$\log g_{\rm phot}^{(V-K)}$	$T_{\rm eff}^{\rm spec}$	$\log g_{\rm spec}$	$\xi_{\rm spec}$	$\log(L/L_\odot)$	$\log(L/L_\odot)$
		(B-V)	(V-K)	(J-K)	(cm s^{-2})	(K)	(cm s^{-2})	(km sec^{-1})	spectroscopy	photometry
NGC 752	77	4780	4623	4553	2.72	4850	2.65	1.26	1.71	1.54
	137	4780	4775	4690	2.56	4850	2.50	1.36	1.81	1.72
	295	4899	4881	4749	2.78	5050	2.85	1.47	1.53	1.53
	311	4761	4732	4601	2.60	4850	2.60	1.45	1.71	1.66
NGC 1342	4	4766	4667	4614	2.21	5100	2.40	1.70	2.31	2.34
	6	5035	4908	5022	2.50	5200	2.80	1.66	1.95	2.14
	7	4948	5058	5120	2.68	5200	2.70	1.51	2.05	2.03
NGC 1662	1	5023	4894	4800	2.32	5100	2.70	1.61	1.97	2.28
	2	5067	4862	4884	2.53	5200	2.85	1.49	1.85	2.06
NGC 1817	8	5177	4932	4762	2.67	5100	2.60	1.39	1.92	1.89
	81	4968	5034	4813	2.69	5100	2.45	1.44	2.07	1.90
	73	5059	4873	4610	2.59	4800	2.40	1.38	2.01	1.94
NGC 1912	3	4852	4875	4883	2.27	4950	2.10	1.81	2.61	2.42
	70	5044	4604	4869	2.28	4950	2.00	1.70	2.71	2.30
NGC 2251	3	4620	4642	4575	2.21	4850	1.90	1.73	2.75	2.36
	33	4693	4647	4624	2.24	4850	2.00	1.67	2.65	2.34
NGC 2266	73	4953	4910	4564	1.80	4850	2.60	1.35	1.85	2.74
NGC 2335	11	5372	5509	5145	2.51	5400	3.10	1.68	1.80	2.34
NGC 2354	183	4822	5132	4854	2.43	4920	2.90	1.24	1.80	2.35
	205	4926	5534	4829	2.47	4850	2.80	1.29	1.88	2.44
NGC 2360	5	4899	6436	6731	3.77	4900	2.70	1.29	1.75	1.89
	6	4899	7972	7345	3.40	5000	2.50	1.34	1.98	1.77
	8	4962	6575	7392	3.32	5050	2.60	1.37	1.90	1.74
	12	4668	4490	4547	2.55	4650	2.10	1.23	2.26	2.10
NGC 2447	28	5257	4849	4837	2.58	5050	2.70	1.42	1.97	2.02
	34	5069	4976	4802	2.64	5050	2.60	1.44	2.05	1.98
	41	5091	4898	5001	2.64	5100	2.80	1.59	1.88	1.97
NGC 2482	9	4802	4945	4756	2.34	4850	2.50	1.73	2.11	2.26
NGC 2506	2212	4710	4679	4550	1.88	4700	1.75	1.21	2.56	2.45
	3231	4893	4937	4762	2.48	5000	2.50	1.42	1.92	1.94
	4138	5048	4883	4670	2.56	5100	2.60	1.47	1.85	1.84
NGC 2527	10	4946	4994	4740	2.80	5150	3.10	1.80	1.59	1.78
	203	4884	4950	4734	2.78	5050	2.80	1.61	1.85	1.78
NGC 2539	346	4934	5002	4888	2.63	5175	3.10	1.70	1.64	1.98
	463	4840	4844	4794	2.47	5050	2.80	1.68	1.90	2.09
NGC 2548	1628	4842	4751	4625	2.50	4800	2.55	1.49	1.98	2.02
NGC 2682	84	4702	4683	4508	2.36	4800	2.60	1.55	1.66	1.81
	151	4720	4696	4552	2.36	4700	2.25	1.38	1.98	1.81
	164	4702	4658	4712	2.36	4650	2.25	1.48	1.96	1.80
Col 350	47	5279	5134	5196	2.90	5150	2.90	1.76	1.74	1.74

4.4.3 Abundances and error estimation

Once the atmospheric parameters were estimated from the spectral line measurements as described in previous section, the corresponding model atmospheres were used in *abfind* and *synth* drives of MOOG to conduct a complete abundance analysis. In most cases, the abundances are derived from the measured EWs but a few lines were analysed with synthetic spectra.

Synthetic spectra

We compared the observed stellar spectra to the synthetic spectra to derive abundances for the lines affected by hyperfine and isotopic splitting or affected by blends. Figures 4.4 and 4.5 show synthetic spectra fit to the observed one using three different abundances. The dotted line is the stellar spectrum. All the model atmospheric parameters and the atomic abundances of other blended lines (when present) were kept fixed and only the abundance of the element of interest was changed until the residuals of the fit were minimized. The blue line is the best fit to the stellar spectrum, with the other lines representing different values for [Ba/H] and [Eu/H] abundances, based on χ^2 goodness of fit provided by MOOG.

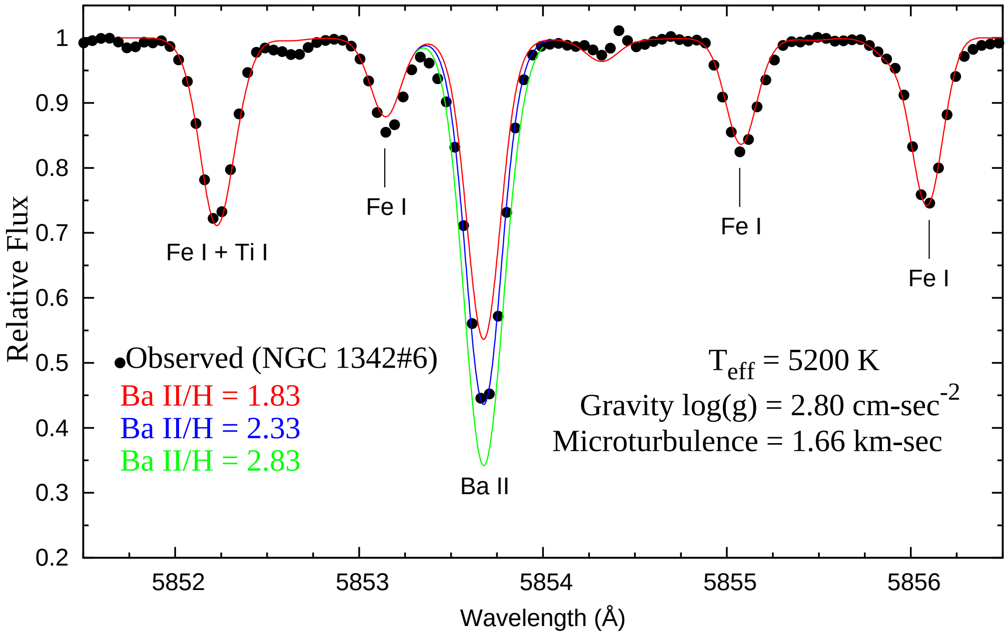

Figure 4.4: Synthetic spectra (continuous lines) and the observed spectrum (dotted line) of NGC 1342 #6 around the Ba II line at 5853 Å. The indicated abundances in the figure are on a logarithmic scale.

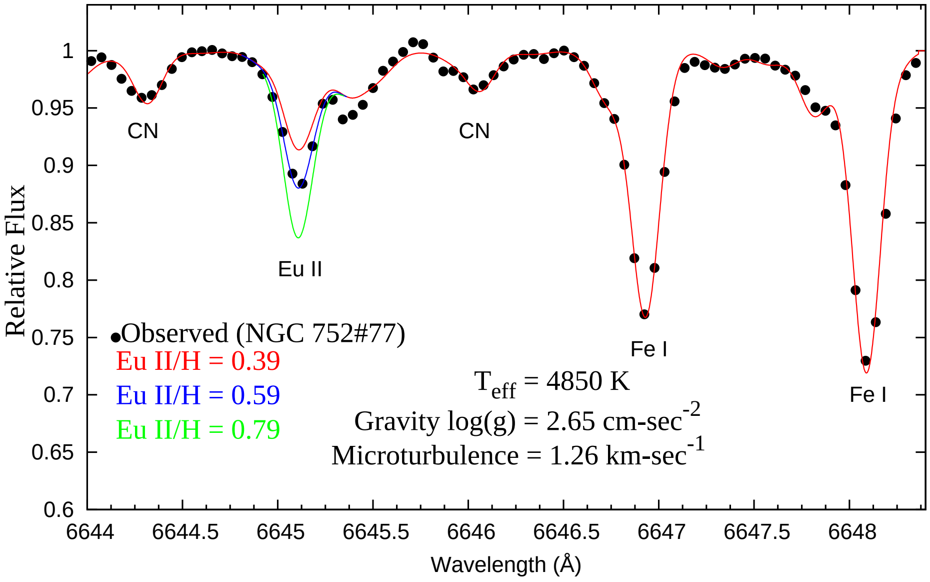

Figure 4.5: Synthetic spectra (continuous lines) and the observed spectrum (dotted line) of NGC 752 #77 around the Eu II line at 6645 Å. The indicated abundances in the figure are on a logarithmic scale.

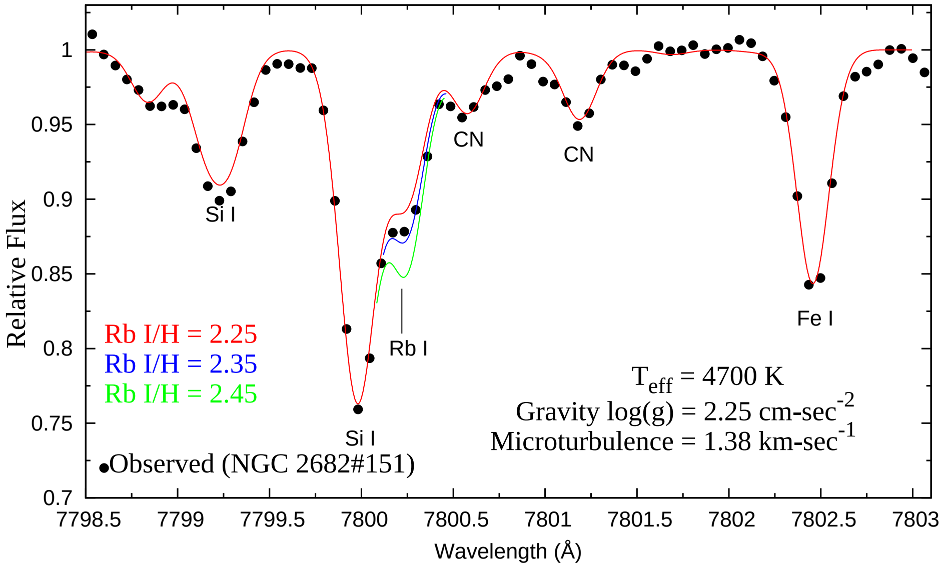

Figure 4.6: Synthetic spectra (continuous lines) and the observed spectrum (dotted line) of NGC 2682 #151 around the Rb I line at 7800 Å. The indicated abundances in the figure are on a logarithmic scale.

In this analysis, we have adopted the hfs data of Prochaska & McWilliam (2000) for the synthesis of Mn I lines at $\lambda\lambda$6013 and 6021 Å, Allen et al. (2011) for Cu I line at λ5218 Å, McWilliam (1998) for Ba II line at λ5853 Å. The hfs data and isotopic ratios for the Eu II line has been kindly provided by C. Sneden whose linelist uses the gf-values provided by Lawler et al. (2001). Isotopic ratios for Cu I, Ba II and Eu II were taken from Lodders (2003). Further, we have synthesized the lines Zn I (4810 Å), Ce II (5472 Å) and Sm II (4577 Å) as the blends make it impossible to measure their EWs. We have tested our linelists extensively to reproduce the solar and Arcturus spectra and measured the solar abundances to establish a reference abundance scale. The spectrum synthesis was carried out by running the MOOG in '*synth*' mode.

For the Rb I line, the number of hfs components, the accurately known wavelengths and the relative strength of each component were taken from Lambert & Luck's (1976) analysis of the Rb I resonance line in the Arcturus spectrum and a reliable log gf value of +0.13±0.04 from Wiese & Martin (1980). A fit to this line includes a Si I blend to the blue. As there are no reliable measurements of experimental gf-values for this line, we have adopted a solar gf-value of -0.75 to model the solar Si I line profile from the solar integrated disc spectrum (Kurucz et al. 1984). Our solar abundance measurement of log $\epsilon_\odot = 2.60$ dex for the Rb is in close agreement with Asplund et al's. (2009) value of log $\epsilon_\odot = 2.52\pm0.10$ dex.

A fit to the Rb I line at 7800 Å in the observed spectrum (dotted line) of NGC 2682 #151 is shown in figure 4.6 as solid lines with [Rb/H] = 2.35 ± 0.10 dex. A visual inspection of the figure shows that the blue line ([Rb/H] = 2.35) is a better match to the stellar spectrum.

Since all odd species exhibit hfs effects of relatively varying strengths, we have performed spectrum synthesis over Sc II line at 6245 Å, V I line at 5727 Å and Co I line at 5647 Å. Here, we have adopted the hfs data of Prochaska & McWilliam (2000) for Sc II and for V I and Co I hfs components were taken from Kurucz linelists[11]. We noticed that these lines are not severely effected by hfs effects, causing an abundance difference of $\lesssim 0.10$ dex with and without the inclusion of hfs components, and negligible while considering the standard deviation around mean what we obtain in the fine analysis using the routine 'abfind' in MOOG.

The largest hfs correction is about -0.11 dex for [Sc/Fe], -0.10 dex for [V/Fe], -0.43 dex for [Mn/Fe], -0.39 dex for [Cu/Fe], -0.12 dex for [Ba/Fe], -0.32 dex for [Eu/Fe].

Abundance results for the individual stars in each of the OCs are presented

---

[11] `http://kurucz.harvard.edu/linelists.html`

in Tables 8.2−8.12. For each abundance value based on the analysis of EWs, the abundance and standard deviation were calculated from all lines of given species. The tables give the [Fe/H] and [X/Fe] for elements considered here relative to solar abundances derived from the adopted gf-values. Therefore, errors in the adopted gf values are unimportant towards differential abundances ([X/H] or [X/Fe]) provided that the solar and stellar abundances depend on the same set of lines.

Inspection of the Tables 8.2−8.12 shows that the compositions [X/Fe] of stars in a given cluster are generally identical to within the (similar) standard deviations computed for an individual star. Exceptions tend to occur for species represented by one or a few lines, as expected when the uncertainty in measuring equivalent widths is a contributor to the total uncertainty. From the spread in the abundances for the stars of a given cluster we obtain the standard deviation σ_1 in the Tables 8.2−8.12 in the column headed 'average'.

We evaluated the sensitivity of the derived abundances to the uncertainties in the adopted atmospheric parameters by varying each time only one of the parameters by the amount corresponding to the typical error. The changes in abundances caused by varying atmospheric parameters by 100 K, 0.25 cm s^{-2} and 0.2 km s^{-1} with respect to the chosen model atmosphere are summarized in Table 4.4. We quadratically added the three contributors, by taking the square root of the sum of the square of individual errors associated with uncertainties in temperature, gravity and microturbulence, to obtain σ_2. The total error σ_{tot} for each of the element is the quadratic sum of σ_1 and σ_2. The error bars in the abundance tables correspond to this total error. The final OC mean abundances from this study are presented in Tables 4.6−4.8. The errors of the average abundance for a cluster are generally in the 0.02 to 0.08 dex range.

4.5 Cluster-to-cluster discussion

In this section, we briefly review each cluster studied in the current analysis and include a summary of available photometry and metallicity results. For the more well studied clusters, we also offer a brief comparison of our results to literature values.

NGC 752: This is a sparsely populated OC centered at $l = 137.12°$, $b = -23.25°$ in the constellation Andromeda. Twarog (1983) derived a mean reddening of E(B-V)= +0.04±0.01 and [Fe/H] = −0.33±0.09 dex relative to Hyades. Anthony-Twarog et al. (2006) obtained extented Strömgren photometry ($uvbyCa$) and derived a mean metallicity of [Fe/H]=−0.06±0.03 dex relative to Hyades ([Fe/H]=+0.12). Bartavsiute et al. (2007) derived a mean reddening of E(B-V)=+0.034±0.13 mag., apparent distance modulus of $(m - M)_V$= 8.38±0.14 mag. and a metallicity of −0.14±0.03

Table 4.4: Sensitivity of abundances to the uncertainties in the model parameters for the star NGC 2335#11 with $T_{\rm eff}$= 5400 K, log g= 3.10 cm s^{-2},and ξ_t= 1.68 km s^{-1}.

Species	$T_{\rm eff}$±100 K	log g± 0.25	ξ_t± 0.20	
	$\sigma_{T_{eff}}$	σ_{logg}	σ_{ξ_t}	σ_2
Na I	$+0.05/-0.06$	$-0.02/+0.02$	$-0.04/+0.05$	0.04
Mg I	$+0.03/-0.03$	$-0.01/+0.01$	$-0.02/+0.03$	0.02
Al I	$+0.03/-0.04$	$-0.01/+0.01$	$-0.02/+0.02$	0.02
Si I	$+0.01/-0.01$	$+0.03/-0.02$	$-0.02/+0.02$	0.02
Ca I	$+0.07/-0.08$	$-0.02/+0.02$	$-0.09/+0.09$	0.07
Sc I	$+0.09/-0.09$	$0.00/+0.01$	$0.00/+0.01$	0.05
Sc II	$-0.02/+0.01$	$+0.12/-0.11$	$-0.05/+0.06$	0.07
Ti I	$+0.10/-0.12$	$-0.01/\ 0.00$	$-0.03/+0.03$	0.06
Ti II	$-0.03/+0.01$	$+0.11/-0.12$	$-0.07/+0.08$	0.08
V I	$+0.02/-0.13$	$-0.01/\ 0.00$	$-0.01/+0.01$	0.05
Cr I	$+0.08/-0.10$	$-0.01/\ 0.00$	$-0.07/+0.07$	0.06
Cr II	$-0.05/+0.04$	$+0.11/-0.11$	$-0.05/+0.06$	0.07
Mn I	$+0.07/-0.09$	$0.00/-0.01$	$-0.04/+0.04$	0.05
Fe I	$+0.08/-0.09$	$0.00/\ 0.00$	$-0.09/+0.10$	0.07
Fe II	$-0.07/+0.05$	$+0.12/-0.13$	$-0.07/+0.07$	0.09
Co I	$+0.08/-0.08$	$+0.01/-0.01$	$-0.01/+0.02$	0.05
Ni I	$+0.07/-0.06$	$+0.02/-0.02$	$-0.05/+0.05$	0.05
Cu I	$+0.07/-0.08$	$+0.02/-0.02$	$-0.04/+0.06$	0.05
Zn I	$+0.02/+0.03$	$+0.07/-0.06$	$-0.05/+0.07$	0.05
Rb I	$+0.07/-0.08$	$-0.01/\ 0.00$	$-0.01/\ 0.00$	0.04
Y II	$-0.01/-0.01$	$+0.11/-0.12$	$-0.07/+0.09$	0.08
Zr I	$+0.13/-0.13$	$0.00/-0.01$	$0.00/+0.01$	0.07
Ba II	$+0.01/-0.03$	$+0.08/-0.10$	$-0.17/+0.17$	0.11
La II	$0.00/-0.02$	$+0.10/-0.12$	$-0.02/+0.01$	0.06
Ce II	$-0.01/-0.01$	$+0.10/-0.11$	$-0.01/+0.01$	0.06
Nd II	$+0.01/-0.02$	$+0.11/-0.11$	$-0.02/+0.02$	0.06
Sm II	$+0.02/-0.01$	$+0.11/-0.11$	$-0.02/+0.03$	0.06
Eu II	$-0.01/\ 0.00$	$+0.11/-0.11$	$-0.01/+0.01$	0.06

(dwarfs) and −0.08±0.09 (clump giants).

Friel & Janes (1993) measured a slightly subsolar metallicity [Fe/H] = −0.16±0.05 using low resolution spectra. High resolution spectroscopic observations were carried out by Sestito et al. (2004) and Carrera & Pancino (2011), who derived a mean metallicity of +0.01±0.04 and +0.08±0.04 dex respectively. We have conducted a comprehensive abundance analysis of four stars from this cluster and measured abundances for many elements from Na to Eu including the s- and r-process elements for which the measurements are often lacking in the literature. Our mean value of [Fe/H] = −0.04±0.03 is in agreement with previous high resolution studies.

Mermilliod et al. (2008) found that all the four stars (NGC 752#77, 137, 295 and 311) included in our analysis are cluster members with no evidence of binarity. The finding chart representing the location of the target stars is shown in figure 4.8. The position of the stars in the CMD (Figure 4.17) seems to indicate that they are clump giants.

NGC 1342: This is a sparsely populated OC in the constellation Perseus centered at $l = 154.95°$, $b = -15.34°$ in the Galactic anticentre direction. This is another OC for which only photometric estimates are available in the literature. More recently, Pena et al. (1994) have done a Strömgren (*uvby*-β) photoelectric photometry of NGC 1342 and derived a mean distance modulus of 8.62±0.22 mag., reddening of E(b-y) = 0.297± 0.112 and an age of 400 Myr. Gratton (2000) has compiled and compared different methods of metallicity estimates and recalibrated a metallicity of [Fe/H] = −0.16±0.11 for this cluster.

We have conducted a first detailed high-dispersion abundance analysis of NGC 1342 using three red giant members and derived a mean metallicity of [Fe/H] = −0.14±0.05 dex. The three sample stars (NGC 1342#4, 6 and 7) analysed here are the potential cluster members with no evidence of binarity as indicated by Mermilliod et al. (2008). The finding chart representing the location of the target stars is shown in figure 4.8. On the basis of their position on the CMD (Figure 4.17), it seem that they are the possible clump giants.

NGC 1662: This is a poor open cluster in the constellation Orion centered at $l = 187.69°$, $b = -21.11°$. This is one more cluster for which only photometric estimates are available in the literature. Recently, Pena & Peniche (1994) have done *uvby*-β photoelectric photometry and derived a mean reddening of E(b-y) = 0.231±0.034, a distance of 381±110 pc, and an age of 486 Myr.

Ths first high resolution and a detailed abundance estimates for this cluster was presented by us using two red giants from which we have derived a metallicity of

[Fe/H] = −0.10±0.06 dex. We have observed and analysed two stars (NGC 1662#1 and 2) from this cluster which turn out to be single potential members as as inferred by their radial velocity measurements (Mermilliod et al. 2008). The finding chart representing the location of the target stars is shown in figure 4.9. The position of both the stars in the CMD (Figure 4.17) indicate that they are the possible clump giants.

NGC 1817: This is a rich open cluster centered at l = 186.16°, b = −13.09° in Taurus constellation in the Galactic anticenter direction. Harris & Harris (1977) provided photographic UBV data and derived a reddening of E(B-V)=+0.28±0.03 mag. and a distance modulus of $(m-M)_0$=11.3±0.3 mag. Balaguer-Nunez et al. (2004) performed deep CCD photometry in the Strömgren ($uvby$-H_β) intermediate-band system, whose analysis yields a mean color excess of E(b-y)=+0.19±0.05 mag, equivalent to E(B-V)=+0.25[12], distance modulus of $V_0 - M_V$= 10.9±0.6 mag, a metallicity of [Fe/H]=−0.34±0.26 dex and an age of log(age)=9.05±0.05 yr. Parisi et al. (2005) found [Fe/H]=−0.33±0.08 dex, a reddening of E(B-V)=+0.25 and an age of 1.1 Gyr on the basis of Washington photometric system.

Jacobson et al. (2009) reported a mean [Fe/H] of −0.07±0.04 dex and a radial velocity of +65.33±0.09 km s^{-1} using high-dispersion echelle spectra of two giants. We have done a detailed abundance analysis and reported a mean metallicity of [Fe/H]=−0.13±0.04 dex using high resolution echelle spectra of three red giants, which is in fair agreement with Jacobson et al's value.

The three stars (NGC 1817#8, 73 and 81) included in our analysis are considered to be potential cluster members by Mermilliod et al. (2008) with no sign of binarity. The finding chart representing the location of the target stars is shown in figure 4.9. The positions of the stars in the CMD (Figure 4.17) indicate that they are clump giants.

NGC 1912: NGC 1912 is a rich OC situated in the anticenter direction of the Galaxy centered at $l = 172.25°$, $b = 0.69°$ in the constellation of Auriga This is another cluster for which only photometric estimates are available in the literature. Johnson (1961) reported a distance of 1.32 kpc and a reddening of 0.27 mag, while the respective values derived by Becker (1963) are 1415 pc and 0.24 mag. Subramaniam & Sagar (1999) carried out a deep (V ∼ 20) BVI CCD photometry and reported a distance of 1820±265 pc, reddening of E(B-V) = 0.25 ± 0.03 and an age of 250 Myr. Recently, Kharchenko et al. (2005) have derived a distance of 1066 pc, $E(B-V) = 0.25$ mag and log(age) = 8.56 yr for the cluster.

---

[12] E(b-y) is related to E(B-V) by the relation E(B-V)=1.351E(b-y) given by Crawford (1978)

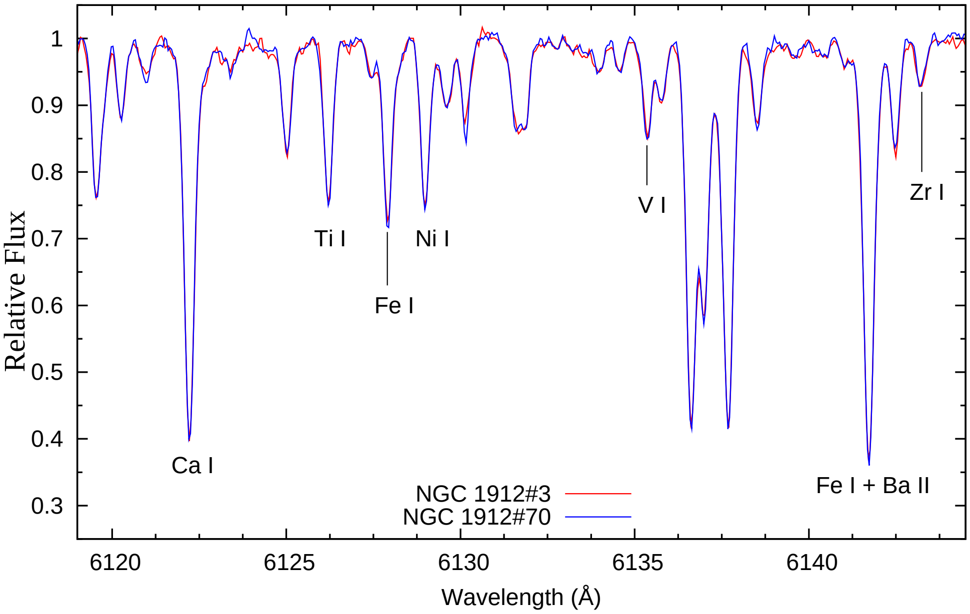

Figure 4.7: Superposition of the normalized spectra around 6100 Å for stars 3 (red line) and 70 (blue line) from the OC NGC 1912.

Based on a cross-correlation technique, Glushkova & Rastorguev (1991) derived a radial velocity of -1.0 ± 0.58 km s^{-1}, in a fair agreement with our mean value of $+0.18\pm0.19$ km s^{-1} (two stars). We have done a first detailed high dispersion abundance analysis of this cluster and reported a mean metallicity of [Fe/H] = -0.11 ± 0.05 using two potential cluster members. The finding chart representing the location of the target stars is shown in figure 4.10. The position of the stars (NGC 1912#3 and 70) in the CMD (Figure 4.17) suggest that they are possible clump giants.

Since we have derived very similar atmospheric parameters (table 4.3) and chemical composition (table 8.7) for both the stars analysed from this cluster, to check the reliability of our estimates, we have superposed the spectra of both stars. It is evident from figure 4.7 that both the spectra are indistinguishable from one another as all the line profiles have very similar strength. In Chapter 3, it is shown that the varied line profiles and line strengths (EWs) are tools to interpret and measure the effective temperature, surface gravity, chemical composition and velocity fields in the stellar atmosphere. Therefore, the derivation of very similar atmospheric parameters implies that our continuum placement and EW measurements are quite accurate. This give us more confidence to state that our abundance estimates are accurate and they are homogeneous since the similar methods are applied for all the clusters studied in our analysis.

NGC 2251: This is an intermediate age OC in the constellation of Monoceros centered at $l = 203.57°$, $b = 0.11°$. To our knowledge, our work is the first detailed high resolution chemical abundance study of NGC 2251. Previous metallicity estimates have been derived from photometry. Hoag et al. (1961) have performed UBV photoelectric and photographic measurements down to V = 17.0 mag. Later, Loktin et al. (2001) derived a color excess of E(B-V) = 0.186, a distance of 1329 pc and an age of 0.3 Gyr using Hoag et al's data. Recently, Parisi et al. (2005) found [Fe/H] = -0.25 ± 0.04 based on Washington photoelectric system, and an iron abundance of -0.14 ± 0.05 using DDO photoelectric photometry. There is a fair agreement between our spectroscopic iron abundance [Fe/H] = -0.10 ± 0.05 derived from two red giants and the photometric measurements.

The two stars (NGC 2251#3 and 33) studied in our analysis are highly probable cluster members with no evidence of binarity as indicated by Mermilliod et al. (2008). The finding chart representing the location of the target stars is shown in figure 4.10. The positions of the stars in the CMD (Figure 4.17) indicate that they are the possible clump giants.

NGC 2266: This is a small, compact and distant open cluster in Gemini towards $l = 187.79°$, $b = 10.20°$ in the Galactic anticentre direction. Kaluzny & Mazur (1991) obtained CCD photometry on the UBV and Washington systems and derived a foreground reddening of E(B-V) = 0.10, metallicity of [Fe/H] = -0.26 ± 0.18 and distance of about 3.4 kpc from the Sun. More recently, Maciejewski et al. (2008) obtained CCD photometry in the UBV system and derived a color excess of E(B-V) = 0.17, a subsolar metallicity of [Fe/H] = -0.68, age of $\log(age) = 9.08 \pm 0.04$ yr and a distance of 2.80 ± 0.15 kpc.

Carrera (2012) performed a first spectroscopic abundance analysis of this cluster using medium-resolution spectra (R $\sim$ 8000) taken in the infrared CaT region ($\sim$8500 Å) and derived a mean radial velocity of $\langle \mathrm{Rv} \rangle = -16 \pm 15$ km s^{-1} (four stars) and a metallicity of [Fe/H] = -0.38 ± 0.06 dex.

We have done a first comprehensive abundance analysis of this cluster and measured a radial velocity of -29.7 ± 0.2 km s^{-1} and [Fe/H] = -0.45 ± 0.04 dex based on a single red giant. For this cluster, we selected the star with ID 73 whose membership has been confirmed through photometry (Kaluzny & Mazur 1991). The finding chart representing the location of the target star is shown in figure 4.11. The position of this star in the CMD (Figure 4.18) indicate that it might be an evolved red giant. Our radial velocity estimate for this OC would appear to be the first measurement available in the literature with negligible dispersion whereas Carrera's measurement suffers from large uncertainty around the mean. Our radial velocity measurement for this OC differs from the Carrera's value by -10 km s^{-1}, but is well within the quoted uncertainty in Carrera (2012).

NGC 2335: This is a sparsely populated OC in the constellation Canis Majoris centered at $l = 223.60°$, $b = -01.18°$ in the Galactic anticentre direction. This is another cluster for which only photometric results are available in the literature. This cluster was observed photoelectrically in the UBV system by Claria (1973), who found a mean E(B-V) of 0.40 mag., distance of 1020 pc, and an age of 150 Myr. Later, these estimates are improved by Claria (1985), who obtained photoelectric UBV and DDO observations and measured a color excess of E(B-V) = 0.47 mag., distance of 1150 pc, and a metallicity of [Fe/H] = 0.2 dex. Twarog et al. (1997) compiled the existing photometric data and deduced a metallicity of [Fe/H] = -0.03 ± 0.09 dex using DDO photoelectric photometry.

We have done a first detailed high resolution abundance analysis of NGC 2335 and measured an iron abundance of [Fe/H] = -0.19 ± 0.04 dex (one star), which is in fair agreement with Twarog et al's value.

The only star (NGC 2335#11) studied in our analysis is a potential cluster member as indicated by the radial velocity measurements of Mermilliod et al. (2008). The finding chart representing the location of the target stars is shown in figure 4.11. On the basis of its position in the CMD (Figure 4.18), it appears that the star 11 might be a possible clump giant.

NGC 2354: This is a moderately populated OC located in Canis Majoris at $l = 238.37°$, $b = -06.79°$ in the Galactic anticentre direction. Inspite of having a well defined red giant branch, this cluster has so far received little attention. Durbeck (1960) published first UBV photographic results for this cluster who derived a reddening E(B-V) = 0.14 mag., a distance of 1.85 kpc and an age of 700 Myr. More recently, Claria et al. (1999) published photoelectric photometric results in the UBV, DDO and Washington systems. They derived a mean radial velocity of 33.40 ± 0.27 km s^{-1}, a reddening E(B-V) = 0.13 ± 0.03, a metallicity [Fe/H] ≈ -0.3 dex, and an age of 1 Gyr.

We have presented a first high resolution and comprehensive abundance analysis for this cluster and derived an iron abundance of [Fe/H] = -0.19 ± 0.04 dex based on two stars. The two stars (NGC 2354#183 and 205) included in our analysis are single stars and probable cluster members as indicated the radial velocity measurements of Mermilliod et al. (2008). The finding chart representing the location of the target stars is shown in figure 4.12. The position of the stars in the CMD (Figure 4.18) indicate that they might be possible clump giants.

NGC 2360: This is a moderately populated OC with a well defined red giant branch situated in the Galactic anticenter at l = 229.81°, b = −1.43° in the Canis Majoris constellation. Eggen (1968) first provided UBV photoelectric observations, who derived a distance from the Sun of 1150 pc and a reddening of E(B-V)= 0.07 mag. McClure (1972) photoelectric UBV and David Dunlap Observatory (DDO) data and determined E(B-V)= 0.09±0.006 mag from the study of 10 giants Geisler et al. (1992) and Clariá et al. (2008) respectively derived an [Fe/H] of −0.29±0.04 dex (six stars) using Washington photometry and −0.12±0.03 dex (13 giants) using DDO photoelectric data.

Spectroscopic abundance analysis has been carried out by Hamdani et al. (2000), Smiljanic et al. (2009), Santos et al. (2009). They measured a metallicity of +0.07 dex (seven giants) , +0.04 (three giants), −0.03±0.01 (three giants) respectively. We found a mean metallicity of [Fe/H]=−0.08±0.03 dex, in good agreement with literature spectroscopy.

All the four stars (NGC 2360#5, 6, 8 and 12) included in our analysis are cluster members as inferred by a fair agreement between our radial velocity measurements with Mermilliod et al. (2008). The finding chart representing the location of the target stars is shown in figure 4.12. The positions of the stars in the CMD (Figure 4.18) seem to indicate that stars 5, 6 and 8 are clump giants, while star 12 is a regular red giant.

NGC 2447: This is a rich open cluster with strong central concentration composed of bright and faint stars. It is situated in the Puppis constellation towards l = 240.04°, b = 0.13°. From the *uvby-β* photometry of A- and F- type stars, Eggen (1983) derived a color excess E(b-y) = 0.012, and a true distance modulus V_0-M_V = 10.15±0.25. Bica & Bonatto (2005) used 2MASS H and J magnitudes and by fitting the cluster color-magnitude diagram they derived E(B-V) = 0.0, a distance to the Sun of 1.05±0.04 kpc and an age of 400±50 Myr. Recently, Claria et al. (2005) obtained photoelectric photometry in the UBV, DDO and Washington systems and derived a mean interstellar reddening E(B-V) = 0.05±0.04 and a slightly subsolar metallicity [Fe/H] = −0.09±0.06 using Washington abundance indices.

The first spectroscopic abundance analysis was provided by Hamdani et al. (2005) using medium resolution (28,000) echelle spectroscopy, who measured abundances of about 15 elements in three giants and found a mean metallicity of [Fe/H] = 0.03. Recently, Santos et al. (2012) performed very high resolution (≈ 100,000) abundance analysis using three red giant members and measured [Fe/H] = −0.03±0.05

dex. We have carried out a comprehensive abundance analysis of the same sample of giants and derived a mean metallicity of −0.10±0.03, in agreement with Santos et al's value.

The three stars (NGC 2447#28, 34 and 41) analysed by Hamdani et al. (2005) are included in our sample. Mermilliod et al's (2008) radial velocity measurements indicate that all the three stars are single and possible cluster members. The finding chart representing the location of the target stars is shown in figure 4.13. The position of the stars in the CMD (Figure 4.18) suggest that they are clump giants.

NGC 2482: This large cluster ($l = 241.62°$, $b = 2.03°$), in the southern Milky Way is barely distinguishable from the field, has been discussed by Moffat & Vogt (1975) on the basis of UBV photoelectric observations, who derived a reddening E(B-V) = 0.04±0.02 and distance of 750 pc using bright stars ($V \lesssim 12.0$ mag). Claria et al. (2008) obtained UBV and DDO photoelectric observations and found a mean color excess E(B-V) = 0.11±0.01 and a metallicity [Fe/H] = 0.14±0.04 dex.

We have done a first high resolution and comprehensive abundance analysis of this cluster, though based on a single star, for which we derived a metallicity [Fe/H] of −0.07±0.04, which is in a decent agreement with the previous photometic results.

The only star (NGC 2489#9) included in our analysis is a potential cluster member as indicated by the radial velocity measurements of Mermilliod et al. (2008). The finding chart representing the location of the target star is shown in figure 4.13. On the basis of its position in the CMD (Figure 4.18), it appears that the star 9 is a possible clump giant.

NGC 2506: This is a rich, old and compact cluster centered at $l = 230.56°$, $b = 9.93°$ in the Galactic anticenter in the constellation Monoceros. Photometric observations were carried out by McClure et al. (1981), Geisler et al. (1992), Piatti et al. (1995), Tadross et al. (2003). They reported an iron abundance of [Fe/H]=−0.55 relative to Hyades, −0.58±0.14, −0.48±0.08 and −0.58 dex respectively. More recently, Lee et al. (2012) obtained a deep (V ≈ 23) VI CCD photometry derived a color excess of 0.03±0.04, $(V\text{-}M_V)_0 = 12.47 \pm 0.08$, an age of 2.31±0.16 Gyr and a metallicity of [Fe/H] = −0.24±0.06.

Spectroscopic abundance analysis has been carried out by Carretta et al. (2004) and Mikolaitis et al. (2011), who measured a mean [Fe/H] of −0.20±0.02 (two clump giants) and −0.24±0.05 dex (four giants) respectively using high resolution echelle spectroscopy. We have conducted a comprehensive abundance analysis of this cluster and derived a mean [Fe/H] of −0.22±0.04 (three stars), in excellent agreement with previous spectroscopic results.

All the three stars (NGC 2506#2212, 3231 and 4138) studied here are the potential cluster members with no evidence of binarity. The finding chart representing the location of the target stars is shown in figure 4.14. The positions of the stars in the CMD (Figure 4.19) indicate that stars 3231 and 4138 are possible clump giants, while the star 2212 is a normal red giant as indicated by their temperature and gravities.

NGC 2527: This is a sparsely populated cluster situated in the Galactic anticenter direction in the constellation of Puppis with the coordinates $l = 246.08°$, $b = 1.85°$. Photographic magnitudes on the UBV system based on a photoelectric sequence have been determined for 25 stars brighter than V $\approx$ 13.0 mag. by Lindoff (1973) and derived a distance of 550 pc with color excess, E(B-V), of about 0.1 mag. and an age of 5 x 10^8 yr . UBV photographic photometry was done by Dodd et al. (1977) for 368 stars to a limiting V magnitude of 16.6 and estimated a distance of 590 pc with a foreground color excess of 0.08 mag. and an age of approximately 10^9 yr.

To our knowledge, our work is the only high resolution spectroscopic abundance analysis available based on two stars in the cluster NGC 2527. Previous metallicity estimates have been determined from photometry: Claria (1985) found [Fe/H] = 0.0 based on UBV and DDO photometry and Piatti et al. (1995) found [Fe/H] = -0.09 based on DDO photometry. These results are in decent agreement with our metallicity estimate of -0.11 ± 0.04.

Two stars (NGC 2527#10 and 203) of this OC included in our sample are single stars and true members as indicated by the radial velocity measurements of Mermilliod et al. (2008). The finding chart representing the location of the target stars is shown in figure 4.14. The positions of the stars in the CMD (Figure 4.19) indicate that they are clump giants.

NGC 2539: This is an intermediate age sparse open cluster in the southern constellation of Puppis towards $l = 233.70°$, $b = 11.11°$. An incomplete survey of Pesch (1961), who obtained a UBV photoelectric observations for 59 stars, results in a mean color excess E(B-V) = 0.10 mag. and a distance of about 1300 pc. Joshi & Sagar (1986) obtained photoelectric UBV magnitudes for 88 stars and derived E(B-V) = 0.08 ± 0.02 mag., distance 1050 ± 150 and an age of about 540 Myr. A complete survey of UBV photoelectric observations for this cluster was done by Lapasset et al. (2000) for a sample of 345 stars in the cluster field and derived a reddening E(B-V) = 0.06 mag., and an apparent distance modulus $(V\text{-}M)_v = 10.60$, equivalent to a distance of 1210 pc with an age of 630 Myr.

Santos et al. (2009) have performed a first high resolution abundance analysis of NGC 2539 using three red giant members and measured only [Fe/H] of 0.08 ± 0.03

dex. We have performed a first comprehensive abundance analysis of this cluster and determined an iron abundance of -0.06 ± 0.04, which is in good agreement with Santos et al's work.

The two stars (NGC 2539#346 and 463) included in our sample are confirmed to be single stars and probable cluster members by the radial velocity measurements of Mermilliod et al. (2008). The finding chart representing the location of the target stars is shown in figure 4.15. The positions of the stars in the CMD (Figure 4.19) seem to indicate that they are possible clump giants.

NGC 2548: NGC 2548 centered at $l = 227.87°$, $b = 15.39°$ in Hydra with an estimated distance of 630 pc (Pesch 1961) is a poor and an extended ($30'$ diameter) open cluster. Claria (1985) obtained photoelectric UBV and DDO intermediate-band photometry and derived E(B-V) = 0.06 ± 0.02, distance of 1150 pc, and a metallicity of [Fe/H] = 0.2 dex. Wu et al. (2005) presented 13 color CCD intermediate-band photometry and found a distance of 780 pc, a reddening of E(B-V) = 0.04, an age of 0.32 Gyr with solar metallicity. Recently, Balaguer-Nunez et al. (2005) performed a deep CCD photometry in the $uvby$-H_β system and measured a reddening of E(b-y) = 0.06 ± 0.03, a distance of 725 pc, an age of 400 Myr and a metallicity of [Fe/H] = -0.24 ± 0.27.

To our knowledge, we have done a first high-dispersion echelle spectroscopy and a detailed abundance analysis of NGC 2548 and measured a metallicity of [Fe/H] = -0.09 ± 0.04 based on the spectra of one star.

The only star (NGC 2548#1628) included in our analysis is a potential cluster member with no sign of binarity as indicated by the radial velocity measurements of Mermilliod et al. (2008). The finding chart representing the location of the target star is shown in figure 4.15. On the basis of its position in the CMD (Figure 4.19), the star might be a clump giant.

NGC 2682 (M67): NGC 2682, also known as M 67, in Cancer towards $l = 215.69°$, $b = +31.89°$ is one of the most thoroughly studied old and rich open cluster in the Galaxy using both the photometry and high resolution spectroscopy. The membership to the cluster has been established through the radial velocity (Mathieu et al. 1986) and proper motion (Sanders 1977) studies. Montgomery et al. (1993) have presented a deep ($V \sim 20$) $UBVI$ CCD photometry of 1468 stars and found E(B-V) = 0.05 ± 0.01 and $(m\text{-}M)_V = 9.6$, and a metallicity, [Fe/H] = -0.05 ± 0.03 though they remarked on the poor match between the photometric data and theoretical isochrones. Balaguer-Nunez et al. (2007) have performed a wide ($50'$ x $50'$) and deep ($V \sim 19$) Strömgren photometic study for 1843 stars in M 67 and found $(m\text{-}M)_V = 9.83 \pm 0.20$ with a

Table 4.5: Comparison of elemental abundance ratios [X/Fe] for open cluster M 67 using data from various sources.

Species	This study	Tautvaišiene00	Yong05	Pancino10	Friel10
[Na I/Fe]	+0.25 ± 0.02	+0.20 ± 0.00	+0.30 ± 0.05	+0.08 ± 0.09	+0.13 ± 0.06
[Mg I/Fe]	+0.16 ± 0.02	+0.09 ± 0.00	+0.16 ± 0.05	+0.27 ± 0.04	+0.05 ± 0.06
[Al I/Fe]	+0.09 ± 0.01	+0.13 ± 0.02	+0.17 ± 0.03	+0.03 ± 0.02	+0.11 ± 0.04
[Si I/Fe]	+0.20 ± 0.02	+0.09 ± 0.04	+0.09 ± 0.06	+0.10 ± 0.02	+0.18 ± 0.06
[Ca I/Fe]	+0.04 ± 0.02	+0.06 ± 0.10	+0.07 ± 0.02	−0.16 ± 0.03	−0.08 ± 0.08
[Ti I/Fe]	−0.01 ± 0.02	+0.03 ± 0.10	+0.12 ± 0.02	−0.04 ± 0.06	−0.14 ± 0.06
[Cr I/Fe]	+0.05 ± 0.02	+0.07 ± 0.09	...	+0.01 ± 0.03	+0.00 ± 0.02
[Fe I/H]	−0.08 ± 0.02	0.00 ± 0.06	+0.02 ± 0.08	+0.05 ± 0.02	+0.03 ± 0.08
[Ni I/Fe]	+0.10 ± 0.02	+0.06 ± 0.09	+0.08 ± 0.05	+0.05 ± 0.01	−0.02 ± 0.05
[Y II/Fe]	+0.03 ± 0.02	−0.02 ± 0.11	...	−0.05 ± 0.04	...
[Zr I/Fe]	−0.07 ± 0.02	−0.19 ± 0.09	−0.28 ± 0.02	...	−0.14 ± 0.03
[Ba II/Fe]	**− 0.16 ± 0.06**	+0.08 ± 0.00	**−0.02 ± 0.05**	+0.25 ± 0.02	...
[La II/Fe]	0.00 ± 0.02	+0.12 ± 0.05	+0.11 ± 0.03	+0.05 ± 0.06	...
[Ce II/Fe]	**−0.02 ± 0.03**	+0.08 ± 0.08	...	...	...
[Nd II/Fe]	+0.02 ± 0.03	...	...	...	...
[Sm II/Fe]	**−0.03 ± 0.03**	+0.06 ± 0.00	...	...	...
[Eu II/Fe]	**+0.08 ± 0.03**	**+0.07 ± 0.00**	**+0.06 ± 0.02**	...	...

Note: Abundances calculated by synthesis are presented in bold numbers and the quoted errors on them are the sensitivity of their abundance to adopted model atmospheric parameters. An internal uncertainty of 0.00 means that the abundance analysis is based on a single line only.

Tautvaišiene00− Tautvaišiene et al. (2000); Yong05− Yong et al. (2005);
Pancino10− Pancino et al. (2010); Friel10− Friel et al. (2010);

reddening of E(b-y) = 0.03 ± 0.03, [Fe/H] = 0.01 ± 0.14 and an age of 4.2 ± 0.2 Gyr.

The three stars (NGC 2682#84, 151, and 164) included in our analysis are single stars and highly probable cluster members as inferred by the radial velocity measurements of Mermilliod et al. (2008). The finding chart representing the location of the target stars is shown in figure 4.16. The positions of the stars in the CMD (Figure 4.19) seem to indicate that all the three stars are the possible clump giants.

High-resolution spectroscopic abundance analyses have been reported by Tautvaišiene et al. (2000, hereafter Tautvaišiene00), Yong et al. (2005, hereafter Yong05), Pancino et al. (2010, hereafter Pancino10) and Friel et al. (2010, hereafter Friel10). Therefore, inclusion of this OC in our work enables us to compare our results with literature studies to place our measurements in a more general framework. Unfortunately, none of the above groups, except Tautvaišiene00 sample, have stars in common with our sample for a direct star-to-star comparison of results, but on the assumption that the intrinsic dispersion in abundances within NGC 2682 is negligible, we may compare results from the separate analyses. Our spectroscopic atmospheric parameters for all three stars are in good agreement with those of Tautvaišiene00 sample, with differences in T_{eff} less than 60 K. Differences in log g are also small, typically 0.25 dex or less and the corresponding differences in ξ_t are typically 0.3 km s^{-1} or less.

For the Tautvaišiene00 sample we give in Table 4.5 the mean of the average abundances of three stars in common with our study and this mean value does not change if we consider the whole sample of stars studied by Tautvaišiene00. Differences in [X/Fe] between our results and the four published analyses are ±0.15 dex or smaller for almost all elements in common: exceptions include Si and Zr for Yong05, Na, Ca, and Ba for Pancino10, Ba for Tautvaišiene00, but all elements considered by Friel10 fall within the ±0.15 limit. Further, a direct star-to-star comparison of [X/Fe] abundance for almost all elements in common between ours and Tautvaišiene00 fall within ±0.15 dex with the exception of [Ba/Fe]. The [Fe/H] estimates for the four published analyses are consistent but our result is consistently slightly sub-solar: [Fe/H] = −0.08 versus 0.00 to +0.05. This comparison (Table 4.5) suggests quite a satisfactory agreement for all elements given the many different choices which enter into a LTE model atmosphere abundance analysis.

Collinder 350: This is very poor open cluster centered at $l = 26.79°$, $b = 14.69°$ in the Constellation of Ophiuchus. This is one more cluster for which only one photometric estimate is available in the literature. Kharchenko et al. (2005) derived a distance of 280 pc, $E(B - V) = 0.37$ mag and $\log(age) = 8.61$ yr for this cluster.

We have carried out a first comprehensive abundance analysis using high-dispersion echelle spectroscopy of one star and measured an iron abundance of [Fe/H] = −0.17±0.05 dex. The only star (Collinder 350#47) included in our analysis is a potential cluster member with no sign of binarity as indicated by the radial velocity measurements of Kharchenko et al. (2007). The finding chart representing the location of the target stars is shown in figure 4.16. On the basis of its position in the CMD (Figure 4.19), it is possibly a clump giant.

Our present sample of OCs includes 36 clump giants and four red giant stars. We notice that both the red clump and giant stars within a given cluster have very similar chemical compositions for almost all the elements and does not show any systematic abundance differences larger than measurement uncertainties (see, for example, table 8.5 for cluster abundance of NGC 2506). Only difference is that the clump giants are

Table 4.6: Elemental abundances for NGC 752, 1817, 2360 and 2506 in this study. Abundances calculated by synthesis are presented in bold typeface.

Species	NGC 752	NGC 1817	NGC 2360	NGC 2506
[Na I/Fe]	$+0.12 \pm 0.03$	$+0.16 \pm 0.02$	$+0.20 \pm 0.03$	$+0.21 \pm 0.03$
[Mg I/Fe]	-0.01 ± 0.03	$+0.08 \pm 0.03$	$+0.07 \pm 0.03$	$+0.05 \pm 0.04$
[Al I/Fe]	$+0.15 \pm 0.02$	$+0.11 \pm 0.02$	$+0.09 \pm 0.02$	$+0.17 \pm 0.01$
[Si I/Fe]	$+0.11 \pm 0.02$	$+0.10 \pm 0.02$	$+0.15 \pm 0.02$	$+0.04 \pm 0.02$
[Ca I/Fe]	$+0.03 \pm 0.05$	$+0.14 \pm 0.04$	$+0.11 \pm 0.04$	$+0.10 \pm 0.05$
[Sc I/Fe]	$+0.07 \pm 0.04$		$+0.06 \pm 0.04$	0.00 ± 0.02
[Sc II/Fe]	$+0.04 \pm 0.04$	0.00 ± 0.04	$+0.03 \pm 0.04$	$+0.05 \pm 0.05$
[Ti I/Fe]	-0.07 ± 0.05	0.00 ± 0.04	-0.03 ± 0.05	$+0.04 \pm 0.05$
[Ti II/Fe]	-0.04 ± 0.05	$+0.02 \pm 0.05$	-0.05 ± 0.05	$+0.03 \pm 0.05$
[V I/Fe]	$+0.03 \pm 0.05$	$+0.01 \pm 0.04$	$+0.08 \pm 0.04$	$+0.01 \pm 0.05$
[V II/Fe]	$+0.04 \pm 0.04$		-0.05 ± 0.03	
[Cr I/Fe]	-0.03 ± 0.04	0.00 ± 0.03	$+0.01 \pm 0.04$	-0.01 ± 0.04
[Cr II/Fe]	$+0.02 \pm 0.05$	$+0.03 \pm 0.04$	0.00 ± 0.05	-0.09 ± 0.04
[Mn I/Fe]	**−0.13**	**−0.18**	**−0.21**	**−0.18**
[Fe I/H]	-0.04 ± 0.03	-0.13 ± 0.04	-0.08 ± 0.03	-0.22 ± 0.04
[Fe II/H]	-0.02 ± 0.05	-0.11 ± 0.05	-0.07 ± 0.06	-0.19 ± 0.06
[Co I/Fe]	-0.02 ± 0.02	$+0.03 \pm 0.03$	$+0.06 \pm 0.03$	-0.02 ± 0.03
[Ni I/Fe]	-0.01 ± 0.03	-0.02 ± 0.03	$+0.01 \pm 0.03$	-0.08 ± 0.03
[Cu I/Fe]	**−0.11**	**−0.23**	**−0.18**	**−0.12**
[Zn I/Fe]	-0.10 ± 0.04	0.00 ± 0.05	$+0.04 \pm 0.08$	$+0.01 \pm 0.05$
[Y II/Fe]	$+0.03 \pm 0.03$	$+0.07 \pm 0.05$	$+0.06 \pm 0.04$	$+0.04 \pm 0.07$
[Zr I/Fe]	$+0.06 \pm 0.05$	$+0.08 \pm 0.05$	$+0.08 \pm 0.05$	$+0.17 \pm 0.06$
[Ba II/Fe]	**+0.13**	**+0.13**	**+0.10**	**+0.31**
[La II/Fe]	$+0.13 \pm 0.03$	$+0.12 \pm 0.03$	$+0.14 \pm 0.05$	$+0.28 \pm 0.04$
[Ce II/Fe]	**+0.13**	**+0.20**	**+0.18**	**+0.18**
[Nd II/Fe]	$+0.06 \pm 0.04$	$+0.14 \pm 0.04$	$+0.06 \pm 0.04$	$+0.16 \pm 0.06$
[Sm II/Fe]	**+0.08**	**+0.21**	**+0.13**	**+0.22**
[Eu II/Fe]	**+0.07**	**+0.13**	**+0.04**	**+0.22**

slightly unevolved and hence are warmer with slightly higher surface gravities over the normal giants. Therefore, the usage of red clumps and giants in our abundance analysis is not going to affect the accuracy of our final OC mean abundances and, in general, the compositions [X/Fe] of stars in a given cluster confirms the chemical homogeneity. As the C, N and O abundances are generally affected by internal mixing in both the red clump and giant stars, we have excluded them from our abundance analysis.

Species	NGC 2527	NGC 2682	NGC 2482	NGC 2539	NGC 2335	NGC 2251	NGC 2266
[Na I/Fe]	+0.32 ± 0.03	+0.25 ± 0.03	+0.30 ± 0.03	+0.27 ± 0.03	+0.24 ± 0.03	+0.33 ± 0.04	+0.23 ± 0.03
[Mg I/Fe]	+0.07 ± 0.01	+0.16 ± 0.02	+0.13 ± 0.02	+0.07 ± 0.02	+0.08 ± 0.02	+0.06 ± 0.02	+0.39 ± 0.02
[Al I/Fe]	+0.05 ± 0.02	+0.09 ± 0.01	+0.07 ± 0.02	0.00 ± 0.01	−0.02 ± 0.02	0.00 ± 0.02	+0.25 ± 0.02
[Si I/Fe]	+0.20 ± 0.02	+0.20 ± 0.02	+0.23 ± 0.04	+0.17 ± 0.02	+0.10 ± 0.02	+0.23 ± 0.02	+0.28 ± 0.02
[Ca I/Fe]	+0.12 ± 0.04	+0.04 ± 0.04	+0.01 ± 0.05	+0.04 ± 0.04	+0.09 ± 0.04	+0.09 ± 0.05	+0.17 ± 0.05
[Sc I/Fe]	+0.25 ± 0.04	+0.04 ± 0.04	+0.12 ± 0.05	+0.21 ± 0.04	+0.13 ± 0.04	+0.04 ± 0.04	+0.31 ± 0.05
[Sc II/Fe]	+0.12 ± 0.04	+0.10 ± 0.04	+0.08 ± 0.05	+0.04 ± 0.04	**+0.16**	**+0.02**	+0.22 ± 0.05
[Ti I/Fe]	+0.11 ± 0.04	−0.01 ± 0.04	+0.01 ± 0.04	+0.10 ± 0.04	+0.17 ± 0.04	−0.04 ± 0.04	+0.23 ± 0.04
[Ti II/Fe]	+0.08 ± 0.04	+0.01 ± 0.05	−0.03 ± 0.04	+0.08 ± 0.04	+0.12 ± 0.04	−0.04 ± 0.04	+0.30 ± 0.04
[V I/Fe]	+0.21 ± 0.04	+0.09 ± 0.05	+0.10 ± 0.05	+0.16 ± 0.04	+0.13 ± 0.03	−0.05 ± 0.05	+0.20 ± 0.06
[Cr I/Fe]	+0.10 ± 0.03	+0.05 ± 0.03	+0.10 ± 0.04	+0.08 ± 0.04	+0.07 ± 0.03	+0.05 ± 0.04	+0.09 ± 0.03
[Cr II/Fe]	+0.06 ± 0.04	+0.08 ± 0.05	+0.09 ± 0.05	+0.08 ± 0.04	0.00 ± 0.04	+0.04 ± 0.05	+0.02 ± 0.04
[Mn I/Fe]	**0.00**	**−0.08**	**−0.11**	**+0.01**	**−0.01**	**−0.13**	**−0.01**
[Fe I/H]	−0.11 ± 0.04	−0.08 ± 0.04	−0.07 ± 0.04	−0.06 ± 0.04	−0.19±0.04	−0.10 ± 0.05	−0.45±0.04
[Fe II/H]	−0.09 ± 0.05	−0.08 ± 0.05	−0.07 ± 0.05	−0.07 ± 0.05	−0.17±0.05	−0.10 ± 0.05	−0.43±0.05
[Co I/Fe]	+0.16 ± 0.04	+0.11 ± 0.02	+0.11 ± 0.03	+0.07 ± 0.02	+0.16±0.04	+0.03 ± 0.03	+0.27 ± 0.03
[Ni I/Fe]	+0.06 ± 0.02	+0.10 ± 0.03	+0.03 ± 0.04	+0.02 ± 0.02	+0.09±0.03	+0.04 ± 0.03	+0.09 ± 0.03
[Cu I/Fe]	**−0.14**	**−0.03**	**−0.21**	**−0.16**	**−0.15**	**−0.22**	**+0.02**
[Zn I/Fe]	**−0.16**	**−0.07**	**−0.22**	**−0.22**	**−0.06**	**−0.13**	**0.00**
[Rb I/Fe]	**+0.07**	**−0.10**	**−0.13**	**+0.04**	**+0.08**	**−0.17**	**+0.14**
[Y II/Fe]	+0.16 ± 0.04	+0.03 ± 0.04	+0.15 ± 0.04	+0.17 ± 0.04	+0.12±0.05	+0.07 ± 0.04	+0.05 ± 0.04
[Zr I/Fe]	+0.31 ± 0.05	−0.07 ± 0.05	+0.11 ± 0.05	+0.21 ± 0.04	+0.06±0.04	0.00 ± 0.05	−0.08±0.05
[Zr II/Fe]	+0.18 ± 0.03	−0.07 ± 0.03	+0.10 ± 0.04	+0.26 ± 0.03	+0.01±0.03	+0.06 ± 0.03	. . .
[Ba II/Fe]	**+0.08**	**−0.16**	**+0.09**	**+0.10**	**+0.25**	**+0.11**	**−0.13**
[La II/Fe]	+0.26 ± 0.03	0.00 ± 0.03	+0.18 ± 0.03	+0.18 ± 0.03	+0.29±0.03	+0.02 ± 0.04	−0.02 ± 0.04
[Ce II/Fe]	**+0.24**	**−0.02**	**+0.11**	**+0.20**	**+0.29**	**+0.07**	**−0.07**
[Nd II/Fe]	+0.20 ± 0.03	+0.02 ± 0.04	+0.13 ± 0.04	+0.23 ± 0.04	+0.32±0.03	+0.08 ± 0.04	+0.13 ± 0.04
[Sm II/Fe]	**+0.18**	**−0.03**	+0.13 ± 0.04	**+0.18**	+0.28±0.04	**+0.02**	**+0.11**
[Eu II/Fe]	**+0.10**	**+0.08**	**+0.07**	**+0.19**	**+0.07**	**+0.04**	**+0.40**

Table 4.7: Elemental abundance ratios [X/Fe] for elements from Na to Eu for NGC 2527, 2682, 2482, 2539, 2335, 2251 and 2266 from this study. Abundances calculated by synthesis are presented in bold typeface.

Species	NGC 1342	NGC 1662	NGC 2447	NGC 2354	NGC 1912	NGC 2548	Col 350
[Na I/Fe]	+0.28 ± 0.04	+0.22 ± 0.04	+0.12 ± 0.04	+0.12 ± 0.04	+0.33 ± 0.04	+0.28 ± 0.03	+0.26 ± 0.04
[Mg I/Fe]	0.00 ± 0.04	−0.06 ± 0.03	−0.02 ± 0.04	−0.17 ± 0.04	+0.03 ± 0.02	+0.07 ± 0.02	+0.05 ± 0.02
[Al I/Fe]	−0.05 ± 0.02	−0.03 ± 0.03	−0.14 ± 0.03	−0.11 ± 0.03	+0.06 ± 0.02	+0.06 ± 0.02	−0.02 ± 0.02
[Si I/Fe]	+0.11 ± 0.02	+0.16 ± 0.03	+0.11 ± 0.03	+0.16 ± 0.03	+0.23 ± 0.02	+0.17 ± 0.02	+0.20 ± 0.02
[Ca I/Fe]	+0.07 ± 0.05	+0.11 ± 0.06	+0.02 ± 0.05	−0.07 ± 0.06	+0.14 ± 0.03	−0.01 ± 0.04	+0.01 ± 0.05
[Sc I/Fe]	+0.04 ± 0.05	+0.02 ± 0.10	+0.04 ± 0.09	...	...	...	...
[Sc II/Fe]	...	+0.11 ± 0.08	+0.10 ± 0.05	+0.05 ± 0.10	**+0.10**	+0.06 ± 0.10	...
[Ti I/Fe]	+0.02 ± 0.05	+0.06 ± 0.05	−0.04 ± 0.05	+0.01 ± 0.07	−0.07 ± 0.03	−0.07 ± 0.04	+0.07 ± 0.04
[Ti II/Fe]	−0.04 ± 0.05	+0.05 ± 0.07	−0.05 ± 0.06	−0.06 ± 0.06	+0.03 ± 0.06	−0.07 ± 0.04	+0.03 ± 0.04
[V I/Fe]	+0.01 ± 0.06	+0.03 ± 0.06	−0.02 ± 0.06	+0.04 ± 0.06	−0.07 ± 0.04	+0.04 ± 0.03	+0.11 ± 0.05
[Cr I/Fe]	+0.01 ± 0.06	0.00 ± 0.04	−0.04 ± 0.04	−0.03 ± 0.05	+0.01 ± 0.06	0.00 ± 0.03	+0.01 ± 0.04
[Cr II/Fe]	+0.03 ± 0.06	+0.07 ± 0.07	+0.02 ± 0.07	−0.03 ± 0.06	+0.05 ± 0.05	+0.07 ± 0.04	+0.03 ± 0.05
[Mn I/Fe]	**−0.12**	**−0.05**	**−0.07**	**−0.05**	**−0.12**	**−0.08**	**−0.06**
[Fe I/H]	−0.14 ± 0.05	−0.10 ± 0.06	−0.13 ± 0.05	−0.19 ± 0.04	−0.11 ± 0.05	−0.09±0.04	−0.17 ± 0.05
[Fe II/H]	−0.13 ± 0.06	−0.11 ± 0.07	−0.11 ± 0.08	−0.16 ± 0.08	−0.09 ± 0.06	−0.10±0.05	−0.15 ± 0.05
[Co I/Fe]	−0.03 ± 0.04	0.00 ± 0.04	−0.04 ± 0.04	+0.07 ± 0.04	−0.10 ± 0.02	+0.07±0.04	+0.02 ± 0.03
[Ni I/Fe]	−0.06 ± 0.04	−0.02 ± 0.04	−0.07 ± 0.04	0.00 ± 0.06	−0.02 ± 0.05	+0.03±0.03	−0.01 ± 0.03
[Cu I/Fe]	**−0.29**	**−0.24**	**−0.28**	**−0.12**	**−0.30**	**−0.04**	**−0.24**
[Zn I/Fe]	**−0.29**	**−0.13**	**−0.38**	**−0.31**	**+0.10**	**−0.05**	**−0.23**
[Rb I/Fe]	**−0.04**	**−0.14**	**−0.18**	**−0.17**	**−0.30**	**−0.11**	**−0.04**
[Y II/Fe]	+0.12 ± 0.05	+0.15 ± 0.05	+0.03 ± 0.06	+0.14 ± 0.05	+0.06 ± 0.04	+0.08±0.05	+0.14 ± 0.04
[Zr I/Fe]	+0.18 ± 0.06	+0.25 ± 0.07	+0.13 ± 0.07	+0.13 ± 0.08	+0.10 ± 0.04	+0.12±0.04	+0.20 ± 0.05
[Zr II/Fe]	+0.25 ± 0.04	+0.31 ± 0.03	+0.16 ± 0.05	...	...	+0.19±0.03	+0.27 ± 0.03
[Ba II/Fe]	**+0.32**	**+0.54**	**+0.23**	**+0.17**	**+0.70**	**+0.09**	**+0.43**
[La II/Fe]	+0.16 ± 0.05	+0.22 ± 0.05	+0.13 ± 0.05	+0.23 ± 0.08	+0.14 ± 0.04	+0.01±0.03	+0.10 ± 0.04
[Ce II/Fe]	+0.36 ± 0.05	+0.37 ± 0.06	+0.32 ± 0.06	+0.38 ± 0.05	+0.23 ± 0.04	+0.23 ± 0.03	+0.25 ± 0.04
[Nd II/Fe]	+0.29 ± 0.04	+0.26 ± 0.05	+0.22 ± 0.05	+0.33 ± 0.05	+0.13 ± 0.04	+0.19±0.03	+0.22 ± 0.04
[Sm II/Fe]	+0.24 ± 0.05	+0.22 ± 0.05	+0.19 ± 0.05	+0.24 ± 0.05	+0.04 ± 0.04	+0.14±0.04	+0.19 ± 0.04
[Eu II/Fe]	**+0.22**	**+0.20**	**+0.22**	**+0.16**	**+0.07**	+0.24	**+0.28**

Table 4.8: Elemental abundance ratios [X/Fe] for elements from Na to Eu for NGC 1342, 1662, 2447, 2354, 1912, 2548 and Collinder 350 from this study. Abundances calculated by synthesis are presented in bold typeface.

Figure 4.8: Digital Sky Survey (DSS) finding charts displaying the location of observed stars in clusters NGC 752 (left) and NGC 1342 (right). North is up and East is to the left. Here we have zoomed in the central portion of clusters for better visibility of our target stars. But the actual size of the cluster is slightly larger than that in figure.

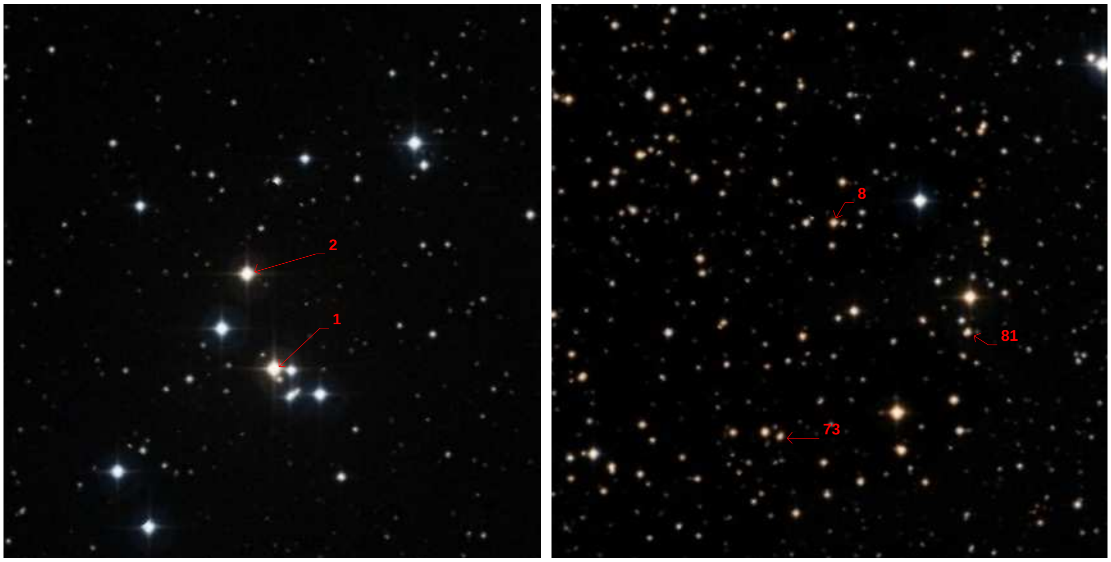

Figure 4.9: DSS finding charts of the observed stars in clusters NGC 1662 (left) and NGC 1817 (right).

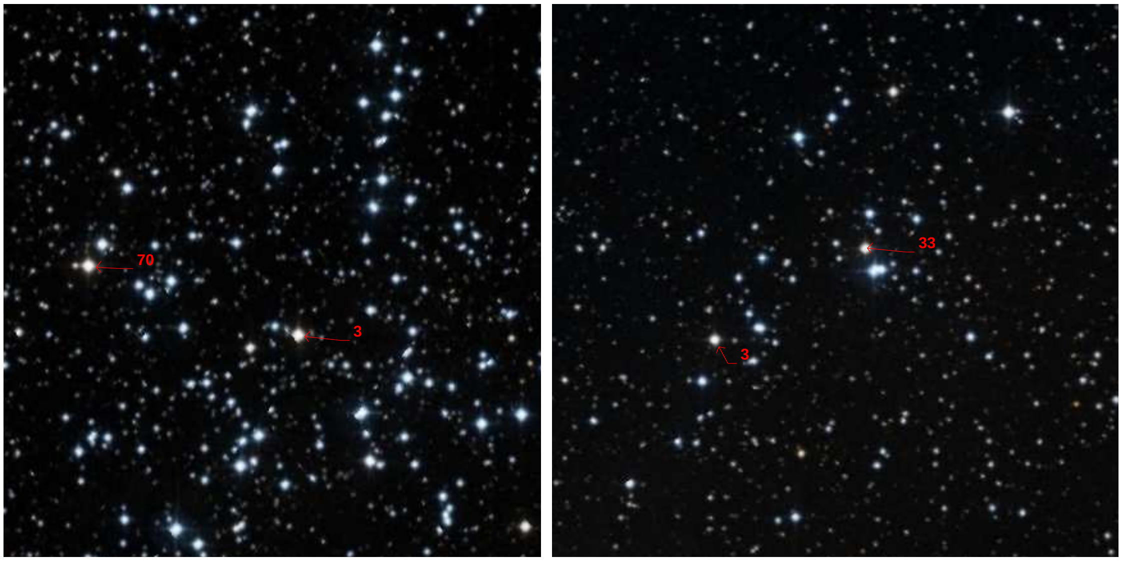

Figure 4.10: DSS finding charts of the observed stars in clusters NGC 1912 (left) and NGC 2251 (right).

Figure 4.11: DSS finding charts of the observed stars in clusters NGC 2266 (left) and NGC 2335 (right).

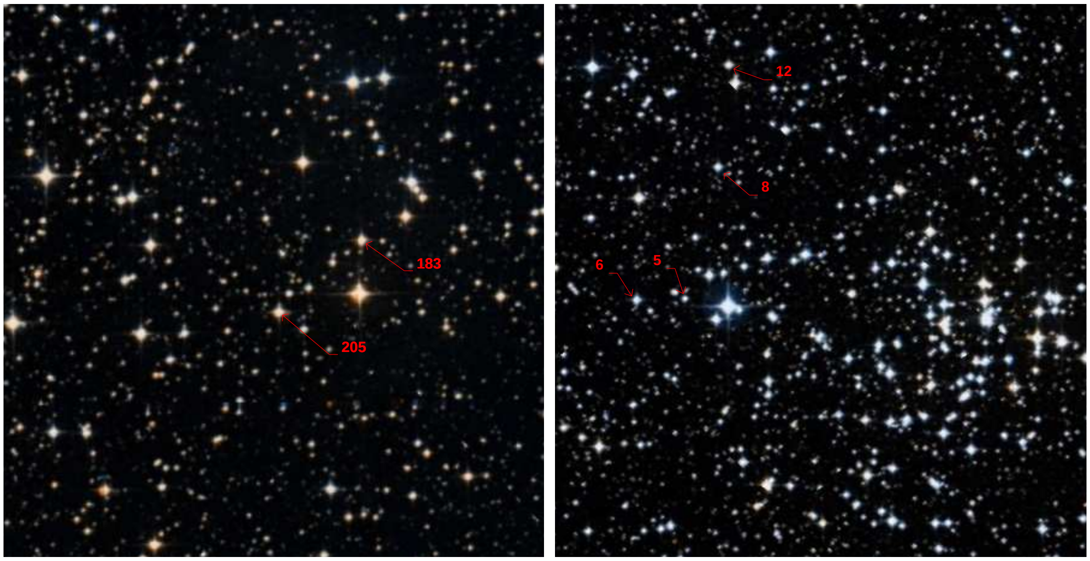

Figure 4.12: DSS finding charts of the observed stars in clusters NGC 2354 (left) and NGC 2360 (right).

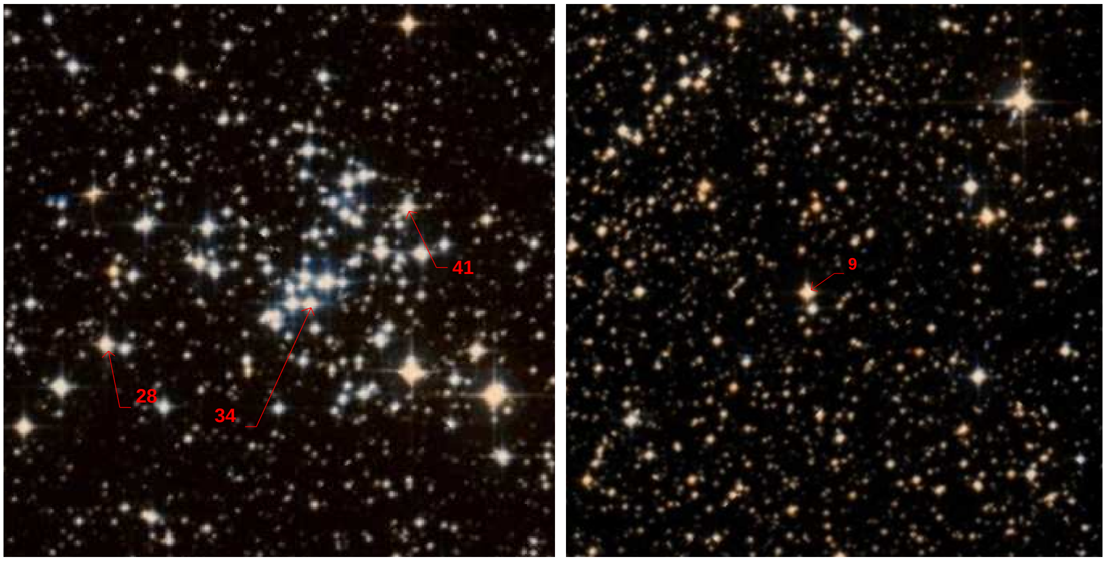

Figure 4.13: DSS finding charts of the observed stars in clusters NGC 2447 (left) and NGC 2482 (right).

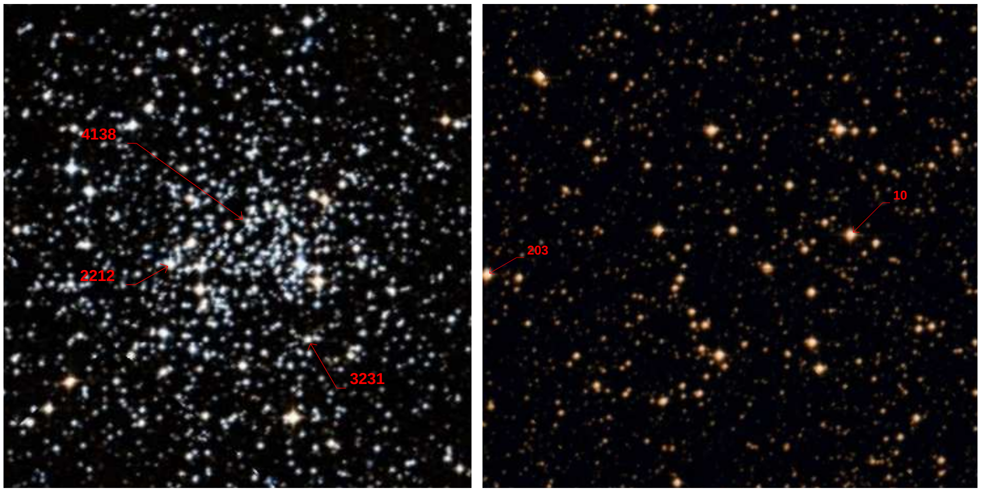

Figure 4.14: DSS finding charts of the observed stars in clusters NGC 2506 (left) and NGC 2527 (right).

Figure 4.15: DSS finding charts of the observed stars in clusters NGC 2539 (left) and NGC 2548 (right).

Figure 4.16: DSS finding charts of the observed stars in clusters NGC 2682 (left) and Collinder 350 (right).

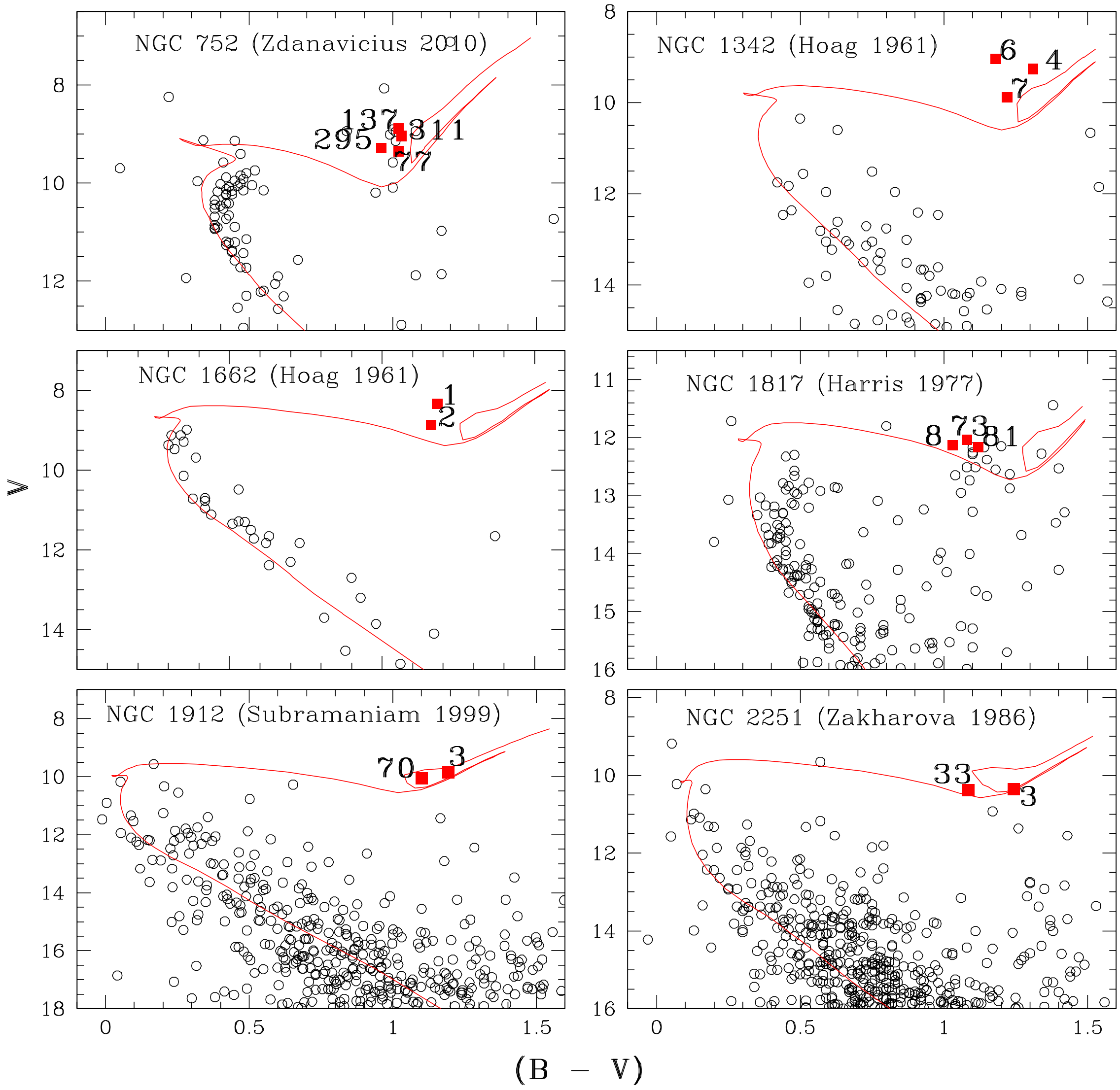

Figure 4.17: The fitting of the BV color-magnitude diagrams of the clusters NGC 752, 1342, 1662, 1817, 1912 & 2251 with the isochrones by Marigo et al. (2008). The open circles (black) represent proper-motion cluster members while the filled squares for the position of the target stars (red).

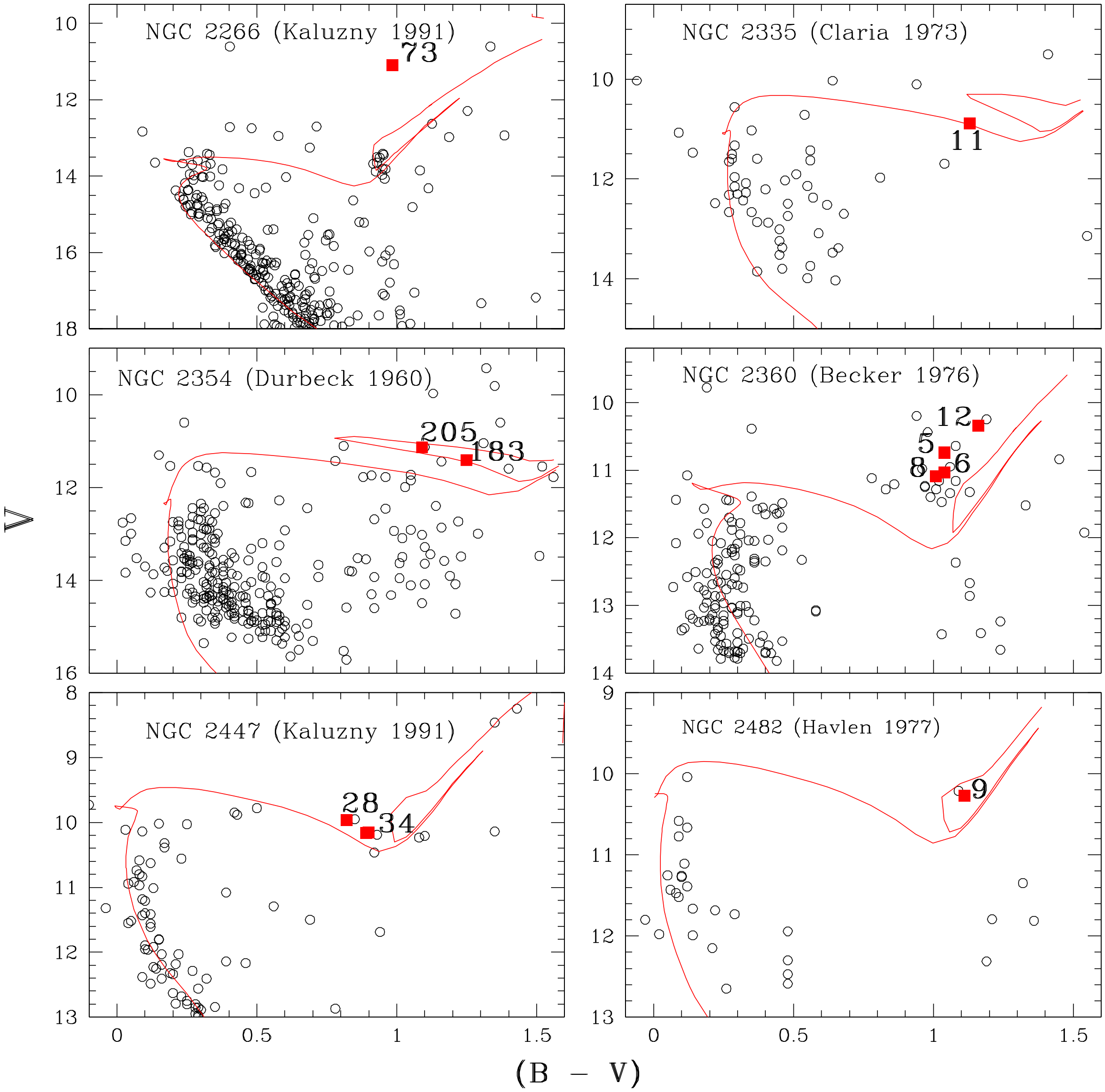

Figure 4.18: Same as figure 4.17, but for NGC 2266, 2335, 2354, 2360, 2447 & 2482.

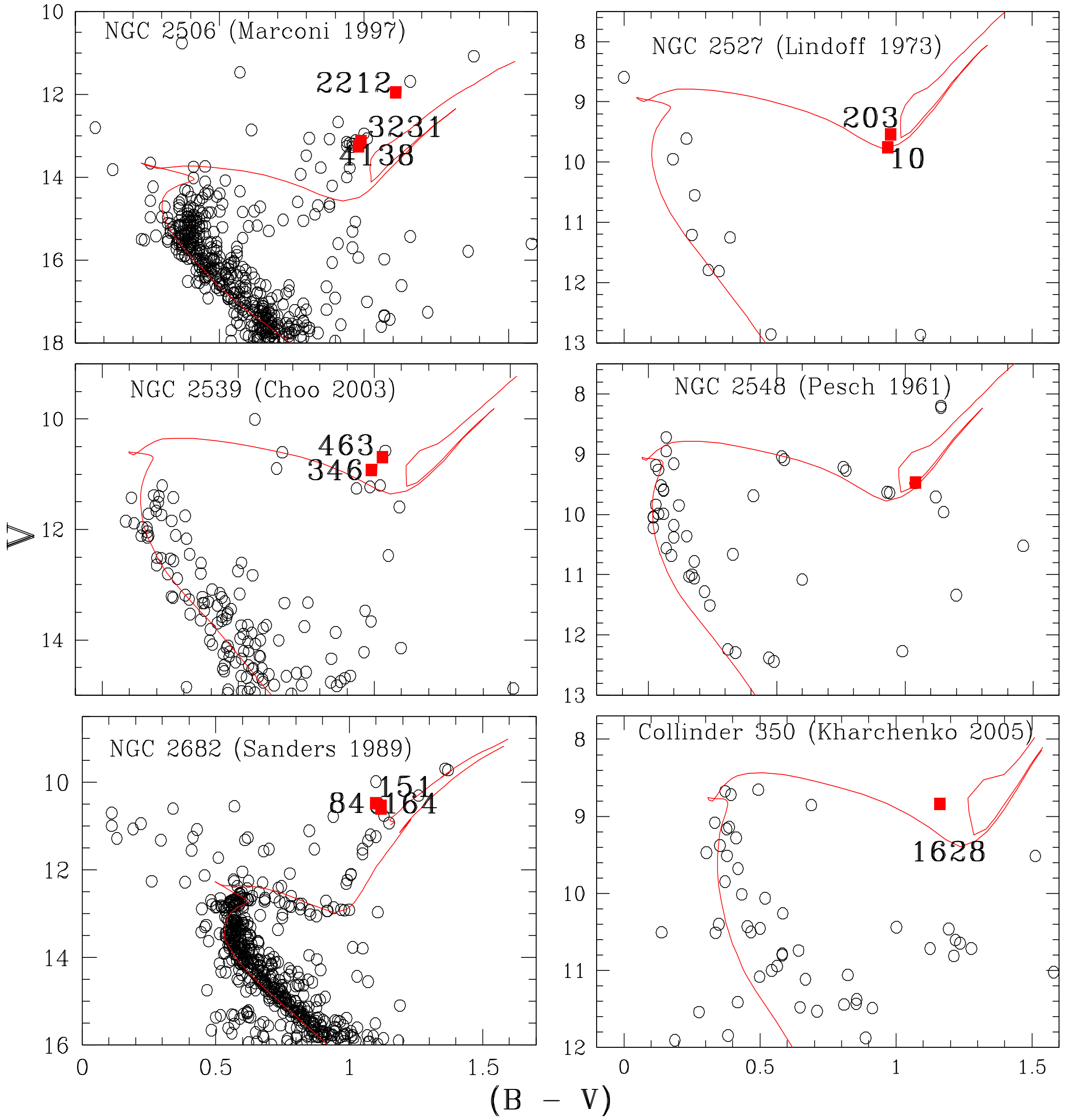

Figure 4.19: Same as figure 4.17, but for NGC 2506, 2527, 2539, 2548, 2682 and Collinder 350.

Chapter 5

Abundances: chemical inhomogeneities in the Galactic disk

5.1 Introduction

The OC sample analysed in the previous chapter confirmed the homogeneity of elemental abundances among cluster members. The presence of chemical homogeneity within a given cluster has been shown by the study of OCs, see, for example, spectroscopic analyses of the Hyades (Paulson et al. 2003; De Silva et al. 2006) and Collinder 261 (Carretta et al. 2005; De Silva et al. 2007). This observed homogeneity signifies that the proto-cloud is well mixed, and hence, the abundance pattern of a cluster bears the signature of chemical evolution of the natal cloud. These abundance ratios help in unraveling the star formation history of the Galactic disk, and the contributions to its chemical inventory by Type II and Type Ia SN and AGB stars as a function of time.

We devote this chapter to discuss our results and compare them with the abundances derived from samples of field thin and thick disk stars (i.e. dwarfs and giants) and finally with the available OC data in the literature.

5.2 Results

5.2.1 Comparison with field giants

If OCs are the principal supplier of field stars, there should be a very close correspondence between the composition of stars in clusters and the field. Such a correspondence represents a stiff challenge to the idea that field stars have come from clusters because modern studies of field stars show that there is no discernible 'cosmic' dispersion in relative abundances – [X/Fe] – at a given [Fe/H] (Reddy et al. 2006). The eighteen OCs are very likely representatives of the Galactic thin disk but at their metallicity ([Fe/H] ≈ -0.5 to solar) thin and thick disk stars very likely have the same relative abundances.

Several studies of thin disk dwarfs and giants have been reported recently, which give very accurate abundance ratios for many elements using a large samples of field stars. For almost all elements over the [Fe/H] range sampled by these eighteen OCs, the field dwarfs and giants show a solar-like mix of elements, i.e., [X/Fe] $\simeq 0$, with very little star-to-star scatter at a given [Fe/H]. Sample papers echoing this assertion include Edvardsson et al. (1993), Bensby et al. (2005), Reddy et al. (2003, 2006), Luck & Heiter (2006) for dwarfs, and Mishenina et al. (2006), and Luck & Heiter (2007), and Takeda et al. (2008) for giants. These papers invoke, as we have done, classical methods of abundance analysis involving standard model atmospheres and LTE line formation.

Methods of abundance analysis including choices of gf-values, selection of model atmosphere grid and determination of solar reference abundances differ among these papers. Yet, the results suggest that differences of ±0.05 and possibly ±0.10 dex may arise among similar analyses by different authors of the same or similar stars. Such differences are attributable to measurement errors with the cosmic dispersion masked by such errors. One expects applications of the classical method to give slightly different results for dwarfs and giants for several reasons, e.g., the effects of departures from LTE will be different for giants and dwarfs, and the ability of standard atmospheres to represent true stellar atmospheres may differ for dwarfs and giants. Thus, we restrict comparisons between our results and those by similar methods for field giants i.e. systematic errors will be very similar across this comparison.

A useful comparison of abundances between our OCs and field giants may be made using the study by Luck & Heiter's (2007) of a large sample of field giants analysed by methods similar to ours, i.e., a differential analysis with respect to the Sun. Using their Table 4, we calculated the mean abundances in field giants across

Table 5.1: Mean elemental abundance ratios, [X/Fe], for Na to Eu for the seventeen OCs from this study and the thin disk mean abundances from Luck & Heiter (2007) in the metallicity of our clusters (0.0 to −0.2 dex). Abundances calculated by synthesis are presented in bold typeface.

Species	OC mean	Thin disk	Species	OC mean	Thin disk
[Na I/Fe]	+0.24 ± 0.07	+0.10 ± 0.06	[Cu I/Fe]	**−0.18 ± 0.08**	+0.01 ± 0.13
[Mg I/Fe]	+0.04 ± 0.08	+0.08 ± 0.10	[Zn I/Fe]	**−0.13 ± 0.13**	...
[Al I/Fe]	+0.03 ± 0.09	+0.09 ± 0.05	[Rb I/Fe]	**−0.08 ± 0.11**	...
[Si I/Fe]	+0.16 ± 0.05	+0.12 ± 0.04	[Y II/Fe]	+0.10 ± 0.05	+0.07 ± 0.15
[Ca I/Fe]	+0.06 ± 0.06	−0.04 ± 0.05	[Zr I/Fe]	+0.12 ± 0.09	...
[Sc I/Fe]	+0.07 ± 0.07	−0.08 ± 0.06	[Ba II/Fe]	**+0.21 ± 0.20**	+0.04 ± 0.16
[Ti I/Fe]	+0.02 ± 0.07	0.00 ± 0.03	[La II/Fe]	+0.15 ± 0.09	+0.05 ± 0.09
[V I/Fe]	+0.05 ± 0.07	−0.09 ± 0.07	[Ce II/Fe]	**+0.22 ± 0.11**	+0.05 ± 0.09
[Cr I/Fe]	+0.02 ± 0.04	+0.01 ± 0.05	[Nd II/Fe]	+0.18 ± 0.09	−0.01 ± 0.07
[Mn I/Fe]	**−0.09 ± 0.06**	+0.06 ± 0.07	[Sm II/Fe]	+0.16 ± 0.08	...
[Co I/Fe]	+0.04 ± 0.07	+0.06 ± 0.08	[Eu II/Fe]	**+0.14 ± 0.08**	+0.08 ± 0.06
[Ni I/Fe]	+0.01 ± 0.05	0.00 ± 0.03			

the [Fe/H] range of our clusters (0.0 to −0.2) and those values are presented in the third and sixth columns of Table 5.1. NGC 2266 at [Fe/H] = −0.44 is excluded from the sample in part because it may belong to the thick rather than the thin disk. One can argue based on the membership probabilities (discussion has been postponed to section 5.3) that this cluster is a part of the thick disk stellar population.

Inspection of Table 5.1 shows that the mean [X/Fe] for the seventeen clusters are within 0.10 dex of Luck & Heiter's results except for Na, Sc, V, Mn, Cu, Ba, Ce and Nd and within 0.15 dex for all but Cu, Ba, Ce and Nd (Luck & Heiter did not include Zr, Rb and Sm in their collection of elements). The range of ±0.15 dex assumes measurement uncertainties of about 0.10 dex in both studies. Luck & Heiter's results for field giants are generally confirmed by Mishenina et al.'s (2006) and Takeda et al.'s (2008) for other large samples of field giants. One may note that Takeda et al.'s Mn, Ce, and Nd abundances (relative to Fe) agree well with ours but their analysis while it gives ionization equilibrium for Fe does not do so for Sc, Ti, V, and Cr.

The over abundance of sodium at all ranges of [Fe/H] is already seen in numerous OC giants (Friel et al. 2006) and our sample presented here behave no differently. The [Na/Fe] values from +0.12 to +0.33 are greater than suggested by Luck & Heiter (2007) from their large sample of giants: their results give a mean [Na/Fe] =+0.10 ± 0.06 for 84 giants with [Fe/H] in the range 0.0 to −0.20. Mishenina et al. (2006) in their Figure 14 show that clump giants have mean [Na/Fe] of about 0.1 and a scatter of about 0.1 dex. These are NLTE abundances for Na with the corrections for NLTE effects having reduced the Na abundances by about 0.1 to 0.15 dex. Thus, their LTE [Na/Fe] values would be comparable to our (LTE) values.

Similarly, Takeda et al. (2008) for a sample of giants give [Na/Fe] a value of about 0.2 from their LTE analysis. Their results too span ours for these seventeen OCs. Takeda et al. (2008) give a mean [Na/Fe]=$+0.14 \pm 0.07$ for 163 giants in the metallicity range 0.0 to -0.20. Measurements of [Na/Fe] in dwarfs in this [Fe/H] range suggest [Na/Fe] close to 0.0 (Edvardsson et al. 1993; Reddy et al. 2003, 2006; Luck & Heiter 2006). Thus, our positive [Na/Fe] are consistent with results by others on giants and all suggest a positive [Na/Fe] with respect to dwarfs of the same metallicity. A small increase in Na abundance is predicted from the first dredge-up (see, for example, Mishenina et al. 2006) but this may be too small to account for the observed increase in [Na/Fe] from dwarfs to giants. At the very least, it would be worthwhile to include both the dwarfs and giants in cluster abundance studies to investigate for further evidence of abundance differences.

Close scrutiny of our and Luck & Heiter's abundances suggest two possible differences: (i) the OCs appear to have a low [Mn/Fe] and [Cu/Fe] ratios than local field giants; (ii) the OCs relative to the field giants may be enriched in Ba and heavier elements.

(i) The [Mn/Fe] ratio decreases with [Fe/H], as shown by Luck & Heiter, and others. If one takes into account the decrease found for field giants, the [Mn/Fe] for the OCs is on average 0.12 dex lower than for the field giants. We suppose that this offset is not implausibly considered to be a systematic error arising from two similar but not identical analyses[1]. Indeed, Luck & Heiter's (2007) [Mn/Fe] abundance ratios for red giants are 0.10 dex lower than their sample of field dwarfs (Luck & Heiter 2006). Both Luck & Heiter's (2007) and Takeda et al. (2008) have employed similar abundance analysis based on the EW measurement of a large set of lines. The estimation of elemental abundances based on EWs measurements of spectral lines is not always regarded as a better option, especially, for the features affected by hfs components. Moreover, the lines affected by hfs components appear typically strong in red giant branch stars than their main sequence counterparts with similar metallicities.

Since, the hfs effect desaturates strong absorption lines and results in features with larger equivalent widths the computed abundances will be overestimated. It will be more complicated for the elements having more than one stable isotope because

---

[1] McWilliam et al. (2003) reported low [Mn/Fe] at [Fe/H] $\simeq$0 for giants in the Galactic bulge but such stars are also enriched in the α- elements and Eu, characteristics not carried by the giants in our OCs.

of the superposition of the spectra of the various isotopes of the same element. The relative strength and isotopic shift vary from element to element. Since, the stellar surface abundance estimates are higly dependent on the line strength, it is important to treat strong lines for hfs effects since the hfs correction increases with line strength. For weak lines, those generally lay on the linear part of the curve of growth, the hfs treatment is not so important because they are already unsaturated. Hence a spectrum synthesis over the separate hfs components is recommended to derive an abundance for the relatively strong lines affected by hfs components. Thus, the number of components, the wavelength splittings, isotopic shifts, if any present, and the relative strength of each the component must be known.

In our analysis largest hfs corrections are applied to [Mn/Fe] ($\simeq -0.43$ dex). From the Figure 15 of Takeda (2007) for a sample field dwarfs, it is evident that the Mn I lines employe in their analysis are all weak (EW < 50 mÅ) for which they have noted a negligible hfs corrections ($\simeq -0.02$ dex). Similarly, in their giant sample Takeda et al.(2008) have employed a single weak line at 5004.8 Å for the abundance analysis for which the hfs effects are less important. Whereas the Mn I abundances from Luck & Heiter (2007) might be based on strong lines for which the hfs effects are not accounted for using the spectrum synthesis, unlike ours. This can fairly explain the observed offset of [Mn/Fe] ratio, as a function of [Fe/H], between field dwarfs and our OC giants with that of Luck & Heiter's (2007) sample of field giants. We estimated the Cu I abundance from spectrum synthesis of λ5218 Å line including both the hfs components and isotopic splitting so the same arguments as for the Mn I lines can apply to explain the observed offset of [Cu/Fe] ratio between field and OC giants.

(ii) We have noticed small but significant enrichment in mean [s/Fe] ratios, as can be in table 5.1. We note especially that D'Orazi et al. (2009) claim that the [Ba/Fe] ratio decreases with cluster age with young clusters showing a [Ba/Fe] ratio of 0.6 dex but older clusters such as M 67 (a few billion years) giving [Ba/Fe] of 0.0, all for clusters with near-solar ([Fe/H] $\sim$ 0.0) metallicity. It is important to extend this work to elements tracing other nucleosynthetic processes using cluster members because field stars of less than about 1000 Myr are difficult to age reliably. Barium abundances of [Ba/Fe] of 0.6 dex have not been seen in field stars with known ages, presumably the majority of young stars are in clusters not yet disrupted.

Recently, Maiorca et al. (2011) have suggested roughly solar [s-process/Fe] values for clusters older than about 1.5 Gyr, while a strong s-process enrichment with a plateau at about 0.2 dex for young metal-rich OCs, after which no further enrichment is seen as noted by D'Orazi et al. (2009). They further suggests that the increment in barium found by D'Orazi et al. (2009) should be attributed to NLTE effects and a saturation of the barium lines used is also a possibility.

To resolve the discrepancy between the enhanced Ba and heavier elemental abundances of our OCs relative to the field giants, we have examined the abundance ratios of these elements as a function of the ages of stars. As Luck & Heiter (2007) did not give ages for their sample of giants, we have derived them using a tight relation established between the turn-off mass and age of red giants (Takeda et al. 2008).

$$\log \mathit{age}\,(\mathrm{yr}) \simeq 10.74 - 1.04\,(M/M_\odot) + 0.0999\,(M/M_\odot)^2 \tag{5.1}$$

Our investigation reveals that our OCs are relatively younger than Luck & Heiter's sample of field giants (see the top panel of figure 5.9), and hence the observed enrichment in [s/Fe] ratios for our cluster sample. This eventually reflects that the Galaxy has enriched in the nucleosynthesis products ejected by the low mass AGB stars. An additional argument in favour of the hypothesis that our OCs natal cloud was already enriched in s-process elements is provided by the observed [Rb/Zr] ratios.

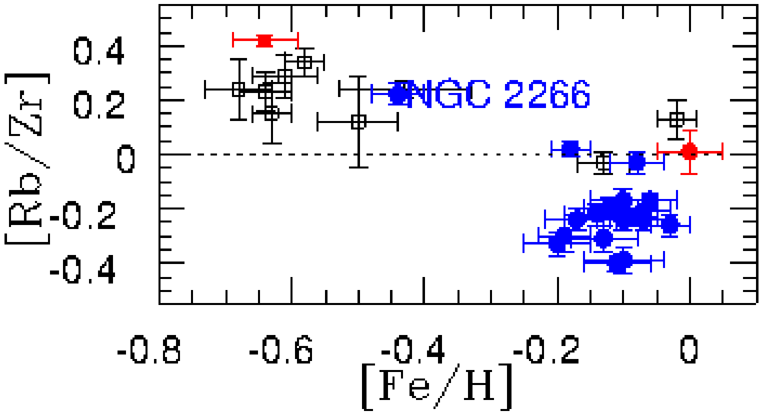

Figure 5.1: The [Rb/Zr] - ratio for our sample of eighteen OCs as a function of their [Fe/H] with corresponding error bars. The filled circles (blue) represent the mean cluster abundances derived in this study. The OC NGC 2266 with a largest [Rb/Zr] ratio (= +0.22) is marked in the figure. The empty squares (black) represents the data taken from Tomkin & Lambert (1999) for a sample of metal-deficient disk and halo stars. The filled square and the filled circle (in red) represents the [Rb/Zr] - ratios for the Arcturus and Sun. The dotted line indicate the solar mix of elements.

The Rb abundance provides an additional diagnostic information on the neutron density at the s-process site which is controlled by both the neutron source and the mass of the parent AGB star responsible for its synthesis. The abundance of Rb relative to its neighboring s-process elements such as Sr, Y and Zr is a useful monitor of neutron density at the time of s-processing. Thanks to the branch in the s-process path at ^{85}Kr with a β-decay half life of 10.7 yr, which at low neutron densities ($N_n \leq 10^7$ cm^{-3}) decays to ^{85}Rb, while at higher neutron densities suffers successive neutron captures and the flow proceeds along the path from ^{85}Kr to ^{86}Kr to ^{87}Kr, that β-decays to stable ^{87}Rb isotope. The sensitivity of the Rb elemental abundance to the neutron density arises then due to the quite different neutron capture cross sections for both of its stable isotopes (^{85}Rb and ^{87}Rb) among which the ^{85}Rb being roughly a factor 10 times more abundant than ^{87}Rb. Thus, at low neutron densities the ratio [Rb/Zr] is about 10 times less than that at high neutron densities. Since, the solar Rb abundance is attributed in almost equal parts to the s-process and r-process, the observed stellar Rb abundance directly indicate the neutron density at the s-process site. Even though the stellar Rb I isotopic ratios can not be measured, the Rb I lines used in our analysis are weak in all the program stars so the derived Rb abundances are not affected by changes in the isotopic mixture. We derived the Zr abundances using 5-7 weak lines (see the individual cluster abundance tables 8.2−8.12 for the number of lines used for each star) for which reliable estimates of gf-values are available and the usage of the same lines will remove the systematic uncertainties.

A comparison of our observed [Rb/Zr] abundance ratios for our OCs (Figure 5.1) with the recent models of AGB nucleosynthesis from Figure 14 in Smith et al. (2000) suggests that the 3 $M_\odot$ models provide complete overlap with observations except for the [Rb/Zr] ratio in the OC NGC 2266. For these low mass AGB stars, the dominant neutron source is ^{13}C(α,n)^{16}O reaction which is responsible for the production of s-process elements to observed values. We note that NGC 2266 has a higher [Rb/Zr] ratio than the other OCs studied here, although our measured Rb abundance is based on a single star. Such a high [Rb/Zr] ratio for the OC NGC 2266, complimented with sub-solar s-process elemental abundances and over-solar r-process and α-elements, reflects the addition of Tyepe II SNe to the chemical enrichment of its parent gas cloud prior to its formation.

5.2.2 Intracluster abundance variations

From figure 5.2, it is obvious that apart from having enrichment in heavy elements, our sample of seventeen OCs show cluster to cluster abundance variations larger than measurement errors for s-process elements, with certain elements such as Ba and Ce showing large variation. The abundance variations, over the [Fe/H] range ($\simeq$ 0.0 to −0.20 dex) sampled by these OCs, span from -0.07 (NGC 2682) to +0.31 (NGC 2527) for [Zr I/Fe], -0.16 (NGC 2682) to +0.70 (NGC 1912) for [Ba II/Fe], 0.0 (NGC 2682) to +0.29 (NGC 2335) for [La II/Fe], -0.02 (NGC 2682) to +0.38 (NGC 2354) for [Ce

II/Fe], +0.02 (NGC 2682) to +0.33 (NGC 2354) for [Nd II/Fe], -0.03 (NGC 2682) to +0.28 (NGC 2335) for [Sm II/Fe] and +0.04 (NGC 2251 & 2360) to +0.28 (Collinder 350) for [Eu II/Fe].

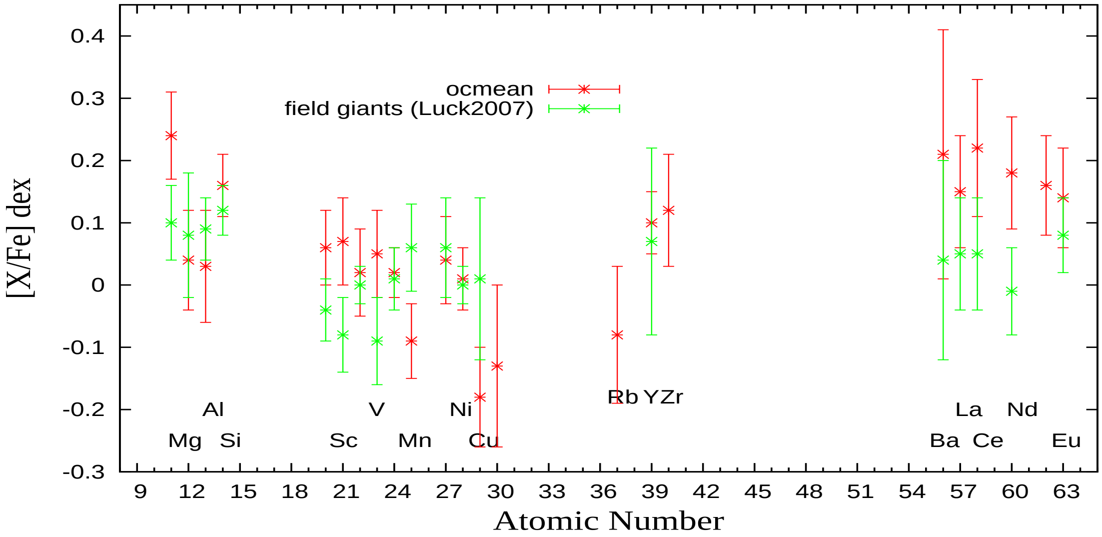

Figure 5.2: A graphical representation of the mean elemental abundance ratios, [X/Fe], from Na to Eu for OCs and Luck & Heiter's (2007) sample of thin disk field giants covering the metallicity range of our OCs (0.0 to −0.2 dex).

Our s- process elemental abundances are the most reliable, since the lines employed in our analysis are mainly on the linear part of the curve of growth and both the hfs and isotopic shifts have been considered for the synthesis of the lines affected by multiple transitions. Moreover, we have analysed 5−7 lines for many heavy elements and also stress that the usage of same lines results in removal of systematic errors.

The Ba II abundance has been derived by spectrum synthesis of an unsaturated line at λ5853 Å including both the hfs and isotopic ratios, as the line at λ6141 Å is often strong and blended with a weak Fe feature and may result in spurious abundance. As noted in table 4.4 from Chapter 4, the Ba II abundance is less sensitive to changes in effective temperature and surface gravity but very much sensitive to microturbulence velocity. Any error in measuring the microturbulence is carried directly over to the derived abundance by almost the same amount. The mean values of effective temperature T_{eff}, surface gravity log g and microturbulence across the sample of 40 stars are about 4975±170 K, 2.56±0.32 cm-s^{-2} and 1.50±0.17 km s^{-1}.

This implies all the stars have very similar ξ_t values with a small spread around the mean. Therefore a change of ξ_t by 0.17 km s^{-1} is unable to mask the abundance variations found for [Ba II/Fe] across the sample of seventeen OCs. Similarly, for Zr I, which is sensitive to T$_{eff}$, a change of temperature by 170 K may not account for the observed spread in [Zr I/Fe] across the sample.

The remaining s-process elements such as La II, Ce II, Nd II and Sm II are unaffected by the changes in T$_{eff}$ and ξ_t, but are sensitive to log g. Again a change of gravity by 0.32 cm-s^{-2} is unable to explain the observed intracluster abundance variations. As described in Chapter 4, we can estimate the stellar atmospheric parameters with an accuracy of 100 K in $T_{\rm eff}$, 0.25 cm s^{-2} in log g and 0.20 km s^{-1} in ξ_t. In addition, as our analysis is strictly differential relative to the Sun, hence possible systematic effects due to the quality of gf-values, chosen model atmosphere are cancelled. Hence the observed intracluster abundance variations for s-process elements suggests that there is a range in the mass of the progenitors such that the production factors for these s-process elements vary with progenitor mass at a given [Fe/H].

Abundance differences found across the present sample highlight the different chemical histories of gas clouds prior to the formation of individual clusters. The difference in the abundances from cluster to cluster and various element to element seen among these clusters demonstrate that if there is a sufficiently large abundance range it will be possible to allocate clusters to common star-forming aggregates and field stars to a parent aggregate. In this vein, we note that Wylie-de Boer et al. (2010) trace stars in the Kapteyn group to ω Cen from their Cu abundances for which [Cu/Fe] is similarly distinct for both ω Cen and the group. Their suggestion may be confirmed by Mn abundances, which as Cunha et al. (2010) have shown are even odder than Cu in ω Cen. Thus, as a final note, the abundance of s-process elements (and ratios such as [Ba/α, Eu]) could serve as useful tools to tag the field stars back to their parent cluster to form large star forming aggregates. Such studies would eventually improve our basic understanding of Galactic chemical evolution processes.

5.3 Comparison with literature

We merged our sample of eighteen OCs with the available high-quality results in the literature to enlarge the dataset. As the abundances are collected from various literature papers, the data are liable to systematic errors concerning the atomic data (not only the quality of gf-values but also the choice of specific lines), model atmosphere grids employed, reference solar abundances adopted, abundance analysis programs and type of stars considered by different authors in their analysis.

Many researchers have noticed a systematic offset when combining abundance results of OCs from different authors to obtain a complete picture of chemical evolution of the Galaxy by constructing a homogeneous set of OC abundances. Among the investigators are Friel et al. (2010), Yong et al. (2012), and more recently a robust analysis by Heiter et al. (2014). All these authors have thoroughly examined the systematic abundance differences between the various studies and noted that it is hard to quantify them for individual studies and for individual elements. In Chapter 4, we offered a comparison of our abundance estimates with literature studies using the OC NGC 2682, and spotted a systematic offset of ±0.15 dex or smaller in [X/Fe] ratios for almost all elements with exception of a few (Table 4.5 of Chapter 4). Therefore, we emphasize that a simple merger of all cluster abundances from various resources can easily wash out or mask subtle abundance trends unless it is done with extreme care.

To cancel out such systematic errors we have followed a different procedure. The only observed quantity that has to be extracted from spectra for abundance estimates is the EW of a spectral line. With no doubt all the authors might have measured these EWs with quite a good accuracy of upto $\sim$ 2-5 mÅ, which may results in abundance uncertainties of $\sim$ 0.05 dex or smaller. Hence we reestimated the cluster abundances from the EWs collected from literature resources and using our models, linelists and reference solar abundances. This approach should minimize, or even cancel out, all sorts of systematics mentioned earlier and place all the results on a common abundance scale. A wide wavelength coverage of echelle data employed by various authors made easy to pick up common set of lines with us for Na, Al, α- elements, Cr I, Fe I, Fe II and Ni I, but note that for s- and r- process elements measurements are often lacking in the literature, thereby making it impossible to homogenize the data for heavy elements, but still we can measure abundances for [Y/Fe] for 13 OCs, [Zr/Fe] for 8 OCs and [Ce/Fe] for 5 OCs in the literature sample. The abundances derived for literature sample of OCs are shown in tables 5.5 - 5.6.

We compiled a list of 77 OCs drawn from our studies and from the literature, covering a range of ~ -0.5 to 0.3 dex in metallicity and an age of few Myr to 9 Gyr. Here, we emphasize that our sample contribute about 23% of the total OCs explored so far with high quality and high-dispersion echelle spectroscopy. Moreover, we have done a homogeneous and comprehensive abundance analysis extending upto s- and r-process elements for which the measurements are often lacking in the literature. Before we use this homogeneous sample of echelle data to look at trends with age and metallicity in the disk, it is worth while to know their kinematic origin.

Positions and Kinematics

In order to specify the position of each OC with time in Galactic phase space, one needs information on present day space coordinates (x, y and z) and the corresponding space velocity components (U, V and W) with respect to the Galactocentric reference frame.

The current positions of OCs are calculated using the array of equations

$$\begin{aligned} x &= R_{\odot} - d\, cos\, l\, cos\, b \\ y &= d\, sin\, l\, cos\, b \\ z &= d\, sin\, b \end{aligned} \tag{5.2}$$

where d is the heliocentric distance and ℓ and b are the Galactic longitude and latitude of the cluster about the Sun with $R_{\odot} = 8.0 \pm 0.6$ kpc (Ghez et al. 2008).

The Galactocentric distance of the cluster are calculated using the equation

$$R_{gc} = \sqrt{(R_{\odot}^2 - 2\, R_{\odot}\, d\, cos\, b\, cos\, l + d^2)} \tag{5.3}$$

The basic data for position of OCs in the sky (α(2000.0), δ(2000.0)), ℓ and b, d and mean absolute proper motions ($\mu_{\alpha} cos\delta$, μ_{δ}) with errors on them ($\sigma_{\mu_{\alpha}}$, $\sigma_{\mu_{\delta}}$) are taken from DAML catalogue (Dias et al. 2002). For clusters without proper motions in DAML, we have made an estimate by averaging the proper motions of potential cluster members taken from UCAC4 catalogue (Zacharias et al. 2013). All these quantities along with the mean radial velocities measured from the spectra are used in calculating the U, V and W and the corresponding uncertainties on them (σ_U, σ_V, σ_W). The final sample of clusters along with the basic input data used in calculating U, V and W velocities is shown in Table 5.3. Since the DAML catalogue has no errors on heliocentric distances, we have adopted a conservative uncertainty of 20% on distance measurements while calculating the uncertainties in U, V and W.

Our code written in Fortran computes the U, V and W velocity components with respect to the Sun and their errors using the method described in Johnson & Soderblom (1987). All the space coordinates and the velocity components refer to a Galactocentric right-handed cartesian coordinate system in a spherical geometry in which the x and U are positive towards the Galactic center, y and V are positive in the direction of Galactic rotation, and z and W are positive in the direction of the North Galactic Pole (NGP).

The Galactic space velocity components are calculated using the matrix form

$$\begin{pmatrix} U \\ V \\ W \end{pmatrix} = T \begin{pmatrix} cos\,\alpha\,cos\,\delta & -sin\,\alpha & -cos\,\alpha\,sin\,\delta \\ sin\,\alpha\,cos\,\delta & +cos\,\alpha & -sin\,\alpha\,sin\,\delta \\ +sin\,\delta & 0 & +cos\,\delta \end{pmatrix} \begin{pmatrix} RV \\ 4.74057\,\mu_\alpha\,d \\ 4.74057\,\mu_\delta\,d \end{pmatrix}$$

with the transformation matrix given by

$$T = \begin{pmatrix} -0.06699 & -0.87276 & -0.48354 \\ +0.49273 & -0.45035 & +0.74458 \\ -0.86760 & -0.18837 & +0.46020 \end{pmatrix}$$

where all the symbols have their usual meanings.

These space velocities are brought to the Local Standard of Rest (LSR) by correcting for the solar motion of ($U_\odot$, $V_\odot$, $W_\odot$) = (+10.0, +5.2, +7.2) km s^{-1} from Dehnen & Binney (1998). These LSR velocities are then converted to the space velocity components with respect to the Galactic Standard of Rest (GSR) by adopting a rotation velocity of the LSR of 220 km s^{-1} (Kerr & Lynden-Bell 1986) at a Galactocentric distance of the Sun $R_\odot$ = 8.0±0.6 kpc (Ghez et al. 2008).

Membership probabilities

A complete knowledge of space velocity components is essential in identifying a cluster as a member of a given stellar kinematic population. The Milky Way stellar populations are broadly divided into three main components: the disk, bulge/stellar-halo and the halo. The bulge population is of little concern to this study as it is largely confined to within a few kiloparsecs of the galactic center.

As described in Chapter 1 the disk is a rotationally supported structure with an exponential stellar distribution in the vertical direction which subdivides into a thin disk, with scale height of 300 parsecs, and a thick disk, that is kinematically hotter and has a scale height of 1.35 kiloparsecs (Binney & Merrifield 1998). The thick disk component rotates more slowly than the thin disk, and as a whole it lags behind the LSR by $\sim$ 48 km s^{-1}, while the thin disk component lags by only $\sim$ 9 km s^{-1}. The thick stars are significantly older and exhibit large velocity dispersions than the thin disk ones (Table 5.2). The stellar halo surrounds the disk and bulge populations and occupies roughly a spherical volume. Stars in the halo population exhibit a roughly isotropic velocity distribution without any strong signature of rotation with respect to LSR and present large velocity dispersions over the both disk populations. The kinematic properties of various stellar populations are shown in figure 5.3.

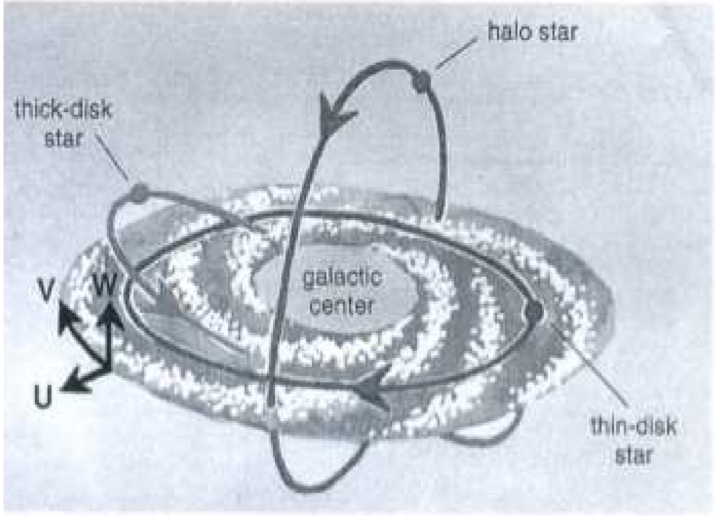

Figure 5.3: The kinematic properties of various stellar populations – Thin disk stars/OCs have a high rotational velocity (V) but a low vertical velocity (W). Thick disk OCs have slightly higher vertical velocities while the halo OCs tend to have the highest vertical velocities and almost no rotational velocity. (Courtesy: Chiappini 2001)

One obvious prerequisite in understanding the difference between various stellar populations is a reliable method, even if statistical, of assigning each OC either to the thin disk, thick disk or the halo, and of recognizing OCs for which the assignment cannot be made with fair certainty. The separation between thin disk, thick disk and halo populations can be made either by selecting OCs based on kinematics, using chemical composition criteria, or a combination of both. In principle, the population segregation based only on kinematics or abundances are not equivalent: thin (thick) disk samples separated based on their kinematics alone may contain OCs with the thick (thin) disk chemical composition (see for example, Mishenina et al. 2004 and Reddy et al. 2006).

Some authors argue that, as the chemical abundances of a cluster does not change, while kinematics may change with time, the selection based on abundances is more reliable. Since our goal is to unravel the formation and evolution of Galactic disk through the study of chemical abundances of OCs, composition alone cannot be considered in defining these components. Therefore, here we invoke the kinematic criteria used in previous studies by Bensby et al. (2005), Mishenina et al. (2004), and Reddy et al. (2006).

Table 5.2: The velocity dispersions, the asymmetric drift velocities relative to LSR (V_{ad}), and the fractional population of thin, thick and halo stellar components.

Component	σ_U	σ_V	σ_W	V_{ad}	Fraction (f)
Thin disk	43	28	17	−9	0.93
Thick disk	67	51	42	−48	0.07
Halo	131	106	85	−220	0.006

The method of assigning OCs either to the thin disk, the thick disk or the halo relies on the assumption that the whole sample is a mixture of three stellar populations with their respective Galactic space velocity U_{LSR}, V_{LSR}, W_{LSR} components representing Gaussian distributions, with given mean values and dispersions σ_U, σ_V, σ_W. The remaining constraints are the relative densities of thin, thick and halo stars in the solar vicinity. With these requirements, the probability distribution functions that assign OCs to the thin disk (P_{thin}), thick disk (P_{thick}), or the halo (P_{halo}) are

$$P_{thin} = \frac{f_1 p_1}{\sum_{i=1}^{3} f_i p_i},\; P_{thick} = \frac{f_2\, p_2}{\sum_{i=1}^{3} f_i\, p_i},\; P_{halo} = \frac{f_3\, p_3}{\sum_{i=1}^{3} f_i p_i} \tag{5.4}$$

with

$$p_i(U,V,W) = K_i\, exp\left[-\frac{U_{LSR}^2}{2\,\sigma_{U_i^2}} - \frac{(V_{LSR}-V_{ad})^2}{2\,\sigma_{V_i^2}} - \frac{W_{LSR}^2}{2\,\sigma_{W_i^2}}\right] \tag{5.5}$$

where $K_i = \frac{1}{(2\pi)^{3/2}\sigma_{U_i}\sigma_{V_i}\sigma_{W_i}}$ (i = 1, 2, 3 for thin disk, thick disk and halo) is a normalization constant. σ_{U_i}, σ_{V_i} and σ_{W_i} are the characteristic velocity dispersions, V_{ad} is the asymmetric drift and f_i are the fraction of stars in each stellar population in the solar vicinity.

As the representative Gaussian distribution functions overlap in velocity space, the definition of the thin, thick and halo populations is very sensitive to the choice of the parameters representing the Gaussian distribution functions and the population fractions f_i. Several studies are devoted to the determination of velocity ellipsoids of the thin disk, thick disk and halo components, as well as the population fractions in the solar neighbourhood. The parameter given in Table 5.2 are taken from Robin et al. (2003). Robin et al. (2003) gave the asymmetric drifts relative to the Sun and, therefore, we have corrected them for the solar motion relative to the LSR $V_\odot = 5.2$ km s^{-1}. The mean values of U_{LSR} and W_{LSR} for any of the three populations are taken to be zero.

We compute the membership probabilities P_{thin}, P_{thick}, P_{halo} and the associated uncertainties due to the error on each of the velocity components (U_{LSR}, V_{LSR} and W_{LSR}) using a FORTRAN program that uses the equations 5.4 and 5.5. Our program

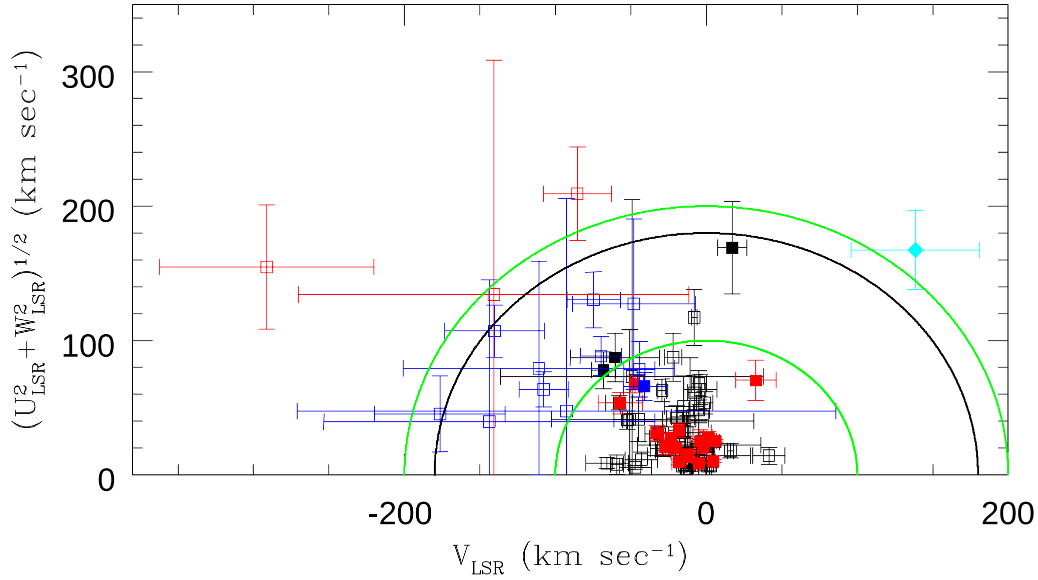

Figure 5.4: Toomre diagram of OCs showing the quadrature sum of radial and vertical velocities (U and V) as a function of the rotational velocity relative to the LSR. The green lines mark the total space velocity, $\sqrt{U^2_{\rm LSR}+V^2_{\rm LSR}+W^2_{\rm LSR}}$, in steps of 100 km s^{-1}. The continuous black line indicates a total space velocity of 180 km s^{-1}, that serves as a potential criteria to separate the thick disk from halo populations (Venn et al. 2004), and the dotted vertical line corresponds to LSR velocity of 220 km s^{-1}. The thin disk, thick disk, halo and intermediate populations are represented by various symbols: Our sample of clusters are designated as filled red squares (thin disk) and filled blue square (thick disk). All the other symbols represent the sample from the literature: thin disk (black open squares), thick disk (blue open squares), halo (red open squares). The intermediate stellar populations are designated as black filled squares (thin - thick disk) and cyan filled diamond (thick disk - halo).

successfully reproduces the probabilities given in Reddy et al. (2006), when their input data are adopted.

We associate the clusters to thin disk population as those that have probabilities greater than 75% and at least twice the probability of belonging to the thin disk over other populations (and likewise for the other populations). We assume that placing a lower limit of 75% in probability ensures a minimum contamination of each subsample from the rest of the stellar populations. On account of these probabilities, NGC 2266 (one out of eighteen OCs) turned out to a thick disk member and the remaining OCs in our sample display probabilities typical of the thin disk, while none seems to belong to the halo. Table 5.4 lists the computed space and GSR velocity components of OCs along with their membership probabilitis.

The Toomre diagram in figure 5.4 provides a way to compare the kinematic properties of various components in the Milky Way, as it represent a relation between the quadratic sum of radial and vertical kinetic energies and the rotational kinetic energy relative to the LSR. As depicted in the figure, the thick disk and halo populations rotate more slowly than the thin disk and show large dispersion about their mean space velocities.

5.3.1 Abundance trends with age and [Fe/H]

In this section, we investigate whether the present sample OCs exhibit any trends such as metallicity versus age, and relative abundance ratios, [X/Fe], as function of age and metallicity, as is observed for field stars of different stellar populations in our Galaxy.

In Figures 5.5−5.11, we plot mean abundance ratios [X/Fe] versus age and metallicity, [Fe/H], for OC sample along with Luck & Heiter's sample of solar neighborhood red giants. It is apparent from the plots that the abundance trend of thick disk OCs join very smoothly with those of thin disk ones against metallicity and a overlapping trends against age, without showing any sign of discontinuity. This leaves a hint for the formation and evolution of thin disk in a sequence from the material enriched with the previous generation of stars from the thick disk.

α-elements

The runs of abundance ratios for [Mg/Fe], [Si/Fe], [Ca/Fe] and [Ti/Fe] against the age and [Fe/H] of OCs are shown in figure 5.5. All the α- elements follow a very similar pattern. In the range $-0.4<$[Fe/H]< -0.2, the [α/Fe] abundances in the thick disk OCs decline steeply with increasing metallicity. While this decline is more prominent for Mg and Ti abundances, it is also presnt in Ca and Si. The decline (or knee) in the α-elemental abundances is in good agreement with the field stars data (Luck & Heiter 2007, Edvardsson et al. 1993, Bensby et al. 2005 and Reddy et al. 2006).

The decline in the thick disk [α/Fe] with metallicity at [Fe/H] ≈ -0.4 can be interpreted as a signature of delayed contribution of type SN Ia ejecta to the chemical enrichment of the cluster population under study. When star formation begins in an ensemble of gas, it is enriched first with the ejecta from the massive stars (M $\gtrsim$ 10 $M_\odot$). Due to the short life times ($\approx$ 10 Myr), of these massive stars, they explode as core collapse supernovae type II (Type II SN) and enrich the interstellar medium mainly with α- and r-process elements (such as Eu) and lesser amounts of the iron peak elements (Tsujimoto et al. 1995; Woosley & Weaver 1995). Thus in the early phase, the chemical evolution of the Galaxy is dominated by the short lived massive stars and produce high [α/Fe] and [Eu/Fe] ratios at lower metallicities.

A little latter ($\approx 10^9$ yr) type Ia supernovae (Type Ia SN) will have begun their contribution and disperse large amounts of iron-peak elements (Sc, V, Cr, Mn, Fe, Co, Ni) into the interstellar medium with none or little of α-elements. Type Ia SN events happen to occur in a binary system where the mass of a C-O white dwarf surpass the Chandrasekhar mass limit ≈ 1.4 $M_\odot$ by accreting the hydrogen-rich material via mass transfer from its binary companion such as a main sequence star, a (super) giant, or a He star. As their low mass progenitors are expected to live longer than the type II SN progenitors, there will be a delay in time for the chemical enrichment of the Galaxy with iron-peak elements. Thus, when type Ia SN has begin to contribute to the enrichment, we see the decline in [α/Fe] ratios.

The fact that we see the signature of type Ia SN at [Fe/H] ≈ -0.4 dex for the thick disk OCs thus mean that the type Ia SN rate peaked at that metallicity and these clusters formed well after the Type Ia SN had begun to enrich the interstellar medium. It appears from the age versus [α/Fe] trends in figure 5.5 that the chemical enrichment might have continued for 3-4 Gyr after the peak in the Type Ia SN rate. The relatively modest range in [Fe/H] exhibited by these OCs make it difficult to provide effective conclusion on the star formation time scale in the thick disk. Although, it appears that the star formation rate is more intense in the thick disk such that [Fe/H] had reached levels as high as [Fe/H] ≈ -0.4 before contributions from type Ia SN became significant. Field stars data indicate that it might have taken 2-3 Gyr for the thick disk to reach [Fe/H] ≈ -0.4 (Bensby et al 2004b).

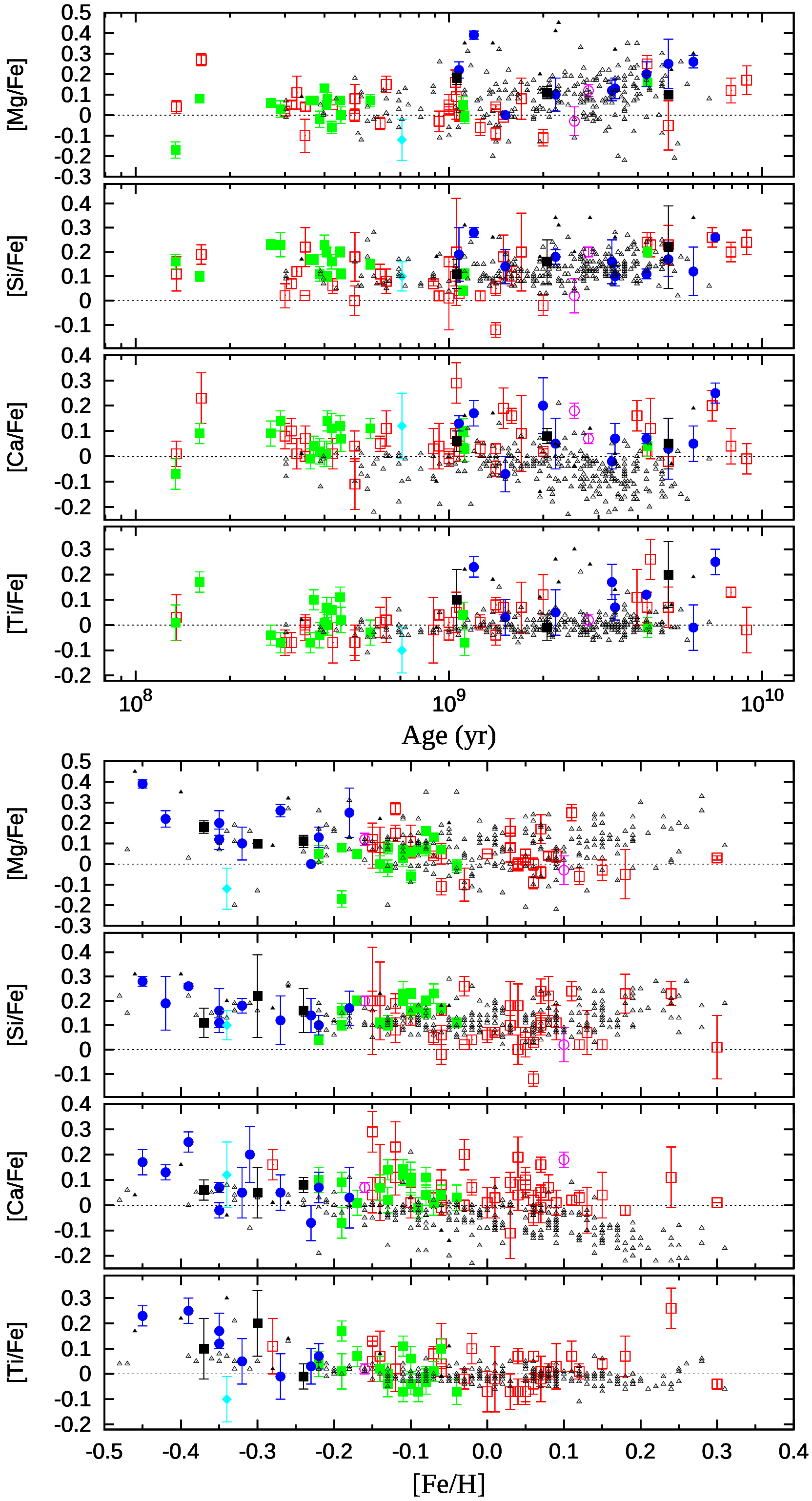

Figure 5.5: Abundance ratios for [X/Fe] vs. Age (top panel) and [X/Fe] vs. [Fe/H] (bottom panel) for alpha elements [Mg/Fe], [Si/Fe], [Ca/Fe] and [Ti/Fe]. Clusters from our study (thin disk members) are presented as green filled squares. Luck & Heiter's sample of field giants are marked as black open triangles (background). Other coloured symbols represent clusters from the literature: red open squares (thin disk), blue filled circles (thick disk), black filled squares (halo). Intermediate stellar populations are designated as magenta open circles (thin - thick disk) and cyan filled diamond (thick disk - halo).

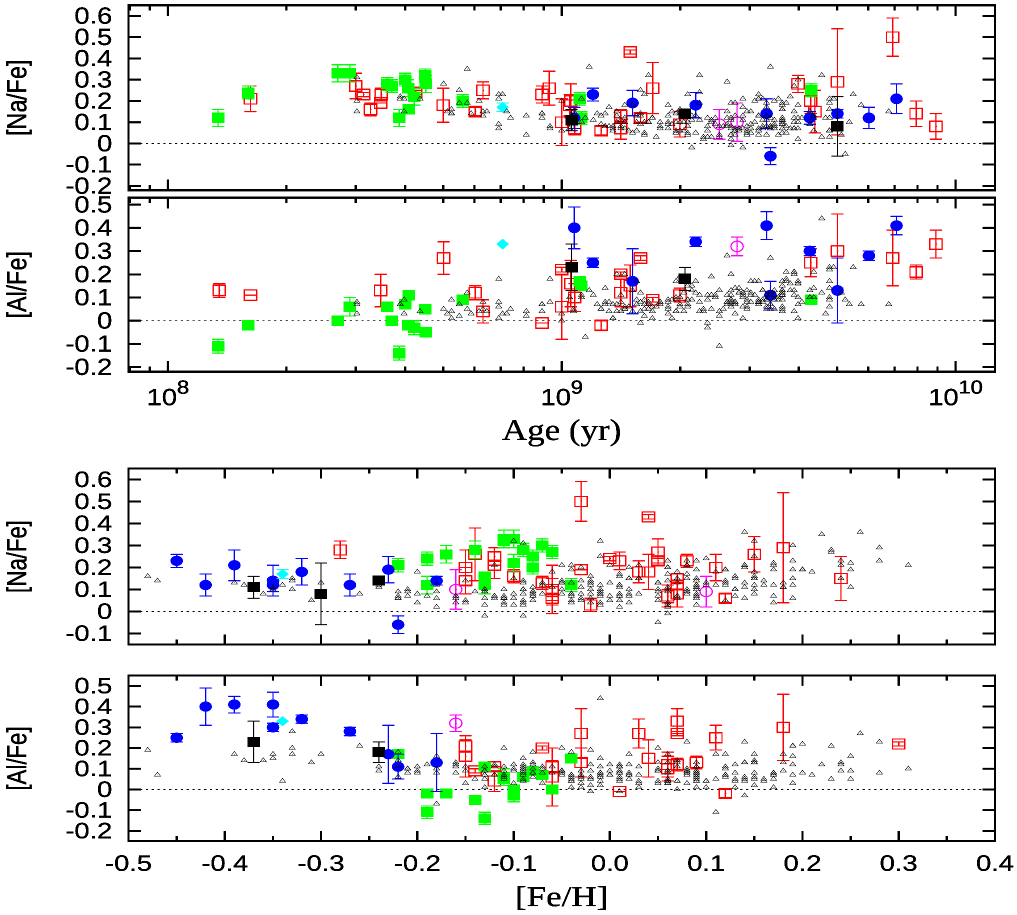

Figure 5.6: Same as figure 5.5 but for light elements [Na/Fe] and [Al/Fe]

Na and Al

The runs of abundance ratios for [Na/Fe] and [Al/Fe] against the age and [Fe/H] of OCs are shown in figure 5.6. At first glance Na abundances show no clear trend with age and metallicity for either the thin or thick disk, although the thin disk abundance is slightly higher (0.05 dex) than that of the thick disk OCs. A close inspection of [Na/Fe] vs. age plot indicates that this enrichment might have occured over the last 1 Gyr. The Al abundance follow the same type of trends shown by the α-elements. As the Mg is a sole product of type II SN whose yield is dominated by hydrostatic carbon burning, the observed behaviour of Al indicates that both the Mg and Al are produced under similar environments and have been dispersed into the interstellar medium on the same time-scales. The extremely high value of [Mg/Fe] ratio along with large [Eu/Fe] ratio for the OC NGC 2266 indicates that it has formed in the neutron rich environment where the yields from type II SNe dominate over the type Ia SNe. This result is also supported by its membership to thick disk population.

Cr, Fe and Ni

As mentioned earlier, a major fraction of iron-peak elements are mainly synthesized in Type Ia SNe with none or little contribution of other. The relative abundances, [X/Fe], for Cr, Fe and Ni over the [Fe/H] range sampled by these OCs match quite well with those of the thin disk field giants of Luck & Heiter (2007) (see figure 5.7).

Cr abundance vary tightly in lock step with age and metallicity i.e., [Cr/Fe] $\simeq 0$, with very little star-to-star scatter at a given age and [Fe/H]. No discernible trends are seen and the thin and thick disk OCs have very similar abundances which strongly emphasize the common origin for Cr and Fe. Whereas Ni and Fe below solar metallicities vary roughly in lock-step. At [Fe/H] $\gtrsim 0.1$ dex, we noticed a prominent upturn in [Ni/Fe] as is seen for Luck & Heiter's sample of field giants. We suspect that there is also a weak tendency that Ni is more abundant in thick disk OCs than that of the thin disk OCs. These results support the Bensby et al. (2005) findings of [Ni/Fe] ratios for solar neighborhood dwarfs. The increasing (decreasing) or constant behaviour of [Cr and Ni/Fe] vs. [Fe/H] in both the disk components can be due to their production (destruction) in different amounts from the progenitors of different masses (i.e., in SNe II and SNe Ia). Therefore, the observed abundance trends suggest that both the solar neighborhood field stars and the OCs giants have very similar chemical composition at any given metallicity.

Theoretical models suggest that the stellar yields of Fe-peak elements from Type Ia SN are strongly depend upon the choice of mass cut between the ejecta

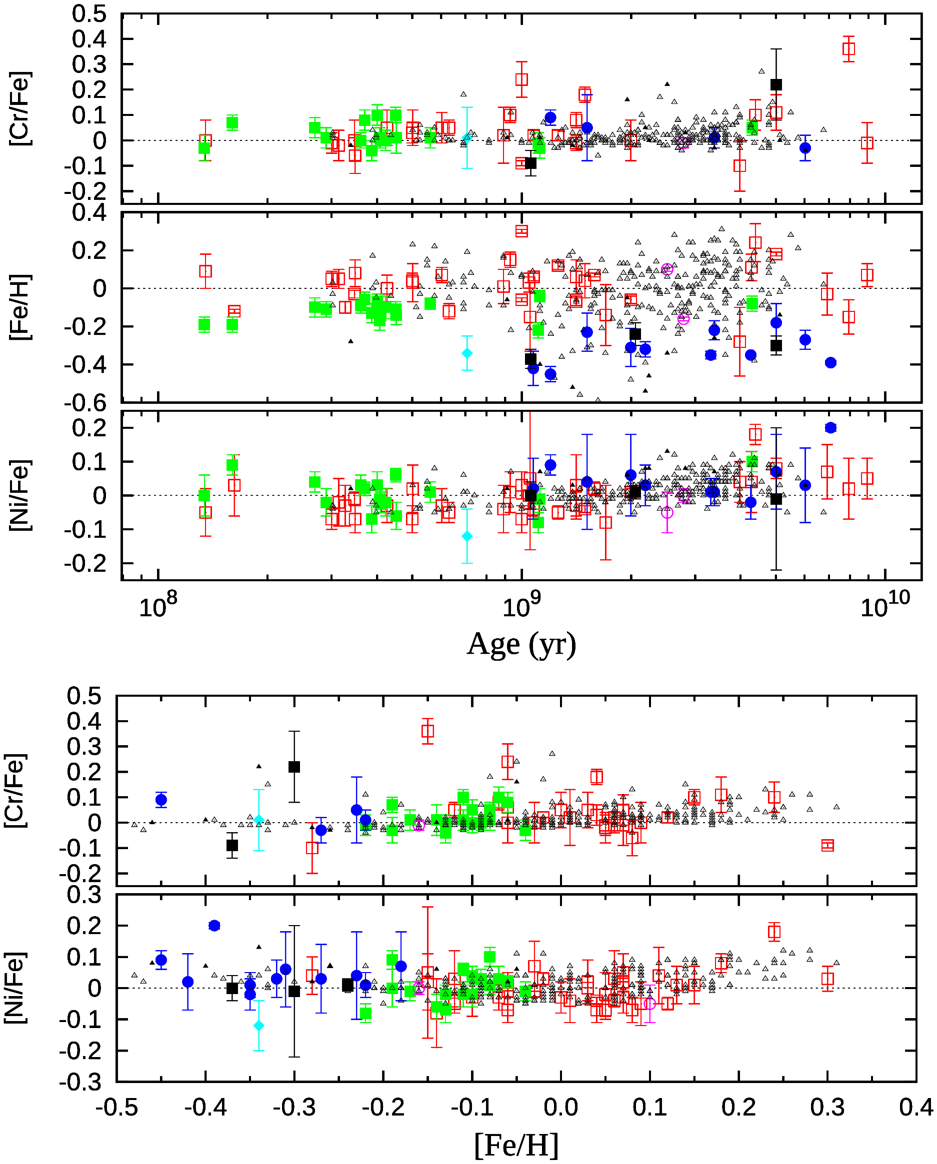

Figure 5.7: Same as figure 5.6 but for [Fe/H] and iron peak elements [Cr/Fe] and [Ni/Fe].

and the proto-neutron star, the explosion energies and the neutron fluxes but less sensitive to the metallicity. Hence, the observed Fe-peak abundance ratios may not truly represent the products of a single nuclear reaction but produced from a complex blend of different flavours of Type II and Type Ia SNe with dominant contribution from SNe Ia over SNe II. This explains why all the Fe-peak elements don't scale closely with [Fe/H] at all metallicities.

Age-metallicity relation

No clear trend of age-metallicity relation is seen for either the thin or thick disk OCs, although the average thick disk metallicity is about -0.25 dex lower than that of the thin disk OCs (see [Fe/H] vs. age in figure 5.7). This is at odds with studies of field star population which show a trend of decreasing [Fe/H] with increasing age (Bensby et al. 2005, Reddy et al. 2006). Reddy et al. (2006) found that the metallicity of the thick disk increases to about [Fe/H] ~ -0.3 (a factor of 5) in 5 Gyr and has increased only slightly since then. From figure 7 in Bensby et al. (2005) and figure 24 in Reddy et al. (2006), a keen eye may suggest that the field stars span a much wider range in metallicity ($\approx$ -1.0 to 0.3 dex) and age ($\approx$ 0 to 15 Gyr) whereas the present OC sample covers only a small range in metallicity (~ -0.5 to 0.3 dex) and age (few Myr to 9 Gyr). We emphasize that no clear trend of age-metallicity is noticeable if we restrict the field star sample to the range spanned by OCs. Thus, the lack of age-metallicity relation for our homogeneous sample of OCs is due to the fact that the metal-poor portion of the cluster sample (or, conversely, the oldest OCs) may be totally disrupted in the early epochs. This might be the reason why the previous studies of OCs (Friel et al. 2010, Yong et al. 2012) ruled out any correlation between age and [Fe/H]. The observed age-metallicity relation for field stars, although missing for OCs due to above mentioned reasons, is an indication of the progressive chemical enrichment history of the Milky Way over time, and also puts an important constraints on the theoretical models of the disk evolution.

Heavy elements

Synthesis of the elements heavier than the iron-peak group are not produced by the thermonuclear burning but via feeding the seed nuclei (Fe or Ni) with the neutrons in a sequence. If the time scale for successive neutron captures is longer (i.e. under low neutron fluxes) than the typical time scale for β-decay, the seed nuclei have enough time to acquire stability over β-decay before capturing another neutron. As this process is rather slow, the resulting elements are called slow or s-process elements where the element synthesis proceeds along the valley of β-stability resulting in the gradual build up of s-process elements and their isotopes. Our suite of s-process elements includes two light (Y and Zr) and four heavy (Ba, La, Ce and Nd) s-process elements. The s-process contribution to the solar composition are 50 % for Rb, 72 % for Y, 81 % for Zr, 85 % for Ba, 75 % for La, 81 % for Ce, and 47 % for Nd (Burris et al. 2000). High neutron fluxes feed the seed nuclei excessively, so that the nuclei decay toward the valley of β-stability after the recession of the neutron flux. Since this process is rapid, the resulting elements are called r-process elements. Our suite of r-process elements includes Sm and Eu. The r-process contribution to the solar composition are 66 % for Sm and 97 % for Eu (Burris et al. 2000).

Two types of neutron sources have been suggested for different astrophysical environments: ^{22}Ne(α,n)^{25}Mg, occuring at high temperatures and ^{13}C(α,n)^{16}O that occurs at low temperatures.

Thermally pulsating AGB stars, of mass 0.8 $M_\odot \leq M_* \leq 8\ M_\odot$, are the potential candidates for the synthesis of both the light and heavy s-process elements. The heavier neutron capture elements, Ba, La and Ce, are thought to be produced in low mass AGB stars ($0.8 \leq M_*\ /M_\odot \leq 4$) where the ^{13}C reaction acts as a neutron source when the temperature in the helium-rich intershell reaches T $\approx 3 \times 10^8$. The ^{22}Ne burns efficiently in intermediate-mass ($5 \leq M_*\ /M_\odot \leq 8$) stars, those host a temperature of T $\geq 3.5 \times 10^8$ at the helium-rich intershell region (Busso et al. 2001). But, this reaction also cause the changes in Mg isotopic ratios and hence its abundance. The lack of Mg-Al anti-correlation in the disk stellar population rules out the ^{22}Ne reaction as a neutron source for the enrichment of s-process elements in the disk. This is also confirmed by the roughly solar isotopic ratio measured for Mg in MS and S stars (Clegg, Lambert & Bell 1979, Smith & Lambert 1986). This supports the view that the ^{22}Ne reaction is not the principle neutron source for the s-process enrichment of the thin disk and the OC samples.

The evolution of s-process elements with time and metallicity for the present sample of OCs is shown in figures 5.8 - 5.10, where our homogeneous set of data is merged with the recent s-process abundances (Y, Zr, La and Ce) in OCs by Maiorca et al. (2011) and with Ba abundances from D'Orazi et al. (2009). The runs from [Y/Fe] to [Nd/Fe] does not show any systematic offset among the studies, as the sample clusters are well mixed. This is partly due to very similar methods of abundance analysis employed among the studies. i.e., both Maiorca et al and D'Orazi et al have employed LTE line analysis, same model atmosphere grids and same abundance analysis program, like ours. Moreover there is a fair agreement between the adopted reference solar values: our mean solar abundances for Y, Zr, La and Ce are differ

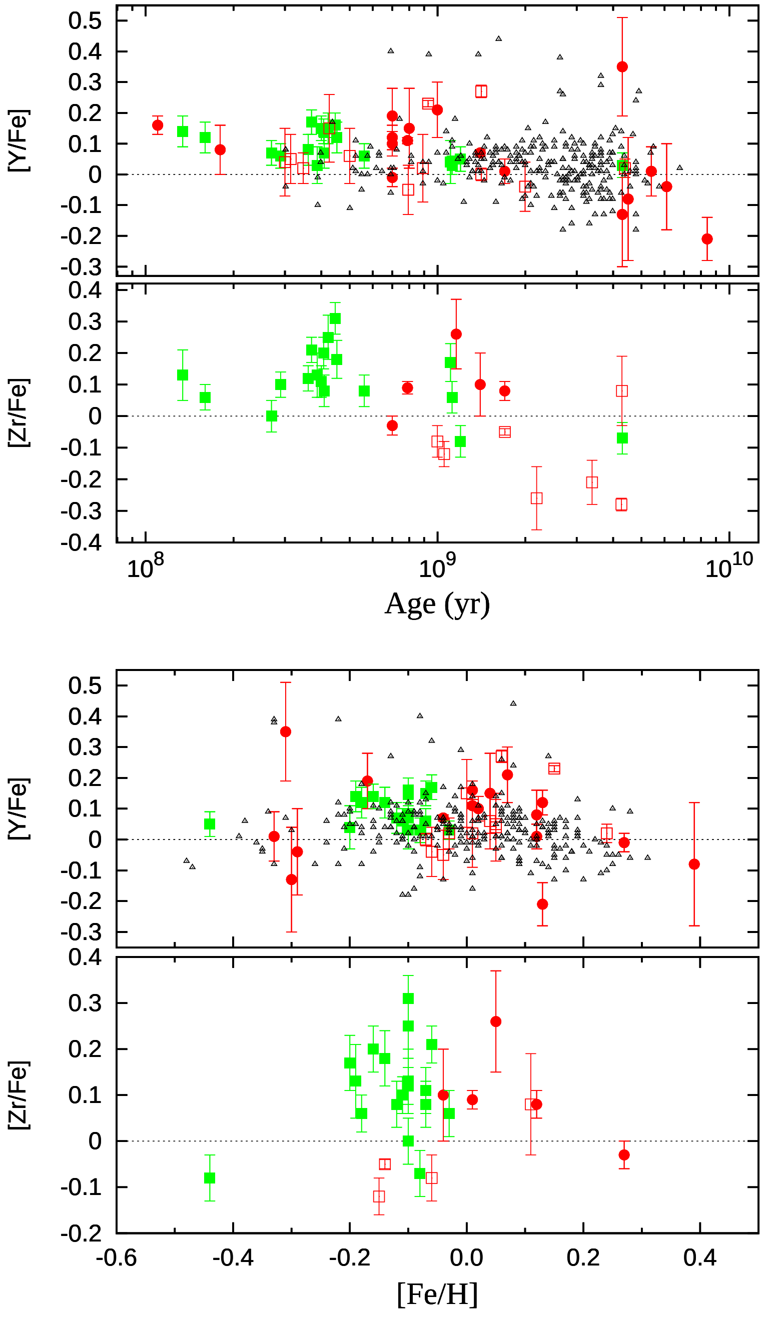

Figure 5.8: Abundance ratios vs. Age (top panel) and [X/Fe] vs. [Fe/H] (bottom panel) for light s-process elements [Y/Fe] and [Zr/Fe]. Clusters from our study (thin disk members) are presented as green filled squares, while those from the literature are marked as red open squares. The red filled circles represent OC data from Maiorca et al. (2011). Luck & Heiter's sample of field giants are marked as black open triangles (background).

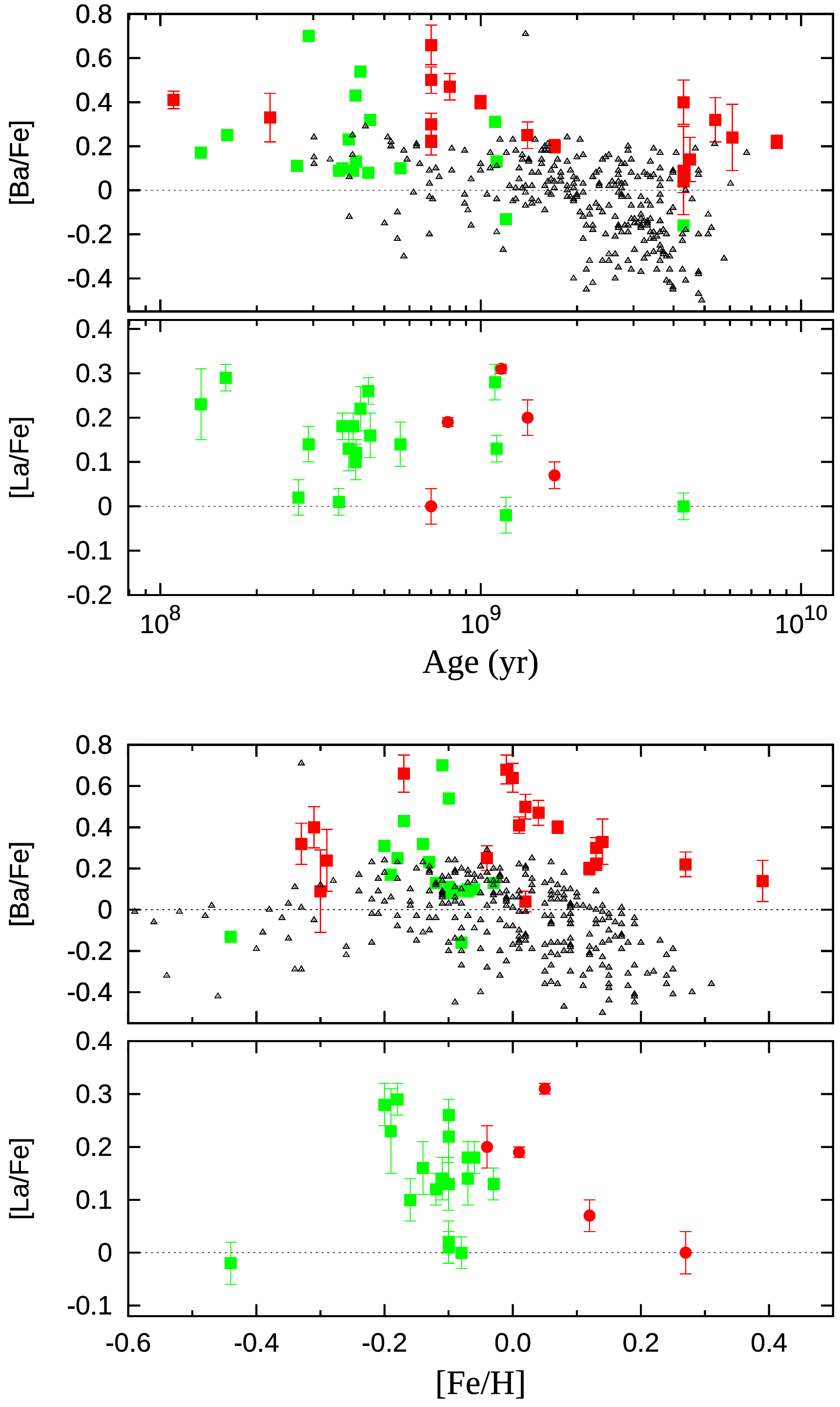

Figure 5.9: Same as figure 5.8 but for [Ba/Fe] and [La/Fe]. Here, the red filled squares denote the [Ba/Fe] values taken from D'Orazi et al. (2009).

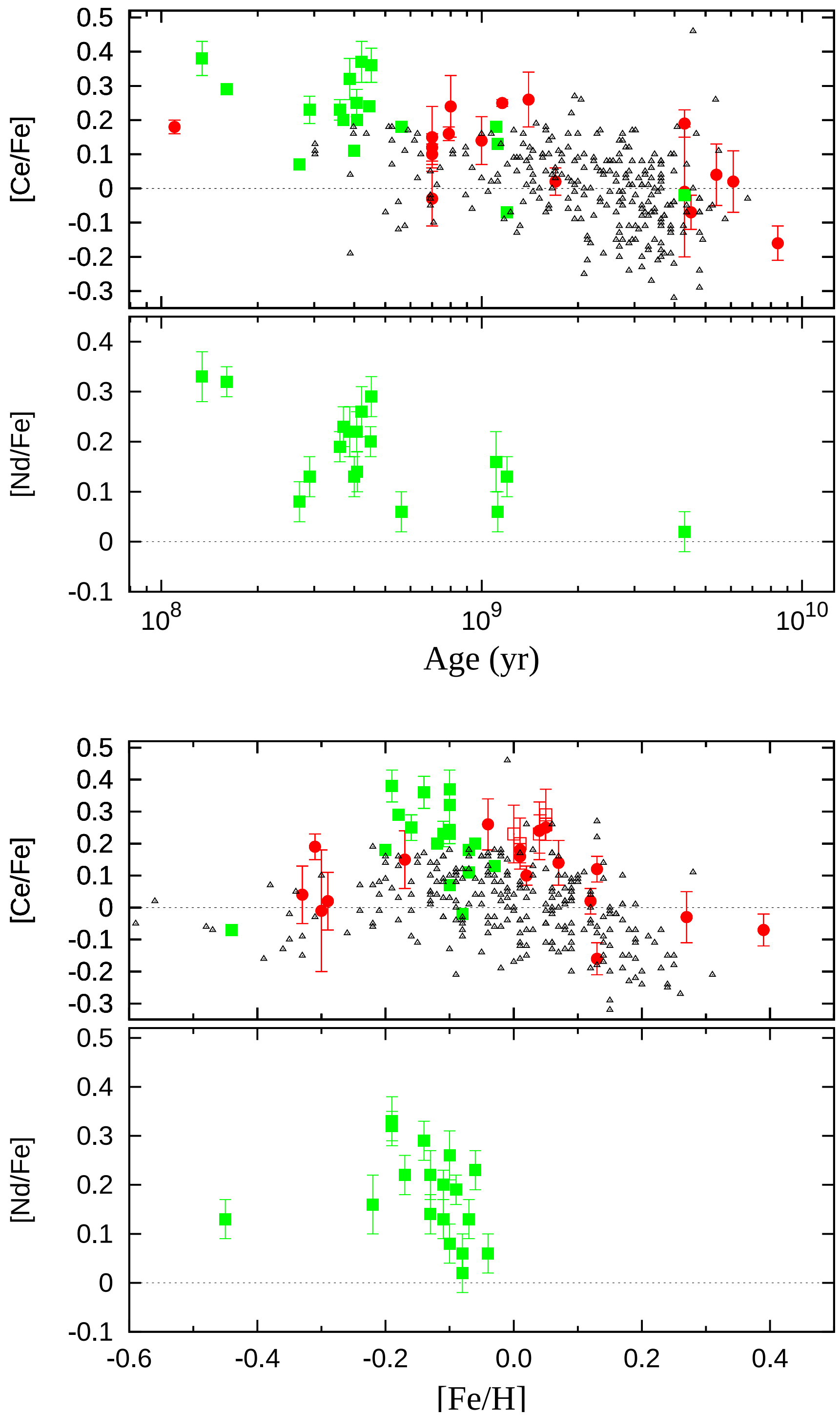

Figure 5.10: Same as figure 5.8 but for [Ce/Fe] and [Nd/Fe].

by +0.01, +0.04, +0.11 and -0.05 with Maiorca et al's values, our solar Ba abundance differ by -0.09 dex with D'Orazi et al. value. The differences seen for La and Ba are minor to wash out any abundance variations, as it involves a measurement uncertainties of about 0.05 dex in all the studies.

The figures 5.8 to 5.10 clearly shows that abundance ratios, [X/Fe], for all the six elements (Y, Zr, Ba, La, Ce and Nd) increase with decreasing cluster age where the older clusters show near solar or subsolar values. Maiorca et al have measured abundances for only Y, Zr, La and Ce, whereas we provide abundances for light s-process elements (Y, Zr) and heavy s-process elements (Ba, La, Ce and Nd). Our sample of 18 OCs along with Maiorca et al's sample increases the statistics of s-element measurements to a total of 36 clusters. The significance of our sample is that it provides a discernible evolutionary trends for Zr and La where Maiorca et al's sample suffer from low number statistics (five clusters each). Moreover, a major fraction of our sample fills the gap (age $\approx$ 0.2 - 0.7 Gyr) left by Maiorca et al's sample and define an effective trend of abundance variation with age.

Maiorca et al. (2011) demonstrated that a steep growth is seen between ages of $\approx$ 1.5 and 0.5 Gyr, after which the [X/Fe] values remain constant around a plateau value of +0.2 dex. The statistically significant sample of present OC data confirms the steep growth and a plateau but for only to light s-process elements whereas the growth continues upto 0.1 Gyr for heavy s-process elements and reaches a value close to +0.4 dex, never reaching a plateau. We notice that the common group abundance ratios (light or heavy) follow very similar runs against age, demonstrating the common site for their production. Our results based on significant number of clusters confirm and strengthen the trend of increasing [Ba/Fe] from the oldest clusters to the youngest ones, as previously obtained by D'Orazi et al. (2009). In addition, our sample contains a cluster (NGC 1912) with largest Ba abundance of [Ba/Fe] = 0.70 dex, which is not seen in field stars with known ages. This implies that the youngest OCs may be intact and the field stars do not fully sample the age distribution of OCs and, in particular, the youngest stellar generations are under-represented by field stars. It also appears that the [Ba/Fe] trend branches into two around $\approx$ 0.5 Gyr: one follows the trend suggested by Maiorca et al. (2011) and the other as noticed for D'Orazi et al. (2009) sample. This need to be investigated in our future studies by observing more young clusters. The enrichment seen in heavier s-process elements for these young OCs indicate that the Galaxy has received significant contribution from low mass AGB stars in the recent past ($\sim$ few Myr).

As a function of metallicity, all the s-process abundance ratios, except [Y/Fe] and [Nd/Fe], show a steep growth in the range ≈ -0.5 $\lesssim$ [Fe/H] $\lesssim$ -0.1 dex, after which they start declining towards higher metallicities. The [Y/Fe] ratios show a weak tendency that it increases slowly with metallicity, but [Y/Fe] ratios at given [Fe/H] are almost same for both thin and thick disk clusters. [Nd/Fe] trend looks flat, although the data suffers from low number statistics. The solar Nd abundance is produced almost in equal parts by the s- and r- process, and thus represent an evolutionary trend mixuture of both the processes. Our results support the trends seen for field star data (Luck & Heiter 2007, Bensby et al. 2005, Reddy et al. 2006). As mentioned earlier, addition of our data to Maiorca et al's sample define a prominent trend of s-process abundance variation against [Fe/H], especially for Zr and La. Together with the general trend of increasing s-process abundances in young clusters, we notice a dispersion at all metallicities, favouring the pollution from progenitors of different masses to the interstellar medium prior to the formation of these clusters.

The low mass AGB stars produce heavier s-process elements more efficiently than lighter species such as Y and Zr in more metal-poor environments ($-0.8 \leq$ [Fe/H] ≤ -0.6) (Busso et al. 1999). This is so because there are plenty of neutrons around to be absorbed with decreasing iron seed abundances. The delay in the introduction of significant s-process element yields leads to the eventual upturn in the evolutionary tracks at higher metallicities, as seen in figures 5.8 to 5.10. Therefore, the trends seen for both the light and heavy s-process abundances are consistent with enrichment by massive stars at low metallicities and a delayed contribution from low mass stars at higher metallicities.

The evolutionary trends for Sm and Eu are shown in figure 5.11. The [Sm/Fe] ratio, against the age and metallicity, behaves more like one of the s-process elements, Nd, which signifies that Sm is also produced under similar conditions as Nd (i.e. both s- and r-process sites). Europium, being a pure r-process element, behaves no differently from the α elements. It follows the similar evolutionary trend as seen for Mg i.e, a turnover at [Fe/H] ≈ -0.4 and a shallow decline towards higher metallicities, thereby indicating that both the α and r-process elements have common origin (Type II SN events).

We emphasize that both OCs and field stars have very similar chemical compositions at every epoch. Hence we conclude that OCs are the representatives of Galactic thin disk, while the s-process enrichment in OCs indicate that the field stars do not fully sample the age distribution of OCs.

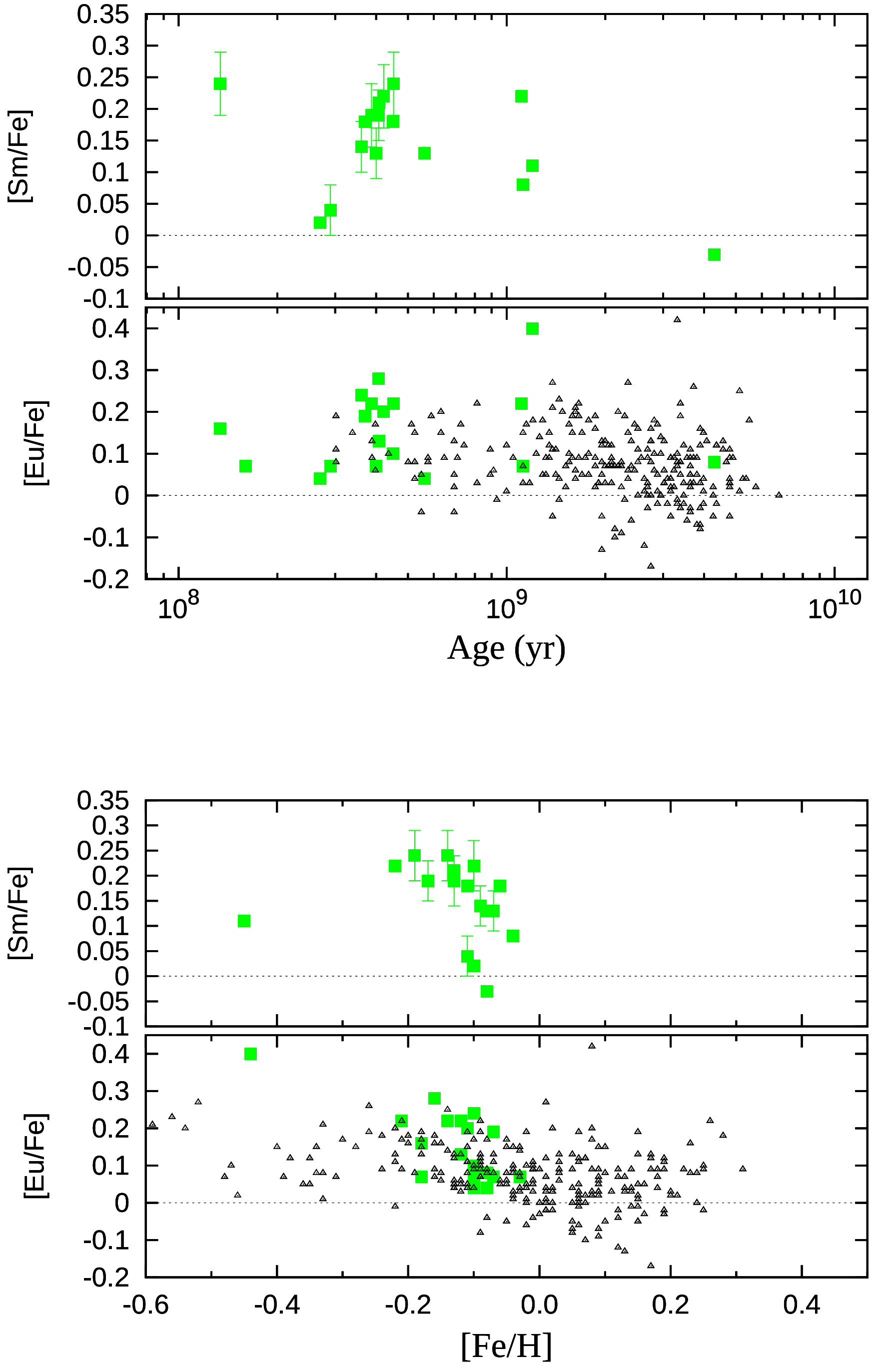

Figure 5.11: Same as figure 5.8 but for [Sm/Fe] and [Eu/Fe].

Table 5.3: The input data used in calculating the OC's space coordinates and velocity components. The full sample contains 77 OCs with the parameters extracted from DAML catalogue, while those from different sources in the literature are shown in bold numbers.

Cluster	α(2000.0) hh:mm:ss	δ(2000.0) $^\circ$ $'$ $''$	l (deg.)	b (deg.)	d$_\odot$ (kpc)	RV (km sec^{-1})	$\mu_\alpha \cos\delta$ (mas yr^{-1})	μ_δ (mas yr^{-1})	Rgc (kpc)	Age (Myr)
NGC 752	01:57:41	+37:47:06	137.125	−23.254	0.457±0.091	6.30±0.10	7.50±0.32	−11.50±0.32	8.3	1122
NGC 1817	05:12:15	+16:41:24	186.156	−13.096	1.972±0.394	66.40±0.11	1.02±1.06	−6.51±1.06	9.9	409
NGC 2360	07:17:43	−15:38:30	229.807	−1.426	1.887±0.377	29.55±0.30	−3.51±1.49	8.07±1.57	9.3	561
NGC 2506	08:00:01	−10:46:12	230.564	9.935	3.460±0.692	84.63±0.18	−2.55±0.20	0.37±0.14	10.5	1109
NGC 2266	06:43:19	+26:58:12	187.790	10.294	3.400±0.680	−29.70±0.20	−1.98±0.59	−4.32±0.59	11.3	1200
NGC 2335	07:06:49	−10:01:42	223.600	−1.183	1.417±0.283	−3.21±0.10	−0.91±1.56	−3.18±1.25	9.1	162
NGC 2482	07:55:12	−24:15:30	241.626	2.035	1.343±0.269	39.00±0.20	−4.93±0.53	1.60±0.53	8.7	402
NGC 2251	06:34:38	+08:22:00	203.58	+00.10	1.349±0.270	26.25±0.14	−0.24±0.55	−2.60±0.51	9.2	267
NGC 2527	08:04:58	−28:08:48	246.087	1.855	0.601±0.120	40.55±0.14	−4.10±0.55	6.40±0.55	8.3	446
NGC 2539	08:10:37	−12:49:06	233.705	11.111	1.363±0.273	29.20±0.14	−4.07±0.27	−1.83±0.27	8.9	371
NGC 2682	08:51:18	+11:48:00	215.696	31.896	0.908±0.182	34.83±0.10	−8.62±0.28	−6.00±0.28	8.7	4300
NGC 1342	03:31:38	+37:22:36	154.952	−15.342	0.665±0.133	−10.67±0.11	−1.15±0.87	−2.80±0.87	8.6	452
NGC 1662	04:48:27	+10:56:12	187.695	−21.114	0.437±0.087	−13.35±0.29	−1.93±0.28	−2.10±0.28	8.4	422
NGC 2447	07:44:30	−23:51:24	240.039	0.135	1.037±0.207	22.08±0.18	−4.85±0.33	4.47±0.33	8.6	387
NGC 2354	07:14:10	−25:41:24	238.368	−6.792	1.445±0.289	34.40±0.26	−2.44±0.64	−2.96±0.64	8.8	134
NGC 1912	05:28:40	+35:50:54	172.250	0.695	1.066±0.213	0.18±0.19	0.23±0.17	−5.44±0.19	9.1	290
NGC 2548	08:13:43	−05:45:00	227.873	15.393	0.770±0.154	7.70±0.18	−0.83±0.21	1.90±0.21	8.5	361
Collinder 350	17:48:06	+01:18:00	26.749	14.663	0.280±0.056	−14.35±0.15	−4.63±0.28	−0.57±0.28	7.8	407
NGC 1193	03:05:56	+44:23:00	146.812	−12.163	4.571±0.914	−88.10±0.20	1.41±0.54	−4.04±0.54	12.0	5012
NGC 1245	03:14:42	+47:14:12	146.647	−8.931	**3.000±0.300**^{2}	**−29.70±1.20**^{2}	−2.98±0.41	−3.05±0.36	10.6	1047
NGC 188	04:72:08	+85:15:18	122.843	22.384	1.700±0.340	−42.36±0.04	−1.48±1.25	−0.56±1.24	9.0	4285
Berkeley 18	05:22:12	+45:24:00	163.632	5.017	5.200±1.040	−5.50±1.10	−2.63±0.35	−5.95±0.35	13.1	4266
NGC 1883	05:25:54	+46:29:24	163.083	6.159	4.800±0.960	−30.80±0.60	−1.62±0.39	−1.23±0.39	12.7	1000
Berkeley 20	05:32:37	+00:11:18	203.483	−17.373	8.400±1.680	70.00±13.00	1.51±0.81	−4.11±0.81	15.9	6026
Berkeley 21	05:51:42	+21:47:00	186.840	−2.509	6.200±1.240	−1.00±1.00	−0.65±0.53	−6.20±0.53	14.2	2188
NGC 2099	05:52:18	+32:33:12	177.635	3.091	1.383±0.277	8.30±0.20	3.78±0.29	−7.09±0.29	9.4	347
Berkeley 22	05:58:27	+07:45:24	199.877	−8.079	6.000±1.200	95.30±0.20	**−0.40±3.87**^{4}	**−3.81±2.90**^{4}	13.8	3311
NGC 2141	06:02:55	+10:26:48	198.044	−5.811	4.033±0.807	24.10±0.30	1.38±0.38	−1.78±0.38	11.9	1702
NGC 2158	06:07:25	+24:05:48	186.634	1.781	**4.036±0.125**^{2}	26.90±1.90	1.43±0.29	−3.28±0.20	12.0	1054
NGC 2194	06:13:45	+12:48:24	197.250	−2.349	**1.903±0.120**^{2}	**7.80±0.80**^{2}	−0.31±0.64	−4.39±0.64	9.8	327
Berkeley 73	06:22:00	−06:21:00	215.278	−9.424	9.800±1.960	95.70±0.20	**+0.54±2.67**^{4}	**−2.60±2.91**^{4}	16.9	1514
NGC 2243	06:29:34	−31:17:00	239.478	−18.014	4.458±0.892	59.84±0.41	2.53±0.54	2.90±1.30	10.9	1076
Collinder 110	06:38:24	+02:01:00	120.996	8.602	2.184±0.437	**41.00±3.80**^{3}	0.59±0.39	−1.41±0.39	9.3	1412
Berkeley 25	06:41:00	−16:31:00	226.612	−9.700	11.400±2.280	134.30±0.20	**−1.27±4.13**^{4}	**−2.53±3.03**^{4}	17.8	5012
Ruprecht 4	06:48:54	−10:32:00	222.047	−5.339	4.700±0.940	47.50±1.00	**−0.33±2.34**^{4}	**+0.93±2.64**^{4}	11.9	794

Cluster	α(2000.0) hh:mm:ss	δ(2000.0) $^\circ\ '\ ''$	l (deg.)	b (deg.)	$d_\odot$ (kpc)	RV (km $\sec^{-1}$)	$\mu_\alpha \cos\delta$ (mas yr^{-1})	μ_δ (mas yr^{-1})	Rgc (kpc)	Age (Myr)
Berkeley 75	06:49:01	−23:59:48	234.307	−11.188	9.100±1.820	94.60±0.35	**−0.61±3.37**[4]	**+0.56±3.36**[4]	15.2	3981
Berkeley 29	06:53:18	+16:55:00	197.983	8.025	14.871±2.974	24.80±0.10	−0.14±0.80	−4.75±0.58	22.6	1059
Berkeley 31	06:57:36	+08:16:00	206.254	5.120	8.272±1.654	55.70±0.70	−4.30±0.52	−3.97±0.52	15.8	2056
Berkeley 32	06:58:06	+06:26:00	207.952	4.404	**3.420±0.684**[1]	105.20±0.86	−2.78±0.88	−3.21±0.88	11.1	3388
Tombaugh 2	07:03:05	−20:49:00	232.832	−6.880	6.080±1.216	120.90±0.40	**−2.89±2.65**[4]	**0.95±2.07**[4]	12.6	1995
NGC 2324	07:04:07	+01:02:42	213.447	3.297	3.800±0.760	41.81±0.22	−1.70±1.01	−2.77±1.01	11.4	631
NGC 2355	07:16:59	+13:45:00	203.390	11.803	**1.928±0.130**[2]	35.02±0.16	−2.50±0.80	−3.00±1.50	9.8	162
Saurer 1	07:20:56	+01:48:29	214.689	7.386	13.200±2.640	98.00±9.00	**+0.48±2.89**[4]	**−0.69±3.55**[4]	20.3	5012
Melotte 66	07:26:23	−47:40:00	259.559	−14.244	4.313±0.863	23.00±6.00	−4.18±0.61	7.67±1.56	9.7	2786
NGC 2423	07:37:06	−13:52:18	230.484	3.537	0.766±0.153	18.47±0.11	0.55±0.28	−2.50±0.28	8.5	736
NGC 2425	07:38:17	−14:52:42	231.504	3.297	**3.062±0.100**[2]	102.90±1.20	−3.64±0.87	−0.76±0.87	10.2	2188
NGC 2420	07:38:23	+21:34:24	198.107	19.634	2.480±0.496	73.57±0.15	−1.32±0.42	−4.18±0.26	10.3	1995
Berkeley 33	06:57:42	−13:13:00	225.424	−4.622	6500±1.300	76.60±0.50	−5.73±0.96	+3.71±0.96	13.4	800
Berkeley 39	07:46:42	−04:36:00	223.462	10.095	4.780±0.956	55.00±7.00	**−1.62±3.61**[4]	**−1.66±3.07**[4]	11.9	7943
NGC 2477	07:52:10	−38:31:48	253.563	−5.838	1.300±0.260	7.26±0.12	−0.73±0.57	1.22±0.54	8.5	603
NGC 2660	08:42:38	−47:12:00	265.929	−3.013	2.826±0.565	21.34±0.46	−5.82±0.81	7.40±0.83	8.7	1079
NGC 3114	10:02:36	−60:07:12	283.332	−3.840	0.911±0.182	−1.72±0.13	−7.54±0.21	3.50±0.21	7.8	124
IC 2602	10:42:58	−64:24:00	289.601	−4.906	0.161±0.032	10.10±0.22	−17.49±0.22	10.10±0.22	7.9	32
NGC 3532	11:05:39	−58:45:12	289.571	1.347	0.492±0.098	4.33±0.34	−10.95±0.28	4.80±0.28	7.8	300
IC 2714	11:17:27	−62:44:00	198.107	19.634	1.320±0.264	−14.10±0.30	−2.56±0.73	−3.40±0.61	9.2	348
NGC 3960	11:50:33	−55:40:24	294.367	6.183	1.850±0.370	−22.26±0.36	−7.01±0.24	−0.45±0.33	7.4	1259
IC 2391	08:40:32	−53:02:00	270.362	−06.839	0.175±0.035	14.40±0.10	−33.21±0.30	−5.97±0.30	8.0	46
NGC 4349	12:24:08	−61:52:18	299.719	0.830	2.176±0.435	−11.87±0.24	−5.77±2.22	1.44±2.17	7.2	206
Collinder 261	12:37:57	−68:22:00	301.684	−5.528	2.190±0.438	−30.00±9.00	−6.53±0.72	−1.04±0.72	7.1	8912
NGC 5822	15:04:21	−54:23:48	321.573	3.593	0.933±0.187	−29.31±0.18	−7.95±0.24	−8.20±0.24	7.3	891
NGC 6087	16:18:50	−57:56:06	327.726	−5.426	0.891±0.178	5.83±0.05	−2.35±0.34	−3.90±0.34	7.3	95
NGC 6134	16:27:46	−49:09:06	334.917	−0.198	0.913±0.183	−25.70±0.19	−0.86±0.88	−4.60±0.88	7.2	929
NGC 6192	16:40:23	−43:22:00	340.647	2.122	1.547±0.309	−7.93±0.21	3.73±0.83	3.18±1.39	6.6	135
NGC 6253	16:59:05	−52:42:30	335.460	−6.251	1.510±0.302	−29.40±1.30	**−1.55±2.27**[4]	**−4.64±2.22**[4]	6.7	5012
NGC 6281	17:04:41	−37:59:06	347.731	1.972	0.479±0.096	−5.58±0.26	−3.43±0.55	−3.60±0.55	7.5	314
IC 4651	17:24:49	−49:56:00	340.088	−7.907	0.888±0.178	−30.80±0.20	−1.07±0.50	−2.20±0.50	7.2	1140
NGC 6404	17:39:37	−33:14:48	355.659	−1.177	2.400±0.480	10.60±1.10	**−0.67±2.93**[4]	**−0.55±3.83**[4]	5.6	501
NGC 6583	18:15:49	−22:08:12	9.283	−2.534	2.040±0.408	3.00±0.40	**+0.32±3.54**[4]	**−1.44±3.57**[4]	6.0	1000
NGC 6633	18:27:15	+06:30:30	36.011	8.328	0.376±0.075	−28.95±0.09	−0.21±0.31	−1.60±0.31	7.7	426
IC 4725	18:31:47	−19:07:00	13.702	−4.434	0.620±0.124	2.40±0.20	−4.01±0.40	−5.70±0.40	7.4	92
IC 4756	18:39:00	+05:27:00	36.381	5.242	0.484±0.097	−25.80±0.60	−0.14±0.23	−3.40±0.23	7.6	500
NGC 6791	19:20:53	+37:46:18	69.959	10.904	5.853±1.171	−47.10±0.70	−0.57±0.13	−2.45±0.12	8.2	4395
NGC 6819	19:41:18	+40:11:12	73.978	8.481	2.360±0.472	2.34±0.05	−3.14±1.01	−3.34±1.01	7.7	1493

Cluster	α(2000.0) hh:mm:ss	δ(2000.0) $^{\circ}\ '\ ''$	l (deg.)	b (deg.)	d$_{\odot}$ (kpc)	RV (km sec^{-1})	$\mu_{\alpha}\cos\delta$ (mas yr^{-1})	μ_{δ} (mas yr^{-1})	Rgc (kpc)	Age (Myr)
NGC 6939	20:31:30	+60:39:42	95.903	12.305	1.800±0.360	−42.00±10.00	0.86±0.46	−2.16±0.53	8.4	1585
NGC 7142	21:45:09	+65:46:30	105.347	9.485	2.344±0.469	−50.30±0.30	1.06±0.51	−4.43±0.34	8.9	6918
NGC 7160	21:53:40	+62:36:12	104.012	6.457	0.789±0.158	−26.28±3.88	−1.57±0.51	−1.60±0.51	8.2	19
NGC 7789	23:57:24	+56:42:30	115.532	−5.385	1.795±0.359	−54.70±1.30	4.08±0.72	0.21±0.68	8.9	1412

Source: 1) Friel et al. (2010), 2) Jacobson et al. (2011), 3) Pancino et al. (2010) and 4) extracted from UCAC4 Catalogue by Zacharias et al. (2013).

Table 5.4: The present positions and space velocity components of 77 OCs in our study, as calculated for use in the orbit code, along with their membership probabilities.

Cluster	x (kpc)	y (kpc)	z (kpc)	U$_{\mathrm{GSR}}$ (km sec^{-1})	V$_{\mathrm{GSR}}$ (km sec^{-1})	W$_{\mathrm{GSR}}$ (km sec^{-1})	probability percent
Thin disk							
NGC 752	-8.308±0.062	0.285±0.057	-0.180±0.036	-4.0± 2.0	207.3± 4.4	-13.0± 3.6	98.9± 0.2
NGC 1817	-9.909±0.382	-0.208±0.042	-0.447±0.089	-42.5± 3.4	163.0±14.7	-32.6±10.9	77.8±22.0
NGC 2360	-9.215±0.243	-1.443±0.289	-0.047±0.009	-69.2±16.1	252.7±13.4	13.2±13.6	97.5± 1.8
NGC 2506	-10.161±0.432	-2.636±0.527	0.597±0.119	-66.8± 5.3	172.6± 2.9	-9.8± 7.1	93.9± 1.5
NGC 2335	-9.024±0.205	-0.979±0.196	-0.029±0.006	23.6± 6.6	216.0± 6.8	-8.1±10.5	99.1± 0.2
NGC 2482	-8.636±0.127	-1.182±0.236	0.048±0.010	-30.9± 5.4	201.8± 2.7	-12.5± 5.4	98.6± 0.3
NGC 2251	-9.236±0.247	-0.541±0.108	0.002±0.000	-8.4± 1.8	201.7± 4.0	-1.5± 3.9	99.1± 0.1
NGC 2527	-8.243±0.049	-0.550±0.110	0.019±0.004	-26.0± 4.2	196.7± 1.8	8.8± 1.6	98.7± 0.1
NGC 2539	-8.790±0.158	-1.079±0.216	0.263±0.053	-13.2± 1.9	199.6± 1.2	-14.9± 5.9	98.6± 0.4
NGC 2682	-8.625±0.125	-0.451±0.090	0.480±0.096	-28.5± 3.1	187.5± 4.2	-11.7± 7.6	98.0± 0.6
NGC 1342	-8.581±0.116	0.271±0.054	-0.176±0.035	20.5±1.3	217.8±2.6	1.0±3.2	99.2±0.0
NGC 1662	-8.404±0.081	-0.055±0.011	-0.157±0.031	24.6±0.6	226.0±0.6	6.5±1.2	99.2±0.0
NGC 2447	-8.516±0.103	-0.899±0.180	0.002±0.000	-27.9±5.6	221.2±3.2	-2.0±2.5	99.2±0.0
NGC 2354	-8.750±0.150	-1.223±0.245	-0.171±0.034	2.4±4.3	192.9±2.4	-20.6±6.5	97.8±0.8
NGC 1912	-9.056±0.211	0.142±0.028	0.013±0.003	6.5±0.7	201.9±4.8	-7.0±3.0	99.0±0.1
NGC 2548	-8.497±0.099	-0.551±0.110	0.204±0.041	-0.4±1.2	224.8±1.2	10.2±0.8	99.2±0.0
Collinder 350	-7.758±0.048	0.122±0.024	0.071±0.014	-1.9±0.3	215.1±0.8	8.7±1.0	99.2±0.0
NGC 1245	-10.477±0.495	1.627±0.325	-0.466±0.093	48.9± 4.4	215.2± 4.9	-47.1±12.9	78.4±29.7
NGC 188	-8.854±0.171	1.320±0.264	0.648±0.130	40.4± 8.9	200.4± 6.6	-13.2± 9.3	97.4± 0.6
NGC 2099	-9.380±0.276	0.055±0.011	0.075±0.015	-0.3± 0.5	172.9±10.7	5.6± 1.9	97.2± 1.2
NGC 2141	-11.813±0.763	-1.248±0.250	-0.408±0.082	0.1± 3.5	177.0±10.7	11.5± 7.3	97.4± 1.2
NGC 2158	-12.006±0.801	-0.471±0.094	0.125±0.025	-8.7± 2.6	154.3±14.2	1.8± 5.4	92.6± 5.7
NGC 2194	-9.815±0.363	-0.566±0.113	-0.078±0.016	13.3± 2.9	191.2± 8.4	-14.4± 7.2	98.2± 0.6
Collinder 110	-9.114±0.223	1.850±0.370	0.327±0.065	-17.6± 4.2	191.1± 4.8	4.9± 4.0	98.6± 0.2
NGC 2355	-9.731±0.346	-0.752±0.150	0.395±0.079	-21.7± 4.6	195.0±12.5	-16.9±10.7	98.2± 1.1

Cluster	x (kpc)	y (kpc)	z (kpc)	U_{GSR} (km sec^{-1})	V_{GSR} (km sec^{-1})	W_{GSR} (km sec^{-1})	probability percent
NGC 2423	-8.486±0.097	-0.591±0.118	0.047±0.009	5.1± 1.6	205.2± 1.3	5.8± 1.2	99.1± 0.0
NGC 2420	-10.219±0.444	-0.729±0.146	0.834±0.167	-53.8± 2.2	162.2± 8.8	1.6± 7.6	92.9± 3.0
NGC 2477	-8.364±0.073	-1.241±0.248	-0.132±0.026	-0.4± 3.7	220.7± 1.1	6.5± 3.4	99.2± 0.0
NGC 2660	-8.195±0.039	-2.815±0.563	-0.149±0.030	-117.2±27.5	212.1± 1.9	7.0±10.9	92.9± 6.9
NGC 2324	-11.162±0.632	-2.096±0.419	0.219±0.044	-10.6±10.6	175.0±16.1	-40.0±20.7	79.8±40.1
NGC 3114	-7.789±0.042	-0.884±0.177	-0.061±0.012	-24.7± 6.9	219.0± 1.6	0.3± 1.7	99.2± 0.0
IC 2602	-7.946±0.011	-0.151±0.030	-0.014±0.003	-1.0± 2.9	210.4± 1.1	6.9± 0.2	99.1± 0.0
NGC 3532	-7.834±0.033	-0.463±0.093	0.012±0.002	-14.7± 5.3	211.6± 1.9	7.8± 0.7	99.1± 0.0
IC 2714	-9.181±0.236	-0.388±0.078	0.444±0.089	-2.9± 4.4	236.0± 1.8	-17.8± 6.4	98.9± 0.4
NGC 3960	-7.238±0.152	-1.674±0.335	0.199±0.040	-52.1±10.7	218.8± 5.4	-12.6± 4.5	98.6± 0.3
NGC 1883	-11.711±0.742	1.124±0.225	0.419±0.084	34.4±2.5	215.2± 6.9	-33.9± 10.3	95.5±4.3
NGC 4349	-6.917±0.217	-1.887±0.377	0.032±0.006	-48.5±22.4	205.1±13.0	16.2±22.5	98.1± 2.0
NGC 261	-6.851±0.230	-1.852±0.370	-0.211±0.042	-63.6±14.0	216.0±11.0	-3.3± 8.0	98.6± 0.4
NGC 5822	-7.269±0.146	-0.577±0.115	0.058±0.012	-42.3± 5.9	204.5± 7.8	-8.4± 3.0	98.7± 0.2
NGC 6087	-7.249±0.150	-0.472±0.094	-0.084±0.017	4.6± 2.2	206.5± 3.4	2.0± 1.7	99.1± 0.0
NGC 6134	-7.172±0.166	-0.385±0.077	-0.003±0.001	-20.6± 2.2	220.6± 4.6	-3.5± 4.4	99.2± 0.0
NGC 6192	-6.540±0.292	-0.509±0.102	0.057±0.011	14.2± 3.6	261.4±10.6	1.8± 8.2	98.8± 0.5
NGC 6281	-7.532±0.094	-0.101±0.020	0.016±0.003	2.2± 0.6	215.4± 2.5	8.4± 1.3	99.2± 0.0
IC 4651	-7.172±0.166	-0.298±0.060	-0.122±0.024	-22.3± 1.1	225.8± 2.8	10.5± 2.1	99.1± 0.1
IC 2391	-7.999±0.000	-0.174±0.035	-0.021±0.004	-2.8± 2.6	213.7± 0.6	-19.1±4.9	99.2± 0.0
NGC 6633	-7.699±0.060	0.219±0.044	0.054±0.011	-11.4± 0.5	206.1± 0.6	2.4± 0.6	99.1± 0.0
IC 4725	-7.399±0.120	0.146±0.029	-0.048±0.010	17.5± 1.1	206.2± 4.1	9.8± 1.3	99.0± 0.1
IC 4756	-7.612±0.078	0.286±0.057	0.044±0.009	-6.2± 1.1	204.3± 1.2	1.9± 0.8	99.1± 0.0
NGC 6404	-5.607±0.479	-0.176±0.035	-0.049±0.010	20.0± 3.5	215.1±40.9	10.0±36.5	99.1±1.0
NGC 6583	-5.989±0.402	0.329±0.066	-0.090±0.018	14.2± 6.1	215.0±34.0	-2.3±34.3	99.2±0.2
NGC 6791	-6.650±0.270	3.707±0.741	0.760±0.152	38.9± 9.2	167.8± 3.0	-12.4± 3.3	91.8± 2.4
NGC 6819	-7.357±0.129	2.244±0.449	0.348±0.070	58.0±14.4	212.3± 4.6	19.9±11.5	97.7± 1.6
NGC 6939	-8.182±0.036	1.749±0.350	0.384±0.077	24.8± 4.9	189.1± 9.8	-17.9± 5.6	97.6± 0.9
NGC 7160	-8.190±0.038	0.761±0.152	0.089±0.018	24.5± 2.6	202.1± 3.8	3.1± 2.0	99.0± 0.1
NGC 7789	-8.772±0.154	1.612±0.322	-0.169±0.034	3.2± 8.3	160.7± 4.3	7.1± 5.9	94.6± 1.3
NGC 6253	-6.633±0.273	-0.620±0.124	-0.164±0.033	-31.4±7.5	207.5±15.8	-0.6±16.2	99.0± 0.2
Ruprecht 4	-11.470±0.694	-3.140±0.628	-0.437±0.087	-39.8±39.3	209.2±42.4	6.1±53.4	98.9±1.2
NGC 7142	-8.614±0.123	2.229±0.446	0.386±0.077	43.3±6.3	190.8± 3.0	-45.7±10.0	73.4±25.9
Berkeley 39	-11.411±0.682	-3.242±0.648	0.838±0.168	-26.4± 52.8	169.2± 52.0	-31.8± 78.4	86.3±89.9
Berkeley 75	-13.196±1.039	-7.259±1.452	-1.766±0.353	-69.4±119.3	170.7±87.1	-23.7±142.8	87.2±120.9
Thin-Thick disk							
Melotte 66	-8.750±0.150	-4.112±0.822	-1.062±0.212	-169.0±45.7	237.2± 9.8	-7.9±17.4	56.4±61.9 (Thin) 42.7±59.6 (Thick)
NGC 2425	-9.899±0.380	-2.396±0.479	0.176±0.035	-68.5±10.4	152.0± 8.0	-37.3±16.2	40.6±44.3 (Thin) 58.9±43.8 (Thick)

Cluster	x (kpc)	y (kpc)	z (kpc)	$U_{\rm GSR}$ (km sec^{-1})	$V_{\rm GSR}$ (km sec^{-1})	$W_{\rm GSR}$ (km sec^{-1})	probability percent
Thick disk							
NGC 2266	-11.314±0.663	-0.458±0.092	0.608±0.122	34.8± 2.4	179.0±13.8	-56.0±14.8	69.6±51.2
Tombaugh 2	-11.639±0.728	-4.816±0.963	-0.729±0.146	-107.6±50.9	171.9±40.8	-67.8±73.8	97.4±5.9
Berkeley 73	-15.884±1.577	-5.595±1.119	-1.605±0.321	6.5±81.4	76.2±109.6	-39.3±125.0	93.8±28.6
Berkeley 32	-11.010±0.602	-1.603±0.321	0.263±0.053	-74.9± 7.1	150.1±13.6	-47.2±19.1	85.7±31.2
NGC 1193	-11.742±0.748	2.442±0.488	-0.963±0.193	54.3± 8.7	112.3±16.5	-33.4±16.4	93.9± 8.2
Berkeley 22	-13.584±1.117	-2.028±0.406	-0.844±0.169	-39.0±32.6	109.0±89.9	-69.3±107.5	96.0±16.4
Berkeley 18	-12.972±0.994	1.454±0.291	0.455±0.091	-21.1± 7.8	145.3±17.7	-128.5±28.4	85.8±19.6
NGC 2243	-10.147±0.429	-3.655±0.731	-1.379±0.276	-61.8±25.2	175.7±11.3	58.1±19.7	84.7±41.7
Berkeley 20	-15.348±1.470	-3.205±0.641	-2.509±0.502	25.1±24.6	43.5±43.2	-38.0±31.5	75.2±43.1
Berkeley 21	-14.149±1.230	-0.746±0.149	-0.272±0.054	33.0± 4.9	79.8±33.0	-101.9±26.8	71.1±37.0
Saurer 1	-18.752±2.150	-7.466±1.493	1.698±0.340	-38.6±121.3	127.4±178.6	27.5±188.5	70.0±430.0
Thick disk-halo							
Berkeley 33	-12.540±0.908	-4.622±0.924	-0.524±0.105	-142.3±20.2	358.4±42.4	-88.5±36.2	56.4±55.7 (Thick)
43.6±55.7 (Halo)							
halo							
Berkeley 29	-22.000±2.800	-4.566±0.913	2.077±0.415	57.7±22.6	-71.2±71.1	-143.6±61.5	100.0± 0.0
Berkeley 31	-15.384±1.477	-3.655±0.731	0.739±0.148	-31.2± 9.5	134.6±22.5	-207.0±48.4	98.5± 6.6
Berkeley 25	-15.706±1.541	-8.178±1.636	-1.922±0.384	0.5±126.6	79.2±129.4	-134.3±211.7	66.4±297.4

Table 5.5: Elemental abundance ratios [X/Fe] for elements Na, Al, Mg, Si, Ca, Ti, Cr and Ni for the literature sample.

Cluster	[Na/Fe]	[Mg/Fe]	[Al/Fe]	[Si/Fe]	[Ca/Fe]	[Ti/Fe]	[Cr/Fe]	[Fe/H]	[Ni/Fe]
Thin disk									
NGC 6404	...	0.08±0.07	0.27±0.07	0.18±0.10	-0.11±0.10	-0.07±0.07	0.05±0.07	0.03±0.10	0.02±0.07
NGC 6583	...	0.03±0.01	0.22±0.01	0.01±0.13	0.01±0.00	-0.04±0.02	-0.09±0.01	0.30±0.01	0.03±0.04
NGC 3960	0.06±0.02	-0.06±0.04	-0.02±0.02	0.02±0.02	0.03±0.03	0.01±0.03	0.02±0.02	0.12±0.02	-0.05±0.02
Collinder 261	0.08±0.06	0.17±0.07	0.33±0.06	0.24±0.05	-0.01±0.06	-0.02±0.09	-0.01±0.08	0.07±0.06	0.05±0.06
NGC 6192	...	0.04±0.03	0.13±0.03	0.11±0.07	0.01±0.05	0.03±0.09	0.00±0.08	0.09±0.09	-0.05±0.07
IC 4756	0.18±0.08	0.00±0.03	...	0.00±0.06	0.04±0.06	-0.07±0.05	0.03±0.04	0.04±0.04	-0.07±0.04
NGC 3532	0.27±0.06	0.02±0.01	...	0.02±0.05	0.08±0.05	-0.07±0.05	-0.01±0.04	0.05±0.04	-0.07±0.03
NGC 6281	0.23±0.01	0.05±0.02	...	0.07±0.02	0.10±0.05	-0.07±0.04	-0.02±0.06	0.05±0.05	-0.02±0.07
NGC 6633	0.24±0.01	0.05±0.00	...	0.06±0.03	0.01±0.06	-0.07±0.08	0.05±0.07	0.00±0.07	-0.03±0.05
IC 2602	0.06±0.01	...	...	0.06±0.04	0.08±0.06	0.04±0.00	0.06±0.00	-0.06±0.05	-0.01±0.06
IC 2391	0.03±0.03	...	...	0.04±0.02	0.07±0.03	0.10±0.06	0.02±0.00	-0.02±0.03	0.03±0.02
NGC 7160	-0.20±0.08	...	...	0.07±0.09	-0.02±0.09	...	...	0.13±0.06	0.01±0.06
NGC 5822	0.23±0.04	...	-0.01±0.00	0.07±0.01	0.03±0.08	-0.02±0.13	0.02±0.11	0.01±0.09	-0.04±0.07
NGC 6134	0.26±0.08	-0.03±0.05	...	0.02±0.02	0.04±0.09	0.04±0.02	0.10±0.03	0.15±0.04	0.01±0.06
NGC 6253	0.29±0.25	-0.05±0.12	0.30±0.16	0.23±0.08	-0.02±0.02	0.07±0.08	0.11±0.07	0.18±0.01	0.08±0.03
NGC 6791	0.15±0.10	...	...	0.23±0.05	0.11±0.12	0.26±0.08	0.10±0.06	0.24±0.10	0.18±0.03
NGC 6819	0.43±0.01	-0.01±0.01	0.15±0.09	0.18±0.09	0.19±0.08	0.07±0.03	0.18±0.03	0.04±0.09	-0.04±0.01
NGC 2660	0.07±0.03	0.00±0.03	0.10±0.06	0.03±0.01	0.02±0.04	0.07±0.02	0.02±0.02	0.06±0.02	-0.04±0.02
NGC 188	0.20±0.06	0.25±0.04	0.25±0.06	0.24±0.04	0.02±0.02	0.07±0.06	...	0.11±0.07	0.04±0.09
NGC 2477	0.15±0.02	-0.04±0.03	0.12±0.03	0.11±0.04	0.05±0.03	0.01±0.06	0.05±0.06	0.07±0.04	-0.03±0.05
NGC 6939	0.12±0.02	...	0.27±0.01	0.10±0.04	0.16±0.03	...	...	0.07±0.01	0.02±0.02
Collinder 110	0.13±0.03	0.04±0.01	0.20±0.01	0.05±0.03	0.03±0.02	0.08±0.03	0.08±0.03	-0.07±0.02	-0.03±0.04
NGC 2099	0.19±0.00	-0.10±0.08	0.13±0.07	0.02±0.00	0.00±0.02	-0.02±0.04	0.00±0.08	-0.03±0.02	-0.01±0.02
NGC 2420	0.09±0.06	-0.11±0.04	0.11±0.03	-0.02±0.04	0.02±0.01	0.12±0.08	0.00±0.08	-0.06±0.02	0.01±0.01
IC 2714	0.23±0.03	0.04±0.02	...	0.22±0.08	0.07±0.05	0.01±0.03	-0.06±0.07	0.08±0.07	-0.07±0.04
NGC 7789	0.07±0.05	-0.09±0.03	0.12±0.06	-0.12±0.03	-0.05±0.03	-0.04±0.04	-0.01±0.03	0.06±0.09	0.03±0.09
NGC 1245	0.18±0.05	0.16±0.06	...	0.10±0.04	0.09±0.04	...	...	0.03±0.05	0.00±0.04
NGC 2194	0.16±0.03	0.11±0.08	...	0.12±0.02	0.01±0.06	...	...	-0.10±0.03	-0.03±0.06
NGC 2355	0.21±0.06	0.27±0.03	0.11±0.00	0.19±0.04	0.23±0.10	...	...	-0.12±0.01	0.03±0.09
NGC 7142	0.50±0.09	...	0.27±0.12	0.26±0.04	0.20±0.06	...	...	-0.03±0.11	0.07±0.08
NGC 2324	0.25±0.04	0.15±0.04	0.04±0.05	0.08±0.05	0.11±0.07	0.02±0.09	0.05±0.03	-0.12±0.04	-0.05±0.03
NGC 2141	0.26±0.12	0.08±0.10	0.09±0.01	0.20±0.16	0.09±0.15	0.07±0.10	...	-0.14±0.16	-0.08±0.11
NGC 2158	0.20±0.08	0.09±0.11	0.16±0.10	0.20±0.22	0.29±0.08	0.05±0.08	...	-0.15±0.18	0.05±0.21
Berkeley 75	0.28±0.04	...	...	...	0.16±0.06	0.11±0.11	-0.10±0.10	-0.28±0.18	0.04±0.06
Berkeley 39	0.14±0.06	0.12±0.06	0.21±0.03	0.20±0.04	0.04±0.07	0.13±0.02	0.36±0.05	-0.15±0.09	0.02±0.09
NGC 1883	0.10±0.11	0.05±0.05	0.06±0.14	0.16±0.02	-0.01±0.03	0.01±0.02	0.24±0.07	-0.06±0.01	-0.07±0.04
Ruprecht 4	0.10±0.01	-0.04±0.00	0.13±0.00	-0.01±0.08	0.11±0.11	0.02±0.06	0.00±0.13	-0.04±0.05	-0.09±0.08

Cluster	[Na/Fe]	[Mg/Fe]	[Al/Fe]	[Si/Fe]	[Ca/Fe]	[Ti/Fe]	[Cr/Fe]	[Fe/H]	[Ni/Fe]
					Thin - Thick disk				
Melotte 66	0.10±0.09	0.12±0.03	0.32±0.04	0.20±0.02	0.07±0.02	0.02±0.02	-0.01±0.02	-0.16±0.01	0.00±0.02
NGC 2425	0.09±0.07	-0.03±0.07	...	0.02±0.07	0.18±0.03	...	...	0.10±0.01	-0.05±0.06
					Thick disk				
NGC 2266	0.23±0.03	0.39±0.02	0.25±0.02	0.28±0.02	0.17±0.05	0.23±0.04	0.09±0.03	-0.45±0.04	0.09±0.03
Tombaugh 2	...	...	...	...	0.20±0.11	...	...	-0.31±0.10	0.06±0.12
Berkeley 73	0.19±0.06	0.00±0.00	0.17±0.14	0.14±0.07	-0.07±0.07	0.03±0.07	0.05±0.13	-0.23±0.10	0.04±0.14
Berkeley 32	-0.06±0.04	0.13±0.05	0.11±0.06	0.10±0.04	0.07±0.06	0.07±0.05	0.01±0.04	-0.22±0.05	0.01±0.04
NGC 1193	0.14±0.02	0.25±0.12	0.13±0.14	0.17±0.07	0.03±0.12	...	...	-0.18±0.10	0.07±0.11
Berkeley 22	0.14±0.07	0.12±0.05	0.41±0.06	0.16±0.09	-0.02±0.03	0.17±0.07	...	-0.35±0.02	0.01±0.04
Berkeley 18	0.12±0.03	0.20±0.06	0.30±0.02	0.11±0.02	0.07±0.02	0.12±0.00	...	-0.35±0.00	-0.02±0.05
NGC 2243	0.12±0.05	0.22±0.04	0.40±0.09	0.19±0.11	0.13±0.03	...	...	-0.42±0.09	0.02±0.09
Berkeley 20	0.12±0.05	0.26±0.03	0.28±0.02	0.12±0.10	0.05±0.07	-0.01±0.09	-0.03±0.05	-0.27±0.05	0.03±0.11
Berkeley 21	0.18±0.06	0.10±0.08	0.34±0.02	0.18±0.03	0.05±0.10	0.05±0.09	...	-0.32±0.04	0.03±0.06
Saurer 1	0.21±0.07	...	0.41±0.04	0.26±0.01	0.25±0.04	0.25±0.05	...	-0.39±0.01	0.20±0.01
					Thick disk - Halo				
Berkeley 33	0.17±0.02	-0.12±0.10	0.33±0.00	0.10±0.06	0.12±0.13	-0.10±0.09	0.01±0.12	-0.34±0.09	-0.12±0.08
					Halo				
Berkeley 25	0.08±0.14	0.10±0.00	...	0.22±0.17	0.05±0.10	0.20±0.13	0.22±0.14	-0.30±0.05	-0.01±0.21
Berkeley 29	0.11±0.05	0.18±0.03	0.23±0.10	0.11±0.06	0.06±0.04	0.10±0.12	-0.09±0.05	-0.37±0.05	0.00±0.04
Berkeley 31	0.14±0.02	0.11±0.03	0.18±0.05	0.16±0.09	0.08±0.03	-0.01±0.05	...	-0.24±0.06	0.01±0.02

Table 5.6: Elemental abundance ratios [X/Fe] for elements Y, Zr and Ce for the literature sample.

Cluster	[Y/Fe]	[Zr/Fe]	[Ce/Fe]	Cluster	[Y/Fe]	[Zr/Fe]	[Ce/Fe]
Thin disk							
IC 4756	0.06±0.09	...	0.23±0.06	**Thick disk**			
NGC 3532	0.04±0.11	...	0.29±0.08	Berkeley 32	...	-0.21±0.07	...
NGC 6281	0.05±0.08	...	0.26±0.02	Berkeley 22	...	-0.44±0.01	...
NGC 6633	0.15±0.11	...	0.23±0.09	Berkeley 18	...	-0.28±0.02	...
NGC 5822	0.02±0.11	...	0.20±0.08	Berkeley 21	...	-0.26±0.10	...
NGC 6134	0.23±0.01	...	...	**Thick disk - Halo**			
NGC 6791	0.02±0.03	...	...	Berkeley 33	-0.22±0.05	...	...
NGC 188	...	0.08±0.11	...				
Collinder 110	0.00±0.02	...	...				
NGC 2099	0.02±0.05	...	...				
NGC 2420	-0.04±0.08	...	...				
NGC 7789	0.27±0.02	...	...				
NGC 2141	...	-0.05±0.01	...				
NGC 2158	...	-0.12±0.04	...				
NGC 1883	...	-0.08±0.05	...				
Ruprecht 4	-0.05±0.08	...	...				

Chapter 6

Radial abundance gradients in the Galactic disk

6.1 Introduction

The first generation stars formed in the galaxies are composed almost entirely of hydrogen and helium. When these stars evolve and return their processed interiors (for example C, N, O, S etc.) to the interstellar medium (ISM), the pre-enriched gas then present will be incorporated into future generation of stars. Therefore, the amount of the chemical elements observed today and the timescales over which the ISM is being enriched with heavy metals are clearly, then, a function of many processes: the star formation rate (SFR), the initial mass function (IMF), the rate of element production and eventual return to the ISM and thresholds on the gas density for the star formation. The synthesis of the chemical elements and their return to the ISM are functions of lifetime and mass of stars. As the physical conditions such as the surface density of gas in the galactic disk and the SFR vary throughout many galaxies, the observed/derived abundances are a function of position as well. Therefore, the accurate measurement of the variation of chemical elements as a function of radius in the galactic disk (i.e. the radial metallicity gradient) and the gradient's temporal variation over the disk's lifetime is essential to develop an accurate picture of galactic evolution, and also to put constraints on Galactic chemical evolution models.

Numerous surveys have been conducted recently to investigate the existence, size and shape of a abundance gradient in the Gaklactic disk. A wide variety of tracers like H II regions (Shaver et al. 1983, Deharveng et al. 2000), hot young stars (Daflon & Cunha 2004), Cepheid variables (Andrievsky et al. 2002a,b,c,2004, Luck & Lambert

2011), planetary nebulae (Maciel et al. 2007, Stanghellini & Haywood 2010), G and K giants (Neese & Yoss 1988) and OCs (Magrini et al. 2010 and references therein), focusing on different chemical elements like Fe and α-elements have been employed to determine the gradients. Various disagreements and inconsistencies remain - see, for example, Magrini et al. (2010). OCs either through spectroscopy of their red giants or cooler main sequence stars provide not only abundance estimates for many elements – essentially, elements sampling all the major processes of stellar nucleosynthesis – but a collection of stars with a well determined age, distance and metallicity. Moreover, it is possible to estimate from an OC's space motion and a model of the Galactic gravitational potential the birthplace of the OC.

The first estimate of the Galactic metallicity gradient using OCs was given by Janes (1979), based on DDO and UBV photometric data. Based on a sample of 41 OCs covering a galactocentric distance range of 8-14 kpc, he derived an iron gradient of -0.05 ± 0.01 dex kpc^{-1}. Several subsequent studies using different techniques have been performed to investigate the variation of radial metallicity gradients: Friel & Janes (1993) presented spectroscopic results for a sample of giants in 24 open clusters with ages greater than 1 Gyr and derived a radial metallicity gradient of about -0.09 dex kpc^{-1}. Based on a more uniform set of 44 OCs, Friel (1995) derived a spectroscopic iron gradient of -0.091 dex kpc^{-1}. In the same year, Piatti et al. (1995) derived a much smaller gradient, -0.07 dex kpc^{-1}, from a sample of 63 open clusters with a wide range of ages. Based on a sample of 37 clusters, Carraro et al. (1998) derived a gradient of about -0.085 dex kpc^{-1}, agreeing with Friel & Janes (1993) value. By dividing the sample into age bins, they found that the present gradient is a little shallower than the past one, while the middle epoch seems to display a steepening of the gradient.

Twarog et al. (1997) gave an alternative description, namely, step function, for the radial abundance distribution of the open clusters. Using a set of 76 OCs, they suggested that the metallicity distribution of clusters with Galactocentric distance is best described by two distinct zones, with a sharp discontinuity at $R_{gc} = 10$ kpc. They found that between $R_{gc} = 6.5$ to 10 kpc, the clusters have a mean metallicity of 0.0 dex with weak evidence for a shallow gradient over this range, while those beyond 10 kpc have a mean metallicity value of about -0.30 dex. By neglecting this two-step phenomena, a least-square fit to the whole sample results in a gradient of about -0.067 dex kpc^{-1}, agreeing with previous measurements. Recently, Chen et al. (2003) have harvested the existing data on OCs and derived a metallicity gradient of about -0.063 ± 0.008 dex kpc^{-1} based on a sample of 45 OCs.

Several studies based on high-resolution spectroscopy have confirmed the presence of steep gradient in the radial range R_{gc} = 7 to 11 kpc, and a flat metallicity distribution in the outer Galactic disk beyond 11 - 12 kpc (Carraro et al. 2004, Yong 2005, Yong 2012). However all these studies are agreeing on a negative slope with increasing galactocentric distance, but various disagreements and inconsistencies remain in predicting the exact behaviour of slope and its space and time variations - see, for example, Magrini et al. (2010). The presence of breaks in oxygen abundance gradient slopes and thence a flat distribution had already been observed in many external spiral galaxies (Scarano & Lépine 2013). This further strengthens the view that understanding the formation and evolution of Milky Way serves as a testing bed to improve our knowledge on the evolution of disks in galaxies in the early universe and their present forms.

Apart from having a flatter abundance gradient, the outer Galactic disk show enhanced [α/Fe] ratios for OCs (Yong et al. 2005, 2012), field stars (Carney et al. 2005b) and Cepheids (Yong et al. 2006). Some authors disagree with the notion of enhanced [α/Fe] in the outer Galactic disk (Sestito et al. 2008, Carraro et al. 2007). Various discrepancies among studies might be due to the systematic differences resulting from the analyses of inhomogeneous dataset.

We devote this chapter to investigate the radial abundance distribution in the Galactic disk using the homogeneous dataset prepared in the previous chapter.

6.2 Metallicity distribution in the disk

The two significant parameters of interest for the radial metallicity distribution in the disk are metallicity and distance. The number of clusters with published metallicity estimates are well over a hundred, but such estimates involve an array of techniques based on spectroscopy (low to high-resolution) and photometry. The compilation of all such abundance estimates can easily wash out or mask subtle observable features in the distribution unless a suitable standardization is adopted with extreme care.

Several recent attempts have been made to construct a homogeneous sets of spectroscopic OC metallicities (Friel et al. 2010, Heiter et al. 2014). Heiter et al. (2014) found that differences in the analysis methods have a strong impact on metallicity than quality differences (S/N-ratio) of the spectra taken at medium and high-resolution. Hence, as mentioned earlier in the previous chapter, we have reestimated the abundances of literature OCs using our models and linelists to place all the results on a common abundance scale. We recalculated the R_{gc} value of each cluster, assuming $R_{\odot} = 8.0 \pm 0.6$ kpc, to bring them to a common distance scale. Thus our final homogeneous sample of 77 OCs cover a range of 5.0 to 24.0 kpc in R_{gc}, ~ -0.5 to 0.3 dex in metallicity and an age of few Myr to 9 Gyr.

In figure 6.1, we shows the variation of iron abundance ([Fe/H] dex) with corresponding error bars as a function of the Galactocentric distance, or in other words the conversion of hydrogen into heavy metals as a function of R_{gc} from the Galactic centre (see caption for color coding). Our homogeneous set of OCs data supports the widely held impression that there is an abundance gradient such that the metallicity [Fe/H] at the solar galactocentric distance decreases outwards (Magrini et al. 2009). We perceive this distribution as a smoothly decreasing function of R_{gc}, with a change of slope at R_{gc} ~13-14 kpc that flattens out at larger radii, modulated by a scattering of clusters along R_{gc} near 8-9 kpc and 11-12 kpc (see figure 6.1 and its caption). In addition, one can see gaps in the distribution at ≈ 8.2 kpc and 11.8 kpc followed by wiggles, exhibited by OCs with both the over-solar and under-solar metallicity.

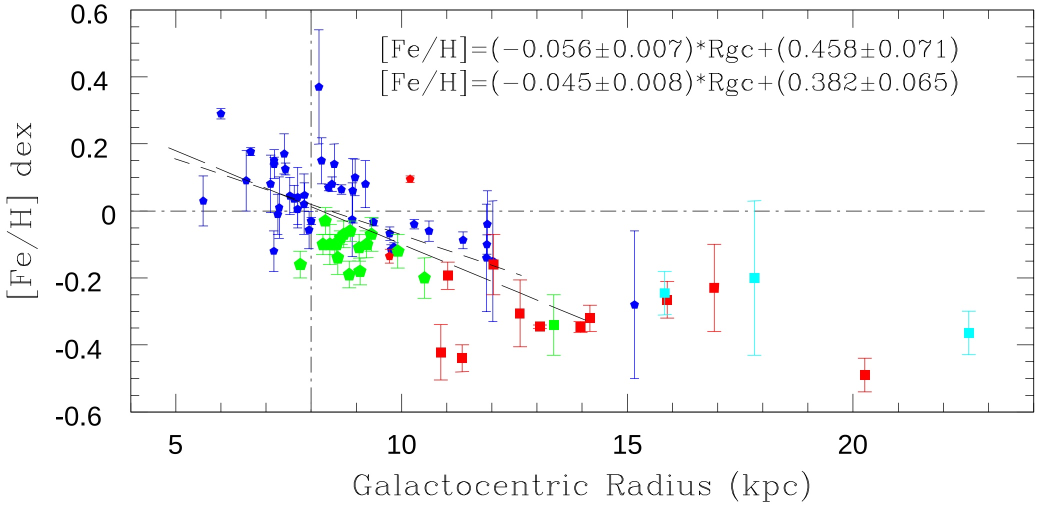

Figure 6.1: Open cluster mean metallicity, [Fe/H], with corresponding error bars as a function of R_{gc} : green dots (ours) and blue dots represent the OCs with thin disk memebership, red filled squares with thick disk membership and the cyan filled squares represent the halo population. The intermediate population between thin-thick and thick-halo are represented by red dots and green square. The vertical line represent the position of Sun and the horizontal line represent the solar mix of elements.

A simple linear fit to the whole data (long dashed line) with Rgc ≤ 14 kpc yields an abundance gradient, $\frac{d[Fe/H]}{dR_{gc}}$, of -0.056 ± 0.007 dex/kpc (with a regression coefficient of -0.85). While a fit to the thin disk sample (short dashed line) alone gives a slope of -0.045 ± 0.008 dex/kpc (for $R_{gc} \leq 12$ kpc), which is not very different from the previous one as the fit in each case is dominated by thin disk sample. Both these gradients are in close agreement with OCs value of -0.063 ± 0.008 dex kpc^{-1} (Chen et al. 2003) and a more recent value of single slope -0.062 ± 0.002 dex kpc^{-1} derived by analyzing a homogeneous and high-dispersion metallicity data of Cepheids (Luck & Lambert, 2011). Though the data is unevenly distributed in the outer disk sample (Rgc $\geq$ 13 kpc), a linear fit to the sample yields a gradient of -0.007$\pm$0.008 dex kpc^{-1} which is consistent with the zero slope. Therefore, we confirm that the metallicity gradient is flatter in the outer part of the Galactic disk, as observed by many authors in the literature (Carraro et al. 2004, Yong 2005, Yong 2012 and Magrini et al. 2009). Before we investigate this further, let us study the spatial appearance of OCs on the Galactic plane.

The Galactic distribution of OCs

In figure 6.2 we have superposed the current Galactic positions of OCs on a logarithmic four arm spiral model of Vallee (2002) parametrized as:

$$x = r\, cos\,\theta; \quad y = r\, sin\,\theta; \quad r = r_0\, e^{kz} \tag{6.1}$$

with θ measured counterclockwise from the x-axis. For each spiral arm, the equation reduces to four similar curves, each rotated by 90° with an inward pitch angle of p = 12°. In equation 6.1, we have z (radians) = $(\theta - \theta_0) > 0$ and k = $\tan p$; r$_0$ and θ_0 are constants obtained by a proper fit to the observations. We have adopted revised model parameter for r$_0$ = 2.52 kpc extracted from an updated statistical data of Vallee (2005). Using this model, we have derived an inter-arm separation of 2.72 kpc at the position of the Sun (i.e. R$_\odot$ = 8.0 kpc). This implies a predicted distance of the Sun to the Sagittarius arm is 1.13 kpc, while that to the Perseus arm is 1.59 kpc in the Galactocentric direction.

From figure 6.2 (see figure for color coding), it is evident that the OC dataset is uniformly distributed in the galactic plane near the solar neighborhood while at large galactic distances it is sparse. We find that young clusters with ages < 0.8 Gyr (younger than that of Hyades, see also Phelps et al. 1994) are uniformly distributed around the Sun, while roughly a few old OCs are inside the solar circle as most of them are away from the galactic center than the Sun. This result is quite consistent with the early comprehensive study of Phelps et al. (1994). The deficiency of old clusters in the inner part of the disk has been attributed to the destruction of clusters by encounters with giant molecular clouds, which were primarily found in the inner Galaxy. We also find that the majority of old clusters located beyond R$_{gc}$ > 11 kpc are metal poor ([Fe/H] < -0.2 dex, figure 6.1) and have appeared away from the

Galactic plane (see figure 6.3). This further strengthens the view that OC destruction may occur close to the plane of the disk and only those clusters whose orbits keep them away from the Galactic plane can survive long enough to appear as outer disk, or metal poor clusters. As a consequence, only the initially richest clusters (which are more gravitationally bound) and those situated at large galactic radii (where the probability of encounter with a giant molecular clouds is lower) can live a few Gyr (Bergond et al. 2001).

Now it appears from the metallicity distribution of OCs, as in figure 6.1, that the flatness of the gradient in the outer disk is mainly due to the metal poor/old clusters. As suggested by Lepine et al. (2011), these outer disk clusters might be travelers born in the inner regions of the Galactic disk. As the OC migration is a relatively slow process, it should effect the old population more than the young ones. Therefore, the sufficiently large age of the OCs, as seen from the smooth increase of age and distance (z) from the Galactic plane with R_{gc} (figure 6.3), might have allowed them to travel to their present position from their birthplaces.

To ascertain the role of radial migration in shaping the abundance distribution we have binned the OC data into four sub-samples, based on the current knowledge of their galactic coordinates and assuming a typical half arm width of 1 kpc, so that each cluster belongs to one of the spiral arms. We then studied the dynamics of these OCs using a multicomponent Galactic gravitational potential model and derived birthplaces and other orbital parameters. Our assignment of clusters to different spiral arms is shown in table 6.2.

Computation of OC birth-sites

We followed the OC's trajectory backward in time for an interval equal to its age and computed their birth-sites and other orbital parameters. We have adopted a Galactic potential model proposed by Flynn, Sommer-Larsen & Christensen (1996, hereafter FSC96) by matching the rotation curve, local disk density and disk scalelength of the Galaxy with good accuracy.

This axisymmetric and time independent model admits three potential components: dark halo, a central component and disk. The potential of the dark halo is assumed to be spherical and contributes to the total potential in a logarithmic form

$$\phi_H = \frac{V_H^2}{2} \ln(r^2 + r_0^2) \tag{6.2}$$

where r ($= \sqrt{R^2 + z^2\, q^{-2}}$) is the Galactocentric radius, q is a flattening parameter, taken as unity here. The potential has a core radius of $r_0 = 8.5$ kpc with halo circular

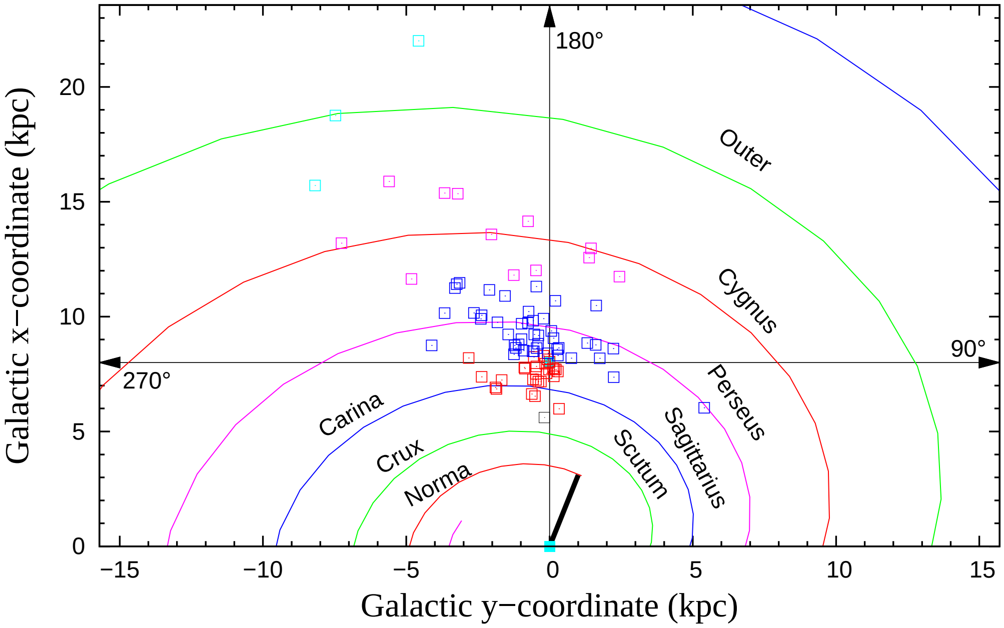

Figure 6.2: Superposition of open cluster positions in the Galactic coordinate system with the logarithmic four arm model of Vallee (2002). Here the x and y- coordinates are interchanged. The red squares are for the the OCs that reside in Sagittarius-Carina arm, blue for Perseus arm, magenta for Cygnus arm, and the cyan symbols for the OCs that belong to the outer arm in Vallee scheme of spiral arm pattern. Sun is placed at a distance of 8 kpc from the Galactic centre, represented by the point of intersection of arrows. The central bar of the Galaxy is, represented as a thick black line, is inclined at an angle of 20° to the line joing the Sun to the Galactic centre.

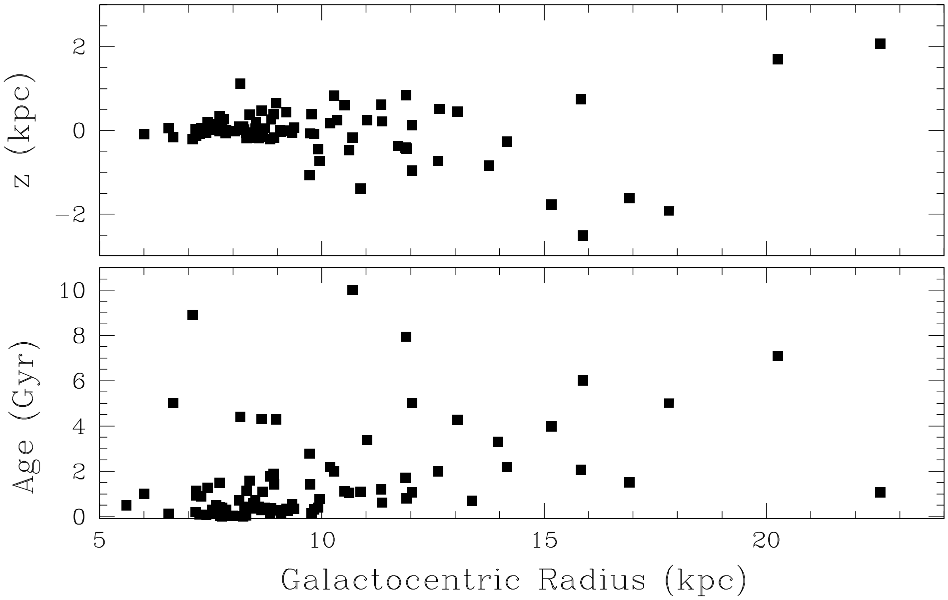

Figure 6.3: The variation of z-component of the position of OCs from the Galactic plane (upper panel) and age (lower panel) of OCs as a function of Galactic radius (R_{gc}).

velocity of $V_H = 220$ km s^{-1} at large r.

The potential of the central component is modelled by two Hernquist spherical components, one representing the bulge/stellar-halo and the other for an inner core component:

$$\phi_C = -\frac{GM_{C_1}}{\sqrt{r^2 + r_{C_1}^2}} - \frac{GM_{C_2}}{\sqrt{r^2 + r_{C_2}^2}} \tag{6.3}$$

Here G is the gravitational constant, $M_{C_1} = 3.0\times10^9$ $M_\odot$ and $r_{C_1} = 2.7$ kpc are the mass and core radius of the bulge/stellar-halo component, $M_{C_2} = 1.6\times10^{10}$ $M_\odot$ and $r_{C_2} = 0.42$ kpc are the mass and core radius of the inner core.

The disk potential is modelled using a combination of three analytical disks of Miyamoto-Nagai (1975) potentials:

$$\phi_D = \phi_{D_1} + \phi_{D_2} + \phi_{D_3} \tag{6.4}$$

with

$$\phi_{D_n} = \frac{-GM_{D_n}}{\sqrt{R^2 + [a_n + \sqrt{z^2 + b^2}]^2}} \quad \text{(for n = 1, 2, 3)} \tag{6.5}$$

where the parameter M_{D_n} are the masses of three disk components, a_n are related to the disk scalelengths and b to the disk scaleheight. The corresponding scaling parameters related to the three disk components with b = 0.3 kpc are $M_{D_1} = 6.6\times10^{10}$ $M_\odot$, $a_1 = 5.81$ kpc, $M_{D_2} = -2.9\times10^{10}$ $M_\odot$, $a_2 = 17.43$ kpc and $M_{D_3} = 3.3\times10^9$ $M_\odot$, $a_3 = 34.86$ kpc.

For this potential, the distance from the Sun to Galactic centre is set at 8 kpc with a local circular velocity of 220 km s^{-1}. According to Flynn, Sommer-Larsen & Christensen (1996), adoptation of a single Miyamoto-Nagai potential for the disk and reasonable dark halo potentials leads to shorter disk scalelength (typically by a factor of 2) for well-fitting rotation curves. They circumvented this problem by combining three Miyamoto-Nagai disks of differing scalelengths and masses. The derived scaling parameters are consistent with the dynamical mass measurements of the disk surface density at the solar circle. Assuming $R_\odot = 8$ kpc, the local disk surface density of matter $\Sigma_{disk}(R = R_\odot)$ is 51 $M_\odot$ pc^{-2}, consistent with recent dynamical measurement of 50 $M_\odot$ pc^{-2} (Kuijken & Gilmore 1989; Flynn & Fuchs 1994).

The relevant code for the integration of the orbits is provided by Zhen-Yu Wu and the same has been used for the analysis of kinematics and orbits of OCs in the Galaxy (Wu et al. 2009). The equations of motion are constructed using the adopted gravitational potential model in cylindrical coordinates R, ϕ and z, where R is the galactocentric radius in the xy plane, ϕ is the azimuthal angle between the x-axis and the projection of the position vector onto the xy plane, and z is the distance of the OC above the xy plane.

The Hamilton's equations, representing a set of first order differential equations are generated using the adopted gravitational potential model which we have integrated using Bulirsch-Stoer algorithm of Press et al.(1992) implemented in FORTRAN code with adaptive time-steps. Starting from the OCs current position and their GSR velocity components (as calculated in Chapter 5), we have integrated their orbits backward in time over a period of 5 Gyr. The integration time is chosen to ensure that even the young OCs with ages less than 100 Myr can complete more galactic orbits so that the averaged orbital parameters can be determined. The relative change in the total energy over a period of 5 Gyr integration time is of the order of 10^{-14} to 10^{-15} (Wu et al. 2009). Later, the birth sites R_{birth} are calculated by integrating their orbit backward in time until the epoch of their birth (i.e. the integration time is equal to cluster's age).

The relevant orbital parameters are listed in Table 6.1. R_a and R_p are the averaged apo galacticon and peri galacticon, as measured from the averaged maximum and minimum galactocentric distance of the OC in its orbit within the integration time of 5 Gyr. The orbital eccentricity e is determined using the expression e = $(R_a-R_p)/(R_a+R_p)$, where R_a and R_p are the averages. The vertical amplitude z_{max} is also the averaged maximum vertical distances of the cluster above the galactic palne in its orbit within the integration time. The orbital period T_p is the time for one complete revolution of the OC around z-axis and the epicyclic period T_z is time interval for the cluster to cross the galactic plane from one z_{max} to the other in the opposite direction. J_z and $J_\perp$ are the azimuthal and perpendicular components of the angular momentum vector per unit mass. The negative/positive component for J_z indicates the prograde/retrograde rotation in the Galaxy, while J_z=0 implies no rotational velocity in the direction of Galactic rotation. Finally, the extent of inclination (tilt) of the orbital plane of the OC with respect to the Galactic plane is deduced from the J_z and $J_\perp$ components of the angular momentum vector. It is obvious from the table that the OCs with thin disk membership have quite small inclination angle.

From the Table 6.1, it is also clear that the thick disk and halo populations have their orbital plane more tilted with respect to the Galactic plane. As a result they spend most of their time away from the plane of the Galactic disk in their orbits, whereas almost all the thin disk OCs, including the seventeen OCs from our sample, have their orbits confined to the Galactic plane within the Galactic latitudes $|b| \simeq$

10°. Our investigation reveals that majority of OCs, even the outer disk clusters situated at large R_{gc} (for example, Berkeley 17, 18, 21, 73, NGC 1193 and Tombaugh 2) were born in the radial range $R_{birth} \simeq 6-11$ kpc (see table 6.1 for R_{birth} (or) figure 6.4) and majority of them formed close to the Galactic plane (i.e. the nominal value of vertical height (z) at birth is small). This may suggest that the radial range $R_{gc} = 6-11$ kpc might be a privileged zone for star formation (Lepine et al. 2011). From figure 6.4, it is evident that all the OCs are nicely tracking the spiral arms, which may suggest that spiral arms are the potential reservoirs to churn the OCs out of the interstellar matter. Therefore old/metal poor clusters (Berkeley 17 (10 Gyr), 18 (4.3 Gyr), 21 (2.2 Gyr), NGC 1193 (5 Gyr), Tombaugh 2 (2 Gyr)), situated very far from their birth-sites, suggest that they were migrated from their birthplaces (in inner region) to the outer disk.

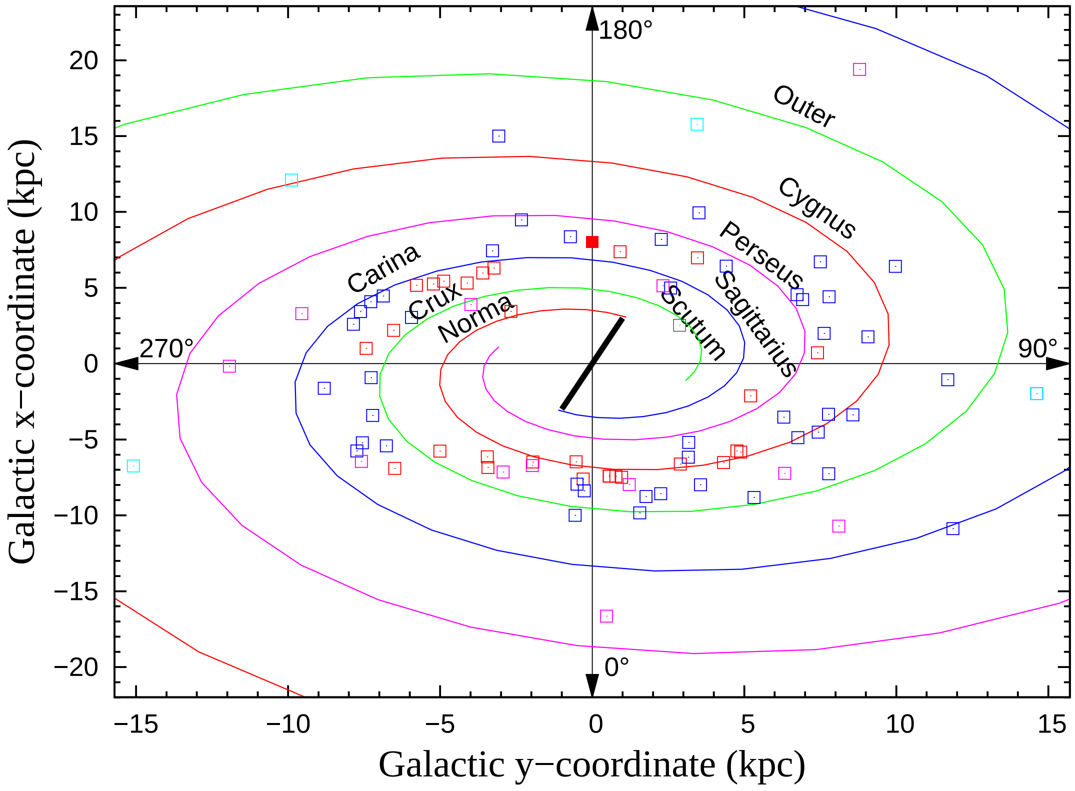

Figure 6.4: Same as figure 6.2, but for the spatial distribution OCs using their birthplaces.

Our further investigation reveals that there are a few clusters showing large values z, with z at birth being -3.7 kpc for Berkeley 20, 5.9 kpc for Berkeley 21, -3.9

for Berkeley 22, 16.6 kpc for Berkeley 29 and -6.3 kpc for Berkeley 31. Also, these clusters have large z_{max}, reaching to maximum vertical height in their orbits within the integration time. From the literature we find two mechanisms for the formation of high altitude Galactic OCs such as these. Martos et al. (1999) modelled the response of gas to spiral arm density wave and concluded that the shock wave pumps up gas from the interarm region to high altitudes thereby triggering star formation, although with a low efficiency. The other mechanism by de la Fuente Marcos & de la Fuente Marcos (2008) suggests that the pre-existing massive clusters such as globular clusters interact tidally with high Galactic altitude clouds and induce star formation. As the clusters, inherently, retain some kinematic memory of the events that happened during their birth, we believe that some of the clusters with high z and possibly eccentric orbits might have originated through the above mechanisms.

As a representative example, a few orbits calculated with FSC96 model in a time interval of 5 Gyr are shown in figure 6.5 for the thick disk and halo populations, and figure 6.6 for the thick disk and thin disk populations. For each cluster, the orbits projected onto the Galactic plane are shown in the left panel, while the panel on the right for the meridional orbits. The filled square marks the present observed position for each cluster. Among the present cluster sample, Berkeley 29 has the maximum of $R_a \sim 23.7$ kpc, Berkeley 20 has the maximum eccentricity $e = 0.79$ and orbits very close to the Galactic centre with $Rp \sim 1.8$ kpc, and Berkeley 29 and 31 have the maximum values of z_{max}.

It is clear from figure 6.5 and figure 6.6 that the orbits projected on the Galactic plane show the periodic motions of clusters. Almost all the OCs show boxy-like orbits in meridional plane and move within the limited areas almost filling the boxes symmetrically. All the thin disk OCs spend most of their time close to the Galactic disk, never reaching a height more than 500 pc, and their orbits are confined well within a relatively small galactocentric radius. The thick disk and halo OCs make large excursions away from the Galactic plane reaching the highest vertical distances (z_{max}) and their orbits are extended over a large galactocentric radii. Their orbits in the meridional plane clearly indicate the increasing value of z coordinate with increasing galactocentric distance. This means, physically, that as the gravity of the disk decreases with Galactic radius, a cluster moving outwards will feel less gravitational pull than it is close to the Galactic centre and finally increases its amplitude of oscillation in the z direction. This is clearly visible in figure 6.5 for thick disk and halo population and is prominent for Berkeley 29 whose orbit extends over 20 kpc both in the disk plane and in vertical direction.

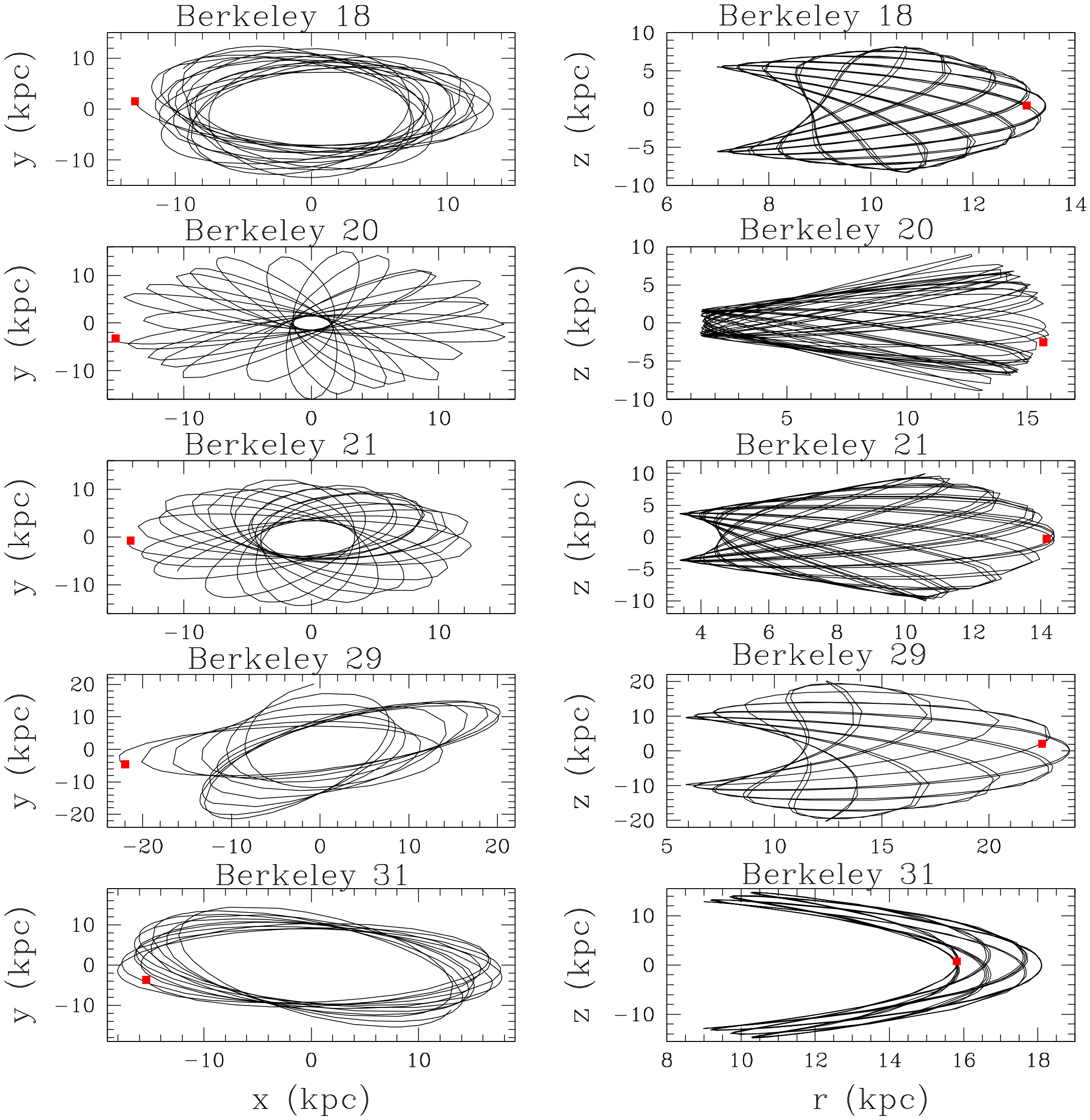

Figure 6.5: The orbits projected onto the Galactic plane (left panel) and the meridional Galactic orbits (right panel) of OCs calculated using the FSC96 model for a time interval of 5 Gyr. The present observed position for each cluster is marked with a filled square. Here Berkeley 18, 20, 21 are thick disk OCs, while Berkeley 29 and Berkeley 31 belongs to halo stellar population.

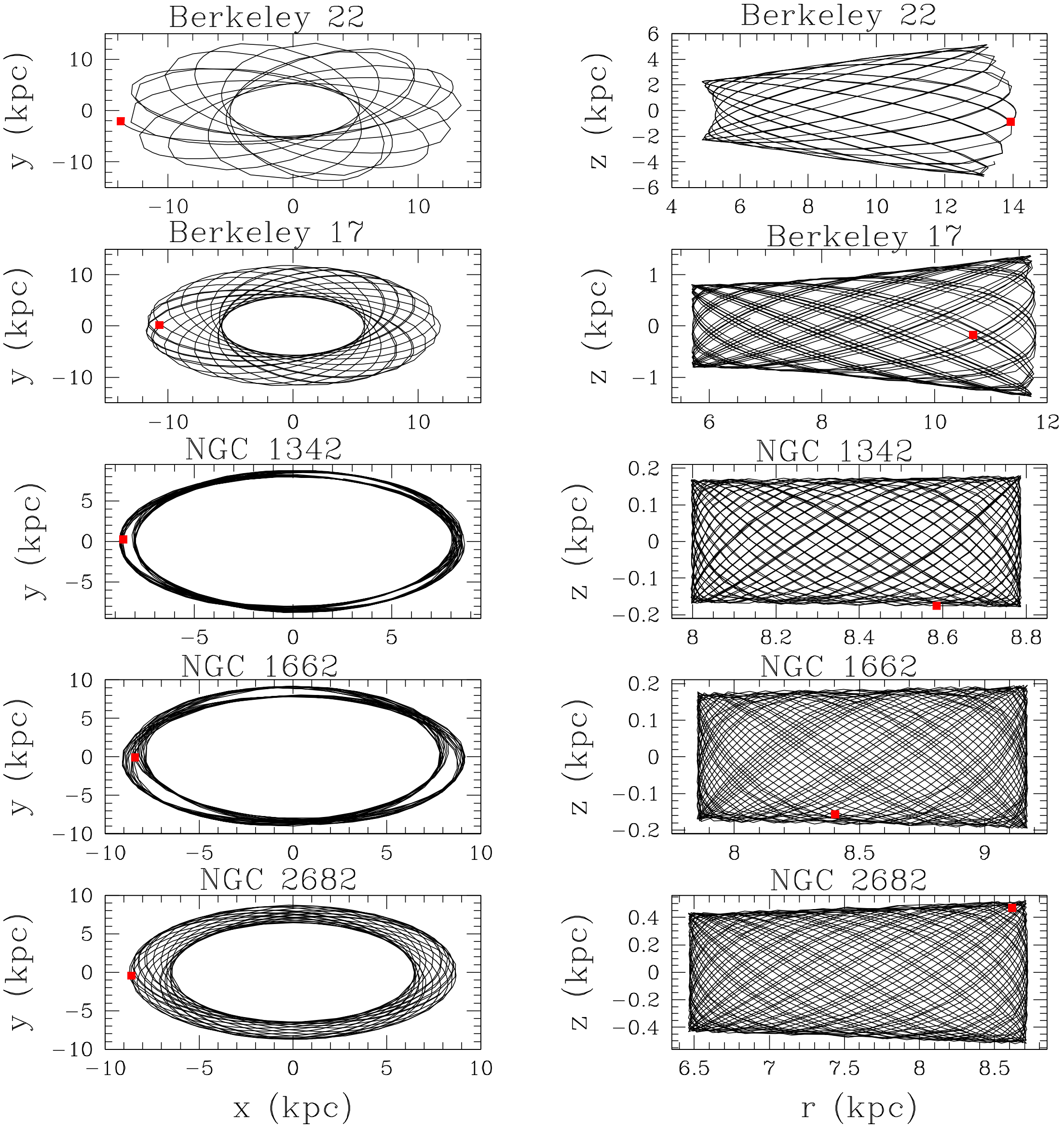

Figure 6.6: The orbits projected onto the Galactic plane (left panel) and the meridional Galactic orbits (right panel) of OCs calculated using the FSC96 model for a time interval of 5 Gyr. The present observed position for each cluster is marked with a filled square. Here Berkeley 22 belongs to thick disk and Berkeley 17 to intermediate population (thin-thick disk) and the OCs NGC 1342, 1662 and 2682 belongs to the thin disk population.

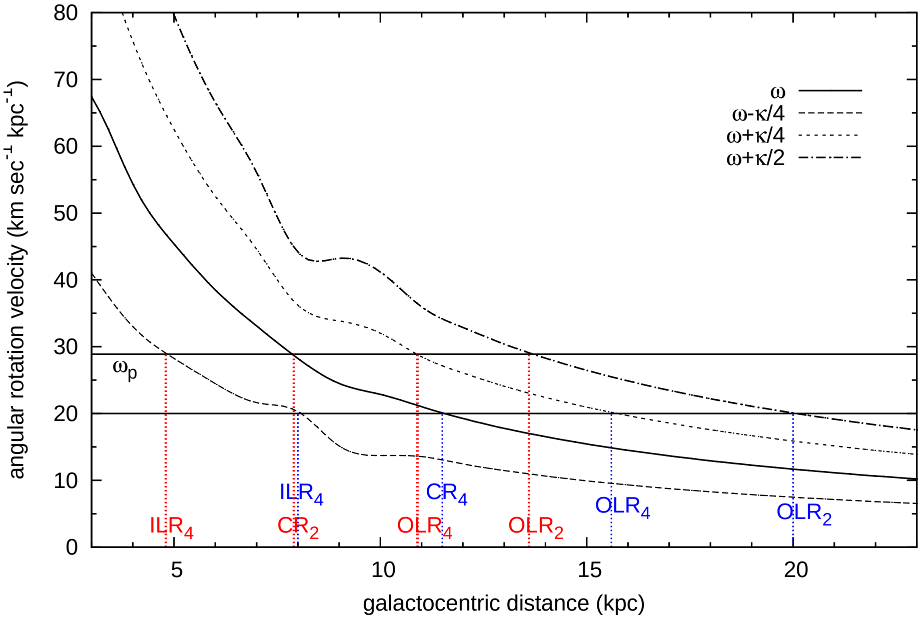

Figure 6.7: Galactic angular rotation velocity as a function of the galactocentric distance, and the position of the 4:1 and 2:1 resonances. The two solid horizontal lines correspond to the spiral pattern rotation speeds 20 km $\sec^{-1}$ kpc^{-1} and 28.9 km $\sec^{-1}$ kpc^{-1}, and the associated resonances are marked with blue and red dotted vertical lines.

Justification of OC migration

To investigate the radial distance at which the OC migration is more effective, we pursued the classical theory of galactic spiral waves (Lin & Shu 1964) and Lin et al. (1969) and their resonance interactions with the disk material. The theory tells us that the spiral arms rotate like a rigid body and are responsible for the perturbations in the velocity field with respect to the circular rotation of the galaxy. As a consequence, the gas and OCs (stars), that are dictated to follow the circular rotation curve of the galaxy exhibit differential rotation about their unperturbed circular orbit with an epicyclic frequency κ. These spiral arms are restricted to exist between the inner and outer Lindblad resonances (ILR and OLR), where the angular rotation velocity of the disk material ω equals $\omega_p \pm \kappa/m$, where ω_p is the pattern speed of spiral pattern, m is the number of arms. For example, the two (four) arm structure exist only between the 2:1 (4:1) resonances which appear at $\omega = \omega_p \pm \kappa/2(\kappa/4)$.

The ILR and OLR acts as a potential barrier at their locations in the disk and blocks the transfer of gas on either side in the radial direction thus, preserving the abundance differences between the separated zones. As a result, a change in SFR and hence a change in the shape (slope) of the metallicity gradient could be expected at these locations. Corotation resonance occurs where the angular rotation velocity of the disk material matches that of the spiral pattern (ω=ω_p). This resonance falls roughly between the ILR and OLR and maximizes the effect of spiral pattern perturbations on the disk material that form a void of gas.

Scarano & Lépine (2013) compiled the literature data on spiral galaxies and showed that the corotation occurs about midway between extremities of the region where the arms are seen. In our Galaxy, the spiral arms extend from about 3 to 13 kpc (Russeil 2003), which would place the corotation at about 8 kpc. Recently Dias & Lépine (2005) studied the dynamics of OCs and find that the corotation radius, R_C, is close to the solar Galactic orbit ($R_{CR}/R_\odot$ = 1.06±0.08). A second direct observation comes from the position of the ring-shaped HI void at corotation (Amôres et al. 2009), and a third one from the position of the square-shaped spiral arm associated with the 4:1 resonance (Lépine et al. 2011a).

For any given rotation curve, the actual location of the Lindblad resonances and corotation tightly depends on the the pattern speed, ω_p, of spiarl arms whose actual value is not well established in our Galaxy. A range of values are available for the spiral pattern rotation speed in the literature. Naoz & Shaviv (2007) studied the Milky Way spiral arm dynamics using the birth place of open clusters and found two sets of pattern speeds. A higher value for $\omega_p = 28.9\pm\, 0.8_{stat}$ km sec^{-1} kpc^{-1} situates the resonances at the galactocentric distances: $R_{CR} \approx$ 7.9 kpc, $R_{ILR_4} \approx$ 4.8 kpc and $R_{OLR_4} \approx$ 10.9 kpc (for m=4 i.e. 4:1 resonances) and $R_{OLR_2} \approx$ 13.6 kpc (for m=2). A lower value for the pattern speed ω_p (= $20.0\pm\, 1.6_{stat}$ km sec^{-1} kpc^{-1}) shifts the location of resonances to larger galactocentric distances: $R_{CR} \approx$ 11.5 kpc, $R_{ILR_4} \approx$ 8.0 kpc and $R_{OLR_4} \approx$ 15.6 kpc (for m=4) and $R_{OLR_2} \approx$ 20.0 kpc (for m=2).

In figure 6.7 we show the behaviour of the disk angular velocity, as well as its combination with epicyclic frequency corresponds to m=4 and m=2 arm patterns. There is a debate on whether the Galaxy hosts two or four spiral arms. Englmaier et al. (2008) study of 3D distribution of molecular CO gas emission support the coexistence of both the m=2 and m=4 arm modes for the Milky Way. Their data shows two prominent spiral arms starting at the bar ends branches into two more arms at about the soalr radius. Lépine et al. (2001) investigated the superposition of m=2 and m=4 modes using Cepheids kinematics and obtained similar values of the pattern speeds for both modes, with $\omega_{sp,m=2} - \omega$= 0.15 ± 0.5 km sec^{-1} kpc^{-1} and $\omega_{sp,m=4} - \omega$= 0.18 ± 0.1 km sec^{-1} kpc^{-1}. Therefore the adoptation of m=2 and m=4 arms does not effect our choice of pattern speeds i.e., ω_p = 28.9 and 20.0 km sec^{-1} kpc^{-1}, and hence the location of the resonances.

From figure 6.1 and figure 6.7, we notice that the corotation resonances are very close to the gaps in the metallicity distribution at $R_{gc} \approx 8.2$ kpc and 11.8 kpc. We notice that the wiggle like structure ($\approx$ 8-9 kpc) on the right of corotation gap is populated with young and old OCs. The young age of the clusters indicate a recent burst of star formation and old OCs might have migrated to present locations from their birth-sites inside the solar circle. For example, the old OC NGC 6791 (age $\approx$ 4.4 Gyr) in the same wiggle might be a result of radial mixing in the disk (Jilkova et al. 2012). Therefore we conclude that the structures (wiggles and gaps along R_{gc}) in metallicity distribution might have shaped due to the dynamical interaction of the disk material with the spiral density waves. A similar argument can explain the observed flattening of the gradient in the outer disk.

As the resonances act as potential barriers for the gaseous component of the disk, the ILR and OLR may effect the SFR in their locations. As the star formation happens in spiral arms through gas compression, the SFR at a given R_{gc} depends not only on the local surface gas density, but also on the rate at which the interstellar gas is injected into the spiral arms (Mishurov et al. 2002). (i.e. SFR $\propto |\omega - \omega_p|$). Therefore the larger the difference in rotational frequencies, the greater the gas compression, and hence the efficient star formation. In the solar neighborhood $\omega \approx \omega_p$, and hence a low SFR. As shown in figure 6.7 the regions close to Galactic center have large angular velocities. Moreover the gas infall rate has a radial dependency, smaller inside the solar circle which increases out with R_{gc} (Andrievsky et al. 2004). As a result the regions close to the Galactic center evolve on a short time scales and convert the available hydrogen quickly into heavy metals. Thus the metallicity decreases outwards with R_{gc}, as in figure 6.1.

6.3 Radial abundance gradient

We plot the light elements (Na and Al; Figure 6.8), the α-elements (Mg, Si, Ca, Ti; Figure 6.9 & 6.10), the Fe-peak elements (Cr and Ni; Figure 6.11) and neutron capture elements (Ba, La, Ce and Nd; Figure 6.12) versus the Galactocentric distance R_{gc}.

Na and Al show almost zero gradient with increasing R_{gc}, with very little cluster-to-cluster scatter at any given radius. For all α-elements, the gradients are negligibly small or zero in the range of $8 \lesssim R_{gc} \lesssim 12$ kpc, afterwhich the slope becomes flat out to 24 kpc. Figure 6.10 provides a convenient way to examine the variation of [α/Fe] with R_{gc} where all α-elemental abundances are averaged to a single measure. A linear fit to the data yields a slope of $+0.017 \pm 0.004$ dex kpc $^{-1}$ ($6 \lesssim R_{gc} \lesssim 12$

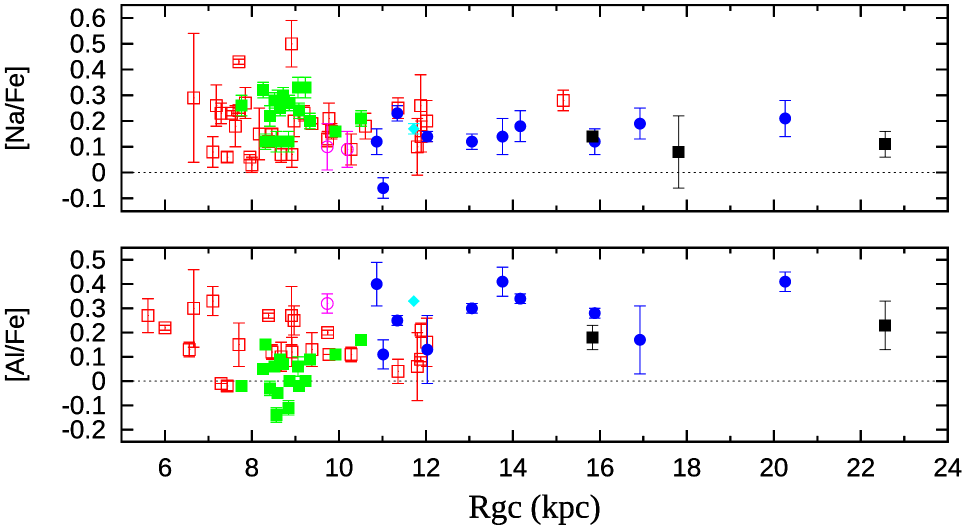

Figure 6.8: Abundance ratios for [X/Fe] vs. R_{gc} for light elements [Na/Fe] and [Al/Fe]. Clusters from our study (thin disk members) are presented as green filled squares. Luck & Heiter's sample of field giants are marked as open triangles (light black color). All the other colors represent clusters from the literature: red open squares (thin disk), blue filled circles (thick disk), black filled triangles (halo). Intermediate stellar populations are designated as magenta open circles (thin - thick disk) and cyan open triangle (thick disk - halo).

kpc), which tells us that the ratio of α-elements to Fe does not vary appreciably with increasing R_{gc}. As the α-elements are primarily synthesized in intense environments like Type II SN events in the early history of the Galaxy, the observed flat gradient signifies an homogeneous history of star formation. This result rule out the tendency of enhanced [α/Fe]-ratios for the outer disk OCs and the claims that the outer disk has unusual chemical evolution history different from that of the solar neighbourhood (Yong et al. 2005, 2012).

Our results are in fair agreement with findings of Sestito et al. (2008) and Carraro et al. (2007) for OCs and Lépine et al. (2011) for Cepheids. But, the Cepheids sample also show abundance gradients in the azimuthal direction. The present OCs data does not offer any clues on such gradients as the data is concentrated more in the radial than in azimuthal direction (see figure 6.2). Such a study will impose severe constraints on the chemical evolution models, which assume instantaneous mixing of the enriched material in the azimuthal direction. This should be verified in our future studies using a larger sample of OCs distributed across the disk.

As expected, all Fe-peak elements show a flat distribution, with a few discrepant points, compatible with zero slope. With a limited set of data in hand, it is hard to examine the trends of neutron capture elements against R_{gc} (Figure 6.12). As heavy elemental content increase with age (as disscused in chapter 5), the presence of young

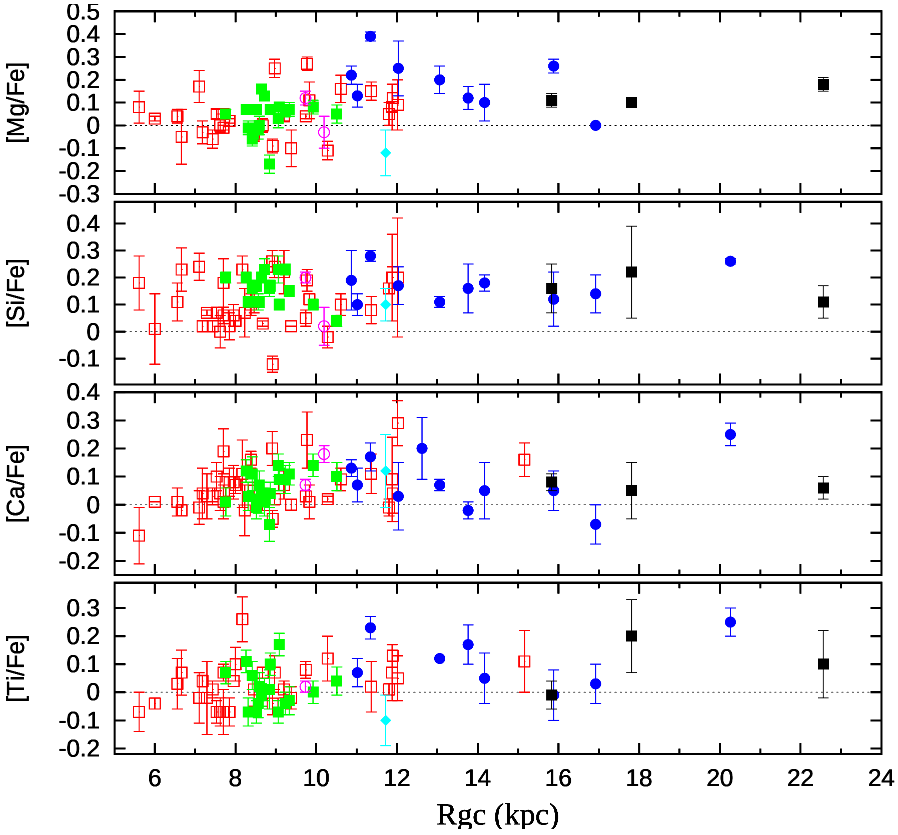

Figure 6.9: Same as figure 6.8 but for alpha elements [Mg/Fe], [Si/Fe], [Ca/Fe] and [Ti/Fe].

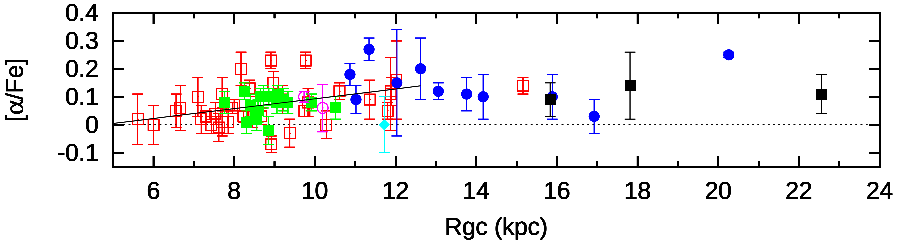

Figure 6.10: Same as figure 6.8 but for the variation of [α/Fe] with R_{gc}. A linear fit to the data (black line) gives a negligibly small gradient of 0.017±0.004 dex kpc $^{-1}$ for $6 \lesssim R_{gc} \lesssim 12$ kpc.

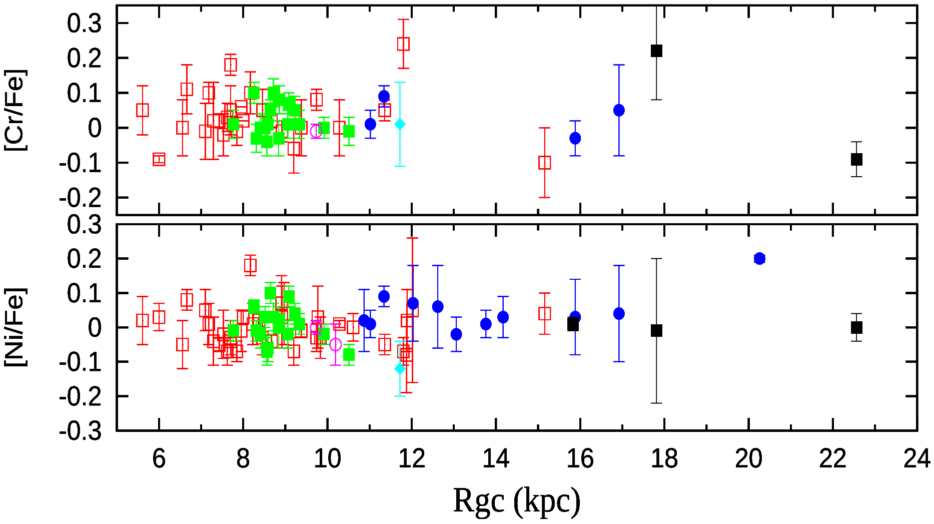

Figure 6.11: Same as figure 6.8 but for iron peak elements [Cr/Fe] and [Ni/Fe].

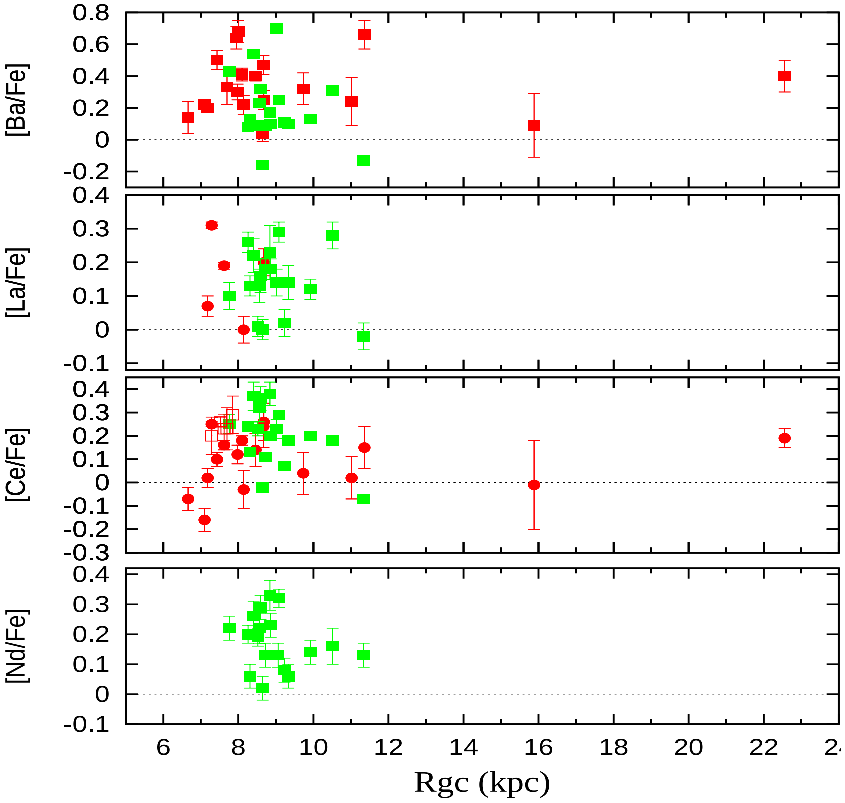

Figure 6.12: Abundance ratios vs. R$_{gc}$ for heavy s-process elements [Ba/Fe], [La/Fe], [Ce/Fe] and [Nd/Fe]. All the symbols have their usual meanings, while the red filled squares are OC data from D'Orazi et al. (2009) and the red filled circles are from Maiorca et al. (2011).

and old OCs in the radial range 7 to 10 kpc has been manifested as a scatter larger than ≈ 0.4 dex in the distribution.

6.4 Theoretical model predictions

Various models have been developed over the years to explain both the dynamical and chemical evolution of the Milky Way: from the simple closed-box model to the open models with infall of gas from outside of the Galaxy (Matteucci & Greggio 1986; Matteucci & Francois 1989; Chiappini et al. 1997) and the models including the radial gas flow (Portinari & Chiosi 2000; Spitoni & Matteucci 2011). All these classical models have incorporated in detail the effect of gas flows on galactic chemical evolution, but paid less attention on the stellar dynamics and its effects on chemical evolution of galaxies.

As suggested by Sellwood & Binney (2002), many recent studies (for example, Schönrich & Binney 2009) have incorporated radial mixing of stars in their models. As the stellar migration, by scattering at an orbital resonance or non-resonance scattering by a giant molecular cloud, causes the transport of disk material to anyplace along (across) the disk, the mixture of chemical elements over large radial extent would reduce the abundance difference along the disk and flatten the abundance gradients. This suggest that as the thick disk population had formed long back ($\approx 9.7\pm3.1$ Gyr ago), its metallicity gradient (if any was present) has been washed away over time, while in the younger thin disk the gradient still persists. The radial stellar migration is quiet successful in explaining the lack of tight age-metallicity relation of stars and the large scatter that would increase with the increasing age. A comprehensive comparison between various models have been discussed in Magrini et al. (2010), Wang et al. (2013) and Heiter et al. (2014).

Although current chemical models predict several observed properties of Galaxy along with the flat metallicity gradient in the outer disk, they differ in predicting the inner gradient, metallicity breaks and the metallicity level at a given R_{gc} (Magrini et al. 2010; Heiter et al. 2014). Now, it is obvious that a statistically significant sample OCs analysed in a homogeneous way is needed to provide strong observational constraints to the models such as the azimuthal and vertical gradients in the disk, variation of [α/Fe], [s/Fe] and [r/Fe]-ratios as a function of [Fe/H], R_{gc} and cluster's age and more importantly extension of observations to the outer disk ($R_{gc} \geq 13$ kpc), where the spectroscopic data is scarce. Then, a combined set of results for OCs across the Galaxy should reveal novel insights into the development of abundance differences in time and space within the Galactic disk.

Table 6.1: The relevant orbital parameters for a sample 77 OCs calculated with the Galactic gravitational model of Flynn, Sommer-Larsen & Christensen (1996). All the columns are self-explanatory (see the text for reference).

Cluster	R_a (kpc)	R_p (kpc)	R_{birth} (kpc)	z_{max} (kpc)	eccentricity	T_p (Myr)	T_z (Myr)	J_z (kpc km sec^{-1})	$J_\perp$ (kpc km sec^{-1})	Tilt (°)
Thin disk										
NGC 752	8.38	7.26	8.35	0.26	0.07	217.4	45.9	-1721.1± 38.8	112.4± 26.3	3.74
NGC 1817	10.23	5.77	9.76	0.82	0.28	226.7	62.5	-1624.0±158.4	314.3±101.2	10.95
NGC 2360	12.46	9.12	10.55	0.25	0.16	289.2	66.7	-2428.5±141.3	125.1±124.0	2.95
NGC 2506	10.63	7.20	10.30	0.58	0.19	245.4	63.3	-1929.9± 88.7	159.4± 77.4	4.72
NGC 2335	10.02	7.45	9.21	0.13	0.15	240.4	48.1	-1926.1± 76.1	75.1± 91.1	2.23
NGC 2482	8.72	7.39	8.13	0.19	0.08	222.8	45.9	-1779.3± 36.0	109.6± 46.3	3.52
NGC 2251	9.25	7.57	8.37	0.02	0.10	231.1	45.0	-1867.4± 62.0	13.9± 35.9	0.43
NGC 2527	8.32	6.71	7.31	0.12	0.11	210.3	41.0	-1635.7± 18.1	72.6± 12.9	2.54
NGC 2539	8.91	7.20	7.23	0.35	0.11	223.5	50.0	-1768.7± 33.4	139.3± 53.5	4.50
NGC 2682	8.74	6.46	8.20	0.49	0.15	213.5	51.5	-1630.0± 43.2	142.5± 63.8	4.99
NGC 1342	8.79	8.00	8.51	0.17	0.05	230.4	45.2	-1874.5±33.7	38.9±11.1	1.19
NGC 1662	9.17	7.85	7.90	0.18	0.08	236.5	46.9	-1898.0±19.0	61.7±12.3	1.86
NGC 2447	8.63	8.38	8.46	0.03	0.02	232.1	48.4	-1908.8±36.2	17.1±21.0	0.51
NGC 2354	9.08	6.57	8.49	0.38	0.16	218.7	47.6	-1684.9±36.1	189.8±50.7	6.42
NGC 1912	9.06	7.46	8.95	0.11	0.10	226.3	48.3	-1829.3±60.9	63.4±27.2	1.98
NGC 2548	8.89	8.18	8.86	0.26	0.04	235.9	51.6	-1910.3±24.5	100.7±1.2	3.02
Collinder 350	7.80	7.36	7.79	0.13	0.03	211.3	41.7	-1668.5±12.0	68.8±7.0	2.36
NGC 1245	10.89	9.97	10.22	1.54	0.04	282.8	98.0	-2334.2±119.5	516.8±135.6	12.48
NGC 188	8.97	7.57	8.06	0.79	0.08	229.7	64.1	-1811.9± 72.9	238.9± 82.2	7.51
NGC 2099	9.37	6.00	6.08	0.11	0.22	216.6	42.0	-1621.8±111.1	54.0± 16.8	1.91
NGC 2141	11.97	7.42	7.75	0.44	0.23	266.5	64.9	-2090.8±185.0	147.6± 86.8	4.04
NGC 2158	11.99	6.16	8.33	0.11	0.32	253.4	50.5	-1856.6±210.6	28.8± 42.8	0.89
NGC 2194	10.00	7.13	10.01	0.26	0.17	236.3	50.5	-1869.1±107.8	144.2± 69.1	4.41
Collinder 110	10.02	6.20	7.33	0.30	0.24	226.3	49.0	-1709.1± 61.9	66.1± 9.6	2.21
NGC 2324	11.45	7.22	8.01	1.21	0.23	259.6	83.3	-1975.6±212.2	451.1±226.5	12.86
NGC 2355	9.78	7.59	9.74	0.51	0.13	238.7	59.5	-1913.9±139.2	184.6±104.1	5.51
NGC 2423	8.67	7.13	8.67	0.09	0.10	219.3	42.7	-1738.3± 22.8	51.2± 9.3	1.68
NGC 2420	10.62	5.96	9.97	0.69	0.28	233.2	61.7	-1696.7±115.5	139.4± 44.0	4.69
NGC 2477	9.14	7.53	8.33	0.16	0.10	229.4	46.3	-1846.4± 19.1	58.4± 29.2	1.81
NGC 1883	11.98	10.54	11.30	1.21	0.06	301.2	100.0	-2558.9±179.1	401.2±124.1	8.91
NGC 2660	10.51	8.04	9.47	0.20	0.13	252.2	53.8	-2068.1±103.2	75.8± 93.3	2.10
NGC 3114	7.84	7.76	7.82	0.06	0.01	216.3	41.7	-1727.6± 17.2	13.6±6.6	0.45
IC 2391	8.00	7.50	7.68	0.28	0.03	215.7	45.5	-1709.9±4.8	152.9±39.1	5.11
IC 2581	8.07	7.10	7.41	0.36	0.06	212.1	47.6	-1660.3± 82.3	189.1± 81.4	6.50

Cluster	R_a (kpc)	R_p (kpc)	R_{birth} (kpc)	z_{max} (kpc)	eccentricity	T_p (Myr)	T_z (Myr)	J_z (kpc km sec^{-1})	$J_\perp$ (kpc km sec^{-1})	Tilt (°)
IC 2602	7.95	7.24	7.76	0.09	0.05	211.7	41.0	-1672.0± 9.1	54.9± 1.6	1.88
NGC 3532	7.85	7.27	7.66	0.10	0.04	210.9	40.7	-1664.5± 16.7	61.2± 5.4	2.11
IC 2714	10.04	9.15	9.20	0.59	0.05	260.2	69.4	-2167.8± 58.1	191.6± 61.5	5.05
NGC 3960	7.76	7.43	7.43	0.27	0.02	211.9	44.6	-1670.9± 57.1	104.0± 34.7	3.56
NGC 4349	7.22	6.71	6.71	0.21	0.04	197.1	39.7	-1510.2±110.4	116.6±133.9	4.41
Collinder 261	7.54	7.07	7.46	0.22	0.03	205.0	41.7	-1597.6± 96.8	52.5± 7.7	1.88
NGC 5822	7.63	6.37	7.56	0.12	0.09	197.8	38.2	-1510.9± 64.4	63.9± 22.1	2.42
NGC 6087	7.44	6.40	6.50	0.08	0.08	196.1	37.3	-1494.7± 39.6	21.6± 10.8	0.83
NGC 6134	7.47	7.06	7.22	0.04	0.03	203.8	38.5	-1590.1± 49.3	25.1± 31.3	0.90
NGC 6192	9.49	6.40	6.74	0.07	0.19	221.9	42.7	-1702.3±103.1	20.2± 29.4	0.68
NGC 6281	7.57	7.21	7.44	0.11	0.02	206.8	40.0	-1622.2± 27.7	63.4± 9.8	2.24
IC 4651	7.79	7.06	7.44	0.18	0.05	207.8	41.7	-1626.1± 42.5	81.8± 16.1	2.88
NGC 6633	7.85	6.70	7.09	0.06	0.08	204.2	38.8	-1584.3± 13.2	20.8± 2.8	0.75
IC 4725	7.51	6.59	6.64	0.13	0.07	199.1	38.8	-1528.2± 39.2	72.6± 9.9	2.72
IC 4756	7.71	6.60	7.62	0.05	0.08	201.5	38.2	-1553.4± 18.4	16.5± 4.3	0.61
NGC 6404	6.26	5.28	5.76	0.11	0.09	171.0	33.4	-1202.5±251.4	55.8±203.3	2.65
NGC 6583	6.20	5.99	6.06	0.09	0.02	176.6	33.3	-1292.3±221.2	23.9±119.7	1.06
NGC 6791	8.79	4.73	5.62	1.15	0.30	199.2	61.0	-1294.0±118.4	276.3± 52.7	12.05
NGC 6819	7.87	7.54	7.79	0.48	0.02	215.0	51.0	-1692.0± 60.1	169.1± 78.2	5.71
NGC 6939	8.44	6.40	6.93	0.47	0.14	209.0	49.5	-1590.6± 81.4	171.9± 48.1	6.17
NGC 7160	8.24	7.02	8.15	0.09	0.08	212.6	41.0	-1673.8± 32.3	31.7± 12.3	1.08
NGC 7789	9.02	5.04	8.38	0.18	0.28	202.6	40.0	-1414.8± 47.1	72.8± 49.9	2.95
NGC 6253	8.18	6.65	6.98	0.21	0.10	208.2	42.5	-1610.4±85.5	75.3± 66.5	2.68
NGC 7142	8.91	7.25	7.35	1.10	0.10	226.4	69.9	-1740.1±42.3	415.8± 92.5	13.43
Berkeley 39	11.95	7.26	11.94	1.39	0.24	266.6	89.2	-2016.3±628.5	386.9±917.5	10.86
Berkeley 75	15.27	9.97	14.75	1.97	0.21	341.8	132.7	-2756.3±1453.5	510.3±267.7	10.48
Ruprecht 4	12.08	10.02	12.80	0.42	0.09	294.8	79.4	-2524.5±522.9	113.4±580.3	2.57
Thin-Thick disk										
Melotte 66	16.49	9.34	15.37	1.39	0.28	349.2	122.0	-2770.4±251.5	305.1±141.6	6.28
NGC 2425	10.36	5.97	6.25	0.91	0.27	231.6	66.7	-1668.8±106.3	386.4±151.9	13.03
Thick disk										
NGC 1193	12.16	4.51	9.28	1.33	0.46	244.6	78.1	-1451.2±213.9	445.3±191.3	17.05
NGC 2243	10.89	8.20	10.74	2.45	0.14	265.8	104.2	-2008.7±171.3	675.4±209.3	18.58
NGC 2266	11.89	7.44	9.03	1.93	0.23	269.6	100.0	-2009.3±196.1	618.0±173.4	17.09
Berkeley 18	13.47	8.87	10.09	6.92	0.21	314.4	151.5	-1854.2±271.6	1695.5±394.2	42.42
Berkeley 20	15.81	1.85	12.51	4.47	0.79	293.1	119.0	-587.2±671.0	686.2±411.1	49.43
Berkeley 21	14.45	4.79	9.94	6.68	0.50	292.6	131.6	-1104.5±477.2	1454.0±396.7	52.76
Berkeley 22	14.09	5.33	14.01	3.68	0.45	285.9	118.2	-1582.6±1246.3	951.1±1373.8	30.99
Berkeley 32	11.73	6.08	8.09	1.30	0.32	252.5	83.3	-1772.7±176.9	540.6±209.4	16.95
Berkeley 73	16.99	3.21	6.02	2.67	0.68	310.1	116.4	-1174.0±1803.5	721.0±1409.2	31.54
Tombaugh 2	13.34	10.02	10.03	2.94	0.14	316.7	124.7	-2518.9±558.6	842.2±531.8	18.48
Saurer 1	20.21	8.03	15.82	2.39	0.43	392.2	153.9	-2677.2±3480.7	616.8±1599.5	12.97

Cluster	R_a (kpc)	R_p (kpc)	R_{birth} (kpc)	z_{max} (kpc)	eccentricity	T_p (Myr)	T_z (Myr)	J_z (kpc km sec^{-1})	$J_\perp$ (kpc km sec^{-1})	Tilt (°)
					Thick disk-halo					
Berkeley 33	51.53	13.35	16.22	6.37	0.59	871.1	400.0	-5152.0±643.9	1195.0±304.2	13.05
					Halo					
Berkeley 25	17.99	8.46	17.38	11.40	0.36	378.5	179.0	-1239.8±2284.1	2453.0±1974.8	63.16
Berkeley 29	23.71	11.28	23.21	14.86	0.36	486.5	250.0	1829.9±1581.1	3143.8±1277.5	59.77
Berkeley 31	18.09	15.71	17.83	13.90	0.07	458.0	227.3	-2184.7±401.3	3274.2±741.6	56.26

Table 6.2: Our assignment of OCs to different spiral arms, based on the figure 6.4. Clusters are arranged in the order of increasing R_{birth}.

Cluster	Birth coordinates (kpc)			R_{birth}	metallicity	$EW_{reference}$
Name	x	y	z	(kpc)	[Fe/H] dex	
Norma arm						
NGC 6583	3.47	4.97	-0.09	6.06	0.29±0.01	Magrini2010
NGC 6087	6.47	-0.53	-0.02	6.50	-0.01±0.06	Gratton2000
IC 4725	6.48	-1.95	-0.13	6.64	0.17±0.06	Gratton2000
NGC 6939	6.17	3.16	0.37	6.93	0.07±0.01	Jacobson2007
NGC 2539	3.53	6.30	-0.31	7.23	-0.06±0.03	Our work
NGC 6281	7.42	0.56	0.07	7.44	0.04±0.06	Smiljanic2009
IC 4651	7.41	0.56	0.18	7.44	0.15±0.01	Santos2009
Collinder 261	7.42	0.78	0.01	7.46	0.08±0.09	Sestito2008
NGC 5822	7.50	0.97	-0.13	7.56	0.01±0.09	Smiljanic2009
IC 4756	7.61	-0.30	-0.03	7.62	0.04±0.04	Smiljanic2009
NGC 3114	6.52	4.32	0.06	7.82	0.02±0.09	Santos2009
NGC 2324	7.95	-0.50	-0.87	8.01	-0.09±0.03	Bragaglia2008
NGC 188	7.98	3.56	0.70	8.06	0.10±0.06	Friel2010
NGC 2158	-6.78	-4.93	-0.07	8.33	-0.15±0.18	Jacobson2009
NGC 2477	4.88	6.76	0.13	8.33	0.08±0.02	Bragaglia2008
NGC 2447	3.34	7.77	0.03	8.46	-0.10±0.03	Our work
NGC 2354	4.52	7.43	0.35	8.49	-0.19±0.04	Our work
NGC 2335	3.38	8.57	-0.10	9.21	-0.18±0.04	Our work
Berkeley 21	7.97	1.22	5.87	9.94	-0.32±0.04	Yong2012
Berkeley 25	6.74	-15.09	-5.38	17.38	-0.20±0.23	Carraro2007
Scutum arm						
NGC 6404	-5.28	2.31	0.11	5.76	0.03±0.07	Magrini2010
NGC 2425	-3.05	-5.94	-0.78	6.25	0.10±0.01	Jacobson2011
Collinder 110	0.92	-7.27	-0.29	7.33	-0.07±0.02	Pancino2010
NGC 3532	6.85	-3.43	0.08	7.66	0.05±0.04	Smiljanic2009
NGC 2141	7.15	-2.93	-0.37	7.75	-0.14±0.16	Jacobson2009
Collinder 350	-6.98	3.46	0.13	7.79	-0.16±0.04	Our work
Berkeley 32	7.73	2.10	-1.13	8.09	-0.19±0.04	Yong2012
NGC 2423	5.42	-6.77	0.01	8.67	0.14±0.06	Santos2009
NGC 2548	8.57	2.25	-0.13	8.86	-0.10±0.03	Our work
NGC 2266	8.76	1.77	1.31	9.03	-0.44±0.04	Our work
IC 2714	5.22	-7.56	-0.50	9.20	0.08±0.07	Smiljanic2009
NGC 1193	8.72	-2.94	-1.18	9.28	-0.16±0.09	Friel2010
NGC 2660	6.91	-6.49	-0.18	9.47	0.06±0.01	Bragaglia2008
NGC 2420	9.83	1.56	0.81	9.97	-0.04±0.01	Pancino2010
Berkeley 18	7.23	6.33	-3.12	10.09	-0.34±0.01	Yong2012
NGC 2506	8.82	5.32	-0.05	10.30	-0.20±0.06	Our work

Sagittarius arm						
NGC 6791	-4.99	2.58	0.18	5.62	0.37±0.17	Carretta2007
NGC 4349	-5.31	-4.11	0.14	6.71	-0.12±0.06	Santos2009
NGC 6253	-5.97	-3.60	-0.19	6.98	0.18±0.01	Carretta2007
NGC 6633	-6.30	-3.23	-0.06	7.09	0.01±0.04	Smiljanic2009
NGC 6134	6.62	2.90	-0.00	7.22	0.14±0.04	Smiljanic2009
NGC 2527	-5.43	-4.88	-0.08	7.31	-0.10±0.03	Our work
NGC 3960	-7.37	0.92	0.26	7.43	0.12±0.02	Bragaglia2008
IC 2602	-5.16	-5.78	-0.07	7.76	-0.06±0.06	D'Orazi2009
NGC 7160	-7.44	-3.28	-0.03	8.15	0.15±0.07	Monroe2010
NGC 2682	-4.46	-6.87	0.39	8.20	-0.08±0.02	Our work
NGC 752	-4.08	-7.28	0.20	8.35	-0.03±0.04	Our work
NGC 2251	-3.43	-7.62	0.00	8.37	-0.10±0.04	Our work
NGC 1912	1.62	-8.81	0.11	8.95	-0.10±0.04	Our work
NGC 2355	5.75	-7.74	-0.44	9.74	-0.12±0.01	Jacobson2011
NGC 1883	3.83	-10.62	0.48	11.30	-0.06±0.01	Jacobson2009
Berkeley 22	10.71	8.11	-3.95	14.01	-0.35±0.02	Yong2012
Berkeley 33	10.87	11.86	-2.02	16.22	-0.34±0.09	Carraro2007
Perseus arm						
NGC 2099	5.19	3.17	-0.01	6.08	-0.03±0.01	Pancino2010
NGC 6192	2.12	5.21	3.71	6.74	0.09±0.09	Magrini2010
NGC 1662	-1.99	7.63	0.03	7.90	-0.10±0.06	Our work
NGC 2482	-4.55	6.74	0.03	8.13	-0.07±0.04	Our work
NGC 7789	-8.37	-0.72	0.14	8.38	0.06±0.10	Pancino2010
NGC 1817	-6.57	7.16	0.96	9.76	-0.12±0.05	Our work
NGC 2194	7.16	-6.98	0.25	10.01	-0.11±0.01	Jacobson2011
Tombaugh 2	6.45	-7.59	-1.19	10.03	-0.31±0.10	Villanova2010
NGC 2360	-9.94	3.51	-0.25	10.55	-0.07±0.05	Our work
Berkeley 20	0.17	-11.93	-3.77	12.51	-0.27±0.06	Sestito2008
Ruprecht 4	-1.89	-12.66	0.27	12.80	-0.04±0.10	Carraro2007
Berkeley 31	16.65	0.47	-6.35	17.83	-0.24±0.07	Friel2010
Cygnus arm						
NGC 1245	5.26	8.65	1.41	10.22	-0.06±0.03	Jacobson2011
NGC 2243	-8.83	-5.48	-2.73	10.74	-0.42±0.08	Jacobson2011
Berkeley 75	1.97	14.61	-0.07	14.75	-0.28±0.22	Carraro2007
Melotte 66	-15.00	-3.07	1.37	15.37	-0.14±0.02	Sestito2008
Outer arm						
Berkeley 39	-6.41	9.97	-1.44	11.94	-0.10±0.03	Friel2010
Berkeley 29	-15.78	3.45	16.62	23.21	-0.36±0.07	Sestito2008

Chapter 7

Conclusions and Future Directions

7.1 Summary

The study of the structure and formation of the Milky Way Galaxy is essential to improve our knowledge on the evolution of disks in galaxies in the early universe and their forms today. In this regard, the Galactic OCs are suitable candidates to provide strong observational constraints to the Galactic chemical evolution models through the study of radial abundance gradients and its evolution with time. In addition, the study of intracluster abundance variations, especially in the α- and the heavy elements, enable us to chemically tag groups of field stars to their parent cluster (Freeman & Bland-Hawthorn 2002). In this thesis work, we have mainly concentrated on the estimatation of chemical abundances from OCs and its implication to the evolution of Milky Way galaxy. Though the chemical tagging is not carried out in this work, we could identify the elements that could serve as useful tools to tag the field stars back to their parent cluster to form large star forming aggregates (see Section 5.2.2 in Chapter 5). However, we have estimated the birthplace of OCs using their space motion and a model of the Galactic gravitational potential. Addressing abundance variations across the Galactic disk as well as azimuthal variations and applying chemical tagging requires homogeneous and accurate abundance analysis of as large sample of OCs as possible.

We have obtained high quality and high-dispersion echelle spectra ($R \geq 55,000$) of red giant members for a sample of eighteen OCs and measured abundances for many elements representing different production mechanisms (α- and r- process, Fe-Peak and s-process) and sites (i.e. SNII, SNIa and AGB environments). The basic observation procedures, data reduction and differential abundance analysis techniques relative to the Sun are discussed in Chapter 2 and Chapter 3.

In Chapter 4, we have discussed spectroscopic abundance analysis techniques employed for the estimatation of chemical composition of OCs under study and presented abundances for various elements from Na to Eu including the s- and r-process elements for which the measurements are lacking in the literature. *We maintained the homogeneity throughout the analysis* i.e. observing only red giants and those with very similar colors to narrow down the spread in temperature and gravities, usage of same linelist/atomic data and model atmosphere grid for abundance analysis to reduce the random errors. The errors of the average abundance for a cluster are generally in the 0.02 to 0.08 dex range. Synthetic spectra were computed for species affected by hyperfine and isotopic splitting or affected by blends. We have tested our linelists extensively to reproduce the solar and Arcturus spectra and measured the solar abundances to establish a reference abundance scale. Our sample of OCs covers galactocentric distances (R_{gc}) of 7.8 to 11.3 kpc, [Fe/H] $\sim$ -0.4 dex to solar and an age range of 0.2 to 1.2 Gyr, with an exception of NGC 2682 (M67) with an age of 4.3 Gyr.

Results and interpretation

In Chapter 5, we have discussed our results while making comparison with the thin and thick disk sample of giants in the field and finally with the available OC data in the literature. We also discussed the evolution of elemental abundance ratios, [X/Fe], as a function of metallicity and age and its connection to chemical enrichment of the Milky Way. Comparison of our results with published abundances for thin disk field giants from Luck & Heiter (2007) suggest that

- Both the field giants and OCs of near-solar metallicity have very similar, if not identical, compositions within the errors of measurements for α-, Fe-peak and r-process elements. *This supports the view that field stars come from disrupted OCs.*

- We have noticed a small but significant enrichment in mean [s/Fe] ratios and depletion of [Mn/Fe] and [Cu/Fe] for OCs over field giant mean values. *The observed offset in Mn and Cu abundances might be lack of hyperfine structure treatment in the analysis of Luck & Heiter's sample of field giants (for details, see Reddy et al. 2013).*

Since, our OCs are relatively younger than the Luck & Heiter's sample of field giants, the enrichment in [s/Fe] ratios reflects that the Galaxy has received significant contribution from low mass AGB stars (Reddy et al. 2013). In this vein, we note that Maiorca et al. (2011) have suggested a strong s-process enrichment for young metal-rich OCs.

- *We find intracluster abundance variations larger than measurement uncertainties for some s-process elements, for example Zr and Ba.* These differences mark the signatures that these clusters had formed under different environmental conditions unique to the time and site of formation.

Hence, the abundance of s-process elements (and ratios such as [Ba/α, r-process]) could serve as useful tools to tag the field stars back to their parent cluster to form large star forming aggregates. Such studies eventually improve our basic understanding of Galactic chemical evolution processes.

Radial metallicity distribution and interpretation: In Chapter 6, we have investigated the radial abundance distribution in the Galactic disk using the homogeneous dataset and a possible connection between the observed gradients and the spiral density waves has been discussed. We merged our sample of OCs with the available high-quality results from the literature to enlarge the dataset. Since, the abundances are collected from various literature papers, the data are liable to systematic errors, especially concerning the atomic data and model atmospheres employed and the reference solar abundances adopted by different authors in their studies. To cancel out such an errors and place all the results on *a common abundance scale*, we have reestimated the cluster abundances from the line equivalent widths collected from varioud literature resources and using our models and linelists. We recalculated the R_{gc} value for each of these clusters, assuming $R_\odot = 8.0\pm0.6$ kpc (Ghez et al.2008), to bring them to *a common distance scale.*

Now, the whole sample (77 OCs) covers a range of 5.0 to 24.0 kpc in R_{gc}, ~ -0.5 to 0.3 dex in metallicity and an age of few Myr to 9 Gyr. Here, we emphasize that *our sample contribute about 23% of the total OCs explored so far with high quality and high-dispersion spectroscopy. However, ours is a homogeneous and comprehensive abundance analysis extending even to s- and r-process elements for which the measurements are often lacking in the literature.* We have also derived membership probabilities, as described in Reddy et al. (2006), and assigned these OCs to either thin, thick or halo populations to know their kinematic origin.

We perceive the distribution of OC mean [Fe/H] with galactocentric distance as a smoothly decreasing function of R_{gc}, with a change of slope at R_{gc} ~13-14 kpc that flattens out at larger radii, modulated by a scattering of clusters along R_{gc} near 8-9 kpc and 11-12 kpc (see Figure 6.1 in Chapter 6). A simple linear fit to the whole data with Rgc $\leq$ 14 kpc yields an abundance gradient, $\frac{d[Fe/H]}{dR_{gc}}$, of -0.056 ± 0.007 dex/kpc and for $14 \lesssim R_{gc} \lesssim 23$ kpc yields a gradient of -0.007 ± 0.008 dex kpc^{-1} which is consistent with the zero slope. However, none of the existing chemical evolution models succeed in predicting the size and shape of observed metallicity gradient in the Galactic disk (e.g., Heiter et al. 2013).

We interpreted our results as due to the dynamical interaction of the disk material with the spiral density waves. Later, in order to ascertain the role of radial migration in shaping the abundance distribution we studied the dynamics of these OCs using a multicomponent Galactic gravitational potential model of Flynn et al. (1996) and derived birthplaces and other orbital parameters. The main results of our investigation are as follows.

- A large fraction of OCs were born close to the Galactic centre in the R_{gc} interval 6-11 kpc and hence it might be a privileged zone for star formation.

- We notice, by the superposition of OC birthplaces on a logarithmic four arm spiral model of Vallee (2002), that all the OCs are nicely tracking the spiral arms. This may suggest that spiral arms are the potential reservoirs to churn the OCs out of the interstellar matter.

- The orbital plane of thick disk and halo populations is more tilted with respect to the Galactic plane, while for the thin disk OCs it is confined to latitudes (b) $\simeq \pm 10^\circ$ (see table 6.1 in Chapter 6). This is beacuse the clusters moving outwards will feel less gravitational pull than those closer to the Galactic centre and finally increases their amplitude of oscillation in the z direction.

- In the current epoch, the presence of many old OCs (most of them showing either thick disk or halo membership) even beyond Rgc $\geq$ 11 kpc (see Figure 6.1 in Chapter 6) favours the OC migration as a possible explanation.

To investigate the radial distance at which the OC migration is more effective, we pursued the classical theory of galactic spiral waves (Lin & Shu 1964) and their resonance interactions with the disk material. For any given rotation curve, the position of the resonances are set by the pattern speed, ω_p, of the spiral waves. More recent values of ω_p from Naoz & Shaviv (2007) places the corotation resonances around Rgc $\sim$ 8.0 kpc (for m = 4) and $\sim$ 11.5 kpc (for m = 2). *This indicate that the metallicity spread near 8-9 kpc and 11-12 kpc might be caused by the resonance interaction of disk material with spiral density waves and hence the subsequent exchange of metal rich gas and OCs near corotation.*

We also notice that clusters with thin, thick and halo memberships show very similar [α/Fe] ratios at all R_{gc} values. This may suggest that at these overlapping metallicities ([Fe/H] $\simeq -0.5$ dex to solar) both the thin and thick disk share same [α/Fe] ratios. Recently, Bensby et al. (2007) demonstrated from their analysis of solar neighborhood field dwarfs that the thick disk has evolved to solar metallicities and experienced strong enrichment from SNe II and SNe Ia. Such stars also show low s-process abundances over thin disk mean values. This is not well established for OCs as there are no thick disk OCs with near solar metallicity in the present sample and many of them lack their s-process abundances measured. *This need to be investigated in our future studies by observing clusters beyond $R_{gc} \geq 13$ kpc where the probability to find the thick disk OCs is high.* This is due to the fact that old OCs survive longer in the outer disk where the probability of encounter with a giant molecular clouds is lower when compared to the inner disk regions (details are given in Section 6.2 of Chapter 6).

As an end note, to strengthen all the above observational aspects and fit them well into the frame work of galaxy formation and evolution theory we need larger sample of OCs with all the parameters analysed in a homogeneous way.

7.2 Future Directions

(1) We would continue high-dispersion abundance analysis to distant OCs, especially for $R_{gc} > 13$ kpc, where the spectroscopic data is scarce. As the cluster members at such a distances are quite faint, we wish to carry out our observations with the 8-10 metre class telescopes such as Keck I & II.

(2) We have a plan to extend our abundance analysis techniques to the young OCs (age ≤ 100 Myr) which are potential candidates to study the s-process enrichment in the Galactic disk.

(3) By coupling the cluster kinematics, dynamics and chemistry we wish to interpret the origin of these OCs. The present thesis is completely based on the observational aspects of galaxy formation and its evolution. In the future we wish to deal with theoretical aspects and would like to evaluate the impact of radial migration in shaping the abundance distribution along and across the Galactic disk.

(4) We are interested in studying the azimuthal gradients in the disk to confirm or deny the same noticed for a sample of Cepheids in the literature. The present OC sample does not give any clues on such gradients as data is concentrated more in the radial than in azimuthal direction (see Figure 6.2 in Chapter 6) . Such a study impose severe constraints on the chemical evolution models based on usual assumption of instantaneous mixing of the enriched gas in the azimuthal direction.

(5) We would like to study the vertical gradients in the disk using OCs, whose absence (presence) indicate a fast (slow) dissipational collapse of halo gas onto the disk. This is one of the important ingredients of the galactic chemical evolution models.

(6) It is also of our interest to study the [α/Fe], [s/Fe] and [r/Fe] ratios as a function of [Fe/H], R_{gc} and cluster's age for a larger sample.

We emphasize that all these studies would provide better insights into the evolution of disks in galaxies in time and space.

Chapter 8

Appendix

Table 8.1: The adopted linelist for the derivation of solar abundances. All the columns of the adopted linelist are self-explanatory and the lines are arranged in the increasing order of LEP.

Atom	Wavelength (Å)	LEP^1 (eV)	log gf	$W_{\lambda,\odot}$ (mÅ)	Ref^a
Na I	4668.567	2.100	-1.31	53.4	NIST
	4982.821	2.100	-0.91	79.0	NIST
	5688.210	2.100	-0.45	115.4	NIST
	6154.224	2.100	-1.55	36.3	NIST
	6160.746	2.100	-1.27	55.9	NIST
Mg I	5711.090	4.340	-1.72	104.5	NIST
	6318.708	5.108	-1.90	42.9	NIST
	6319.234	5.108	-2.32	22.7	NIST
	6319.486	5.108	-2.80	10.6	NIST
	7691.552	5.750	-0.78	115.2	NIST
	5528.453	4.340	-0.50	256.1	NIST
	7659.897	5.110	-1.96	41.5	NIST
Al I	7084.564	4.020	-0.93	21.4	KUR
	5557.044	3.140	-2.10	13.0	NIST
	7835.296	4.020	-0.47	41.2	NIST
	7836.119	4.020	-0.34	55.4	NIST
Si I	5665.551	4.920	-2.04	39.4	NIST
	5645.606	4.930	-2.14	34.9	LUCK
	5701.100	4.930	-2.15	37.7	NIST
	5753.632	5.610	-1.30	42.5	LUCK
	6131.570	5.610	-1.71	22.3	LUCK
	6131.851	5.610	-1.69	23.3	LUCK
	6145.013	5.610	-1.48	36.5	LUCK
	6237.319	5.610	-1.14	56.7	LUCK
	6244.470	5.610	-1.26	45.1	LUCK
	6243.812	5.613	-1.26	46.5	KUR
	6142.486	5.620	-1.54	33.0	LUCK
	6721.840	5.862	-1.06	42.8	LUCK
	6195.445	5.873	-1.80	14.9	LUCK
Ca I	6122.221	1.890	-0.32	161.9	LUCK
	5581.971	2.520	-0.56	93.7	LUCK
	5590.117	2.520	-0.74	91.7	LUCK
Ca I	6166.434	2.520	-1.14	69.2	LUCK
	6169.560	2.520	-0.47	108.5	LUCK
	6455.599	2.520	-1.29	56.2	LUCK
	6499.649	2.520	-0.82	85.0	LUCK
	6471.662	2.526	-0.69	90.7	LUCK
Sc I	5686.832	1.440	0.38	8.3	LUCK
	5356.090	1.860	0.17	2.3	LUCK
	5671.813	1.448	0.49	13.8	NIST
Sc II	6604.587	1.357	-1.31	35.1	NIST
	5667.141	1.500	-1.20	30.0	KUR
	6245.615	1.507	-1.03	35.4	KUR
	6300.681	1.507	-1.89	8.1	KUR
	5526.813	1.768	-0.22	75.6	KUR
Ti I	5039.960	0.021	-1.13	75.7	NIST
	5460.497	0.048	-2.75	9.6	LUCK
	4999.510	0.826	0.31	103.6	LUCK
	5020.026	0.836	-0.35	72.6	KUR
	5295.776	1.067	-1.63	13.1	NIST
	5474.223	1.460	-1.17	10.8	NIST
	5490.148	1.460	-0.88	21.6	NIST
	4617.274	1.749	0.39	61.2	NIST
	5739.980	2.236	-0.67	7.3	NIST
	5702.656	2.292	-0.57	8.1	NIST
Ti II	4764.528	1.237	-2.77	37.2	LUCK
	4708.665	1.240	-2.37	52.9	NIST
	5005.168	1.566	-2.73	25.5	NIST
	5381.022	1.566	-1.85	57.3	LUCK
	5396.244	1.580	-3.02	12.1	LUCK
	5336.788	1.582	-1.63	69.2	NIST
	5418.767	1.582	-2.11	48.1	KUR
V I	6251.823	0.286	-1.34	15.8	NIST
	6111.647	1.043	-0.71	10.7	NIST

V I	5727.653	1.051	-0.87	8.9	NIST
	6135.366	1.051	-0.75	10.4	NIST
	5737.062	1.064	-0.74	10.8	NIST
	5668.365	1.081	-1.03	5.6	NIST
	5670.848	1.081	-0.42	19.0	NIST
	5727.044	1.081	-0.01	39.9	NIST
Cr I	4545.958	0.941	-1.37	81.1	SLS
	5296.696	0.983	-1.36	91.0	SLS
	5300.747	0.983	-2.00	58.3	SLS
	5345.802	1.004	-0.95	112.2	SLS
	5238.959	2.709	-1.30	16.1	SLS
	5329.139	2.910	-0.06	65.8	KUR
	5784.967	3.321	-0.38	31.2	NIST
	5214.129	3.369	-0.74	17.1	NIST
	5628.640	3.422	-0.74	14.4	SLS
	5287.174	3.440	-0.87	10.7	SLS
	5312.853	3.449	-0.55	19.8	SLS
	5304.178	3.463	-0.67	15.4	SLS
Cr II	5279.874	4.070	-2.10	19.0	NIST
	5308.424	4.071	-1.81	25.3	NIST
	5237.321	4.073	-1.16	52.6	NIST
	5334.864	4.073	-1.56	33.6	KUR
	5313.578	4.074	-1.65	33.4	NIST
	5502.081	4.170	-1.99	18.3	NIST
Mn I	6013.488	3.072	-0.25	84.9	NIST
	6021.796	3.075	0.03	90.7	NIST
	5377.608	3.845	-0.11	48.0	KUR
	5399.480	3.850	-0.29	37.4	KUR
Fe I	6136.995	2.198	-2.95	65.6	F&W
	6252.562	2.404	-1.69	120.9	F&W
	5141.742	2.424	-2.24	84.5	F&W
Fe I	5701.548	2.559	-2.22	83.8	F&W
	6646.931	2.608	-3.95	9.3	KUR
	5036.918	3.018	-3.04	24.5	F&W
	5215.184	3.266	-0.87	119.7	F&W
	5576.093	3.431	-0.94	106.2	F&W
	5568.863	3.635	-2.95	10.3	LUCK
	5636.695	3.640	-2.61	20.7	F&W
	5760.343	3.642	-2.44	22.9	F&W
	5539.278	3.643	-2.61	18.7	F&W
	6411.653	3.654	-0.72	116.9	F&W
	5466.986	3.655	-2.23	32.5	F&W
	6336.828	3.687	-0.86	101.9	F&W
	5379.574	3.695	-1.51	60.5	F&W
	6003.014	3.882	-1.15	81.6	NIST
	6187.988	3.943	-1.67	46.0	F&W
	5293.957	4.143	-1.84	28.7	F&W
	6165.358	4.143	-1.47	43.9	F&W
	5608.973	4.209	-2.40	10.4	LUCK
	5618.631	4.209	-1.28	49.6	F&W
	5074.753	4.221	-0.23	114.3	F&W
	5738.230	4.221	-2.34	11.8	LUCK
	5579.338	4.231	-2.40	10.6	LUCK
	5016.477	4.256	-1.69	32.7	LUCK
	5090.783	4.256	-0.44	90.1	NIST
	5243.777	4.256	-1.12	59.9	F&W
	5646.682	4.261	-2.50	7.1	LUCK
	5717.832	4.284	-1.10	60.5	F&W
	5197.934	4.301	-1.62	35.5	F&W
	5466.398	4.371	-0.63	77.0	LUCK
	5295.312	4.415	-1.67	28.5	F&W
	5560.210	4.435	-1.16	50.5	F&W

Fe II	6369.460	2.891	-4.11	19.5	M&B
	6432.680	2.891	-3.57	40.9	M&B
	5256.931	2.892	-4.06	21.1	M&B
	5425.260	3.199	-3.22	42.6	M&B
	6084.103	3.199	-3.88	20.2	F&W
	5234.620	3.221	-2.18	84.8	M&B
	5414.067	3.221	-3.58	27.7	M&B
	6149.244	3.889	-2.84	35.8	F&W
	6247.559	3.892	-2.43	52.1	F&W
	6456.383	3.903	-2.19	61.0	F&W
Co I	6116.994	1.785	-2.49	6.0	NIST
	5647.232	2.280	-1.56	13.8	NIST
	5212.680	3.514	-0.14	19.2	KUR
	6454.990	3.632	-0.25	14.6	NIST
	5342.701	4.022	0.69	30.8	KUR
Ni I	5578.720	1.676	-2.64	55.3	NIST
	5748.352	1.676	-3.26	27.6	NIST
	6191.181	1.677	-2.35	71.0	KUR
	6177.242	1.826	-3.51	14.4	NIST
	4998.229	3.606	-0.78	52.9	NIST
	5462.493	3.847	-0.93	38.6	NIST
	5468.103	3.847	-1.61	12.4	NIST
	5589.357	3.898	-1.14	27.6	NIST
	5593.736	3.898	-0.84	40.2	NIST
	5638.745	3.898	-1.73	9.5	NIST
Ni I	6111.072	4.088	-0.87	32.7	NIST
	5625.316	4.089	-0.70	37.7	NIST
	5682.199	4.105	-0.47	50.4	NIST
	5760.830	4.105	-0.80	33.9	NIST
Cu I	5218.201	3.820	0.26	49.3	NIST
Zn I	4722.160	4.030	-0.34	65.0	KUR
	6362.342	5.790	0.27	28.1	LUCK
Y II	5200.409	0.992	-0.57	36.3	HLG
	4982.133	1.033	-1.29	13.3	HLG
	5289.817	1.033	-1.85	4.0	HLG
	4883.688	1.080	0.07	54.3	HLG
	5402.773	1.840	-0.63	12.3	LUCK
Zr I	6143.201	0.070	-1.10	2.1	BGHL
	4739.483	0.650	0.23	6.2	BGHL
Ba II	5853.678	0.604	-1.02	62.5	LUCK
	6496.905	0.604	-0.37	97.8	LUCK
La II	5303.538	0.321	-1.35	4.4	LBS
	6390.486	0.321	-1.41	3.0	LBS
Ce II	5472.281	1.240	-0.18	2.1	LUCK
Nd II	5092.800	0.380	-0.61	6.5	DLS
	5319.813	0.550	-0.14	11.4	DLS
	5485.539	1.260	-0.12	4.1	DLS
Sm II	4519.630	0.544	-0.35	6.1	LDS
Eu II	6645.108	1.379	0.12	4.80	LWD

[a] References for the adopted gf-values:

BGHL−Biémont et al. (1981)
F&W−Führ & Wiese (2006)
HLG−Hannaford et al. (1982)
KUR−Kurucz (1998)
LWD−Lawler et al. (2001)
LBS−Lawler et al. (2001)
LDS−Lawler et al. (2006)
LSC−Lawler et al. (2009)
LUCK−Luck (Private communication)
M&B−Meléndez & Barbuy (2009)
SLS−Sobeck et al. (2007);
NIST−Atomic Spectra Database[1]

Table 8.2: Elemental abundances for stars in the OC NGC 752. The abundances calculated by synthesis are presented in bold typeface while the remaining elemental abundances were calculated using line EWs. Numbers in the parentheses indicate the number of lines used in calculating the abundance of that element.

Species	#77	#137	#295	#311	Average
[Na I/Fe]	+0.13 ± 0.05(3)	+0.10 ± 0.03(3)	+0.14 ± 0.02(3)	+0.13 ± 0.07(3)	+0.12 ± 0.02
[Mg I/Fe]	−0.01 ± 0.07(3)	+0.02 ± 0.05(2)	−0.06 ± 0.05(3)	−0.01 ± 0.04(3)	−0.01 ± 0.03
[Al I/Fe]	+0.19 ± 0.04(3)	+0.11 ± 0.03(4)	+0.14 ± 0.04(3)	+0.17 ± 0.02(3)	+0.15 ± 0.02
[Si I/Fe]	+0.12 ± 0.05(13)	+0.03 ± 0.05(10)	+0.11 ± 0.07(12)	+0.18 ± 0.06(14)	+0.11 ± 0.03
[Ca I/Fe]	+0.01 ± 0.07(8)	+0.03 ± 0.05(7)	+0.06 ± 0.05(7)	+0.01 ± 0.06(8)	+0.03 ± 0.03
[Sc I/Fe]	+0.07 ± 0.04(6)	+0.06 ± 0.10(3)	+0.12 ± 0.03(5)	+0.03 ± 0.05(4)	+0.07 ± 0.03
[Sc II/Fe]	−0.03 ± 0.04(6)	+0.19 ± 0.03(5)	+0.01 ± 0.05(5)	+0.01 ± 0.03(6)	+0.04 ± 0.02
[Ti I/Fe]	−0.03 ± 0.06(13)	−0.14 ± 0.04(15)	−0.02 ± 0.06(13)	−0.08 ± 0.06(13)	−0.07 ± 0.03
[Ti II/Fe]	−0.06 ± 0.08(6)	−0.06 ± 0.09(5)	0.00 ± 0.09(7)	−0.03 ± 0.06(7)	−0.04 ± 0.04
[V I/Fe]	+0.11 ± 0.06(10)	−0.05 ± 0.07(6)	+0.05 ± 0.04(12)	+0.03 ± 0.05(10)	+0.03 ± 0.03
[V II/Fe]	0.00 ± 0.07(3)	...	+0.04 ± 0.08(3)	+0.07 ± 0.08(3)	+0.04 ± 0.04
[Cr I/Fe]	−0.02 ± 0.05(12)	−0.07 ± 0.04(11)	−0.04 ± 0.07(11)	0.00 ± 0.06(11)	−0.03 ± 0.03
[Cr II/Fe]	+0.06 ± 0.05(4)	−0.03 ± 0.06(6)	+0.01 ± 0.02(4)	+0.04 ± 0.02(4)	+0.02 ± 0.02
[Mn I/Fe]	**−0.11**	**−0.18**	−0.12	**−0.10**	**−0.13**
[Fe I/H]	−0.04 ± 0.05(48)	−0.02 ± 0.06(46)	−0.05 ± 0.05(43)	−0.04 ± 0.05(43)	−0.04 ± 0.03
[Fe II/H]	−0.02 ± 0.05(13)	0.00 ± 0.05(12)	−0.04 ± 0.06(13)	−0.04 ± 0.04(13)	−0.02 ± 0.02
[Co I/Fe]	−0.03 ± 0.05(5)	−0.08 ± 0.05(7)	0.00 ± 0.08(6)	+0.04 ± 0.06(5)	−0.02 ± 0.03
[Ni I/Fe]	+0.01 ± 0.03(12)	−0.04 ± 0.06(11)	−0.01 ± 0.05(14)	0.00 ± 0.05(13)	−0.01 ± 0.02
[Cu I/Fe]	**−0.03**	**−0.12**	**−0.15**	**−0.13**	**−0.11**
[Zn I/Fe]	−0.09 ± 0.00	...	−0.07 ± 0.00	−0.14 ± 0.00	−0.10 ± 0.00
[Rb I/Fe]	**−0.24**	**−0.22**	**−0.16**	**−0.19**	**−0.20**
[Y II/Fe]	+0.03 ± 0.01(3)	−0.01 ± 0.04(6)	+0.06 ± 0.02(4)	+0.03 ± 0.03(4)	+0.03 ± 0.01
[Zr I/Fe]	+0.06 ± 0.01(3)	−0.05 ± 0.01(3)	+0.16 ± 0.02(3)	+0.06 ± 0.01(4)	+0.06 ± 0.01
[Ba II/Fe]	**+0.14**	**+0.12**	**+0.16**	**+0.11**	**+0.13**
[La II/Fe]	+0.15 ± 0.06(2)	+0.07 ± 0.08(2)	+0.14 ± 0.06(2)	+0.16 ± 0.06(2)	+0.13 ± 0.03
[Ce II/Fe]	**+0.13**	**+0.08**	**+0.14**	**+0.16**	**+0.13**
[Nd II/Fe]	+0.07 ± 0.09(3)	+0.02 ± 0.04(4)	+0.06 ± 0.03(3)	+0.10 ± 0.04(4)	+0.06 ± 0.03
[Sm II/Fe]	**+0.08**	...	**+0.07**	**+0.11**	**+0.08**
[Eu II/Fe]	**+0.10**	**+0.00**	**+0.09**	**+0.08**	**+0.07**

Table 8.3: Same as table 8.2 but for stars in cluster NGC 1817.

Species	#8	#81	#73	Average
[Na I/Fe]	+0.15 ± 0.04(3)	+0.23 ± 0.03(4)	+0.09 ± 0.04(4)	+0.16 ± 0.02
[Mg I/Fe]	+0.03 ± 0.03(3)	+0.12 ± 0.06(4)	+0.08 ± 0.01(2)	+0.08 ± 0.02
[Al /Fe]I	+0.10 ± 0.03(3)	+0.12 ± 0.03(2)	+0.12 ± 0.06(2)	+0.11 ± 0.02
[Si I/Fe]	+0.05 ± 0.06(12)	+0.12 ± 0.06(10)	+0.14 ± 0.06(10)	+0.10 ± 0.03
[Ca I/Fe]	+0.19 ± 0.04(9)	+0.20 ± 0.05(9)	+0.04 ± 0.04(9)	+0.14 ± 0.02
[Sc II/Fe]	0.00 ± 0.05(5)	−0.04 ± 0.08(5)	+0.04 ± 0.06(5)	0.00 ± 0.04
[Ti I/Fe]	+0.07 ± 0.05(8)	+0.04 ± 0.06(7)	−0.11 ± 0.03(8)	0.00 ± 0.03
[Ti II/Fe]	+0.09 ± 0.04(9)	−0.06 ± 0.06(9)	+0.03 ± 0.05(9)	+0.02 ± 0.03
[V I/Fe]	+0.06 ± 0.04(8)	−0.01 ± 0.05(8)	−0.01 ± 0.07(10)	+0.01 ± 0.03
[Cr I/Fe]	−0.02 ± 0.05(11)	−0.02 ± 0.05(11)	+0.03 ± 0.06(13)	0.00 ± 0.03
[Cr II/Fe]	−0.01 ± 0.05(6)	+0.01 ± 0.05(4)	+0.08 ± 0.06(5)	+0.03 ± 0.03
[Mn I/Fe]	**−0.17**	**−0.14**	**−0.24**	**−0.18**
[Fe I/H]	−0.15 ± 0.05(30)	−0.14 ± 0.05(43)	−0.11 ± 0.05(45)	−0.13 ± 0.03
[Fe II/H]	−0.11 ± 0.06(11)	−0.14 ± 0.06(11)	−0.09 ± 0.06(11)	−0.11 ± 0.03
[Co I/Fe]	+0.03 ± 0.08(5)	+0.10 ± 0.05(4)	−0.03 ± 0.07(5)	+0.03 ± 0.04
[Ni I/Fe]	0.00 ± 0.03(11)	−0.03 ± 0.05(13)	−0.02 ± 0.05(12)	−0.02 ± 0.02
[Cu I/Fe]	**−0.22**	**−0.23**	**−0.24**	**−0.23**
[Zn I/Fe]	−0.06 ± 0.00(1)	+0.11 ± 0.00(1)	−0.07 ± 0.00(1)	0.00 ± 0.00
[Rb I/Fe]	**−0.02**	**−0.13**	**−0.20**	**−0.12**
[Y II/Fe]	+0.10 ± 0.08(5)	+0.03 ± 0.07(5)	+0.07 ± 0.03(4)	+0.07 ± 0.04
[Zr I/Fe]	+0.14 ± 0.00(1)	+0.11 ± 0.08(2)	−0.01 ± 0.06(2)	+0.08 ± 0.03
[Ba II/Fe]	**+0.16**	**+0.11**	**+0.12**	**+0.13**
[La II/Fe]	+0.16 ± 0.06(1)	+0.09 ± 0.06(1)	+0.12 ± 0.06(2)	+0.12 ± 0.03
[Ce II/Fe]	**+0.22**	**+0.19**	**+0.18**	**+0.20**
[Nd II/Fe]	+0.14 ± 0.07(4)	+0.17 ± 0.03(3)	+0.12 ± 0.05(3)	+0.14 ± 0.03
[Sm II/Fe]	**+0.22**		**+0.21**	**+0.21**
[Eu II/Fe]	**+0.16**	...	**+0.11**	**+0.13**

Table 8.4: Same as table 8.2 but for stars in cluster NGC 2360.

Species	#5	#6	#8	#12	Average
[Na I/Fe]	$+0.14 \pm 0.07(3)$	$+0.23 \pm 0.06(4)$	$+0.21 \pm 0.05(3)$	$+0.24 \pm 0.04(4)$	$+0.20 \pm 0.03$
[Mg I/Fe]	$-0.06 \pm 0.01(3)$	$+0.13 \pm 0.07(4)$	$+0.13 \pm 0.08(4)$	$+0.10 \pm 0.04(2)$	$+0.07 \pm 0.03$
[Al I/Fe]	$+0.18 \pm 0.06(2)$	$0.00 \pm 0.01(3)$	$+0.19 \pm 0.05(3)$	$-0.01 \pm 0.05(3)$	$+0.09 \pm 0.02$
[Si I/Fe]	$+0.14 \pm 0.06(15)$	$+0.18 \pm 0.06(14)$	$+0.14 \pm 0.05(11)$	$+0.16 \pm 0.06(5)$	$+0.15 \pm 0.03$
[Ca I/Fe]	$+0.03 \pm 0.05(8)$	$+0.14 \pm 0.06(9)$	$+0.16 \pm 0.04(8)$	$+0.13 \pm 0.06(11)$	$+0.11 \pm 0.03$
[Sc I/Fe]	$+0.19 \pm 0.01(2)$	$+0.14 \pm 0.06(4)$	...	$-0.10 \pm 0.06(3)$	$+0.06 \pm 0.03$
[Sc II/Fe]	$0.00 \pm 0.03(6)$	$+0.15 \pm 0.07(5)$	$+0.05 \pm 0.06(5)$	$-0.09 \pm 0.03(5)$	$+0.03 \pm 0.02$
[Ti I/Fe]	$+0.04 \pm 0.04(13)$	$+0.02 \pm 0.07(12)$	$+0.01 \pm 0.05(11)$	$-0.18 \pm 0.07(13)$	-0.03 ± 0.03
[Ti II/Fe]	$+0.07 \pm 0.02(2)$	$0.00 \pm 0.07(8)$	$0.00 \pm 0.05(7)$	$-0.10 \pm 0.02(7)$	0.00 ± 0.02
[V I /Fe]	$+0.23 \pm 0.05(12)$	$+0.04 \pm 0.06(9)$	$+0.06 \pm 0.05$	$-0.01 \pm 0.07(5)$	$+0.08 \pm 0.03$
[V II/Fe]	...	$-0.05 \pm 0.09(3)$	$-0.06 \pm 0.09(2)$	...	-0.05 ± 0.02
[Cr I/Fe]	$0.00 \pm 0.05(11)$	$+0.02 \pm 0.06(14)$	$+0.02 \pm 0.03(10)$	$+0.02 \pm 0.05(13)$	$+0.01 \pm 0.02$
[Cr II/Fe]	$+0.02 \pm 0.08(4)$	$+0.01 \pm 0.06(6)$	$-0.04 \pm 0.03(6)$	$+0.02 \pm 0.06(7)$	0.00 ± 0.03
[Mn I/Fe]	$-\mathbf{0.14}$	$-\mathbf{0.18}$	$-\mathbf{0.20}$	...	$-\mathbf{0.21}$
[Fe I/H]	$-0.07 \pm 0.07(54)$	$-0.13 \pm 0.05(32)$	$-0.05 \pm 0.06(43)$	$-0.06 \pm 0.07(60)$	-0.08 ± 0.03
[Fe II/H]	$-0.07 \pm 0.04(11)$	$-0.10 \pm 0.04(10)$	$-0.06 \pm 0.06(10)$	$-0.04 \pm 0.05(9)$	-0.07 ± 0.02
[Co I/Fe]	$+0.17 \pm 0.07(7)$	$0.00 \pm 0.07(6)$	$+0.05 \pm 0.06(6)$	$+0.03 \pm 0.09(9)$	$+0.06 \pm 0.04$
[Ni I/Fe]	$-0.02 \pm 0.06(15)$	$+0.01 \pm 0.04(13)$	$+0.02 \pm 0.06(14)$	$+0.04 \pm 0.08(16)$	$+0.01 \pm 0.03$
[Cu I/Fe]	$-\mathbf{0.20}$	$-\mathbf{0.16}$	$-\mathbf{0.23}$	$-\mathbf{0.13}$	$-\mathbf{0.18}$
[Zn I/Fe]	...	$+0.05 \pm 0.00(1)$	...	$+0.03 \pm 0.00(1)$	$+0.04 \pm 0.08$
[Rb I/Fe]	$-\mathbf{0.06}$	$-\mathbf{0.06}$	$-\mathbf{0.15}$	$-\mathbf{0.25}$	$-\mathbf{0.13}$
[Y II/Fe]	$+0.14 \pm 0.03(3)$	$+0.08 \pm 0.05(4)$	$-0.04 \pm 0.06(4)$	$+0.07 \pm 0.06(5)$	$+0.06 \pm 0.02$
[Zr I/Fe]	$+0.13 \pm 0.02(3)$	$+0.16 \pm 0.01(2)$	$+0.10 \pm 0.06(4)$	$-0.06 \pm 0.06(3)$	$+0.08 \pm 0.02$
[Ba II/Fe]	$+\mathbf{0.06}$	$+\mathbf{0.13}$	$+\mathbf{0.11}$	...	$+\mathbf{0.10}$
[La II/Fe]	...	$+0.17 \pm 0.10(2)$	$+0.17 \pm 0.09(2)$	$+0.08 \pm 0.09(2)$	$+0.14 \pm 0.05$
[Ce II/Fe]	$+0.18$	$+0.19$	...	...	$+0.18$
[Nd II/Fe]	...	$+0.07 \pm 0.05(4)$	$+0.07 \pm 0.06(7)$	$+0.07 \pm 0.05(3)$	$+0.06 \pm 0.03$
[Sm II/Fe]	$+\mathbf{0.13}$	...	$+\mathbf{0.12}$	$+\mathbf{0.13}$	$+0.13$
[Eu II/Fe]	...	$+\mathbf{0.05}$	$+\mathbf{0.04}$	$+\mathbf{0.02}$	$+\mathbf{0.04}$

Table 8.5: Same as table 8.2 but for stars in cluster NGC 2506.

Species	#2212	#3231	#4138	Average
[Na I/Fe]	+0.18 ± 0.09(3)	+0.14 ± 0.08(5)	+0.32 ± 0.03(3)	+0.21 ± 0.04
[Mg I/Fe]	+0.19 ± 0.03(3)	+0.03 ± 0.07(3)	−0.08 ± 0.08(2)	+0.05 ± 0.04
[Al I/Fe]	+0.11 ± 0.01(2)	+0.19 ± 0.03(2)	+0.21 ± 0.03(2)	+0.17 ± 0.01
[Si I/Fe]	+0.03 ± 0.09(12)	+0.03 ± 0.08(7)	+0.06 ± 0.06(10)	+0.04 ± 0.04
[Ca I/Fe]	+0.09 ± 0.09(9)	+0.09 ± 0.09(9)	+0.11 ± 0.06(8)	+0.10 ± 0.05
[Sc I/Fe]	+0.07 ± 0.00(1)	−0.01 ± 0.00(1)	−0.06 ± 0.00(1)	0.00 ± 0.00
[Sc II/Fe]	−0.01 ± 0.08(5)	+0.09 ± 0.09(5)	+0.08 ± 0.07(3)	+0.05 ± 0.05
[Ti I /Fe]	−0.08 ± 0.07(9)	−0.01 ± 0.09(9)	+0.17 ± 0.07(6)	+0.04 ± 0.04
[Ti II/Fe]	−0.07 ± 0.07(9)	+0.13 ± 0.06(6)	+0.04 ± 0.08(8)	+0.03 ± 0.04
[V I /Fe]	−0.14 ± 0.08(9)	+0.05 ± 0.07(8)	+0.12 ± 0.08(8)	+0.01 ± 0.04
[Cr I/Fe]	−0.02 ± 0.07(6)	−0.02 ± 0.08(11)	0.00 ± 0.04(8)	−0.01 ± 0.04
[Cr II/Fe]	−0.14 ± 0.07(6)	−0.04 ± 0.06(6)	−0.08 ± 0.09(4)	−0.09 ± 0.04
[Mn I/Fe]	**−0.21**	**−0.16**	**−0.16**	**−0.18**
[Fe I/H]	−0.19 ± 0.06(33)	−0.25 ± 0.06(38)	−0.21 ± 0.05(31)	−0.22 ± 0.03
[Fe II/H]	−0.17 ± 0.05(8)	−0.22 ± 0.06(8)	−0.19 ± 0.07(9)	−0.19 ± 0.03
[Co I/Fe]	−0.02 ± 0.07(5)	−0.05 ± 0.09(4)	+0.02 ± 0.05(3)	−0.02 ± 0.04
[Ni I/Fe]	−0.08 ± 0.06(12)	−0.09 ± 0.08(10)	−0.07 ± 0.05(11)	−0.08 ± 0.04
[Cu I/Fe]	**−0.10**	**−0.10**	**−0.15**	**−0.12**
[Zn I/Fe]	−0.01 ± 0.00(1)	+0.05 ± 0.00(1)	0.00 ± 0.00(1)	+0.01 ± 0.00
[Rb I/Fe]	**−0.32**	**−0.02**	**−0.13**	**−0.16**
[Y II/Fe]	+0.07 ± 0.12(1)	+0.03 ± 0.12(1)	+0.01 ± 0.12(1)	+0.04 ± 0.07
[Zr I/Fe]	+0.17 ± 0.06(2)	...	...	+0.17 ± 0.06
[Ba II/Fe]	**+0.29**	**+0.31**	**+0.31**	**+0.31**
[La II/Fe]	+0.21 ± 0.09(2)	+0.31 ± 0.07(1)	+0.31 ± 0.07(1)	+0.28 ± 0.04
[Ce II/Fe]	**+0.14**	...	**+0.23**	**+0.18**
[Nd II/Fe]	...	...	+0.16 ± 0.09(3)	+0.16 ± 0.09
[Sm II/Fe]	**+0.24**	...	**+0.21**	**+0.22**
[Eu II/Fe]	**+0.17**	**+0.26**	**+0.23**	**+0.22**

Table 8.6: Same as table 8.2 but for stars in cluster NGC 1342.

Species	#4	#6	#7	Average
[Na I/Fe]	+0.35 ± 0.03(5)	+0.27 ± 0.03(5)	+0.21 ± 0.03(4)	+0.28 ± 0.03
[Mg I/Fe]	+0.02 ± 0.03(5)	−0.04 ± 0.05(6)	+0.02 ± 0.05(6)	0.00 ± 0.03
[Al I/Fe]	−0.06 ± 0.02(6)	−0.06 ± 0.01(3)	−0.02 ± 0.03(3)	−0.05 ± 0.01
[Si I/Fe]	+0.12 ± 0.03(15)	+0.11 ± 0.05(12)	+0.09 ± 0.04(12)	+0.11 ± 0.02
[Ca I/Fe]	+0.02 ± 0.04(12)	+0.09 ± 0.03(14)	+0.11 ± 0.04(10)	+0.07 ± 0.02
[Sc I/Fe]	−0.01 ± 0.06(6)	−0.01 ± 0.07(5)	+0.15 ± 0.05(2)	+0.04 ± 0.03
[Ti I /Fe]	−0.03 ± 0.04(12)	+0.04 ± 0.04(20)	+0.04 ± 0.03(15)	+0.02 ± 0.02
[Ti II/Fe]	−0.06 ± 0.036)	−0.01 ± 0.04(8)	−0.06 ± 0.02(5)	−0.04 ± 0.02
[V I /Fe]	−0.07 ± 0.04(14)	+0.04 ± 0.03(13)	+0.06 ± 0.02(9)	+0.01 ± 0.02
[Cr I/Fe]	−0.03 ± 0.04(12)	+0.03 ± 0.02(12)	+0.03 ± 0.04(8)	+0.01 ± 0.02
[Cr II/Fe]	+0.02 ± 0.03(6)	+0.04 ± 0.03(7)	+0.04 ± 0.02(6)	+0.03 ± 0.02
[Mn I/Fe]	**−0.09**	**−0.10**	**−0.18**	**−0.12**
[Fe I/H]	−0.12 ± 0.04(126)	−0.12 ± 0.03(106)	−0.17 ± 0.04(107)	−0.14 ± 0.02
[Fe II/H]	−0.10 ± 0.04(19)	−0.11 ± 0.02(19)	−0.17 ± 0.04(14)	−0.13 ± 0.02
[Co I/Fe]	−0.06 ± 0.04(9)	0.00 ± 0.05(8)	−0.04 ± 0.06(6)	−0.03 ± 0.03
[Ni I/Fe]	−0.10 ± 0.04(33)	−0.03 ± 0.04(32)	−0.06 ± 0.04(32)	−0.06 ± 0.02
[Cu I/Fe]	**−0.26**	**−0.30**	**−0.30**	**−0.29**
[Zn I/Fe]	**−0.33**	**−0.27**	**−0.27**	**−0.29**
[Rb I/Fe]	**−0.06**	**−0.08**	**+0.02**	**−0.04**
[Y II/Fe]	+0.12 ± 0.03(6)	+0.13 ± 0.04(8)	+0.12 ± 0.04(6)	+0.12 ± 0.02
[Zr I/Fe]	+0.14 ± 0.04(5)	+0.18 ± 0.04(5)	+0.21 ± 0.04(5)	+0.18 ± 0.02
[Zr II/Fe]	+0.24 ± 0.02(3)	+0.22 ± 0.05(3)	+0.29 ± 0.00(2)	+0.25 ± 0.02
[Ba II/Fe]	**+0.36**	**+0.32**	**+0.27**	**+0.32**
[La II/Fe]	+0.17 ± 0.04(4)	+0.15 ± 0.05(7)	+0.16 ± 0.04(5)	+0.16 ± 0.03
[Ce II/Fe]	+0.30 ± 0.04(5)	+0.43 ± 0.02(6)	+0.36 ± 0.00(2)	+0.36 ± 0.01
[Nd II/Fe]	+0.27 ± 0.03(12)	+0.33 ± 0.02(15)	+0.26 ± 0.03(9)	+0.29 ± 0.02
[Sm II/Fe]	+0.17 ± 0.03(7)	+0.27 ± 0.05(8)	+0.27 ± 0.03(7)	+0.24 ± 0.02
[Eu II/Fe]	**+0.21**	**+0.22**	**+0.22**	**+0.22**

Table 8.7: Same as table 8.2 but for stars in clusters NGC 1662 & 1912

Species	NGC 1662#1	NGC 1662#2	NGC 1662$_{\mathrm{Avg.}}$	NGC 1912#3	NGC 1912#70	NGC 1912$_{\mathrm{Avg.}}$
[Na I/Fe]	$+0.23 \pm 0.03(4)$	$+0.21 \pm 0.04(4)$	$+0.22 \pm 0.03$	$+0.33 \pm 0.05(4)$	$+0.34 \pm 0.02(4)$	$+0.33 \pm 0.04$
[Mg I/Fe]	$-0.07 \pm 0.02(6)$	$-0.05 \pm 0.01(4)$	-0.06 ± 0.01	$-0.01 \pm 0.05(4)$	$+0.08 \pm 0.03(5)$	$+0.03 \pm 0.04$
[Al I/Fe]	$-0.02 \pm 0.03(3)$	$-0.05 \pm 0.04(6)$	-0.03 ± 0.03	$+0.05 \pm 0.05(4)$	$+0.07 \pm 0.01(2)$	$+0.06 \pm 0.04$
[Si I/Fe]	$+0.17 \pm 0.04(13)$	$+0.15 \pm 0.04(12)$	$+0.16 \pm 0.03$	$+0.20 \pm 0.05(9)$	$+0.26 \pm 0.05(7)$	$+0.23 \pm 0.05$
[Ca I/Fe]	$+0.12 \pm 0.03(13)$	$+0.11 \pm 0.04(13)$	$+0.11 \pm 0.03$	$+0.11 \pm 0.04(9)$	$+0.18 \pm 0.04(7)$	$+0.14 \pm 0.04$
[Sc I/Fe]	$+0.02 \pm 0.11(4)$	...	$+0.02 \pm 0.11$	...	...	...
[Sc II/Fe]	$+0.15 \pm 0.08(5)$	$+0.07 \pm 0.08(5)$	$+0.11 \pm 0.06$	**+0.10**	**+0.10**	**+0.10**
[Ti I/Fe]	$+0.07 \pm 0.03(16)$	$+0.05 \pm 0.04(13)$	$+0.06 \pm 0.03$	$-0.08 \pm 0.05(11)$	$-0.06 \pm 0.04(9)$	-0.07 ± 0.04
[Ti II/Fe]	$+0.03 \pm 0.04(9)$	$+0.06 \pm 0.03(6)$	$+0.05 \pm 0.03$	$-0.07 \pm 0.03(3)$	$+0.01 \pm 0.04(4)$	$+0.03 \pm 0.03$
[V I/Fe]	$+0.04 \pm 0.03(11)$	$+0.02 \pm 0.04(10)$	$+0.03 \pm 0.03$	$-0.13 \pm 0.03(8)$	$-0.01 \pm 0.05(7)$	-0.07 ± 0.04
[Cr I/Fe]	$0.00 \pm 0.03(15)$	$+0.01 \pm 0.03(10)$	0.00 ± 0.02	$-0.01 \pm 0.05(6)$	$+0.04 \pm 0.03(4)$	$+0.01 \pm 0.04$
[Cr II/Fe]	$+0.10 \pm 0.04(7)$	$+0.04 \pm 0.04(7)$	$+0.07 \pm 0.03$	$+0.05 \pm 0.05(6)$	$+0.06 \pm 0.00(2)$	$+0.05 \pm 0.03$
[Mn I/Fe]	−0.05	−0.04	−0.05	**−0.15**	**−0.10**	**−0.12**
[Fe I/H]	$-0.09 \pm 0.03(112)$	$-0.11 \pm 0.04(107)$	-0.10 ± 0.03	$-0.12 \pm 0.05(49)$	$-0.10 \pm 0.04(45)$	-0.11 ± 0.04
[Fe II/H]	$-0.10 \pm 0.03(15)$	$-0.12 \pm 0.04(16)$	-0.11 ± 0.03	$-0.09 \pm 0.05(13)$	$-0.10 \pm 0.04(12)$	-0.09 ± 0.04
[Co I/Fe]	$+0.01 \pm 0.04(9)$	$0.00 \pm 0.04(8)$	0.00 ± 0.03	$-0.10 \pm 0.01(4)$	$-0.11 \pm 0.05(8)$	-0.10 ± 0.03
[Ni I/Fe]	$0.00 \pm 0.03(31)$	$-0.04 \pm 0.04(28)$	-0.02 ± 0.03	$-0.01 \pm 0.05(16)$	$-0.04 \pm 0.04(11)$	-0.02 ± 0.04
[Cu I/Fe]	−0.27	−0.21	−0.24	**−0.30**	**−0.30**	**−0.30**
[Zn I/Fe]	−0.14	−0.13	−0.13	**+0.10**	**+0.10**	**+0.10**
[Rb I/Fe]	−0.15	−0.14	−0.14	**−0.30**	**−0.30**	**−0.30**
[Y II/Fe]	$+0.18 \pm 0.04(6)$	$+0.13 \pm 0.04(5)$	$+0.15 \pm 0.03$	$+0.04 \pm 0.01(4)$	$+0.09 \pm 0.03(5)$	$+0.06 \pm 0.02$
[Zr I/Fe]	$+0.26 \pm 0.02(5)$	$+0.25 \pm 0.04(4)$	$+0.25 \pm 0.02$	$+0.12 \pm 0.02(3)$	$+0.09 \pm 0.05(4)$	$+0.10 \pm 0.03$
[Zr II/Fe]	$+0.30 \pm 0.04(4)$	$+0.32 \pm 0.05(4)$	$+0.31 \pm 0.03$	...	...	...
[Ba II/Fe]	+0.55	+0.54	+0.54	**+0.70**	**+0.70**	**+0.70**
[La II/Fe]	$+0.23 \pm 0.02(4)$	$+0.21 \pm 0.04(5)$	$+0.22 \pm 0.02$	$+0.13 \pm 0.02(4)$	$+0.16 \pm 0.03(3)$	$+0.14 \pm 0.02$
[Ce II/Fe]	$+0.37 \pm 0.04(5)$	$+0.38 \pm 0.02(6)$	$+0.37 \pm 0.02$	$+0.24 \pm 0.02(3)$	$+0.23 \pm 0.03(3)$	$+0.23 \pm 0.02$
[Nd II/Fe]	$+0.25 \pm 0.03(13)$	$+0.28 \pm 0.03(13)$	$+0.26 \pm 0.02$	$+0.14 \pm 0.03(6)$	$+0.13 \pm 0.04(9)$	$+0.13 \pm 0.03$
[Sm II/Fe]	$+0.24 \pm 0.03(7)$	$+0.20 \pm 0.04(8)$	$+0.22 \pm 0.03$	$+0.06 \pm 0.04(4)$	$+0.03 \pm 0.03(5)$	$+0.04 \pm 0.03$
[Eu II/Fe]	+0.20	+0.20	+0.20	**+0.10**	**+0.05**	**+0.07**

Table 8.8: Same as table 8.2 but for stars in cluster NGC 2251.

Species	NGC 2251#3	NGC 2251#33	Average
[Na I/Fe]	+0.36 ± 0.04(4)	+0.31 ± 0.04(4)	+0.33 ± 0.03
[Mg I/Fe]	+0.10 ± 0.05(6)	+0.02 ± 0.05(5)	+0.06 ± 0.03
[Al I/Fe]	+0.03 ± 0.04(5)	−0.02 ± 0.03(5)	0.00 ± 0.02
[Si I/Fe]	+0.21 ± 0.01(14)	+0.25 ± 0.05(14)	+0.23 ± 0.02
[Ca I/Fe]	+0.10 ± 0.04(16)	+0.08 ± 0.03(13)	+0.09 ± 0.02
[Sc I/Fe]	+0.09 ± 0.03(5)	−0.01 ± 0.03(3)	+0.04 ± 0.02
[Sc II/Fe]	+**0.01**	+**0.03**	+**0.02**
[Ti I/Fe]	−0.01 ± 0.04(18)	−0.07 ± 0.04(15)	−0.04 ± 0.03
[Ti II/Fe]	−0.06 ± 0.04(8)	−0.02 ± 0.05(4)	−0.04 ± 0.03
[V I/Fe]	−0.01 ± 0.04(16)	−0.10 ± 0.03(13)	−0.05 ± 0.02
[Cr I/Fe]	+0.08 ± 0.05(10)	+0.02 ± 0.05(8)	+0.05 ± 0.03
[Cr II/Fe]	0.00 ± 0.05(8)	+0.08 ± 0.05(7)	+0.04 ± 0.03
[Mn I/Fe]	−**0.12**	−**0.14**	−**0.13**
[Fe I/H]	−0.11 ± 0.04(56)	−0.09 ± 0.05(57)	−0.10 ± 0.03
[Fe II/H]	−0.11 ± 0.04(11)	−0.09 ± 0.04(12)	−0.10 ± 0.03
[Co I/Fe]	+0.08 ± 0.05(6)	−0.01 ± 0.04(5)	+0.03 ± 0.03
[Ni I/Fe]	+0.05 ± 0.04(22)	+0.04 ± 0.04(17)	+0.04 ± 0.03
[Cu I/Fe]	−**0.19**	−**0.27**	−**0.22**
[Zn I/Fe]	−**0.11**	−**0.16**	−**0.13**
[Rb I/Fe]	−**0.17**	−**0.18**	−**0.17**
[Y II/Fe]	+0.05 ± 0.03(5)	+0.10 ± 0.05(5)	+0.07 ± 0.03
[Zr I/Fe]	+0.03 ± 0.05(5)	−0.02 ± 0.03(4)	0.00 ± 0.03
[Zr II/Fe]	+0.06 ± 0.01(2)	+0.06 ± 0.02(2)	+0.06 ± 0.01
[Ba II/Fe]	+**0.12**	+**0.10**	+**0.11**
[La II/Fe]	+0.05 ± 0.04(5)	0.00 ± 0.03(3)	+0.02 ± 0.02
[Ce II/Fe]	+**0.07**	+**0.08**	+**0.07**
[Nd II/Fe]	+0.08 ± 0.03(9)	+0.09 ± 0.04(8)	+0.08 ± 0.02
[Sm II/Fe]	+**0.03**	+**0.01**	+**0.02**
[Eu II/Fe]	+**0.05**	+**0.04**	+**0.04**

Table 8.9: Same as table 8.2 but for stars in clusters NGC 2266, 2335 & 2354

Species	NGC 2266#73	NGC 2335#11	NGC 2354#183	NGC 2354#205	NGC 2354$_{\text{Avg.}}$
[Na I/Fe]	+0.23 ± 0.03(5)	+0.24 ± 0.02(6)	+0.14 ± 0.04(3)	+0.11 ± 0.03(2)	+0.12 ± 0.03
[Mg I/Fe]	+0.39 ± 0.02(5)	+0.08 ± 0.02(6)	−0.18 ± 0.04(3)	−0.16 ± 0.04(5)	−0.17 ± 0.03
[Al I/Fe]	+0.25 ± 0.02(5)	−0.02 ± 0.02(6)	−0.14 ± 0.05(5)	−0.09 ± 0.03(3)	−0.11 ± 0.03
[Si I/Fe]	+0.28 ± 0.02(15)	+0.10 ± 0.02(15)	+0.15 ± 0.03(8)	+0.17 ± 0.03(7)	+0.16 ± 0.02
[Ca I/Fe]	+0.17 ± 0.05(16)	+0.09 ± 0.04(15)	−0.07 ± 0.05(9)	−0.07 ± 0.04(5)	−0.07 ± 0.03
[Sc I/Fe]	+0.31 ± 0.05(3)	+0.13 ± 0.04(3)	...	...	...
[Sc II/Fe]	+0.22 ± 0.05(5)	+**0.16**	+0.05 ± 0.10(3)	...	+0.05 ± 0.10
[Ti I/Fe]	+0.23 ± 0.04(16)	+0.17 ± 0.04(14)	−0.07 ± 0.04(12)	+0.09 ± 0.04(16)	+0.01 ± 0.03
[Ti II/Fe]	+0.30 ± 0.04(7)	+0.12 ± 0.04(10)	−0.12 ± 0.03(3)	0.00 ± 0.03(4)	−0.06 ± 0.02
[V I/Fe]	+0.20 ± 0.06(17)	+0.13 ± 0.04(10)	0.00 ± 0.05(8)	+0.08 ± 0.05(7)	+0.04 ± 0.04
[Cr I/Fe]	+0.09 ± 0.03(12)	+0.07 ± 0.03(10)	−0.07 ± 0.04(5)	+0.01 ± 0.04(6)	−0.03 ± 0.03
[Cr II/Fe]	+0.02 ± 0.04(9)	0.00 ± 0.04(8)	−0.03 ± 0.03(2)	−0.03 ± 0.04(2)	−0.03 ± 0.03
[Mn I/Fe]	−**0.01**	−**0.01**	−0.01	−0.09	−0.05
[Fe I/H]	−0.45±0.04(88)	−0.19±0.04(59)	−0.20 ± 0.03(71)	−0.18 ± 0.03(67)	−0.19 ± 0.02
[Fe II/H]	−0.43±0.05(12)	−0.17±0.03(12)	−0.18 ± 0.02(5)	−0.15 ± 0.03(8)	−0.16 ± 0.02
[Co I/Fe]	+0.27 ± 0.03(5)	+0.16±0.03(3)	0.00 ± 0.03(5)	+0.14 ± 0.01(3)	+0.07 ± 0.02
[Ni I/Fe]	+0.09 ± 0.03(20)	+0.09±0.03(21)	−0.01 ± 0.04(18)	+0.01 ± 0.04(13)	0.00 ± 0.03
[Cu I/Fe]	+**0.02**	−**0.15**	−0.13	−0.11	−0.12
[Zn I/Fe]	**0.00**	−**0.06**	−0.30	−0.33	−0.31
[Rb I/Fe]	+**0.14**	+**0.08**	−0.21	−0.14	−0.17
[Y II/Fe]	+0.05 ± 0.04(4)	+0.12±0.05(5)	+0.16 ± 0.03(3)	+0.12 ± 0.03(3)	+0.14 ± 0.02
[Zr I/Fe]	−0.08±0.05(5)	+0.06±0.04(2)	+0.11 ± 0.04(3)	+0.16 ± 0.01(3)	+0.13 ± 0.02
[Zr II/Fe]	...	+0.01 ± 0.02(2)	...	...	...
[Ba II/Fe]	−**0.13**	+**0.25**	+0.19	+0.16	+0.17
[La II/Fe]	−0.02 ± 0.04(6)	+0.29±0.03(4)	+0.25 ± 0.04(4)	+0.22 ± 0.04(4)	+0.23 ± 0.03
[Ce II/Fe]	−**0.07**	+**0.29**	+0.34 ± 0.03(4)	+0.43 ± 0.03(4)	+0.38 ± 0.02
[Nd II/Fe]	+0.13 ± 0.04(4)	+0.32±0.03(8)	+0.35 ± 0.04(4)	+0.32 ± 0.02(8)	+0.33 ± 0.02
[Sm II/Fe]	+**0.11**	+0.28±0.03(3)	+0.26 ± 0.02(3)	+0.22 ± 0.02(6)	+0.24 ± 0.01
[Eu II/Fe]	+**0.40**	+**0.07**	...	+0.16	+0.16

Table 8.10: Same as table 8.2 but for stars in clusters NGC 2447 & 2482

Species	NGC 2447#28	NGC 2447#34	NGC 2447#41	NGC 2447$_{\text{Avg.}}$	NGC 2482#9
[Na I/Fe]	+0.13 ± 0.04(5)	+0.13 ± 0.04(3)	+0.09 ± 0.02(4)	+0.12 ± 0.02	+0.30 ± 0.03(6)
[Mg I/Fe]	−0.08 ± 0.02(5)	+0.01 ± 0.02(4)	0.00 ± 0.02(4)	−0.02 ± 0.01	+0.13 ± 0.02(4)
[Al I/Fe]	−0.16 ± 0.03(5)	−0.13 ± 0.03(7)	−0.12 ± 0.03(6)	−0.14 ± 0.02	+0.07 ± 0.02(4)
[Si I/Fe]	+0.09 ± 0.05(8)	+0.11 ± 0.04(9)	+0.12 ± 0.03(12)	+0.11 ± 0.02	+0.23 ± 0.04(13)
[Ca I/Fe]	+0.02 ± 0.04(10)	+0.01 ± 0.04(9)	+0.02 ± 0.05(10)	+0.02 ± 0.03	+0.01 ± 0.05(15)
[Sc I/Fe]	...	...	+0.04 ± 0.09(2)	+0.04 ± 0.09	+0.12 ± 0.05(6)
[Sc II/Fe]	...	...	+0.10 ± 0.01(2)	+0.10 ± 0.01	+0.08 ± 0.05(4)
[Ti I/Fe]	−0.05 ± 0.04(19)	−0.06 ± 0.04(17)	−0.01 ± 0.05(17)	−0.04 ± 0.03	+0.01 ± 0.04(14)
[Ti II/Fe]	−0.05 ± 0.045)	−0.05 ± 0.04(8)	−0.06 ± 0.03(6)	−0.05 ± 0.02	−0.03 ± 0.04(7)
[V I/Fe]	−0.03 ± 0.04(13)	−0.04 ± 0.04(14)	+0.02 ± 0.03(16)	−0.02 ± 0.02	+0.10 ± 0.05(16)
[Cr I/Fe]	−0.05 ± 0.04(13)	−0.01 ± 0.03(10)	−0.06 ± 0.03(9)	−0.04 ± 0.02	+0.10 ± 0.04(12)
[Cr II/Fe]	+0.03 ± 0.02(3)	0.00 ± 0.02(5)	+0.02 ± 0.04(4)	+0.02 ± 0.02	+0.09 ± 0.05(7)
[Mn I/Fe]	−0.05	−0.08	−0.07	−0.07	−**0.11**
[Fe I/H]	−0.11 ± 0.04(101)	−0.13 ± 0.04(102)	−0.14 ± 0.04(120)	−0.13 ± 0.02	−0.07 ± 0.04(62)
[Fe II/H]	−0.09 ± 0.04(9)	−0.12 ± 0.03(11)	−0.13 ± 0.04(16)	−0.11 ± 0.02	−0.07 ± 0.05(12)
[Co I/Fe]	−0.07 ± 0.04(6)	−0.01 ± 0.05(7)	−0.03 ± 0.04(6)	−0.04 ± 0.03	+0.11 ± 0.03(7)
[Ni I/Fe]	−0.08 ± 0.04(25)	−0.07 ± 0.04(30)	−0.05 ± 0.04(27)	−0.07 ± 0.02	+0.03 ± 0.04(17)
[Cu I/Fe]	−0.27	−0.25	−0.32	−0.28	−**0.21**
[Zn I/Fe]	−0.34	−0.32	−0.49	−0.38	−**0.22**
[Rb I/Fe]	−0.20	−0.18	−0.17	−0.18	−**0.13**
[Y II/Fe]	−0.01 ± 0.04(7)	−0.02 ± 0.03(5)	+0.12 ± 0.05(7)	+0.03 ± 0.02	+0.15 ± 0.04(5)
[Zr I/Fe]	+0.12 ± 0.02(4)	+0.11 ± 0.05(5)	+0.16 ± 0.04(5)	+0.13 ± 0.02	+0.11 ± 0.05(5)
[Zr II/Fe]	...	+0.12 ± 0.04(2)	+0.20 ± 0.00(1)	+0.16 ± 0.03	+0.10 ± 0.04(3)
[Ba II/Fe]	...	...	+0.23	+0.23	+**0.09**
[La II/Fe]	+0.15 ± 0.04(5)	+0.11 ± 0.05(3)	+0.12 ± 0.03(6)	+0.13 ± 0.02	+0.18 ± 0.03(5)
[Ce II/Fe]	+0.32 ± 0.01(4)	+0.32 ± 0.03(3)	+0.31 ± 0.03(5)	+0.32 ± 0.01	+**0.11**
[Nd II/Fe]	+0.22 ± 0.05(14)	+0.22 ± 0.05(10)	+0.22 ± 0.04(14)	+0.22 ± 0.03	+0.13 ± 0.04(7)
[Sm II/Fe]	+0.22 ± 0.05(6)	+0.16 ± 0.05(5)	+0.20 ± 0.04(5)	+0.19 ± 0.03	+0.13 ± 0.04(4)
[Eu II/Fe]	+0.20	+0.22	+0.23	+0.22	+**0.07**

Table 8.11: Same as table 8.2 but for stars in clusters NGC 2527 & 2539

Species	NGC 2527#10	NGC 2527#203	NGC 2527$_{\rm Avg.}$	NGC 2539#346	NGC 2539#463	NGC 2539$_{\rm Avg.}$
[Na I/Fe]	+0.31 ± 0.03(5)	+0.33 ± 0.03(4)	+0.32 ± 0.02	+0.27 ± 0.01(4)	+0.27 ± 0.04(4)	+0.27 ± 0.02
[Mg I/Fe]	+0.07 ± 0.01(4)	+0.08 ± 0.02(5)	+0.07 ± 0.01	+0.06 ± 0.05(5)	+0.08 ± 0.02(4)	+0.07 ± 0.02
[Al I/Fe]	+0.06 ± 0.04(6)	+0.04 ± 0.03(4)	+0.05 ± 0.02	−0.05 ± 0.02(5)	+0.05 ± 0.01(4)	0.00 ± 0.01
[Si I/Fe]	+0.20 ± 0.03(13)	+0.21 ± 0.03(10)	+0.20 ± 0.02	+0.14 ± 0.03(12)	+0.21 ± 0.03(12)	+0.17 ± 0.02
[Ca I/Fe]	+0.09 ± 0.05(14)	+0.15 ± 0.04(11)	+0.12 ± 0.03	+0.02 ± 0.04(12)	+0.06 ± 0.04(15)	+0.04 ± 0.03
[Sc I/Fe]	+0.30 ± 0.06(6)	+0.21 ± 0.04(7)	+0.25 ± 0.04	+0.21 ± 0.03(7)	+0.21 ± 0.04(5)	+0.21 ± 0.02
[Sc II/Fe]	+0.15 ± 0.05(5)	+0.07 ± 0.04(5)	+0.12 ± 0.03	+0.05 ± 0.06(5)	+0.03 ± 0.05(5)	+0.04 ± 0.04
[Ti I/Fe]	+0.12 ± 0.02(13)	+0.11 ± 0.04(16)	+0.11 ± 0.02	+0.10 ± 0.04(15)	+0.11 ± 0.04(14)	+0.10 ± 0.03
[Ti II/Fe]	+0.08 ± 0.04(6)	+0.09 ± 0.03(7)	+0.08 ± 0.02	+0.08 ± 0.03(7)	+0.08 ± 0.05(6)	+0.08 ± 0.03
[V I/Fe]	+0.24 ± 0.03(14)	+0.18 ± 0.05(16)	+0.21 ± 0.03	+0.18 ± 0.05(13)	+0.14 ± 0.04(13)	+0.16 ± 0.03
[Cr I/Fe]	+0.11 ± 0.04(9)	+0.10 ± 0.04(10)	+0.10 ± 0.03	+0.10 ± 0.03(10)	+0.07 ± 0.04(8)	+0.08 ± 0.02
[Cr II/Fe]	+0.09 ± 0.04(9)	+0.03 ± 0.05(7)	+0.06 ± 0.03	+0.09 ± 0.02(6)	+0.07 ± 0.03(6)	+0.08 ± 0.02
[Mn I/Fe]	**−0.03**	**+0.04**	**0.00**	**0.00**	**+0.02**	**+0.01**
[Fe I/H]	−0.14 ± 0.04(47)	−0.09 ± 0.04(55)	−0.11 ± 0.03	−0.07 ± 0.04(51)	−0.05 ± 0.04(66)	−0.06 ± 0.03
[Fe II/H]	−0.11 ± 0.04(13)	−0.07 ± 0.03(12)	−0.09 ± 0.02	−0.07 ± 0.03(13)	−0.07 ± 0.04(14)	−0.07 ± 0.02
[Co I/Fe]	+0.21 ± 0.04(4)	+0.11 ± 0.06(4)	+0.16 ± 0.04	+0.13 ± 0.04(4)	+0.01 ± 0.04(6)	+0.07 ± 0.03
[Ni I/Fe]	+0.05 ± 0.04(18)	+0.08 ± 0.03(17)	+0.06 ± 0.02	0.00 ± 0.04(17)	+0.05 ± 0.03(21)	+0.02 ± 0.02
[Cu I/Fe]	**−0.11**	**−0.18**	**−0.14**	**−0.18**	**−0.15**	**−0.16**
[Zn I/Fe]	**−0.17**	**−0.16**	**−0.16**	**−0.23**	**−0.22**	**−0.22**
[Rb I/Fe]	**+0.11**	**+0.03**	**+0.07**	**+0.07**	**+0.01**	**+0.04**
[Y II/Fe]	+0.17 ± 0.03(5)	+0.15 ± 0.03(5)	+0.16 ± 0.02	+0.15 ± 0.05(6)	+0.19 ± 0.04(5)	+0.17 ± 0.03
[Zr I/Fe]	+0.38 ± 0.07(5)	+0.25 ± 0.07(4)	+0.31 ± 0.05	+0.23 ± 0.07(5)	+0.19 ± 0.03(5)	+0.21 ± 0.04
[Zr II/Fe]	+0.26 ± 0.02(3)	+0.10 ± 0.04(2)	+0.18 ± 0.02	+0.28 ± 0.04(2)	+0.25 ± 0.03(2)	+0.26 ± 0.02
[Ba II/Fe]	**+0.09**	**+0.07**	**+0.08**	**+0.13**	**+0.08**	**+0.10**
[La II/Fe]	+0.26 ± 0.04(3)	+0.27 ± 0.03(3)	+0.26 ± 0.02	+0.18 ± 0.02(4)	+0.18 ± 0.04(5)	+0.18 ± 0.02
[Ce II/Fe]	+0.26	**+0.22**	**+0.24**	**+0.21**	**+0.20**	**+0.20**
[Nd II/Fe]	+0.20 ± 0.01(4)	+0.20 ± 0.04(6)	+0.20 ± 0.02	+0.22 ± 0.05(5)	+0.24 ± 0.03(5)	+0.23 ± 0.03
[Sm II/Fe]	**+0.19**	**+0.18**	**+0.18**	**+0.16**	**+0.20**	**+0.18**
[Eu II/Fe]	**+0.12**	**+0.08**	**+0.10**	**+0.19**	**+0.19**	**+0.19**

Table 8.12: Same as table 8.2 but for stars in clusters NGC 2548, 2682 & Col 350

Species	NGC 2548#1628	NGC 2682#84	NGC 2682#151	NGC 2682#164	NGC 2682$_{\text{Avg.}}$	Col 350#47
[Na I/Fe]	+0.28 ± 0.03(5)	+0.23 ± 0.05(6)	+0.27 ± 0.02(6)	+0.26 ± 0.02(6)	+0.25 ± 0.02	+0.26 ± 0.04(6)
[Mg I/Fe]	+0.07 ± 0.02(4)	+0.12 ± 0.04(7)	+0.17 ± 0.04(8)	+0.20 ± 0.04(8)	+0.16 ± 0.02	+0.05 ± 0.02(4)
[Al I/Fe]	+0.06 ± 0.02(5)	+0.09 ± 0.02(5)	+0.05 ± 0.03(4)	+0.12 ± 0.03(6)	+0.09 ± 0.01	−0.02 ± 0.02(4)
[Si I/Fe]	+0.17 ± 0.02(12)	+0.19 ± 0.04(13)	+0.18 ± 0.05(14)	+0.23 ± 0.03(15)	+0.20 ± 0.02	+0.20 ± 0.02(16)
[Ca I/Fe]	−0.01 ± 0.04(15)	+0.06 ± 0.03(14)	+0.02 ± 0.05(13)	+0.03 ± 0.03(15)	+0.04 ± 0.02	+0.01 ± 0.05(13)
[Sc I/Fe]	. . .	+0.11 ± 0.04(4)	+0.01 ± 0.05(6)	−0.01 ± 0.06(7)	+0.04 ± 0.03	. . .
[Sc II/Fe]	+0.06 ± 0.10(5)	+0.20 ± 0.01(4)	+0.09 ± 0.06(3)	0.00 ± 0.04(2)	+0.10 ± 0.02	. . .
[Ti I/Fe]	−0.07 ± 0.04(22)	+0.06 ± 0.04(18)	−0.04 ± 0.04(19)	−0.06 ± 0.04(18)	−0.01 ± 0.02	+0.07 ± 0.04(20)
[Ti II/Fe]	−0.07 ± 0.04(7)	+0.08 ± 0.02(9)	−0.01 ± 0.04(9)	−0.03 ± 0.02(7)	+0.01 ± 0.02	+0.03 ± 0.04(6)
[V I/Fe]	+0.04 ± 0.03(15)	+0.13 ± 0.05(13)	+0.08 ± 0.04(12)	+0.06 ± 0.04(14)	+0.09 ± 0.02	+0.11 ± 0.05(10)
[Cr I/Fe]	0.00 ± 0.03(14)	+0.08 ± 0.03(14)	+0.02 ± 0.04(18)	+0.05 ± 0.03(14)	+0.05 ± 0.02	+0.01 ± 0.04(9)
[Cr II/Fe]	+0.07 ± 0.04(5)	+0.09 ± 0.02(9)	+0.06 ± 0.05(10)	+0.10 ± 0.02(10)	+0.08 ± 0.02	+0.03 ± 0.05(5)
[Mn I/Fe]	**−0.08**	**−0.08**	**−0.12**	**−0.03**	**−0.08**	**−0.06**
[Fe I/H]	−0.09±0.04(140)	−0.08 ± 0.03(66)	−0.06 ± 0.04(64)	−0.11 ± 0.04(64)	−0.08 ± 0.02	−0.17 ± 0.05(120)
[Fe II/H]	−0.10±0.05(14)	−0.07 ± 0.04(11)	−0.06 ± 0.04(10)	−0.11 ± 0.03(11)	−0.08 ± 0.02	−0.15 ± 0.05(17)
[Co I/Fe]	+0.07±0.04(8)	+0.14 ± 0.04(4)	+0.06 ± 0.05(4)	+0.13 ± 0.02(5)	+0.11 ± 0.02	+0.02 ± 0.03(10)
[Ni I/Fe]	+0.03±0.03(30)	+0.11 ± 0.03(20)	+0.08 ± 0.03(21)	+0.10 ± 0.04(20)	+0.10 ± 0.02	−0.01 ± 0.03(32)
[Cu I/Fe]	**−0.04**	**+0.05**	**+0.01**	**−0.16**	**−0.03**	**−0.24**
[Zn I/Fe]	**−0.05**	**+0.04**	**−0.12**	**−0.14**	**−0.07**	**−0.23**
[Rb I/Fe]	**−0.11**	**−0.10**	**−0.19**	**−0.11**	**−0.10**	**−0.04**
[Y II/Fe]	+0.08±0.05(7)	+0.07 ± 0.04(5)	−0.01 ± 0.02(6)	+0.04 ± 0.02(7)	+0.03 ± 0.02	+0.14 ± 0.04(9)
[Zr I/Fe]	+0.12±0.04(5)	0.00 ± 0.04(7)	−0.11 ± 0.03(7)	−0.11 ± 0.05(7)	−0.07 ± 0.02	+0.20 ± 0.05(6)
[Zr II/Fe]	+0.19±0.03(4)	−0.01 ± 0.03(2)	−0.07 ± 0.05(3)	−0.13 ± 0.00(1)	−0.07 ± 0.03	+0.27 ± 0.03(3)
[Ba II/Fe]	**+0.09**	**−0.16**	**−0.16**	**−0.17**	**−0.16**	**+0.43**
[La II/Fe]	+0.01±0.03(5)	+0.09 ± 0.03(6)	−0.03 ± 0.04(6)	−0.07 ± 0.02(6)	0.00 ± 0.02	+0.10 ± 0.04(6)
[Ce II/Fe]	+0.23 ± 0.03(4)	**−0.09**	**+0.01**	**+0.02**	**−0.02**	+0.25 ± 0.04(7)
[Nd II/Fe]	+0.19±0.03(12)	+0.07 ± 0.07(7)	−0.02 ± 0.03(10)	0.00 ± 0.03(10)	+0.02 ± 0.03	+0.22 ± 0.04(16)
[Sm II/Fe]	+0.14±0.04(7)	**+0.02**	**−0.07**	**−0.04**	**−0.03**	+0.19 ± 0.04(6)
[Eu II/Fe]	+0.24	**+0.12**	**+0.07**	**+0.05**	**+0.08**	**+0.28**

Table 8.13: The atomic data used for the abundance analysis of stars in OCs NGC 1342, 1662, 2447, 2354 and 1912.

Wavelength	Z^a	LEP^b	log gf	Equivalent Width W_λ (mÅ)											
				NGC 1342			NGC 1662		NGC 2447			NGC 2354		NGC 1912	
λ (Å)		(eV)		[#4	#6	#7]	[#1	#2]	[#28	#34	#41]	[#183	#205]	[#3	#70]
4668.561	11.0	2.100	-1.31	90.8	82.3	73.0	79.0	73.1	...	...	...	...	...	...	...
4982.820	11.0	2.100	-0.91	116.4	104.9	...	...	...	101.5	101.8	96.2	97.1	...	...	...
5688.218	11.0	2.100	-0.45	149.3	141.9	128.8	143.1	134.0	129.3	...	130.4	...	...	158.1	156.5
6154.230	11.0	2.100	-1.55	76.4	66.9	60.9	71.9	67.7	66.2	62.6	60.3	67.2	66.0	...	96.3
6160.753	11.0	2.100	-1.27	96.7	88.1	75.4	91.9	83.7	80.9	80.5	...	80.1	87.8	101.7	105.8
5528.453	12.0	4.340	-0.50	217.6	211.1	205.5	212.1	205.4	208.6	213.2	217.3	198.4	207.1	...	226.1
5711.100	12.0	4.340	-1.75	125.2	119.7	113.6	121.0	112.7	113.4	120.0	...	102.3	108.8	135.7	133.7
6319.234	12.0	5.108	-2.32	32.8	29.8	30.0	50.6	48.3	30.2	...	...	...	...	...	...
7691.564	12.0	5.750	-0.78	94.9	90.5	87.4	93.2	88.0	156.1	146.3	154.8	...	155.1	219.3	214.1
5556.995	13.0	3.140	-1.95	17.3	...	16.6	21.3	15.6	...	16.9	16.6	14.8	21.2	...	...
7835.320	13.0	4.020	-0.47	49.2	47.0	44.3	52.8	44.9	45.7	45.2	43.8	42.0	47.3	62.9	...
7836.133	13.0	4.020	-0.34	63.0	58.7	103.3	63.2	57.4	57.2	56.4	109.6	55.3	61.3	71.3	75.3
5665.564	14.0	4.920	-2.04	65.1	58.0	...	64.9	60.0	57.1	...	...	48.7	...	73.4	...
5645.611	14.0	4.930	-2.14	56.1	52.1	46.6	...	...	16.4	53.4	18.3	...	...	...	...
5701.112	14.0	4.930	-2.15	55.0	52.8	...	58.8	59.0	...	...	...	...	...	67.5	...
5772.144	14.0	5.080	-1.75	71.2	...	59.7	72.5	64.2	...	...	...	...	...	83.2	86.6
5753.627	14.0	5.610	-1.30	59.7	...	51.5	62.4	61.6	58.1	55.0	59.2	...	51.7	...	75.6
6131.581	14.0	5.610	-1.71	37.8	33.0	...	36.3	37.3	...	...	33.2	26.8	29.8	...	...
6131.853	14.0	5.610	-1.69	38.6	33.2	...	38.4	37.3	...	...	37.0	27.3	31.2	...	...
6145.020	14.0	5.610	-1.48	49.0	46.9	45.3	...	...	42.1	47.7	48.1	40.1	38.5	54.6	58.7
6237.325	14.0	5.610	-1.14	74.3	73.3	64.4	74.3	71.3	67.2	70.4	70.1	58.8	60.7	83.3	85.4
6244.474	14.0	5.610	-1.26	63.0	57.2	51.2	61.0	53.6	51.4	54.9	55.2	...	49.2	75.2	75.3
6243.824	14.0	5.613	-1.26	63.5	56.8	55.1	64.5	58.2	...	56.6	58.3	49.5	...	75.9	...
6142.490	14.0	5.620	-1.54	45.4	41.3	37.9	42.9	41.1	37.4	40.4	41.2	34.5	36.3	51.1	55.6
6721.844	14.0	5.862	-1.06	61.7	56.3	52.1	59.2	58.3	55.4	54.3	53.4	49.3	63.6	68.5	...
6741.621	14.0	5.980	-1.56	26.3	...	19.8	27.5	...	...	...	22.1	...	...	...	...
7760.675	14.0	6.206	-1.47	21.8	18.8	19.7	22.6	19.7	26.7	19.3	30.5	...	...	...	...
5590.118	20.0	2.520	-0.57	123.4	118.7	...	...	...	...	116.2	...	...	...	...	...
6161.289	20.0	2.520	-1.27	90.7	88.4	84.4	94.0	83.3	84.1	90.8	...	80.8	...	107.3	107.5
6166.439	20.0	2.520	-1.14	98.8	93.9	90.3	99.3	89.4	94.1	96.2	96.7	84.6	86.7	109.5	111.2
6169.039	20.0	2.520	-0.70	124.0	119.4	110.9	124.6	111.4	...	112.8	115.0	107.9	115.1	144.8	145.4
6169.560	20.0	2.520	-0.48	137.4	132.0	119.9	136.4	129.2	...	124.8	128.0	104.9	...	...	...
6455.612	20.0	2.520	-1.29	88.9	82.1	79.0	91.5	83.0	85.2	81.0	84.2	74.2	82.3	103.4	104.2
6471.666	20.0	2.520	-0.69	125.1	122.1	114.8	126.6	117.5	118.9	118.6	120.7	106.7	116.1	...	...
6493.792	20.0	2.520	-0.11	157.5	155.5	147.8	163.9	154.8	154.8	152.9	153.2	139.9	...	177.1	...

6499.655	20.0	2.520	-0.82	118.5	113.1	106.6	118.7	111.0	113.5	113.2	115.6	105.1	109.0	134.9	129.9
5349.473	20.0	2.710	-0.31	122.0	121.5	112.5	126.7	116.5	118.2	...	...	...	...	...	...
5512.992	20.0	2.930	-0.40	105.2	104.5	101.3	112.2	101.4	...	98.4	...	...	...	...	...
5857.454	20.0	2.930	0.24	152.2	...	...	...	...	139.7	...	140.4	131.0	...	...	...
6210.666	21.0	0.000	-1.53	20.1	16.3	17.8	24.4	16.1	34.0	25.5	19.2	...	...	...	...
6239.366	21.0	0.000	-1.27	25.6	20.6	...	27.2	20.0	23.1	23.1	24.9	11.1	16.5	...	...
6604.596	21.1	1.357	-1.31	93.3	81.3	78.3	88.0	76.2	76.9	78.8	79.6	63.5	70.0	96.1	95.5
5318.354	21.1	1.360	-1.79	43.0	37.4	25.8	29.4	32.7	25.0	27.9	26.7	...	33.5	...	...
5667.144	21.1	1.500	-1.21	84.4	72.5	...	76.9	61.9	...	60.7	...	...	...	97.1	...
5684.196	21.1	1.507	-1.25	84.1	74.9	67.7	...	...	...	...	...	...	...	...	...
6245.625	21.1	1.510	-1.03	85.7	79.0	72.1	83.7	77.8	72.0	74.9	77.5	57.1	64.4	104.8	105.0
5526.823	21.1	1.768	-0.22	131.7	116.4	111.4	121.8	113.0	110.2	113.4	111.1	94.6	92.2	127.5	129.5
5671.805	21.0	1.448	0.52	37.6	...	31.6	41.5	...	...	...	...	45.1	55.1	...	53.5
5520.515	21.0	1.865	0.33	8.7	8.7	...	...	...	...	...	...	...	18.6	...	...
5392.044	21.0	1.987	0.67	13.7	10.3	...	...	...	10.8	...	...	10.2	25.4	...	...
5039.965	22.0	0.021	-1.13	127.9	...	113.1	66.4	56.1	124.2	...	...	...	...	...	...
5219.704	22.0	0.021	-2.16	79.1	74.5	66.5	...	...	77.5	...	78.6	80.6	...	88.3	91.3
6599.117	22.0	0.899	-1.93	33.5	29.2	26.9	35.2	27.0	35.0	...	34.8	41.6	57.4	46.9	46.3
6064.631	22.0	1.046	-1.77	32.1	27.2	25.4	34.0	25.6	32.5	29.3	...	...	53.9	35.6	40.4
5282.404	22.0	1.053	-1.30	49.3	45.1	...	...	...	51.5	...	51.0	56.3	...	...	...
5295.784	22.0	1.067	-1.58	36.1	34.5	30.4	43.3	34.4	38.5	...	40.2	...	57.4	47.2	44.4
5866.454	22.0	1.067	-0.70	96.0	91.4	85.4	99.7	87.8	91.5	88.0	...	89.5	106.9	111.5	104.7
6126.222	22.0	1.067	-1.27	63.4	58.0	53.8	65.2	55.1	62.4	61.0	59.0	63.3	83.0	74.2	76.0
4708.672	22.1	1.237	-2.37	95.9	90.7	...	91.4	87.1	10.1	84.7	86.1	65.9	74.4	103.3	108.5
5005.169	22.1	1.566	-2.73	61.9	52.3	48.4	56.9	...	47.2	52.6	46.1	35.4	44.6	...	...
5418.778	22.1	1.582	-2.11	91.8	86.2	79.5	86.3	87.2	...	...	82.3	64.0	72.0	104.3	106.2
5396.249	22.1	1.584	-3.02	42.2	37.0	33.3	39.9	38.6	87.2	55.1	65.4	...	30.0	...	59.3
6219.947	22.1	2.061	-3.13	16.8	13.3	...	...	...	...	15.6	...	...	...	...	...
4911.202	22.1	3.124	-0.46	87.1	41.1	33.8	40.4	35.9	32.9	77.6	33.9	...	...	...	...
5113.446	22.0	1.443	-0.73	62.5	57.4	...	68.6	56.7	...	58.9	57.0	...	76.3	75.7	68.5
5453.651	22.0	1.443	-1.55	17.2	15.5	12.5	20.3	14.5	...	...	17.2	22.1	33.6	...	...
5145.465	22.0	1.460	-0.52	71.7	69.0	61.3	79.2	116.8	68.2	14.3	73.0	71.6	...	83.0	79.9
5474.229	22.0	1.460	-1.17	32.5	11.1	...	16.8	12.1	33.9	...	12.0	12.3	52.6	...	...
5978.542	22.0	1.873	-0.44	47.9	48.6	43.0	61.0	49.0	51.3	...	50.8	...	...	58.3	...
5000.985	22.0	1.997	-0.02	65.1	60.9	57.8	...	...	65.5	...	63.8	61.1	...	...	...
5201.098	22.0	2.092	-0.66	24.8	24.0	21.3	...	...	27.8	...	26.5	28.3	...	...	...
4778.255	22.0	2.236	-0.21	34.6	...	29.5	...	...	34.7	35.2	37.3	36.6	...	...	...
5739.980	22.0	2.236	-0.67	16.6	17.3	...	21.5	16.9	...	21.5	...	...	30.1	...	...
5739.470	22.0	2.249	-0.60	18.6	18.3	...	22.8	17.7	20.7	21.3	21.1	21.8	34.7	25.1	...
5720.441	22.0	2.292	-0.90	10.6	...	...	...	...	13.5	14.5	9.1	...	18.6	...	...

5648.569	22.0	2.495	-0.20	23.0	22.5	21.5	30.3	...	29.7	25.9	24.2	...	40.8	...	...
6221.339	22.0	2.662	0.11	33.9	31.0	28.9	...	...	...	...	...	...	...	...	...
6221.339	22.0	2.662	0.11	33.9	31.0	28.9	...	...	...	...	...	...	...	...	...
6242.839	23.0	0.262	-1.55	41.5	37.2	...	...	...	...	43.9	42.9	51.5	67.7	...	...
6274.659	23.0	0.267	-1.67	32.9	26.4	28.1	38.2	27.3	39.8	33.6	35.4	49.9	62.1	...	...
6256.893	23.0	0.275	-2.19	10.7	11.1	...	...	...	20.7	16.0	...	...	...	...	...
6266.320	23.0	0.275	-2.29	11.7	9.4	...	94.2	86.0	15.7	13.3	11.8	19.6	...	108.6	...
6251.836	23.0	0.286	-1.34	50.9	50.8	46.2	61.2	48.8	57.8	56.5	56.4	68.2	84.1	68.3	69.4
6111.652	23.0	1.043	-0.71	32.6	33.0	31.8	44.3	30.3	41.6	36.1	37.8	44.8	...	44.7	...
5727.664	23.0	1.051	-0.87	25.8	16.2	15.2	33.8	25.6	28.5	31.5	80.9	...	114.9	36.8	40.7
6135.375	23.0	1.051	-0.75	31.8	32.9	29.2	38.6	29.0	36.3	35.4	37.4	47.1	54.5	43.3	52.6
5657.444	23.0	1.064	-1.02	20.5	18.1	...	25.3	17.0	...	21.4	...	...	...	23.9	32.1
5737.076	23.0	1.064	-0.74	32.2	30.7	30.7	38.2	29.1	38.6	35.7	36.3	...	58.7	38.7	46.5
6039.736	23.0	1.064	-0.68	37.9	34.6	31.3	45.5	35.6	41.2	13.9	39.3	...	59.3	47.5	50.1
6119.542	23.0	1.064	-0.32	62.1	...	52.5	67.7	57.1	...	...	62.1	66.1	...	75.4	81.2
5668.368	23.0	1.081	-1.03	16.7	16.8	...	21.7	...	23.2	...	...	...	...	...	...
5670.851	23.0	1.081	-0.42	47.3	48.0	46.2	57.4	48.2	...	51.4	55.3	...	71.6	...	...
5303.223	23.1	2.276	-1.94	25.8	...	...	24.1	18.3	18.8	23.1	14.4	12.3	19.6	26.6	36.0
5819.940	23.1	2.522	-1.80	16.8	11.9	...	...	...	9.8	...	...	...	...	...	...
4884.040	23.1	3.757	0.05	19.5	...	100.3	...	42.6	61.5	81.9	104.5	...	9.3	...	...
5296.702	24.0	0.983	-1.36	139.2	135.7	125.2	137.4	127.9	133.7	133.3	135.8	...	140.9	158.9	155.7
5300.755	24.0	0.983	-2.00	102.0	98.0	90.2	100.9	91.5	69.3	98.3	97.0	...	106.4	120.2	...
5348.330	24.0	1.004	-1.19	146.5	...	131.1	144.5	135.2	...	...	...	...	...	164.1	160.1
5305.871	24.1	3.827	-2.09	51.9	46.7	44.1	48.2	42.2	41.1	41.1	40.9	27.5	28.8	53.3	64.7
5308.429	24.1	4.071	-1.81	52.9	45.8	46.1	50.9	45.4	42.9	44.5	44.2	...	...	56.8	...
5237.319	24.1	4.073	-1.16	84.1	80.5	74.4	76.3	72.2	...	70.5	...	51.8	...	92.9	...
5334.876	24.1	4.073	-1.56	61.8	58.0	54.5	61.5	55.8	...	...	...	...	...	72.8	127.5
5313.589	24.1	4.074	-1.65	62.4	52.7	53.1	57.6	55.3	50.6	...	46.5	...	33.2	68.6	68.2
5502.090	24.1	4.168	-1.99	38.2	35.2	32.0	35.6	33.2	...	...	29.6	...	...	43.2	...
5329.142	24.0	2.913	-0.06	96.5	90.9	86.0	96.6	88.8	...	...	...	...	...	109.1	102.7
5844.589	24.0	3.013	-1.76	10.0	8.4	...	...	...	9.9	9.8	36.1	7.9	38.0	...	...
5784.980	24.0	3.321	-0.38	55.4	49.8	...	...	...	...	...	...	...	...	...	...
5787.929	24.0	3.322	-0.08	66.2	...	63.9	70.4	...	68.9	...	67.0	...	70.3	80.5	...
5214.138	24.0	3.369	-0.74	28.4	...	...	28.6	24.8	...	36.6	...	28.1	...	39.0	...
5628.645	24.0	3.422	-0.74	26.4	24.8	24.5	27.5	25.0	28.9	26.8	...	26.6	...	...	...
5287.176	24.0	3.438	-0.87	20.7	19.2	...	21.5	18.4	21.1	...	...	20.9	...	...	...
5312.850	24.0	3.449	-0.55	33.4	...	...	35.8	...	32.2	...	29.6	...	43.5	...	...
6013.499	25.0	3.072	-0.25	116.7	113.6	91.2	119.2	110.5	119.4	121.2	116.6	115.3	124.5	130.7	135.5
6016.646	25.0	3.074	-0.22	123.4	120.7	104.5	124.8	120.6	121.9	116.3	121.6	128.1	132.7	127.0	144.5
6021.803	25.0	3.075	0.03	133.6	120.3	108.6	130.5	121.0	125.8	116.1	125.3	121.1	130.3	140.3	141.0
5377.620	25.0	3.845	-0.11	69.8	63.4	61.7	76.0	62.8	62.2	71.7	64.0	67.0	...	88.0	...
5413.677	25.0	3.860	-0.59	39.0	33.2	32.6	41.1	32.0	...	...	...	...	...	...	...

6120.253	26.0	0.915	-5.97	23.3	190.2	...	203.5	188.1	181.5	24.4	24.3	...	39.1	213.9	211.3
5501.477	26.0	0.958	-3.05	186.8	34.3	160.4	41.5	36.4	...	48.1	...	...	...	66.3	62.7
6498.948	26.0	0.958	-4.69	106.7	100.3	90.4	105.4	...	104.1	100.3	99.7	96.7	102.6	131.2	127.7
4993.357	26.1	2.807	-3.68	75.8	65.1	65.7	67.6	61.7	...	64.4	61.4	47.0	47.4	82.1	83.3
4491.401	26.1	2.855	-2.71	114.4	107.3	...	104.4	...	98.8	...	102.1	...	...	...	...
4508.285	26.1	2.855	-2.44	126.3	...	...	...	111.5	...	...	111.9	...	...	...	...
4731.465	26.1	2.891	-3.10	97.0	90.8	...	86.2	...	83.5	...	...	...	...	...	...
5284.116	26.1	2.891	-3.11	100.5	...	...	...	...	85.9	85.1	88.5	...	...	...	...
6369.466	26.1	2.891	-4.11	47.1	42.4	38.2	38.9	39.8	...	43.0	37.1	26.4	...	53.9	56.8
5256.944	26.1	2.892	-4.06	54.4	44.4	42.7	45.7	43.8	...	42.4	...	...	...	57.4	60.6
5991.377	26.1	3.150	-3.54	66.6	58.6	54.1	56.4	54.6	...	...	...	38.6	...	42.5	70.3
5425.260	26.1	3.199	-3.22	76.2	...	...	69.8	65.7	...	64.4	63.1	...	...	81.8	83.8
5234.631	26.1	3.221	-2.18	123.0	118.8	109.4	115.2	112.4	82.4	78.9	83.1	88.6	89.7	130.4	130.5
5325.556	26.1	3.221	-3.22	77.8	69.1	65.2	68.7	...	62.3	...	...	...	...	83.7	79.2
5414.069	26.1	3.221	-3.58	59.6	50.0	...	50.3	45.9	...	...	...	...	32.6	65.0	66.8
6113.329	26.1	3.221	-4.14	34.0	27.7	27.9	...	22.9	...	...	20.6	...	...	...	...
5264.816	26.1	3.230	-3.13	79.3	73.5	69.5	72.5	67.4	65.3	...	66.2	...	...	85.6	...
5534.845	26.1	3.245	-2.75	98.7	90.3	...	...	86.5	17.6	83.3	88.2	...	...	...	...
6149.251	26.1	3.889	-2.84	61.4	53.1	50.6	54.2	53.0	49.5	...	48.9	...	35.2	66.8	68.8
6247.567	26.1	3.892	-2.43	83.1	74.7	73.9	73.8	71.4	68.0	70.2	65.7	...	...	90.5	...
6416.924	26.1	3.892	-2.64	68.7	63.0	59.9	148.7	135.1	...	...	57.6	39.5	...	192.4	179.5
6456.395	26.1	3.900	-2.19	91.0	87.3	83.6	84.5	84.5	...	79.2	82.1	...	57.9	98.6	102.0
5853.152	26.0	1.484	-5.28	27.5	24.9	...	31.9	24.9	...	...	27.9	...	41.5	...	...
6710.324	26.0	1.485	-4.87	55.6	48.9	44.4	57.1	46.5	34.2	20.3	35.0	17.9	61.4	74.3	68.1
4772.823	26.0	1.557	-2.80	142.4	140.3	21.4	...	...	...	26.3	...	129.2	...	156.0	...
5194.957	26.0	1.557	-2.09	193.6	183.7	173.5	107.8	101.3	101.1	99.7	...	187.4	...	215.9	210.2
5307.363	26.0	1.608	-2.87	145.4	139.4	128.0	147.3	133.1	131.9	131.1	141.7	...	134.6	157.4	...
6851.633	26.0	1.608	-5.32	22.9	...	18.1	...	...	...	...	...	24.6	...	...	...
6151.624	26.0	2.176	-3.40	94.6	87.3	...	96.9	85.4	88.6	87.1	91.2	84.4	94.2	...	...
6265.143	26.0	2.176	-2.55	143.1	134.4	124.1	...	...	...	...	138.4	125.8	...	155.5	152.8
6137.003	26.0	2.198	-2.95	118.4	...	...	...	...	174.2	172.5	115.9	...	...	201.5	...
6219.289	26.0	2.198	-2.43	143.4	139.1	127.2	...	...	133.8	...	139.9	126.1	...	166.0	161.5
6335.342	26.0	2.198	-2.35	153.8	145.7	133.5	152.1	139.9	...	138.6	...	134.3	...	178.2	...
8824.294	26.0	2.198	-1.64	240.5	232.6	211.8	113.0	99.7	108.3	...	...	...	...	...	...
5198.723	26.0	2.223	-2.13	145.3	139.1	128.6	144.9	133.7	140.7	139.1	141.0	131.5	...	...	...
6012.229	26.0	2.223	-4.04	52.8	...	44.2	...	...	113.2	115.2	117.7	...	63.5	62.4	65.3
6015.265	26.0	2.223	-4.68	16.5	12.2	...	...	...	...	...	...	...	...	...	...
6173.335	26.0	2.223	-2.88	117.0	113.4	103.4	117.8	102.5	...	114.6	...	...	...	134.3	135.1
6213.440	26.0	2.223	-2.58	133.5	15.0	118.6	135.1	124.2	21.8	...	19.1	24.7	...	156.0	151.5
6297.798	26.0	2.223	-2.74	127.0	...	114.7	...	...	...	...	...	...	...	146.0	140.6

5253.029	26.0	2.279	-3.91	50.1	...	40.9	48.2	41.7	...	...	47.6	...	...	57.1	61.0
5322.043	26.0	2.279	-2.95	103.2	96.8	91.1	103.3	92.6	102.8	...	100.1	...	...	125.1	119.3
5436.601	26.0	2.279	-3.39	79.4	...	...	62.7	59.9	...	58.2	...	57.3	...	115.2	114.5
6481.882	26.0	2.279	-2.98	116.8	107.4	96.4	...	...	104.3	104.7	107.6	101.8	...	128.2	127.6
6608.032	26.0	2.279	-4.03	49.8	43.8	40.2	51.1	42.2	52.1	22.8	48.2	49.8	52.7	63.7	60.7
6252.569	26.0	2.404	-1.69	172.3	169.7	155.0	173.6	160.4	166.0	164.0	170.2	160.8	169.9	191.6	186.7
6494.997	26.0	2.404	-1.27	207.4	...	188.3	...	...	203.9	207.2	210.1	203.4	...	235.9	225.5
6750.169	26.0	2.424	-2.62	126.6	117.6	108.3	125.6	113.5	122.1	16.3	17.8	111.1	118.8	143.5	138.2
6861.943	26.0	2.424	-3.89	51.1	...	39.2	...	...	50.8	...	46.2	47.1	...	...	...
6911.512	26.0	2.424	-4.04	37.7	...	32.8	46.6	...	9.1	7.1	8.0	...	...	...	...
6344.158	26.0	2.433	-2.92	107.8	99.7	92.9	...	...	...	97.8	...	...	...	...	...
6393.612	26.0	2.433	-1.58	183.0	174.1	159.7	50.0	40.0	171.6	171.4	175.0	165.4	171.3	206.9	197.4
6593.887	26.0	2.433	-2.42	134.2	126.2	117.1	...	...	...	...	129.5	120.5	126.9	...	...
6136.631	26.0	2.453	-1.40	188.0	184.5	166.8	...	...	178.1	178.6	175.5	177.6	...	...	207.0
5701.553	26.0	2.559	-2.22	129.5	123.4	...	125.0	115.6	...	...	...	...	...	...	...
6609.120	26.0	2.559	-2.69	115.9	107.2	97.7	...	...	109.1	108.8	108.6	98.7	...	131.7	126.2
6322.695	26.0	2.588	-2.43	122.4	115.1	104.9	...	...	...	...	...	...	...	136.4	136.9
6065.489	26.0	2.608	-1.53	169.5	162.3	149.2	169.9	57.9	161.8	...	163.2	...	157.2	183.7	184.3
6180.204	26.0	2.728	-2.65	99.9	94.2	87.0	...	...	...	...	...	...	...	...	...
6592.927	26.0	2.728	-1.57	162.9	...	144.5	166.7	143.5	...	33.4	157.7	146.7	31.5	...	...
8838.497	26.0	2.858	-1.98	153.7	144.8	133.6	149.4	135.2	...	...	...	...	...	...	...
5281.795	26.0	3.038	-0.83	168.0	166.6	157.1	170.4	159.5	...	31.4	168.3	...	...	...	...
7189.156	26.0	3.077	-2.85	71.2	...	60.1	...	...	...	...	62.7	62.8	64.9	85.6	81.3
5217.398	26.0	3.211	-1.16	140.9	131.3	125.3	137.8	124.9	131.7	132.1	131.6	121.7	132.0	...	145.3
5262.890	26.0	3.251	-2.94	39.7	35.1	32.6	41.7	37.3	...	...	40.7	...	...	...	...
5215.193	26.0	3.266	-0.87	147.0	148.1	133.2	148.5	140.7	141.7	141.2	143.7	...	143.1	166.9	...
5253.470	26.0	3.283	-1.57	111.6	...	103.1	...	...	...	...	...	...	...	...	...
5569.625	26.0	3.417	-0.49	170.6	164.2	153.5	166.8	155.4	...	161.8	161.7	...	161.1	182.4	175.6
5624.559	26.0	3.417	-0.65	160.8	151.8	141.2	59.6	50.7	22.2	23.1	22.1	...	154.2	73.0	...
5576.095	26.0	3.431	-0.94	141.5	139.3	126.2	140.1	129.6	...	...	...	124.8	...	159.9	152.8
5466.987	26.0	3.573	-2.23	63.1	59.6	52.0	61.8	54.9	63.2	62.9	60.7	60.1	63.5	...	...
5242.496	26.0	3.634	-0.97	119.2	119.4	72.7	118.2	108.2	78.2	...	79.4	...	...	135.3	127.3
5568.858	26.0	3.635	-2.95	24.2	19.4	...	21.7	19.3	23.6	25.7	...	21.6	...	...	...
5294.556	26.0	3.640	-2.81	27.6	46.9	24.4	31.6	29.0	29.8	27.6	...	...	...	...	60.2
5636.705	26.0	3.640	-2.61	37.9	33.9	31.1	39.8	32.9	39.4	40.0	34.4	36.9	41.8	...	...
5529.165	26.0	3.642	-2.68	34.9	30.4	...	...	...	...	...	31.7	32.6	34.9	...	...
5539.286	26.0	3.643	-2.61	35.9	35.0	31.1	37.9	32.8	57.5	57.5	78.0	36.3	110.1	49.1	49.1
4704.957	26.0	3.686	-1.53	87.9	87.9	79.0	88.8	78.4	81.2	83.4	84.4	...	...	...	...
6336.833	26.0	3.687	-0.86	136.4	131.4	123.3	136.4	126.3	130.5	129.3	130.5	122.1	125.5	...	...
5288.534	26.0	3.695	-1.66	90.8	...	...	85.6	79.7	82.5	80.7	84.3	78.7	...	...	...
5379.583	26.0	3.695	-1.51	92.3	92.0	84.6	92.3	87.1	91.0	87.3	91.4	82.4	88.9	102.3	...
5549.979	26.0	3.695	-2.61	35.0	...	...	...	...	25.2	12.5	17.9	31.9	...	...	...

6003.020	26.0	3.882	-1.02	110.0	108.2	99.2	114.6	103.2	100.4	104.3	...	98.8	...	...	...
5809.221	26.0	3.884	-1.63	80.9	77.9	72.4	82.2	74.3	75.0	77.6	79.3	...	...	...	...
4985.263	26.0	3.929	-0.56	122.8	16.7	15.8	17.1	15.7	15.3	118.5	14.5	...	16.6	...	...
6187.989	26.0	3.943	-1.67	77.8	73.8	64.4	74.9	69.0	...	...	...	...	...	...	...
6027.022	26.0	4.076	-1.09	97.8	92.2	84.7	92.5	86.6	85.1	...	89.1	87.3	86.1	...	...
6157.737	26.0	4.077	-1.22	96.6	91.0	81.6	95.7	85.8	89.1	17.7	17.1	79.8	...	...	...
7132.997	26.0	4.083	-1.63	71.4	68.0	61.8	...	...	88.2	88.1	68.1	...	66.2	77.2	80.3
4982.510	26.0	4.103	-0.14	133.5	27.8	127.7	26.1	23.9	25.3	40.8	23.2	123.1	24.7	...	...
6127.915	26.0	4.140	-1.40	76.3	73.6	68.9	...	...	...	...	72.5	65.6	74.0	...	...
5464.282	26.0	4.143	-1.42	74.1	67.5	...	73.0	63.6	68.6	67.4	68.6	63.9	67.3	...	...
5811.924	26.0	4.143	-2.42	20.0	18.3	16.1	23.5	18.1	...	24.0	20.5	...	...	...	...
6165.362	26.0	4.143	-1.47	72.5	67.5	62.2	72.3	66.8	5.5	...	68.6	65.6	66.6	80.3	...
4983.261	26.0	4.154	-0.26	128.7	123.2	119.0	129.7	122.6	105.9	106.4	107.4	114.2	101.8	...	...
5386.337	26.0	4.154	-1.77	49.5	50.8	45.3	53.0	46.2	53.5	55.5	49.8	49.7	51.3	...	...
5473.905	26.0	4.154	-0.79	107.1	101.8	93.9	106.8	...	99.0	102.7	103.3	92.9	...	...	...
4999.117	26.0	4.186	-1.71	57.3	52.5	...	52.4	50.8	55.7	50.9	54.0	...	163.9	...	...
5543.945	26.0	4.218	-1.11	87.4	81.4	78.5	87.5	79.7	85.3	84.4	85.7	75.1	...	...	...
5738.245	26.0	4.221	-2.34	22.1	19.7	17.9	...	...	...	...	23.9	...	...	...	...
5858.782	26.0	4.221	-2.26	23.6	19.9	20.0	...	...	...	...	...	...	...	...	...
5641.450	26.0	4.256	-0.95	94.7	...	81.2	94.6	86.6	...	90.3	90.9	80.8	84.7	...	...
5731.772	26.0	4.256	-1.14	82.4	81.0	72.2	82.5	77.1	78.9	81.6	81.6	72.5	...	...	...
5652.318	26.0	4.260	-1.80	...	...	...	...	...	...	...	...	...	...	...	...
5753.127	26.0	4.260	-0.69	103.3	...	95.4	104.8	95.9	...	97.9	104.5	93.8	...	...	...
5652.318	26.0	4.261	-1.82	43.0	40.9	36.1	44.1	38.4	42.6	56.0	41.8	42.2	58.2	48.0	...
5635.830	26.0	4.264	-1.60	53.7	50.5	47.0	57.1	48.8	53.4	51.3	51.5	49.7	...	...	...
5814.818	26.0	4.283	-1.94	...	...	...	...	...	...	...	...	...	...	...	...
5814.818	26.0	4.283	-1.94	38.8	36.6	33.8	38.5	33.3	...	37.8	36.6	...	38.9	...	...
5861.103	26.0	4.283	-2.45	14.7	...	...	...	...	...	...	...	...	...	...	...
5661.351	26.0	4.284	-1.91	42.5	35.4	...	37.9	...	36.4	40.2	35.2	...	66.2	...	...
5197.945	26.0	4.301	-1.62	55.6	49.1	110.9	...	...	53.7	49.2	51.3	46.0	88.4	...	...
5705.473	26.0	4.301	-1.46	61.5	58.8	53.2	61.6	54.5	...	63.7	63.5	...	...	...	...
5383.380	26.0	4.310	0.45	164.8	163.2	155.9	168.1	163.6	160.3	161.2	164.8	156.1	163.6	179.8	178.5
5546.519	26.0	4.371	-1.15	76.4	69.8	66.7	75.3	69.7	74.0	72.2	73.6	66.4	71.9	...	...
5466.404	26.0	4.379	-0.63	100.1	97.7	90.1	99.7	93.4	95.2	92.3	97.0	89.0	91.3	...	...
5445.054	26.0	4.386	-0.01	135.8	128.4	123.8	134.6	125.7	126.0	125.5	126.7	...	124.9	...	...
5619.608	26.0	4.386	-1.54	53.5	49.1	45.5	21.5	18.2	52.8	52.8	72.4	46.9	72.2	72.0	71.9
5624.033	26.0	4.386	-1.15	74.0	74.0	62.7	74.7	65.1	69.6	68.3	69.9	64.3	69.9	...	...
5295.319	26.0	4.415	-1.67	45.6	...	37.4	46.1	39.7	44.8	...	44.7	41.1	45.8	52.4	52.1
5367.473	26.0	4.415	0.24	145.0	139.2	131.9	145.1	135.7	139.6	138.2	141.7	131.8	134.4	170.8	151.3

7832.224	26.0	4.434	-0.02	148.2	144.5	134.4	151.4	139.4	139.3	141.6	141.1	129.9	136.2	166.1	159.1
5285.139	26.0	4.435	-1.62	47.2	...	38.0	44.5	40.9	43.6	42.7	42.5	39.7	...	...	...
5463.285	26.0	4.435	-0.07	130.2	128.0	118.8	125.0	116.5	120.7	...	123.8	110.6	117.7	...	...
5560.218	26.0	4.435	-1.11	71.1	69.4	62.7	71.0	65.5	69.0	...	70.3	64.0	...	...	...
5562.714	26.0	4.435	-0.86	90.7	82.8	80.5	87.6	80.7	80.1	83.0	86.4	77.5	...	...	...
5364.883	26.0	4.446	0.23	140.7	133.2	129.8	139.3	126.3	104.2	103.0	105.6	...	131.5	153.3	145.4
5461.553	26.0	4.446	-1.63	41.3	42.0	39.3	45.8	39.2	44.4	43.7	38.3	...	69.1	...	...
5470.098	26.0	4.446	-1.64	38.4	41.1	33.2	43.2	37.9	42.5	42.3	38.7	38.1	...	...	...
5373.715	26.0	4.473	-0.84	83.9	80.3	76.7	83.8	77.8	79.7	...	78.8	75.2	78.1	...	...
5462.971	26.0	4.473	-0.26	116.3	111.2	107.2	113.9	107.8	109.1	109.6	112.6	...	105.8	...	...
5651.471	26.0	4.473	-1.75	34.3	29.6	28.8	...	...	...	...	34.3	34.2	35.8	...	...
5859.591	26.0	4.549	-0.40	102.9	...	...	94.6	87.0	...	...	89.5	...	...	...	...
5862.362	26.0	4.549	-0.36	111.4	107.3	...	111.0	100.5	99.0	...	...	...	...	...	...
5848.108	26.0	4.604	-1.15	65.7	63.4	60.0	...	...	63.7	...	61.2	57.1	...	...	...
5806.731	26.0	4.608	-1.03	70.4	67.4	62.0	70.9	64.7	68.9	...	67.7	...	63.9	...	...
5855.077	26.0	4.608	-1.58	35.4	...	33.0	40.1	35.0	54.8	57.9	...	35.0	...	...	...
5679.027	26.0	4.652	-0.77	79.4	74.4	...	77.1	72.4	...	...	...	...	...	...	...
5930.193	26.0	4.652	-0.28	108.8	16.9	98.2	105.0	98.3	11.5	14.2	102.9	...	76.6	...	...
8764.019	26.0	4.652	-0.24	124.0	141.7	114.8	153.0	136.5	118.4	117.6	122.5	...	...	...	...
6253.844	26.0	4.733	-1.64	27.5	26.2	...	28.1	23.7	27.4	28.4	24.8	...	...	...	...
5633.954	26.0	4.991	-0.27	89.0	82.6	78.3	87.5	82.5	...	82.7	82.1	77.2	...	94.9	92.4
5732.305	26.0	4.991	-1.49	23.5	...	18.4	23.0	19.6	24.1	22.7	22.5	...	...	...	...
7807.933	26.0	4.991	-0.51	79.0	77.2	71.4	83.2	73.6	59.1	79.0	60.0	71.8	55.8	...	...
5649.990	26.0	5.100	-0.82	48.6	48.3	...	50.6	45.7	48.9	50.1	47.6	...	43.2	...	...
5301.046	27.0	1.710	-1.99	50.9	45.8	...	...	45.0	37.0	55.4	48.2	...	61.9	...	...
5530.783	27.0	1.710	-2.06	47.0	43.7	36.8	52.6	41.9	46.8	46.2	45.2	46.0	59.9	57.5	58.9
6116.999	27.0	1.785	-2.49	22.3	18.8	17.7	25.4	19.8	19.7	24.4	...	...	...	28.4	29.0
5647.239	27.0	2.280	-1.56	39.3	36.3	29.7	41.4	33.7	39.3	38.3	...	41.3	...	47.1	44.3
5212.695	27.0	3.514	-0.14	40.0	...	...	43.2	33.1	36.7	39.6	38.0	37.3	48.6	...	42.0
6454.995	27.0	3.632	-0.25	30.6	26.3	14.9	20.3	13.4	...	14.8	18.2	20.3	18.6	...	38.5
5342.709	27.0	4.022	0.69	51.0	...	44.0	55.4	...	51.9	...	...	...	...	60.5	54.8
5343.433	27.0	4.025	1.44	93.5	89.8	80.0	95.3	86.2	...	89.7	92.7	...	...	...	98.5
5454.577	27.0	4.072	0.14	20.4	19.4	...	22.7	...	...	...	21.4	...	...	...	24.7
5578.721	28.0	1.676	-2.64	101.5	121.0	87.0	124.6	114.7	113.9	94.7	119.0	...	...	...	114.1
5748.356	28.0	1.676	-3.26	66.6	64.5	55.1	71.5	58.7	45.2	60.2	46.9	63.7	...	...	...
6108.125	28.0	1.676	-2.55	111.3	105.3	94.7	111.9	98.3	103.4	105.3	96.4	...	...	132.5	126.9
6128.984	28.0	1.676	-3.33	65.1	...	54.3	...	...	...	58.6	60.2	61.9	69.4	79.4	82.1
6191.184	28.0	1.677	-2.35	123.7	116.7	103.9	...	...	...	...	...	...	...	...	...
6177.247	28.0	1.826	-3.50	39.3	39.3	34.2	45.0	37.0	39.6	...	38.7	43.6	...	...	...
6767.781	28.0	1.826	-2.12	130.0	125.1	111.0	133.1	119.3	122.4	120.0	123.8	...	118.9	149.2	145.8
5754.666	28.0	1.935	-1.99	117.9	...	...	...	...	...	...	117.8	...	...	...	...
6586.316	28.0	1.951	-2.75	80.2	78.3	69.2	84.4	76.9	79.0	79.1	82.8	75.1	...	100.4	94.5

7788.945	28.0	1.951	-1.82	147.0	138.4	127.3	148.6	133.1	142.5	139.3	140.0	134.2	135.0	159.6	153.5
7422.293	28.0	3.635	-0.13	129.3	125.5	108.5	129.7	116.7	32.9	...	...	111.0	...	143.5	142.3
6772.320	28.0	3.658	-0.98	74.1	70.6	65.5	75.6	68.3	67.3	71.1	71.5	62.4	68.9	...	...
7826.780	28.0	3.699	-1.84	22.4	23.0	20.0	26.6	23.3	24.2	26.0	24.2	23.0	...	...	...
5452.851	28.0	3.841	-1.55	26.9	24.4	15.8	21.5	...	18.1	17.9	16.9	25.1	20.8	24.3	...
5462.507	28.0	3.847	-0.93	60.5	56.9	52.4	63.3	56.5	56.8	58.3	60.7	...	56.0	...	...
5468.106	28.0	3.847	-1.61	19.9	18.9	...	24.2	...	21.1	18.2	13.1	20.4	17.3	...	...
5589.359	28.0	3.898	-1.14	42.0	39.2	36.5	43.2	36.0	39.9	...	...	...	...	188.9	...
5593.744	28.0	3.898	-0.84	59.3	56.6	51.5	63.9	55.2	...	...	...	...	...	...	...
5638.754	28.0	3.898	-1.72	15.7	16.6	14.8	...	...	...	17.5	17.9	17.4	...	...	...
7797.607	28.0	3.898	-0.26	107.0	101.8	90.0	106.9	98.0	97.5	99.3	99.4	87.3	95.5	121.2	116.4
6111.077	28.0	4.088	-0.71	52.1	49.5	42.5	51.5	45.0	48.4	48.1	...	...	...	...	...
6176.812	28.0	4.088	-0.26	83.4	80.4	74.1	87.6	79.6	...	77.1	79.1	...	...	...	...
6175.364	28.0	4.089	-0.56	68.3	65.0	58.6	68.5	62.8	61.7	62.5	...	...	...	...	...
5641.886	28.0	4.105	-1.07	35.5	34.7	31.5	38.0	35.3	36.9	37.3	33.2	34.7	37.6	47.5	43.0
5682.202	28.0	4.105	-0.47	68.3	64.8	61.7	72.3	65.2	...	...	...	...	...	...	...
5760.831	28.0	4.105	-0.80	47.3	49.1	46.7	54.2	45.8	...	45.8	46.7	43.4	...	...	...
6223.988	28.0	4.105	-0.99	41.6	38.9	36.3	43.3	37.6	36.3	29.3	40.0	...	44.0	...	...
5392.323	28.0	4.154	-1.32	20.5	19.7	16.7	23.1	18.1	20.4	...	...	17.3	...	...	...
5805.225	28.0	4.167	-0.64	56.2	45.0	51.2	58.0	52.9	...	47.9	46.4	...	46.9	...	...
6360.808	28.0	4.167	-1.01	33.0	30.7	32.8	39.0	32.0	31.6	42.8	52.9	34.3	...	...	...
6598.601	28.0	4.236	-0.88	36.8	35.7	32.5	41.9	33.3	40.8	39.4	40.5	...	...	42.6	...
6130.137	28.0	4.266	-0.96	31.3	31.8	28.3	37.2	34.5	30.5	33.7	30.1	31.9	...	...	...
6635.121	28.0	4.419	-0.73	35.4	37.5	33.1	42.0	35.7	36.1	36.2	37.0	32.2	...	...	...
5218.210	29.0	3.820	0.27	77.9	74.3	64.0	69.2	70.0	73.1	...	78.4	...	71.0	...	87.1
4722.162	30.0	4.030	-0.39	97.7	91.3	91.3	98.3	98.4	89.9	89.9	89.3	80.3	...	108.3	121.2
5119.121	39.1	0.990	-1.36	53.1	44.5	43.5	52.5	42.1	40.8	...	43.6	...	39.5	62.6	63.1
5200.421	39.1	0.992	-0.57	96.8	86.8	...	90.2	81.8	76.3	79.2	81.2	69.3	...	...	104.5
5205.740	39.1	1.033	-0.34	105.3	93.9	...	...	...	83.7	85.2	93.3	78.0	...	...	...
5289.827	39.1	1.033	-1.85	29.2	22.2	20.3	24.5	...	...	19.4	...	...	...	32.6	37.4
5544.615	39.1	1.738	-1.09	29.6	25.1	23.4	28.3	22.6	20.9	...	24.5	17.2	18.3	31.2	37.6
5402.775	39.1	1.842	-0.62	48.0	40.7	38.7	44.1	39.2	...	31.4	35.7	...	...	50.2	54.2
4575.525	40.0	0.000	-0.36	42.2	39.2	38.2	50.5	38.8	...	39.7	40.4	...	63.2	...	...
6134.581	40.0	0.000	-1.28	9.9	8.8	...	13.8	9.0	12.5	12.7	12.0	15.6	24.0	17.0	14.1
6143.202	40.0	0.070	-1.10	13.7	11.2	9.9	18.4	13.4	15.2	15.4	14.9	18.0	27.5	22.4	19.7
6127.473	40.0	0.150	-1.06	11.6	9.4	10.3	15.5	11.8	13.7	...	12.3	18.6	...	19.0	19.3
4739.502	40.0	0.650	0.23	38.2	31.8	28.5	43.3	...	38.8	37.8	...	...	...	...	43.8
5112.280	40.1	1.665	-0.85	43.5	36.2	35.4	42.1	36.5	38.1	32.2	31.0	...	...	...	41.7
6114.797	40.1	1.665	-1.85	7.8	5.2	...	6.6	6.2	...	...	...	...	...	9.6	...

5350.091	40.1	1.827	-0.85	35.8	25.1	18.8	21.2	21.8	22.8	14.8	...	...	6.8	...	...
5853.682	56.1	0.604	-1.02	157.4	140.8	129.5	144.2	132.9	...	...	118.6	...	100.0	...	165.0
6496.917	56.1	0.604	0.13	220.8	199.8	185.8	210.1	190.0	190.3	179.1	190.9	157.8	167.4	...	238.9
4662.506	57.1	0.000	-1.24	52.6	44.3	39.7	50.6	41.3	41.0	...	39.4	40.6	41.9	63.4	...
6774.248	57.1	0.126	-1.82	26.2	18.7	18.4	...	19.5	19.8	19.6	...	...	...	32.0	35.3
5303.546	57.1	0.321	-1.35	30.5	22.0	23.1	28.6	24.3	26.9	26.7	23.5	20.5	25.7	39.8	42.2
6390.494	57.1	0.321	-1.41	35.4	26.7	23.7	31.2	26.9	26.6	...	22.7	24.0	26.4	42.5	46.1
4486.912	58.1	0.295	-0.18	69.1	48.2	48.4	65.8	25.4	47.6	48.9	60.4	...	43.5	...	...
4562.365	58.1	0.478	0.21	76.3	73.2	67.5	...	67.3	...	...	...	...	...	...	...
5274.245	58.1	1.040	0.13	49.9	45.6	...	45.3	41.3	39.8	41.5	36.8	29.3	...	55.0	57.9
6043.374	58.1	1.206	-0.48	16.5	13.7	...	14.8	11.7	12.3	16.3	11.4	8.8	11.5	16.9	22.2
5472.285	58.1	1.240	-0.18	23.8	20.8	...	20.9	18.5	18.3	23.9	16.6	14.1	17.7	27.9	29.6
4706.556	60.1	0.000	-0.71	70.2	60.2	49.8	57.8	53.3	52.3	53.6	51.3	...	...	74.2	71.4
5451.123	60.1	0.000	-1.39	36.8	33.8	23.6	34.8	26.3	28.0	25.7	27.4	20.9	29.4	40.1	42.5
6740.089	60.1	0.064	-1.80	18.3	...	...	12.6	10.7	14.7	12.3	...	12.1	51.2	...	20.6
5092.801	60.1	0.380	-0.61	53.0	43.1	38.5	44.1	41.8	37.5	123.5	...	...	...	57.6	55.7
4998.540	60.1	0.471	-1.10	24.6	...	...	...	16.8	16.8	19.0	14.0	...	16.4	27.6	...
5319.817	60.1	0.550	-0.14	71.5	...	...	18.4	54.3	56.5	...	54.3	...	53.6	...	...
4989.940	60.1	0.630	-0.31	54.5	46.5	40.5	48.8	41.6	41.4	44.3	39.9	...	...	56.9	62.4
5276.874	60.1	0.859	-0.61	25.1	20.8	18.4	19.6	17.8	19.9	21.4	16.7	19.2	20.4	...	29.5
5306.465	60.1	0.859	-0.97	13.5	10.8	...	11.2	...	...	11.4	8.3	...	10.3	13.7	17.1
5811.582	60.1	0.859	-0.86	17.1	13.9	...	14.4	...	11.2	14.4	10.4	...	...	...	...
5311.459	60.1	0.986	-0.42	30.1	23.9	20.9	...	22.6	20.4	23.7	18.0	...	21.5	...	35.0
5431.523	60.1	1.121	-0.47	22.5	17.4	...	15.5	13.1	16.6	...	...	...	...	...	22.5
4676.904	62.1	0.041	-0.87	40.5	36.5	...	37.9	31.7	31.4	...	...	...	...	47.1	46.3
4577.700	62.1	0.248	-0.65	37.2	33.3	30.4	34.6	31.7	...	34.0	31.3	28.8	29.9	43.3	42.5
4566.206	62.1	0.333	-0.59	37.8	34.7	31.9	34.8	26.6	30.4	27.9	27.7	...	...	...	...
4642.238	62.1	0.379	-0.46	40.6	36.7	35.1	38.6	29.2	...	...	31.4	29.5	31.0	43.4	45.0
4523.916	62.1	0.434	-0.39	44.0	39.2	37.2	38.4	33.3	37.8	37.7	36.0	...	33.0	47.9	44.3
4537.931	62.1	0.485	-0.48	36.6	27.8	28.1	30.4	25.7	31.7	...	121.0	23.9	...	...	...
4519.618	62.1	0.544	-0.35	39.0	35.6	32.6	37.9	27.8	34.7	30.6	30.9	...	27.7	...	43.2
6645.155	63.1	1.380	0.12	35.6	30.8	27.9	28.3	25.6	25.0	14.9	17.9	21.6	16.7	45.9	34.4

Table 8.14: The atomic data used for the abundance analysis of stars in OCs (1) = NGC 2251, (2) = NGC 2335, (3) = NGC 2482, (4) = NGC 2527, (5) = NGC 2539, (6) = NGC 2682 and (7) = NGC 2266.

Wavelength	Z^a	LEP^b	log gf	Equivalent Width W_λ (mÅ)											
				(1)		(2)	(3)	(4)		(5)		(6)			(7)
λ (Å)		(eV)		[#3	#33]	[#11]	[#9]	[#10	#203]	[#346	#463]	[#84	#151	#164]	[#73]
4668.561	11.0	2.100	-1.31	90.8	82.3	73.0	79.0	73.1	...	...	...	...	...	...	...
4982.820	11.0	2.100	-0.91	116.4	104.9	...	...	...	101.5	101.8	96.2	97.1	...	...	...
5688.218	11.0	2.100	-0.45	149.3	141.9	128.8	143.1	134.0	129.3	...	130.4	...	...	158.1	156.5
6154.230	11.0	2.100	-1.55	76.4	66.9	60.9	71.9	67.7	66.2	62.6	60.3	67.2	66.0	...	96.3
6160.753	11.0	2.100	-1.27	96.7	88.1	75.4	91.9	83.7	80.9	80.5	...	80.1	87.8	101.7	105.8
5528.453	12.0	4.340	-0.50	217.6	211.1	205.5	212.1	205.4	208.6	213.2	217.3	198.4	207.1	...	226.1
5711.100	12.0	4.340	-1.75	125.2	119.7	113.6	121.0	112.7	113.4	120.0	...	102.3	108.8	135.7	133.7
4702.996	12.0	4.347	-0.44	212.2	211.5	208.0	210.8	...	...	210.9	223.0	194.4	205.0	213.0	219.2
6319.234	12.0	5.108	-2.32	32.8	29.8	30.0	50.6	48.3	30.2	...	...	...	...	...	...
7691.564	12.0	5.750	-0.78	94.9	90.5	87.4	93.2	88.0	156.1	146.3	154.8	...	155.1	219.3	214.1
5556.995	13.0	3.140	-1.95	17.3	...	16.6	21.3	15.6	...	16.9	16.6	14.8	21.2	...	...
7835.320	13.0	4.020	-0.47	49.2	47.0	44.3	52.8	44.9	45.7	45.2	43.8	42.0	47.3	62.9	...
7836.133	13.0	4.020	-0.34	63.0	58.7	103.3	63.2	57.4	57.2	56.4	109.6	55.3	61.3	71.3	75.3
5665.564	14.0	4.920	-2.04	65.1	58.0	...	64.9	60.0	57.1	...	...	48.7	...	73.4	...
5645.611	14.0	4.930	-2.14	56.1	52.1	46.6	...	...	16.4	53.4	18.3	...	...	...	...
5701.112	14.0	4.930	-2.15	55.0	52.8	...	58.8	59.0	...	...	...	...	...	67.5	...
5772.144	14.0	5.080	-1.75	71.2	...	59.7	72.5	64.2	...	...	...	...	...	83.2	86.6
5753.627	14.0	5.610	-1.30	59.7	...	51.5	62.4	61.6	58.1	55.0	59.2	...	51.7	...	75.6
6131.581	14.0	5.610	-1.71	37.8	33.0	...	36.3	37.3	...	...	33.2	26.8	29.8	...	...
6131.853	14.0	5.610	-1.69	38.6	33.2	...	38.4	37.3	...	...	37.0	27.3	31.2	...	...
6145.020	14.0	5.610	-1.48	49.0	46.9	45.3	...	...	42.1	47.7	48.1	40.1	38.5	54.6	58.7
6237.325	14.0	5.610	-1.14	74.3	73.3	64.4	74.3	71.3	67.2	70.4	70.1	58.8	60.7	83.3	85.4
6244.474	14.0	5.610	-1.26	63.0	57.2	51.2	61.0	53.6	51.4	54.9	55.2	...	49.2	75.2	75.3
6243.824	14.0	5.613	-1.26	63.5	56.8	55.1	64.5	58.2	...	56.6	58.3	49.5	...	75.9	...
6142.490	14.0	5.620	-1.54	45.4	41.3	37.9	42.9	41.1	37.4	40.4	41.2	34.5	36.3	51.1	55.6
6155.150	14.0	5.620	-0.87	102.9	102.9	73.7	92.6	...	...	...	96.7	90.1	...	...	63.9
6721.830	14.0	5.860	-1.06	69.7	69.4	...	72.8	63.5	...	58.8	67.8	63.3	64.7	61.1	43.0
5349.450	20.0	2.710	-0.31	138.7	139.3	107.8	137.1	125.4	...	...	128.7	136.6	131.2	134.2	111.6
5512.980	20.0	2.930	-0.30	123.7	...	...	125.8	113.8	...	106.1	...	...	122.0	122.7	102.3
5857.450	20.0	2.930	0.24	164.8	...	137.3	165.8	155.9	157.3	151.7	157.3	167.1	163.5	164.0	136.3
6122.220	20.0	1.890	-0.32	219.7	212.6	173.6	220.5	...	210.9	199.9	205.4	221.0	216.8	224.0	183.5
6162.180	20.0	1.900	0.10	258.4	250.2	190.0	248.4	...	241.1	225.1	229.6	261.5	243.0	262.4	209.0
5581.970	20.0	2.520	-0.56	137.7	136.7	107.8	136.7	127.9	...	122.7	129.2	138.5	133.8	138.4	114.3

5588.760	20.0	2.520	0.24	186.8	...	...	...	...	...	...	186.0	...	...	...	160.0
5590.120	20.0	2.520	-0.74	131.6	129.1	98.4	129.7	119.5	122.7	112.6	122.5	128.6	124.4	130.1	104.6
6161.290	20.0	2.520	-1.27	107.5	105.0	75.6	102.3	92.6	97.9	86.5	97.9	106.1	103.2	106.0	86.0
6166.440	20.0	2.520	-1.14	110.6	108.6	81.5	111.3	102.3	102.5	96.6	105.1	111.2	108.8	115.4	89.3
6169.040	20.0	2.520	-0.47	148.5	147.2	101.0	147.8	119.9	121.5	...	123.8	133.2	141.7	153.1	123.6
6169.560	20.0	2.520	-0.48	150.1	152.1	117.6	153.5	138.3	...	132.3	143.4	153.0	148.9	153.0	124.8
6455.610	20.0	2.520	-1.29	105.2	105.9	74.2	105.3	94.7	100.2	...	99.0	106.4	105.8	108.7	85.0
6471.660	20.0	2.520	-0.69	143.6	139.5	107.5	142.5	130.8	136.2	123.2	131.1	140.0	140.4	143.1	115.2
6493.780	20.0	2.520	-0.11	180.5	179.3	141.5	179.5	165.1	169.2	158.2	164.6	179.1	171.9	178.8	150.0
6499.650	20.0	2.520	-0.82	137.7	131.9	103.6	135.7	124.0	126.1	118.3	123.8	135.8	131.2	138.3	108.2
6210.660	21.0	0.000	-1.53	39.4	...	...	49.8	27.3	32.9	21.9	36.3	63.6	60.3	70.6	33.2
6239.370	21.0	0.000	-1.68	31.6	29.5	...	29.7	23.9	26.8	...	25.0	36.1	47.5	43.9	21.6
5520.480	21.0	1.860	0.33	18.8	14.7	...	21.2	15.5	15.9	13.0	16.8	26.3	25.4	26.8	...
5686.830	21.0	1.440	0.38	...	...	17.2	50.5	38.9	40.8	...	40.4	...	57.6	57.1	...
5671.810	21.0	1.450	0.49	56.2	48.9	22.6	64.7	...	50.3	45.4	51.5	...	...	...	49.4
5356.080	21.0	1.860	0.17	...	...	...	...	...	10.1	...	...	16.6	15.7	17.1	...
5392.010	21.0	1.990	0.47	18.4	...	...	21.6	14.6	16.9	18.3	...	...	...	...	...
5552.230	21.1	1.460	-2.12	...	...	14.5	...	...	...	...	15.2	...	...	...	...
6300.700	21.1	1.510	-1.89	...	...	20.2	...	...	...	...	30.1	...	...	...	...
5318.340	21.1	1.360	-1.79	59.2	57.5	34.2	48.7	38.9	41.1	37.9	47.1	52.9	...	45.7	28.2
6604.590	21.1	1.360	-1.31	94.4	91.2	72.8	89.7	75.0	76.9	73.2	82.5	...	...	...	63.2
5658.350	21.1	1.500	-1.38	...	...	76.9	...	...	...	...	...	...	...	...	...
5640.990	21.1	1.500	-1.35	...	...	83.5	...	...	...	...	...	...	...	...	...
5667.150	21.1	1.500	-1.21	...	...	67.7	...	...	...	...	...	...	...	...	...
5669.030	21.1	1.500	-1.05	...	...	76.2	...	...	...	...	...	...	...	...	...
5657.880	21.1	1.510	-0.82	...	...	112.3	...	...	...	...	...	...	...	...	...
5684.190	21.1	1.510	-1.25	83.6	80.0	...	...	67.0	67.8	...	...	75.0	74.6	69.6	67.7
6245.620	21.1	1.510	-1.03	97.1	94.3	72.7	84.2	74.6	77.9	71.1	84.8	89.4	83.8	78.3	65.7
5526.810	21.1	1.770	-0.22	123.7	127.0	112.2	119.3	103.7	101.5	100.8	109.0	71.0	71.4	77.8	90.9
6599.110	22.0	0.900	-2.03	55.8	50.9	19.2	...	...	46.1	...	...	71.0	71.4	77.8	...
6064.630	22.0	1.050	-1.89	49.6	38.7	...	54.8	...	39.3	33.6	42.4	62.1	64.1	67.3	44.5
5295.770	22.0	1.070	-1.58	59.9	55.4	28.7	64.8	44.1	51.8	43.5	55.5	68.9	69.6	73.8	50.0
5866.460	22.0	1.070	-0.78	117.2	117.7	74.3	125.8	101.2	104.2	97.5	111.8	129.8	124.7	125.4	97.9
5039.950	22.0	0.020	-1.13	...	...	113.9	...	...	...	...	...	...	...	...	...
5460.490	22.0	0.050	-2.75	...	...	25.4	...	...	...	...	...	...	...	...	...
5474.230	22.0	1.460	-1.17	...	...	24.7	...	...	...	...	...	...	...	...	...
5490.150	22.0	1.460	-0.88	...	...	43.1	...	...	...	...	...	...	...	...	...
6126.220	22.0	1.070	-1.37	83.9	79.2	...	89.3	65.2	...	62.2	78.4	94.6	92.0	96.8	71.3
5471.200	22.0	1.440	-1.39	46.3	38.5	...	49.0	29.2	42.7	31.8	39.1	55.7	57.1	58.3	40.2
5978.550	22.0	1.870	-0.44	74.2	70.2	...	...	...	...	...	...	55.7	57.1	58.3	61.9
5739.980	22.0	2.240	-0.67	34.5	30.1	16.0	40.6	24.0	28.2	24.7	...	40.0	42.0	42.5	26.0

5720.440	22.0	2.290	-0.84	20.5	...	...	23.7	15.1	18.7	13.3	19.1	28.4	27.1	30.6	15.9
5064.640	22.0	0.050	-0.94	...	...	...	...	146.9	...	141.5	...	...	...	...	...
5689.460	22.0	2.300	-0.41	42.2	41.3	20.0	...	...	...	...	42.8	54.5	56.2	55.8	39.9
6221.340	22.0	2.660	0.11	54.8	49.7	...	...	...	47.3	...	49.8	62.0	61.5	64.3	...
5384.620	22.0	0.830	-2.85	10.8	...	...	14.4	...	10.3	...	...	22.1	21.9	23.4	...
5113.430	22.0	1.440	-0.73	80.2	84.9	51.1	87.9	70.1	74.8	68.3	...	90.9	93.6	90.2	73.3
5453.640	22.0	1.440	-1.55	33.7	27.7	13.1	38.1	22.1	30.2	24.7	31.6	47.6	49.2	46.1	...
5145.450	22.0	1.460	-0.52	96.5	93.0	58.0	95.2	80.8	...	77.6	87.8	99.4	101.9	100.5	82.0
4778.230	22.0	2.240	-0.16	55.2	...	...	61.2	...	52.0	...	52.5	64.2	63.2	65.7	44.3
5716.450	22.0	2.300	-0.64	31.1	24.8	12.0	36.1	22.0	25.9	...	29.2	...	...	...	24.3
5648.560	22.0	2.500	-0.20	39.6	38.0	...	45.1	32.0	32.9	31.4	39.1	50.3	50.9	51.5	35.6
6219.930	22.1	2.060	-2.83	34.0	...	...	...	19.6	23.8	19.3	...	25.9	25.3	...	...
4708.640	22.1	1.240	-2.37	103.5	102.2	82.8	92.6	85.3	...	85.6	91.3	90.3	87.3	87.2	77.9
5005.150	22.1	1.570	-2.73	64.2	61.9	55.4	58.0	...	53.2	50.3	56.3	56.1	57.9	53.5	46.2
4764.510	22.1	1.240	-2.77	...	...	62.2	...	...	...	...	...	...	...	...	...
5336.780	22.1	1.580	-1.63	121.8	...	103.8	114.3	105.6	110.1	109.8	110.2	111.1	109.8	106.3	97.3
5418.760	22.1	1.580	-2.11	102.7	100.9	81.8	87.8	84.1	87.2	81.0	92.3	88.7	87.3	83.5	77.6
5396.240	22.1	1.580	-3.02	48.1	50.2	31.9	39.0	30.7	39.5	30.3	39.6	38.8	40.2	38.4	32.3
5185.900	22.1	1.890	-1.35	118.7	...	99.3	111.1	102.6	106.2	105.5	106.5	105.7	103.7	102.7	94.6
4873.990	22.1	3.090	-0.79	74.8	...	64.5	66.9	...	65.3	...	...	65.1	60.6	60.9	56.1
4911.190	22.1	3.120	-0.34	...	...	84.3	...	...	...	...	...	87.1	73.9	...	...
5584.510	23.0	1.060	-1.20	...	...	...	37.4	19.0	26.6	...	...	...	...	...	22.0
6242.830	23.0	0.260	-1.55	74.8	73.9	25.9	85.2	59.6	65.0	55.5	68.8	94.8	96.0	102.3	64.8
6256.890	23.0	0.280	-2.01	43.1	37.4	...	...	...	...	...	...	57.7	64.1	70.1	25.6
6251.820	23.0	0.290	-1.34	88.8	82.3	35.0	100.8	68.1	79.5	70.5	80.2	108.3	...	117.3	72.8
6111.660	23.0	1.040	-0.71	62.9	55.6	24.1	75.9	55.3	55.7	46.4	59.0	87.7	86.1	90.2	51.8
6292.830	23.0	0.290	-1.47	77.8	70.6	...	91.4	62.6	66.4	...	...	94.3	100.9	106.9	63.1
6213.880	23.0	0.300	-2.05	40.3	...	...	52.2	24.7	...	...	...	...	62.3	65.5	...
5727.660	23.0	1.050	-0.87	52.6	44.8	...	65.8	44.2	46.7	38.3	48.6	...	74.2	...	44.6
6081.450	23.0	1.050	-0.58	70.0	...	29.1	...	61.5	67.0	55.8	62.8	85.5	...	...	58.7
6135.360	23.0	1.050	-0.75	61.5	55.7	...	71.3	51.3	51.4	43.0	52.8	76.5	83.0	81.9	48.5
5657.430	23.0	1.060	-1.02	43.6	34.6	11.5	48.7	30.9	35.2	30.2	36.6	55.5	58.4	61.6	30.1
5737.110	23.0	1.060	-0.74	61.3	53.8	...	70.9	49.1	55.4	45.4	54.1	81.7	82.5	...	46.4
6039.730	23.0	1.060	-0.65	63.7	62.0	26.2	73.3	52.5	57.4	44.5	60.5	77.0	...	...	...
6119.540	23.0	1.060	-0.32	91.0	81.8	...	97.2	...	81.3	...	82.7	92.7	...	96.1	...
6274.660	23.0	0.270	-1.67	64.5	58.0	18.8	74.3	...	63.0	...	60.7	...	...	...	51.4
6233.190	23.0	0.280	-2.07	39.6	55.6	...	49.6	...	35.4	...	34.3	...	...	...	31.6
6266.320	23.0	0.280	-2.29	29.9	...	...	39.2	17.1	24.6	16.9	...	48.5	52.3	54.0	22.8
5668.370	23.0	1.080	-1.03	...	...	...	47.6	28.1	33.2	25.4	...	53.7	55.9	64.3	30.1

4884.060	23.1	3.760	0.05	...	...	...	...	19.5	...	...	...	37.6	39.6	38.8	...
4883.440	23.1	3.800	-0.18	...	...	...	...	27.3	...	23.0	26.2	...	...	...	...
5303.210	23.1	2.280	-1.94	32.5	28.5	13.9	22.8	20.4	22.9	18.1	21.0	20.2	22.8	20.9	11.3
5819.910	23.1	2.520	-1.70	...	17.0	11.6	19.2	9.4	...	13.3	...	11.4	18.4	15.3	...
5928.840	23.1	2.520	-1.60	29.8	30.0	16.2	25.4	24.4	19.6	15.8	24.5	23.2	26.0	...	16.3
5784.960	24.0	3.320	-0.38	...	...	42.4	...	58.2	62.7	...	...	...	...	...	50.1
5783.060	24.0	3.320	-0.50	...	...	35.7	...	49.7	...	...	...	...	...	...	...
5312.850	24.0	3.450	-0.55	...	...	24.1	...	40.2	44.7	...	...	...	...	...	29.8
5238.950	24.0	2.710	-1.30	48.4	43.9	25.2	53.0	42.4	45.9	37.8	...	...	...	...	29.0
4707.990	24.0	3.170	0.07	...	...	...	...	...	...	...	...	96.3	95.4	99.5	73.1
6630.000	24.0	1.030	-3.56	48.0	40.5	...	53.2	...	...	...	...	...	62.8	...	...
5214.120	24.0	3.370	-0.74	...	...	...	...	...	39.1	33.3	...	47.6	51.8	...	...
5719.830	24.0	3.010	-1.58	20.5	...	...	24.5	...	...	14.2	...	25.5	24.3	26.9	11.5
5296.690	24.0	0.980	-1.36	163.5	163.9	119.8	168.4	145.2	145.3	142.4	149.3	168.7	162.4	170.0	130.0
5345.800	24.0	1.000	-0.95	193.2	187.3	...	196.9	170.8	168.8	166.5	179.6	197.1	193.2	199.1	...
5329.130	24.0	2.910	-0.06	109.6	106.4	81.6	113.9	...	99.5	99.2	103.1	113.4	107.4	113.1	85.7
5628.640	24.0	3.420	-0.74	39.3	38.8	17.4	43.4	32.8	36.5	33.0	35.5	42.3	46.5	47.4	24.1
5844.600	24.0	3.010	-1.56	...	...	...	29.0	...	...	16.0	...	...	26.4	31.0	13.7
6882.500	24.0	3.440	-0.38	...	64.1	...	...	...	...	...	...	...	...	...	...
5287.150	24.0	3.440	-0.87	36.0	...	...	37.9	...	...	25.3	28.9	36.7	40.0	39.5	17.0
5304.170	24.0	3.460	-0.67	39.1	...	...	45.3	31.6	35.3	32.6	34.6	44.5	46.1	47.6	24.2
4764.270	24.0	3.550	-0.28	55.7	...	...	58.0	...	51.2	47.0	49.2	57.0	53.7	61.0	35.1
5502.080	24.1	4.170	-1.99	43.2	44.3	...	35.8	31.2	...	33.5	34.4	30.2	31.0	29.0	...
5420.930	24.1	3.760	-2.58	...	...	23.3	...	...	...	...	...	25.5	29.4	26.1	12.8
5305.850	24.1	3.830	-1.99	57.6	62.5	41.6	52.3	46.7	49.1	46.4	51.6	45.0	45.5	45.6	31.1
4588.180	24.1	4.070	-0.63	...	...	...	...	97.9	93.0	...	...	...	...	...	...
4616.610	24.1	4.070	-1.29	...	...	...	...	69.8	67.9	...	...	...	...	...	...
4848.230	24.1	3.860	-1.14	99.4	101.3	81.8	94.2	...	...	...	...	83.9	85.3	82.6	61.5
5308.420	24.1	4.070	-1.81	57.0	59.3	42.1	51.6	44.5	45.6	45.4	47.6	44.1	42.7	41.1	24.2
5237.310	24.1	4.070	-1.16	87.5	89.0	71.7	79.6	76.0	73.2	76.2	78.7	73.2	69.6	70.5	51.8
5279.870	24.1	4.070	-2.10	...	...	...	...	...	...	...	...	32.1	33.1	31.6	17.8
5334.850	24.1	4.070	-1.56	65.7	68.3	50.5	...	56.0	54.0	56.1	...	...	54.9	52.8	34.2
4592.020	24.1	4.070	-1.22	77.9	...	67.2	75.5	69.6	...	...	72.7	69.2	66.5	69.1	48.5
5313.580	24.1	4.070	-1.65	61.5	68.0	50.9	56.6	47.5	51.8	53.0	55.1	49.5	50.3	47.7	28.8
6013.500	25.0	3.070	-0.25	139.9	139.5	92.1	149.0	128.2	134.0	126.4	141.5	150.9	152.5	155.0	108.2
6016.640	25.0	3.070	-0.22	146.9	142.9	...	153.7	132.4	143.7	127.1	141.6	158.4	155.7	158.9	109.9
6021.790	25.0	3.080	0.03	148.0	149.7	104.2	150.5	131.7	134.8	122.3	133.7	154.3	153.0	160.8	111.1
5377.600	25.0	3.850	-0.11	88.3	...	46.2	96.4	71.2	89.2	78.9	81.3	100.4	95.3	103.4	51.5
5413.670	25.0	3.860	-0.59	56.6	59.1	...	65.1	52.6	62.8	43.0	51.2	72.5	70.0	78.0	25.8
5198.720	26.0	2.220	-2.13	...	...	...	...	...	...	145.4	...	...	...	...	...

8804.520	26.0	2.280	-3.23	143.1	143.9	89.8	140.0	111.3	116.8	...	123.1	133.5	...	...	99.5
8757.120	26.0	2.850	-2.03	...	175.9	124.1	...	151.0	156.7	...	157.6	166.5	163.5	168.0	128.5
8838.330	26.0	2.860	-1.98	179.5	175.6	128.8	...	150.5	156.0	152.2	161.5	168.8	170.9	173.8	...
5538.510	26.0	3.630	-2.14	...	...	48.4	...	...	...	...	...	...	...	...	...
5568.870	26.0	3.630	-2.95	...	...	11.7	...	...	...	...	27.5	...	...	...	18.1
5294.530	26.0	3.640	-2.81	40.1	...	18.9	42.1	...	...	...	...	41.4	41.7	46.3	21.9
5298.770	26.0	3.640	-1.96	90.1	89.6	58.0	92.1	73.5	...	...	...	83.5	87.3	89.0	59.2
6003.020	26.0	3.880	-1.12	120.7	121.0	93.4	120.4	...	...	...	113.6	117.8	114.0	115.0	90.6
6188.000	26.0	3.940	-1.67	...	88.8	59.6	89.8	76.4	77.9	...	...	86.2	87.1	87.9	60.1
6027.060	26.0	4.080	-1.19	105.3	109.0	81.7	106.2	95.7	91.2	...	99.3	...	...	...	77.3
6157.730	26.0	4.080	-1.22	...	...	78.1	...	...	...	...	...	102.9	98.8	...	75.0
6165.360	26.0	4.140	-1.47	86.9	83.2	58.5	87.7	71.8	73.7	...	81.6	81.9	79.5	...	58.4
5295.300	26.0	4.420	-1.67	55.3	49.6	31.8	55.2	...	...	...	...	56.1	51.6	54.6	...
7832.160	26.0	4.430	-0.02	165.7	167.5	130.4	168.8	150.3	153.2	...	158.5	161.3	156.4	153.1	122.5
5300.390	26.0	4.590	-2.42	11.6	...	...	13.1	...	...	...	...	12.6	14.4	12.9	...
5398.280	26.0	4.450	-0.67	...	...	84.8	...	...	...	...	...	...	...	...	...
8763.890	26.0	4.650	-0.24	143.5	141.4	110.3	141.3	126.1	127.4	...	133.5	136.4	134.7	129.1	100.5
6120.250	26.0	0.920	-5.97	51.0	45.0	...	51.1	...	...	...	37.4	49.6	59.3	61.7	24.8
5501.470	26.0	0.960	-3.05	212.9	210.6	152.8	212.9	188.3	184.6	178.9	194.6	209.9	210.9	225.5	164.3
6498.940	26.0	0.960	-4.69	138.3	135.4	...	130.9	...	108.5	102.7	118.7	128.3	133.3	136.1	99.4
6710.320	26.0	1.490	-4.87	...	81.1	...	...	...	...	53.2	...	128.3	133.3	136.1	52.2
5194.940	26.0	1.560	-2.09	228.4	219.2	169.4	...	201.4	200.3	...	207.5	...	...	...	175.7
6151.620	26.0	2.180	-3.40	116.5	113.5	72.8	116.0	90.8	93.5	93.6	103.4	111.6	111.7	112.6	81.5
6265.140	26.0	2.180	-2.55	161.9	163.9	119.4	163.5	142.1	...	139.6	149.3	158.4	...	160.2	121.9
6137.000	26.0	2.200	-2.95	...	...	...	136.7	116.2	119.2	113.4	125.6	...	133.4	136.3	100.1
6219.290	26.0	2.200	-2.43	169.6	168.0	120.1	166.0	144.4	145.3	...	152.1	160.4	162.3	166.0	124.1
6335.350	26.0	2.200	-2.35	178.2	167.7	135.4	173.0	150.9	153.2	...	153.4	164.0	175.3	177.9	135.4
6012.230	26.0	2.220	-4.04	76.6	70.3	...	...	...	...	...	...	71.8	72.6	71.5	...
6015.250	26.0	2.220	-4.68	34.2	27.1	...	30.0	...	20.4	16.5	22.3	...	33.4	36.5	14.8
6173.340	26.0	2.220	-2.88	139.2	139.4	97.3	137.9	118.4	120.5	115.0	127.4	133.3	132.7	135.1	101.5
6213.440	26.0	2.220	-2.48	161.7	162.4	117.7	160.6	133.8	140.8	134.6	143.1	156.7	155.0	157.2	...
6297.800	26.0	2.220	-2.74	150.9	...	105.1	149.0	...	...	124.1	137.1	...	...	...	112.7
5322.030	26.0	2.280	-2.80	127.0	126.3	89.6	119.6	114.5	...	105.1	114.2	121.0	122.3	122.9	...
5253.020	26.0	2.280	-3.94	...	...	...	70.0	...	53.5	...	57.2	66.3	71.3	...	...
6392.540	26.0	2.280	-4.03	72.2	63.7	...	68.9	...	53.2	47.9	56.4	66.6	67.6	74.4	41.2
6481.880	26.0	2.280	-2.98	134.0	132.1	88.7	134.2	112.2	118.5	...	122.1	...	...	...	99.9
6608.030	26.0	2.280	-4.03	...	...	...	72.9	...	59.9	49.6	58.7	70.7	75.5	75.4	44.3
6252.560	26.0	2.400	-1.69	197.1	197.3	154.3	198.9	177.5	178.2	175.2	181.8	195.5	197.0	197.2	153.1
6494.990	26.0	2.400	-1.27	...	246.9	...	...	...	...	...	...	250.2	246.7	255.6	186.7
6750.160	26.0	2.420	-2.62	151.1	146.0	102.6	146.2	124.3	128.6	122.6	135.9	142.4	141.8	142.6	106.7

6344.150	26.0	2.430	-2.92	...	...	85.0	126.1	...	...	104.0	113.8	...	...	...	90.9
6911.510	26.0	2.420	-4.04	...	...	...	...	34.2	43.8	37.3	...	...	...	...	...
6393.610	26.0	2.430	-1.58	211.6	211.4	161.9	214.7	191.3	188.8	188.7	193.2	207.9	203.9	214.2	161.6
6136.630	26.0	2.450	-1.40	214.8	213.8	164.5	...	...	194.3	184.3	201.2	217.1	214.7	216.8	165.7
5701.550	26.0	2.560	-2.22	146.7	142.5	106.0	146.7	127.8	130.5	126.6	135.9	143.2	140.2	142.6	109.7
6475.630	26.0	2.560	-2.94	120.8	116.5	...	...	95.1	99.5	94.3	...	112.8	112.8	114.4	...
6609.110	26.0	2.560	-2.69	137.3	136.5	92.1	134.0	113.3	115.0	111.7	119.8	128.4	...	...	94.2
6137.700	26.0	2.590	-1.40	206.8	...	153.5	204.3	...	...	181.2	192.2	...	...	...	157.6
6322.700	26.0	2.590	-2.43	142.5	140.3	100.0	144.4	123.1	124.7	117.4	130.4	136.4	135.0	139.6	104.1
6575.020	26.0	2.590	-2.71	...	...	88.5	130.7	107.2	109.5	105.9	116.2	124.5	126.1	127.4	91.5
6065.490	26.0	2.610	-1.53	192.1	191.6	146.3	191.5	169.0	172.2	166.8	177.1	184.1	185.7	188.2	144.4
6180.210	26.0	2.730	-2.65	...	...	78.4	116.3	101.6	101.7	94.7	104.1	115.4	...	...	82.8
6270.230	26.0	2.860	-2.61	113.8	111.9	75.3	113.8	94.1	97.5	89.4	102.0	106.3	108.0	109.0	76.0
7189.140	26.0	3.080	-2.85	91.8	84.8	54.8	95.4	...	...	70.9	79.2	86.5	89.2	83.3	...
5215.170	26.0	3.270	-0.87	163.4	...	144.1	168.3	152.0	154.4	...	...	...	...	...	127.7
5302.300	26.0	3.280	-0.72	174.9	176.5	...	...	164.0	161.0	...	166.0	...	...	...	136.1
5569.620	26.0	3.420	-0.49	184.4	186.3	...	189.1	172.6	173.3	173.9	176.8	188.5	178.1	182.2	145.4
5576.090	26.0	3.430	-0.94	159.6	160.8	125.5	151.5	...	141.9	140.9	145.9	152.0	151.1	151.5	123.5
5242.490	26.0	3.630	-0.97	135.7	135.8	105.6	128.2	115.2	124.3	119.4	121.6	...	122.3	128.5	102.8
5397.610	26.0	3.630	-2.48	59.2	58.6	...	...	...	...	...	...	58.0	100.3	103.3	36.7
5636.700	26.0	3.640	-2.61	...	...	25.1	53.5	...	43.6	40.3	48.7	51.2	52.4	53.0	30.1
5529.160	26.0	3.640	-2.68	...	...	...	48.3	...	39.1	33.6	40.9	...	...	...	26.2
5539.270	26.0	3.640	-2.61	54.3	52.4	...	51.8	35.4	45.5	38.1	46.3	50.7	...	...	29.2
6336.840	26.0	3.690	-0.86	...	...	...	...	...	137.5	...	145.5	...	...	...	...
5858.780	26.0	4.220	-2.26	...	...	...	...	...	29.3	26.6	...	35.4	38.0	34.8	17.4
5379.570	26.0	3.690	-1.51	106.4	109.7	77.9	108.2	94.2	96.7	93.6	100.6	103.3	100.3	103.3	78.8
5074.740	26.0	4.220	-0.16	139.7	143.2	117.4	...	140.4	...	...	140.4	140.2	136.0	136.8	110.6
7022.940	26.0	4.200	-1.20	...	...	...	103.8	...	...	88.0	96.7	...	...	...	73.9
5652.310	26.0	4.260	-1.92	54.4	50.6	31.6	53.1	44.5	48.1	...	49.7	51.6	52.0	52.9	31.1
5814.810	26.0	4.280	-1.94	50.4	44.7	...	50.2	...	...	...	...	50.0	51.1	52.5	29.1
5717.830	26.0	4.280	-1.10	...	...	72.8	...	...	...	...	...	...	...	...	69.9
5383.370	26.0	4.310	0.45	183.8	180.4	153.9	183.9	180.0	...	175.7	183.0	...	183.0	178.0	142.3
5369.960	26.0	4.370	0.32	167.2	175.6	...	170.0	168.9	...	...	...	167.5	158.4	162.2	129.7
5546.510	26.0	4.370	-1.15	...	...	59.5	84.5	...	74.0	70.8	...	...	...	...	59.2
5367.460	26.0	4.420	0.44	...	161.5	...	...	...	...	...	...	...	...	...	130.8
5619.600	26.0	4.390	-1.54	...	...	...	64.1	55.0	58.6	...	...	...	...	...	41.7
5364.870	26.0	4.450	0.23	152.1	147.6	126.6	158.0	146.7	147.2	...	...	150.7	143.0	147.0	114.9
5855.080	26.0	4.610	-1.58	...	...	26.0	52.2	38.1	44.1	39.9	44.9	...	48.4	52.2	25.9
5285.120	26.0	4.430	-1.62	...	...	...	57.0	...	49.5	45.6	51.1	52.9	58.8	58.2	34.0
5633.950	26.0	4.990	-0.27	...	...	73.7	...	87.9	...	86.3	94.3	92.6	92.2	91.6	70.5

5679.030	26.0	4.650	-0.90	86.1	85.9	...	85.1	...	...	75.1	80.3	82.2	79.6	81.3	58.5
6253.840	26.0	4.730	-1.66	36.8	35.3	...	40.4	...	...	31.2	34.0	37.8	38.7	39.7	17.4
5991.380	26.1	3.150	-3.54	72.0	68.7	53.4	...	53.0	54.2	54.9	57.1	...	...	...	...
5000.710	26.1	2.780	-4.61	...	...	...	...	...	23.5	...	...	...	...	...	...
5534.840	26.1	3.250	-2.75	101.3	98.9	86.9	91.5	85.0	...	...	88.8	77.9	78.1	75.5	63.7
4993.330	26.1	2.810	-3.62	...	78.9	60.9	72.2	62.4	65.1	67.1	66.4	64.0	65.5	61.2	46.2
5284.100	26.1	2.890	-3.11	...	100.0	86.2	93.4	89.2	86.4	87.4	...	81.1	83.2	80.5	59.9
6369.460	26.1	2.890	-4.11	53.3	55.2	37.7	43.2	36.1	38.7	37.1	39.6	37.8	39.6	35.5	23.1
5256.920	26.1	2.890	-4.06	60.5	...	...	...	...	44.3	38.8	47.2	...	...	...	...
5425.240	26.1	3.200	-3.22	81.2	81.6	63.7	68.3	62.1	...	66.5	66.3	...	...	...	...
5234.620	26.1	3.220	-2.18	128.3	...	115.5	119.4	111.4	112.6	112.7	118.3	106.2	103.3	103.2	87.2
5414.070	26.1	3.220	-3.58	63.2	59.0	46.1	52.3	42.0	49.3	46.4	51.6	42.4	46.2	41.9	28.2
5197.570	26.1	3.230	-2.22	...	...	...	...	115.0	113.0	...	...	...	...	...	...
5264.800	26.1	3.230	-3.13	...	...	...	71.5	65.6	68.6	67.3	68.7	63.3	...	61.6	...
6149.250	26.1	3.890	-2.69	70.4	70.0	55.4	57.6	51.4	56.8	54.1	59.6	46.7	48.4	46.1	34.7
6247.560	26.1	3.890	-2.43	85.4	83.2	70.3	71.5	68.8	...	68.2	69.3	61.8	63.9	58.7	46.5
6416.930	26.1	3.890	-2.64	72.2	61.9	50.6	61.3	57.9	60.3	58.0	62.8	53.0	52.2	50.6	37.2
6456.390	26.1	3.900	-2.19	97.5	95.0	85.3	83.9	...	...	83.1	83.5	...	72.3	70.0	55.8
5301.030	27.0	1.710	-2.00	80.1	...	...	89.6	57.9	61.5	...	...	89.6	80.0	86.5	59.8
5530.770	27.0	1.710	-2.06	75.8	71.2	...	...	56.4	60.5	...	...	85.5	83.9	87.5	54.3
6189.010	27.0	1.710	-2.37	...	...	...	...	...	...	...	...	...	...	...	...
6117.000	27.0	1.780	-2.49	38.4	34.3	14.4	44.3	...	...	...	31.4	47.2	47.4	50.1	25.2
5647.230	27.0	2.280	-1.56	59.9	55.5	30.8	61.4	45.2	47.4	26.7	51.9	63.7	65.0	66.5	46.9
5212.680	27.0	3.510	-0.11	62.0	54.6	...	59.0	50.0	46.8	46.7	52.6	...	...	...	42.9
6454.990	27.0	3.630	-0.25	47.8	44.5	24.1	51.9	...	...	34.6	41.5	47.1	48.5	51.0	30.8
5342.700	27.0	4.020	0.69	...	...	46.3	71.6	...	...	...	61.5	...	...	...	...
5280.620	27.0	3.630	-0.03	...	...	...	54.2	...	...	...	...	...	...	...	...
5578.720	28.0	1.680	-2.64	125.4	125.3	85.5	120.0	101.4	106.1	97.5	109.3	118.5	115.4	119.0	87.7
6108.120	28.0	1.680	-2.45	141.8	136.3	98.0	132.3	...	...	109.8	121.7	134.0	132.2	134.7	99.6
6177.260	28.0	1.830	-3.50	...	...	29.2	...	...	...	...	...	...	...	...	...
6767.770	28.0	1.830	-2.12	158.9	155.4	114.5	148.7	129.5	134.3	124.9	137.2	147.8	144.4	147.2	113.7
6586.310	28.0	1.950	-2.81	105.2	106.1	66.2	103.7	84.7	91.8	78.4	...	104.1	103.2	105.2	74.6
7422.250	28.0	3.630	-0.14	...	...	121.9	...	131.1	133.0	128.3	...	137.5	...	141.2	107.5
7525.100	28.0	3.630	-0.55	...	...	91.7	...	...	...	...	...	...	...	...	...
6772.320	28.0	3.660	-0.98	90.5	91.2	60.0	89.0	74.3	82.1	...	81.3	87.5	86.3	84.2	61.5
7797.540	28.0	3.900	-0.26	126.7	125.0	96.9	120.3	109.9	...	104.1	112.3	114.5	115.3	113.6	85.9
4701.500	28.0	4.090	-0.39	...	...	...	...	70.6	...	...	...	...	...	...	...
6176.810	28.0	4.090	-0.26	103.7	97.6	73.7	96.6	84.7	93.3	...	88.6	94.1	94.3	91.5	68.8
6175.370	28.0	4.090	-0.56	81.2	...	58.9	79.6	67.9	74.5	...	76.5	77.5	74.7	76.0	54.4
6223.980	28.0	4.110	-0.99	56.0	54.4	35.0	52.3	44.5	51.1	...	51.5	54.1	57.9	54.0	32.9

5614.770	28.0	4.160	-0.51	76.6	…	…	…	64.5	71.7	61.0	71.0	…	…	…	…
6191.190	28.0	1.680	-2.35	…	…	…	…	128.5	…	…	132.6	…	…	…	…
5462.500	28.0	3.850	-0.93	…	…	…	…	63.7	68.9	62.6	66.1	…	…	…	…
5805.220	28.0	4.170	-0.64	…	…	…	71.6	…	…	…	64.8	…	…	…	…
6128.980	28.0	1.680	-3.33	90.6	86.4	50.6	87.8	…	73.5	62.0	76.6	91.0	88.1	92.2	60.2
5197.150	28.0	3.900	-1.19	60.0	57.9	35.3	…	…	…	…	…	…	…	…	32.3
5589.360	28.0	3.900	-1.22	57.4	57.0	35.0	53.7	44.1	47.9	42.5	48.6	52.9	53.0	55.6	32.4
5638.750	28.0	3.900	-1.72	29.5	…	15.4	…	…	…	18.7	24.3	30.2	29.4	27.8	15.6
5453.220	28.0	4.090	-1.49	29.1	…	…	…	…	…	…	…	30.3	29.3	…	…
5625.320	28.0	4.090	-0.70	72.9	72.3	48.6	71.7	60.7	64.3	59.6	63.8	…	68.7	69.0	49.3
5392.320	28.0	4.150	-1.32	…	…	…	32.4	…	27.5	23.5	30.4	36.1	34.6	37.4	19.0
5641.880	28.0	4.110	-1.07	55.0	50.8	32.1	…	…	…	…	…	48.0	50.7	52.9	31.2
5996.730	28.0	4.240	-1.06	45.1	42.8	…	43.7	…	36.0	32.3	40.9	…	…	…	24.6
6053.680	28.0	4.240	-1.07	44.7	…	…	…	…	…	…	…	42.9	45.0	46.2	25.0
6598.590	28.0	4.240	-0.98	53.9	49.7	29.3	50.5	44.6	…	43.5	48.6	48.2	50.7	49.9	…
6130.130	28.0	4.270	-0.96	45.5	46.9	…	46.9	37.0	37.2	32.4	44.1	44.9	45.3	49.5	…
6635.120	28.0	4.420	-0.83	49.8	48.7	29.4	…	40.7	…	36.2	46.5	52.7	48.0	48.7	…
5218.190	29.0	3.820	0.26	83.1	95.1	59.8	81.8	77.1	87.1	77.9	85.2	92.8	94.4	69.9	66.4
4722.140	30.0	4.030	-0.39	88.9	103.7	…	93.9	94.4	84.4	79.1	86.4	95.7	85.5	78.6	70.9
6362.350	30.0	5.790	0.27	…	…	27.2	…	48.3	…	…	…	…	…	…	…
5119.100	39.1	0.990	-1.36	58.6	62.3	33.2	55.9	39.7	45.5	40.5	52.0	42.5	48.2	47.6	…
5200.400	39.1	0.990	-0.57	99.3	102.3	69.9	94.2	82.5	83.0	79.1	88.0	84.8	81.4	84.0	59.2
5205.730	39.1	1.030	-0.34	…	…	79.9	…	89.3	…	90.4	…	…	…	92.5	70.9
5289.810	39.1	1.030	-1.85	33.2	31.8	…	26.6	…	21.0	…	22.7	19.5	23.2	23.6	10.2
5320.800	39.1	1.080	-1.93	26.1	23.6	…	20.6	11.7	15.3	…	…	…	18.4	18.1	…
5402.770	39.1	1.840	-0.62	49.6	50.7	29.1	42.3	32.0	37.6	32.3	39.5	36.6	36.3	36.7	18.2
4883.670	39.1	1.080	…7	…	…	96.4	…	…	…	100.5	108.3	104.0	99.8	105.2	…
4982.130	39.1	1.030	-1.29	…	…	…	…	…	…	43.0	…	…	…	…	…
6134.570	40.0	0.000	-1.28	21.6	18.0	…	26.2	16.3	15.2	11.7	16.4	104.0	99.8	105.2	…
6140.490	40.0	0.520	-1.41	…	…	…	5.1	…	…	…	…	…	…	…	…
4772.290	40.0	0.620	…4	36.7	38.6	10.7	…	31.8	34.8	26.9	33.9	…	45.9	47.4	…
6143.200	40.0	0.070	-1.10	…	…	…	…	19.7	22.4	…	19.6	31.7	35.3	39.1	10.7
4828.030	40.0	0.620	-0.64	11.4	…	…	…	…	…	…	…	14.6	15.5	19.5	…
6127.460	40.0	0.150	-1.06	23.2	19.2	3.2	27.9	18.0	20.9	14.6	18.2	27.7	30.9	36.1	8.4
4739.470	40.0	0.650	0.23	52.6	…	…	53.4	41.9	…	37.8	…	52.5	56.6	60.1	…
5853.680	56.1	0.600	-1.02	152.6	158.8	114.8	137.5	108.6	117.4	113.8	127.6	107.8	116.5	118.6	81.5
6496.910	56.1	0.600	0.13	225.6	233.1	169.0	204.6	174.7	176.6	172.8	187.0	178.3	179.0	177.6	124.0
4662.490	57.1	0.000	-1.24	59.6	…	34.3	…	…	…	…	43.3	47.0	48.5	43.5	…
5482.250	57.1	0.000	-2.06	19.7	17.6	…	18.0	…	…	9.0	12.5	14.7	14.2	13.9	4.9
5122.980	57.1	0.320	-0.85	66.0	…	…	…	…	…	…	…	…	51.6	46.1	24.9

6774.240	57.1	0.130	-1.82	30.5	...	...	25.6	14.5	...	13.0	19.5	...	...	19.1	8.1
4804.010	57.1	0.230	-1.49	...	...	...	...	...	23.6	...	...	...	...	...	...
5301.900	57.1	0.400	-1.00	...	...	28.1	46.2	...	40.3	...	...	36.2	39.0	36.1	...
5303.520	57.1	0.320	-1.35	35.8	34.2	17.1	32.9	18.6	25.5	18.9	26.3	26.9	26.6	...	9.1
6390.480	57.1	0.320	-1.41	...	32.3	18.0	32.1	21.3	...	20.3	25.1	23.7	26.9	24.8	...
5274.220	58.1	1.040	0.13	50.7	49.0	30.9	43.1	32.9	34.1	31.9	40.9	36.4	...	41.6	23.7
6043.370	58.1	1.210	-0.48	22.0	15.5	9.9	14.4	...	9.6	13.4	...	...	11.3	12.8	...
5472.270	58.1	1.240	-0.18	34.4	26.9	...	20.9	17.0	...	...	16.5	13.4	19.8	19.6	5.0
5468.370	58.1	1.400	-0.07	...	...	12.3	...	13.0	13.4	...	...	...	...	...	...
4706.530	60.1	0.000	-0.71	76.1	74.9	12.2	...	...	...	...	...	56.7	61.7	60.6	...
5092.790	60.1	0.380	-0.61	...	...	34.4	49.4	...	...	...	46.7	...	45.4	45.4	...
5311.440	60.1	0.990	-0.42	28.6	...	...	...	...	21.8	17.3	...	...	...	21.3	...
4998.540	60.1	0.470	-1.10	...	...	...	...	11.3	...	...	...	...	19.3	17.3	8.9
4914.360	60.1	0.380	-0.70	...	...	...	...	...	36.0	...	...	...	39.5	38.4	...
5319.800	60.1	0.550	-0.14	74.8	75.4	48.2	66.9	49.0	53.9	54.5	61.9	52.4	58.1	61.2	37.4
5431.540	60.1	1.120	-0.47	...	21.6	...	16.1	...	13.8	...	14.4	14.0	15.3	...	...
5842.360	60.1	1.280	-0.60	13.5	11.1	...	...	...	...	...	...	...	...	...	...
5092.780	60.1	0.380	-0.61	57.1	56.0	34.4	49.4	...	...	...	...	...	45.4	45.4	...
4989.920	60.1	0.630	-0.31	58.7	57.3	34.2	49.0	33.4	43.8	34.9	...	45.3	45.0	46.5	...
5276.850	60.1	0.860	-0.61	28.2	26.7	13.7	23.9	13.2	...	12.8	20.9	16.4	19.3	21.3	...
5811.560	60.1	0.860	-0.86	21.0	...	8.9	...	...	12.5	...	13.6	11.4	12.8	12.0	...
5485.690	60.1	1.260	-0.12	33.5	31.3	15.3	25.1	...	...	17.6	...	...	...	...	...
4591.810	62.1	0.180	-1.12	32.1	...	...	...	16.1	17.6	...	...	...	...	...	...
4519.600	62.1	0.540	-0.35	50.4	52.6	29.1	...	29.2	33.6	...	47.5	42.4	45.6	41.4	26.8
4577.680	62.1	0.250	-0.65	...	...	30.6	...	34.7	31.6	30.2	39.8	50.1	...	...	28.3
4523.900	62.1	0.430	-0.39	...	...	37.1	43.7	35.9	40.8	...	...	...	...	54.6	47.0
4566.190	62.1	0.330	-0.59	...	...	...	38.1	...	...	...	...	...	...	...	...
4642.210	62.1	0.380	-0.46	...	...	...	41.3	...	...	...	...	...	...	...	...
4537.930	62.1	0.480	-0.48	...	...	...	35.6	...	...	...	...	43.9	...	...	...
6645.110	63.1	1.380	0.12	43.1	33.6	18.6	32.4	23.1	28.3	24.9	25.5	33.0	31.4	22.5	25.3

Table 8.15: The atomic data used for the abundance analysis of stars in OCs NGC 752, 1817 and 2360

Wavelength	Z^a	LEP^b	log gf	Equivalent Width W_λ (mÅ)										
				NGC 752				NGC 1817			NGC 2360			
λ (Å)		(eV)		[#77	#137	#295	#311]	[#8	#81	#73]	[#5	#6	#8	#12]
4668.530	11.0	2.100	-1.25	. . .	. . .	. . .	. . .	. . .	79.6	. . .	. . .	84.6	. . .	97.0
4982.790	11.0	2.100	-0.91	. . .	111.6	. . .	. . .	99.4	104.2	107.2	. . .	. . .	. . .	121.3
5688.210	11.0	2.100	-0.45	145.9	. . .	140.7	151.1	. . .	. . .	. . .	141.2	143.4	140.7	155.1
6154.230	11.0	2.100	-1.55	74.5	75.4	69.9	75.5	59.5	64.6	70.8	67.6	70.1	68.9	91.3
6160.760	11.0	2.100	-1.25	96.1	98.5	89.5	96.3	83.5	85.4	93.0	94.6	91.7	91.4	. . .
5711.090	12.0	4.340	-1.72	130.1	135.3	124.2	132.9	119.8	117.9	. . .	119.9	127.7	125.1	134.4
5528.410	12.0	4.350	-0.50	238.0	232.8	225.0	237.7	206.9	212.8	233.9	219.7	219.0	225.5	. . .
5785.260	12.0	5.110	-2.11	. . .	. . .	. . .	. . .	. . .	. . .	. . .	. . .	. . .	. . .	65.8
7811.040	12.0	5.940	-1.29	. . .	. . .	. . .	. . .	. . .	56.2	. . .	. . .	65.4	65.7	. . .
5557.020	13.0	3.140	-2.10	34.0	29.4	25.3	31.8	19.6	. . .	. . .	. . .	24.6	27.0	24.6
7084.560	13.0	4.020	-0.75	. . .	44.7	. . .	. . .	. . .	. . .	. . .	. . .	. . .	. . .	. . .
7835.220	13.0	4.020	-0.47	65.7	60.2	55.0	65.1	47.1	49.7	61.8	63.9	58.0	56.1	58.1
7836.040	13.0	4.020	-0.34	75.7	77.3	71.6	76.7	60.4	58.3	68.4	69.8	70.6	70.7	71.0
5665.570	14.0	4.920	-2.04	60.2	63.2	64.3	66.8	51.5	63.4	56.5	. . .	61.0	65.7	. . .
5645.610	14.0	4.930	-2.14	55.1	54.2	56.5	59.1	46.8	51.1	. . .	52.4	56.1	56.3	. . .
5701.100	14.0	4.930	-2.05	57.4	59.3	51.6	58.8	51.0	. . .	56.1	56.0	67.4	59.5	. . .
5621.610	14.0	5.080	-2.50	. . .	. . .	. . .	. . .	. . .	. . .	. . .	22.9	. . .	. . .	. . .
5772.150	14.0	5.080	-1.75	69.3	69.9	72.0	74.9	59.4	69.3	71.5	67.7	75.5	70.3	. . .
5753.640	14.0	5.610	-1.30	59.9	. . .	. . .	69.1	56.8	58.9	63.3	61.8	66.3	59.9	. . .
6125.010	14.0	5.610	-1.51	. . .	. . .	. . .	. . .	. . .	. . .	. . .	. . .	. . .	. . .	52.8
6131.580	14.0	5.610	-1.71	34.0	34.9	33.7	37.1	29.1	32.2	37.1	33.9	38.5	. . .	40.6
6131.840	14.0	5.610	-1.69	34.0	34.1	36.8	38.8	34.0	. . .	. . .	35.3	39.5	. . .	. . .
6145.020	14.0	5.610	-1.48	45.5	45.2	49.0	51.5	. . .	. . .	. . .	52.4	50.8	50.1	47.6
6237.310	14.0	5.610	-1.14	69.5	68.7	74.8	76.9	69.7	68.2	66.3	68.5	75.8	72.0	. . .
6243.810	14.0	5.610	-1.26	. . .	58.7	56.3	59.9	59.2	57.8	58.3	54.5	59.7	. . .	58.7
6244.470	14.0	5.610	-1.36	56.9	. . .	59.1	60.4	55.2	57.6	56.9	55.3	61.6	61.7	60.0
6142.490	14.0	5.620	-1.54	43.8	42.5	43.7	46.8	36.1	40.9	41.2	41.3	47.0	43.3	. . .
6155.180	14.0	5.620	-0.97	. . .	. . .	. . .	. . .	. . .	. . .	. . .	79.0	. . .	. . .	. . .
6721.820	14.0	5.860	-1.06	56.9	. . .	60.1	62.5	52.3	55.3	58.8	54.7	64.6	58.6	. . .
6195.440	14.0	5.870	-1.80	23.3	. . .	. . .	26.6	. . .	. . .	. . .	23.3	24.4	25.4	. . .
6122.220	20.0	1.900	-0.32	. . .	213.4	. . .	. . .	191.8	190.0	207.7	. . .	190.9	. . .	229.7
5581.970	20.0	2.520	-0.56	127.5	129.1	. . .	129.2	121.6	120.3	126.9	120.1	126.3	121.7	136.2
5588.740	20.0	2.520	0.36	. . .	. . .	. . .	. . .	. . .	. . .	. . .	. . .	. . .	. . .	205.3
5590.120	20.0	2.520	-0.74	116.2	122.4	117.5	123.1	116.6	115.1	121.8	111.7	116.8	115.9	128.8
6166.440	20.0	2.520	-1.14	107.0	100.7	98.2	107.4	96.5	94.5	105.9	92.7	96.3	97.1	114.2

6169.560	20.0	2.520	-0.48	134.3	…	135.4	139.5	129.5	136.2	138.7	134.1	136.6	137.3	156.3
6455.600	20.0	2.520	-1.29	99.2	99.7	90.1	97.5	86.3	86.3	95.5	94.8	93.5	90.9	106.6
6493.780	20.0	2.520	-0.11	161.3	…	156.2	165.1	156.3	156.7	171.9	160.1	155.3	159.0	174.3
6499.650	20.0	2.520	-0.82	124.5	…	119.3	127.5	113.7	116.5	125.7	119.5	113.0	119.5	137.8
6471.650	20.0	2.530	-0.68	134.3	132.8	128.7	137.2	124.3	118.2	127.3	124.3	120.6	127.8	147.1
4753.150	21.0	0.000	-1.66	27.8	…	17.3	24.7	…	…	…	29.0	18.0	…	…
6239.360	21.0	0.000	-2.27	…	15.1	…	…	…	…	…	…	…	…	…
6239.800	21.0	0.000	-1.78	28.7	…	…	…	…	…	…	…	…	…	…
6258.950	21.0	0.020	-1.80	29.5	…	17.9	…	…	…	…	…	15.6	…	…
5724.070	21.0	1.430	-0.66	10.1	…	5.2	…	…	…	…	…	…	…	…
5686.840	21.0	1.440	0.38	49.3	45.6	37.8	47.0	…	…	…	50.1	37.4	…	57.6
5717.300	21.0	1.440	-0.53	10.5	…	…	10.3	…	…	…	…	…	…	…
5392.020	21.0	1.990	0.17	…	11.2	…	…	…	…	…	…	…	…	13.0
5318.330	21.1	1.360	-1.79	…	…	…	…	…	…	…	…	…	…	45.5
6604.580	21.1	1.360	-1.31	69.1	77.0	72.2	74.7	69.8	75.3	76.3	66.9	77.5	76.9	75.4
5667.140	21.1	1.500	-1.21	64.8	64.7	60.0	69.6	63.8	67.1	68.3	61.8	73.2	70.0	…
5657.870	21.1	1.510	-0.82	…	96.8	…	…	…	…	…	…	…	…	…
5684.190	21.1	1.510	-1.25	57.4	77.4	63.8	66.6	66.6	66.8	68.9	57.8	75.3	68.7	66.9
6245.620	21.1	1.510	-1.03	70.3	…	71.5	77.0	73.9	70.6	75.5	71.3	79.4	74.0	76.6
6300.690	21.1	1.510	-1.89	28.7	…	…	30.0	…	…	…	25.4	…	…	…
5526.810	21.1	1.770	0.02	104.6	113.0	108.3	112.3	105.9	107.5	115.6	104.8	115.9	110.8	98.1
5039.950	22.0	0.020	-1.13	136.2	139.8	125.7	141.1	…	116.2	138.6	133.9	…	…	…
5219.680	22.0	0.020	-2.24	…	92.8	…	…	…	…	…	…	…	…	…
5064.630	22.0	0.050	-0.93	…	…	…	…	…	…	…	…	…	…	148.4
5460.500	22.0	0.050	-2.75	69.8	…	51.2	71.4	43.4	39.8	64.7	…	48.0	46.9	…
4926.120	22.0	0.820	-2.11	…	…	…	…	…	…	…	…	…	50.6	…
4548.750	22.0	0.830	-0.30	…	…	…	…	…	…	…	…	…	108.1	…
4999.500	22.0	0.830	0.31	161.6	…	150.7	…	…	…	158.8	156.9	140.2	141.6	…
5384.630	22.0	0.830	-2.85	…	10.3	…	…	…	…	…	…	…	…	24.0
5020.020	22.0	0.840	-0.36	120.5	…	116.1	128.5	113.0	110.9	125.2	125.8	…	114.0	…
5295.780	22.0	1.070	-1.58	59.4	…	44.8	57.8	…	38.4	56.7	61.3	50.1	45.0	…
5113.420	22.0	1.440	-0.73	…	74.0	…	…	…	…	…	…	…	…	87.6
5453.660	22.0	1.440	-1.55	…	…	…	…	…	…	…	…	…	43.3	…
6336.100	22.0	1.440	-1.69	37.7	…	24.1	34.9	22.0	…	…	…	22.7	23.1	…
5145.440	22.0	1.460	-0.52	…	86.5	…	…	…	…	…	…	…	…	…
5145.440	22.0	1.460	-0.52	…	…	…	…	…	…	…	…	…	93.8	…
5474.230	22.0	1.460	-1.17	53.6	…	40.3	54.0	37.5	36.6	53.4	53.7	39.3	…	…
5490.150	22.0	1.460	-0.88	73.2	73.3	60.0	73.3	52.2	52.3	71.8	68.9	59.4	59.8	…
4617.250	22.0	1.750	0.45	101.8	…	…	106.4	…	…	…	…	98.6	96.1	…
4913.590	22.0	1.870	0.22	…	92.7	…	…	…	…	…	…	…	…	…
4915.200	22.0	1.890	-0.96	…	32.8	…	…	…	…	…	…	…	…	…

5222.670	22.0	2.080	-0.56	46.8	...	...	...	...	33.3	...	46.5	43.0	44.6	...
5223.610	22.0	2.090	-0.50	54.0	...	44.2	...	35.0	...	...	48.4	44.2	...	...
4928.300	22.0	2.150	0.11	...	75.4	...	...	...	...	...	...	...	74.2	...
5212.980	22.0	2.230	-1.09	...	11.4	10.3	11.4	...	...	...	14.9	...	...	...
4778.220	22.0	2.240	-0.16	...	49.6	...	...	...	...	...	...	...	...	55.3
5739.990	22.0	2.240	-0.61	34.3	35.8	27.0	33.2	23.6	...	30.2	34.7	24.2	27.2	...
5739.480	22.0	2.250	-0.54	...	...	...	...	...	...	...	...	...	...	42.3
5702.660	22.0	2.290	-0.52	...	...	24.6	31.5	...	...	...	31.9	27.0	26.0	...
5720.440	22.0	2.290	-0.84	25.3	...	16.1	22.7	13.7	...	...	20.9	16.3	...	...
5716.440	22.0	2.300	-0.64	...	26.5	...	...	...	...	...	...	...	...	30.8
5474.480	22.0	2.340	-0.85	...	...	...	...	...	...	...	...	...	...	20.7
5679.910	22.0	2.470	-0.51	...	21.1	...	22.5	...	...	...	26.5	...	...	...
5648.550	22.0	2.490	-0.20	...	36.7	...	...	...	...	...	...	...	...	44.7
5503.900	22.0	2.580	0.08	...	...	...	...	...	...	...	...	...	...	49.9
4470.840	22.1	1.160	-2.28	...	...	...	93.7	...	...	...	...	86.0	...	...
4609.250	22.1	1.180	-3.43	...	...	...	...	...	...	...	...	...	43.9	...
4589.930	22.1	1.240	-1.67	...	...	...	...	...	...	...	...	...	113.8	...
4708.650	22.1	1.240	-2.34	...	...	...	...	88.8	86.0	92.2	...	...	...	88.4
4764.510	22.1	1.240	-2.77	...	...	70.3	...	74.8	71.2	75.9	...	73.4	71.7	...
5005.170	22.1	1.570	-2.73	52.0	60.0	55.4	57.3	59.8	54.0	58.6	...	61.9	58.3	61.6
5381.030	22.1	1.570	-1.97	88.8	...	96.5	98.0	100.1	96.3	98.2	91.8	94.8	95.9	...
5336.780	22.1	1.580	-1.63	100.2	106.4	103.9	105.7	110.2	105.8	109.0	104.3	108.5	107.2	109.1
5396.240	22.1	1.580	-3.02	...	...	...	...	44.7	39.8	42.6	...	42.3	...	40.5
5418.770	22.1	1.580	-2.11	78.0	90.7	80.9	87.8	87.9	88.1	92.8	...	82.5	83.1	85.9
5492.880	22.1	1.580	-3.31	29.9	34.0	30.7	29.9	34.8	32.2	34.0	...	34.3	...	32.3
4911.190	22.1	3.120	-0.34	74.8	81.0	80.6	81.4	77.3	73.9	78.6	...	...	...	78.1
4577.150	23.0	0.000	-1.05	...	...	87.3	...	...	...	104.2	...	...	86.1	...
6251.830	23.0	0.290	-1.34	95.0	...	69.3	92.8	60.1	52.8	87.4	88.6	67.4	63.9	...
5626.020	23.0	1.040	-1.24	38.2	28.6	23.3	32.6	15.8	13.3	30.5	39.5	24.6	20.8	43.1
6058.150	23.0	1.040	-1.37	29.8	...	18.3	27.4	...	...	...	34.4	...	15.4	...
6111.650	23.0	1.040	-0.71	74.7	...	48.2	68.9	40.1	34.1	66.8	70.6	46.5	46.1	...
5624.860	23.0	1.050	-1.06	...	36.0	...	...	...	...	...	...	...	...	58.0
5727.660	23.0	1.050	-0.87	62.4	53.9	40.2	60.1	...	29.6	59.1	60.5	36.1	37.7	...
6135.370	23.0	1.050	-0.75	64.6	...	45.3	61.6	44.1	38.5	57.1	62.6	41.8	43.1	...
5584.500	23.0	1.060	-1.20	34.4	...	18.3	29.1	...	...	...	38.6	22.2	...	...
5657.430	23.0	1.060	-1.02	...	37.5	...	...	...	...	...	...	...	...	...
5737.070	23.0	1.060	-0.74	70.0	60.4	48.0	66.4	36.9	30.9	59.7	65.8	49.5	49.3	80.4
5668.370	23.0	1.080	-1.03	44.8	...	28.7	41.6	20.9	16.6	39.7	45.0	25.5	27.1	53.4
5670.850	23.0	1.080	-0.42	79.1	81.6	65.4	82.5	53.6	48.2	78.4	84.9	62.8	63.9	...
5727.050	23.0	1.080	-0.01	...	...	90.2	...	81.5	...	104.2	103.0	...	85.6	...

5303.220	23.1	2.280	-1.94	16.8	...	17.2	19.4	20.3	...	...	...	17.7	15.8	...
5819.930	23.1	2.520	-1.70	13.0	...	12.5	13.7	15.4	...	...	...	13.7	...	...
5928.870	23.1	2.520	-1.60	14.9	...	15.5	19.7	20.9	...	...	...	15.0	14.6	...
4545.940	24.0	0.940	-1.37	129.0	...	...	143.0	...	...	141.7	...	125.2	...	...
4616.110	24.0	0.980	-1.19	140.6	...	126.4	143.9	...	...	...	136.6	...	127.8	...
5296.700	24.0	0.980	-1.36	147.8	149.4	135.5	151.0	122.8	...	148.9	139.3	135.7	137.3	155.5
5300.750	24.0	0.980	-2.00	113.8	119.1	103.4	...	...	...	126.6	111.6	100.5	...	...
5345.800	24.0	1.000	-0.95	178.1	174.6	161.2	182.4	146.8	143.3	181.9	163.2	156.7	159.3	191.0
5348.310	24.0	1.000	-1.21	...	156.7	...	...	...	...	...	...	...	...	...
5238.960	24.0	2.710	-1.30	47.7	...	39.0	48.3	35.7	33.5	48.1	48.2	40.3	37.1	...
5241.460	24.0	2.710	-1.92	...	...	...	...	11.1	9.8	20.6	...	13.6	...	21.0
5329.140	24.0	2.910	-0.06	...	...	...	...	...	85.5	105.5	...	90.6	...	108.1
5783.070	24.0	3.320	-0.50	62.0	...	54.2	63.8	46.0	42.8	60.3	53.3	53.7	53.1	...
5784.970	24.0	3.320	-0.38	61.2	...	56.6	69.5	47.8	46.6	63.1	54.9	59.8	54.8	...
5214.130	24.0	3.370	-0.74	38.7	37.3	33.2	39.6	25.6	29.6	38.6	39.5	31.3	32.1	...
5628.650	24.0	3.420	-0.74	37.6	36.0	31.9	38.6	29.1	22.1	...	34.0	33.0	27.0	47.3
5287.150	24.0	3.440	-0.87	...	29.9	...	...	20.0	20.3	33.2	...	23.5	...	36.4
5318.760	24.0	3.440	-0.67	...	35.6	...	...	...	...	...	...	...	...	...
5340.430	24.0	3.440	-0.73	...	...	...	...	...	...	...	...	...	...	48.5
5312.860	24.0	3.450	-0.55	46.6	42.2	37.6	48.0	31.6	30.1	44.6	40.6	38.7	41.7	49.7
5304.190	24.0	3.460	-0.69	37.4	39.4	30.7	38.9	24.5	23.8	40.6	37.5	30.6	30.9	45.4
5237.310	24.1	4.070	-1.16	68.7	72.2	71.1	71.1	70.6	73.7	74.8	62.3	71.5	69.6	73.1
5279.870	24.1	4.070	-2.10	...	32.9	...	...	35.7	...	31.9	...	34.2	...	33.4
5308.430	24.1	4.070	-1.81	43.3	45.5	42.6	43.0	45.5	49.1	44.7	35.5	45.5	64.5	46.5
5313.580	24.1	4.070	-1.65	46.1	45.7	49.5	49.8	49.4	56.6	47.0	46.9	53.9	50.9	49.4
5334.850	24.1	4.070	-1.56	48.6	50.9	51.8	52.0	54.5	...	...	50.8	53.1	55.9	54.8
5502.070	24.1	4.170	-1.99	...	32.3	...	...	31.8	33.3	33.0	...	38.1	...	29.7
5457.460	25.0	2.160	-2.61	58.5	...	...	...	...	...	...	59.8	...	...	60.5
6013.490	25.0	3.070	-0.25	130.9	133.9	120.7	133.9	109.8	106.8	127.3	127.3	120.3	125.3	...
6016.640	25.0	3.070	-0.22	131.9	136.9	128.8	137.8	113.8	118.3	132.5	125.0	123.2	131.6	...
6021.800	25.0	3.080	-0.08	135.5	138.1	130.3	142.6	116.7	118.5	136.5	127.1	128.5	130.1	...
5377.610	25.0	3.850	-0.11	83.4	86.0	80.1	84.8	64.1	70.3	84.0	82.5	78.1	81.1	81.9
5399.470	25.0	3.850	-0.29	81.5	73.6	...	...	...	61.5	79.5	...	67.6	...	74.1
5413.660	25.0	3.860	-0.59	...	56.3	...	...	...	...	...	...	...	...	60.8
6710.310	26.0	1.490	-4.87	72.7	...	60.4	...	...	...	78.2	...	...	...	...
4772.810	26.0	1.560	-2.90	136.7	...	131.5	147.8	...	126.4	141.5	133.5	...	130.7	...
5307.360	26.0	1.610	-2.99	137.7	...	135.2	148.2	124.3	...	142.9	137.5	...	135.7	...
6137.000	26.0	2.200	-2.95	117.9	...	...	128.2	104.6	106.7	125.3	111.4	...	...	...
6335.340	26.0	2.200	-2.18	159.5	...	...	...	...	...	...	154.0	...	150.1	...

6392.540	26.0	2.280	-4.03	60.6	...	53.2	62.2	46.9	47.7	61.8	57.8	...	53.9	...
6608.020	26.0	2.280	-4.04	61.6	...	55.0	65.2	...	47.5	61.8	57.8	...	58.0	...
6252.560	26.0	2.400	-1.69	175.2	...	...	182.2	158.0	160.4	...	170.6	162.4	168.4	...
6750.150	26.0	2.420	-2.62	123.8	...	...	...	...	...	...	...	...	120.6	...
6136.630	26.0	2.450	-1.40	196.1	...	...	200.5	173.4	174.6	194.3	181.2	176.0	177.2	...
5701.550	26.0	2.560	-2.22	126.3	129.7	122.9	136.3	...	...	132.3	124.1	...	124.5	...
6646.920	26.0	2.610	-3.99	47.8	...	36.6	46.9	28.9	27.3	49.2	40.1	32.3	34.5	...
4683.540	26.0	2.830	-2.32	94.4	...	...	...	...	...	...	92.6	88.6	90.9	...
5036.910	26.0	3.020	-3.04	64.1	...	58.9	65.6	...	...	...	59.6	...	55.2	...
5215.190	26.0	3.270	-0.87	147.0	157.5	147.6	155.4	133.9	...	153.5	142.9	143.3	139.8	153.9
5302.290	26.0	3.280	-0.72	...	166.4	...	...	...	...	...	...	...	...	166.0
4946.370	26.0	3.370	-1.01	...	136.1	...	...	...	...	...	...	...	...	136.6
5569.630	26.0	3.420	-0.49	176.7	178.8	164.7	175.6	150.1	155.5	175.0	...	159.3	160.9	178.8
5576.100	26.0	3.430	-1.01	130.8	145.1	131.8	146.2	...	124.2	133.6	133.7	130.0	...	151.9
4547.830	26.0	3.550	-1.01	114.9	...	118.5	118.2	...	107.3	...	107.9	106.2	108.7	...
5242.490	26.0	3.630	-0.97	115.2	120.0	...	...	108.5	113.5	121.6	116.8	112.1	114.8	124.1
5568.870	26.0	3.630	-2.95	34.7	...	28.2	34.9	22.5	...	34.2	31.4	25.1	27.4	...
4979.560	26.0	3.640	-2.58	...	52.7	...	...	...	...	...	...	...	...	...
5294.550	26.0	3.640	-2.86	39.4	...	...	40.3	...	27.5	39.3	38.3	29.3	33.0	...
5529.150	26.0	3.640	-2.68	...	...	...	...	...	...	...	...	...	...	47.8
5539.280	26.0	3.640	-2.66	46.7	49.2	42.2	47.4	37.2	32.3	47.4	48.9	40.5	39.6	50.6
5636.700	26.0	3.640	-2.61	51.3	51.7	42.6	50.0	...	36.9	50.4	50.9	41.4	39.8	57.0
5760.350	26.0	3.640	-2.49	53.5	...	48.9	56.4	44.2	44.4	51.8	50.0	...	47.8	...
5466.990	26.0	3.650	-2.23	66.9	...	65.4	71.5	...	...	70.1	62.7	61.0	...	...
6411.650	26.0	3.650	-0.72	143.7	...	149.9	155.7	131.2	139.0	146.9	143.6	139.2	146.4	...
5379.580	26.0	3.690	-1.51	90.3	97.2	90.8	95.6	85.1	87.3	93.9	88.3	87.0	89.2	96.7
6336.840	26.0	3.690	-0.86	...	...	131.6	140.6	122.4	128.0	138.0	133.2	127.5	...	...
6003.020	26.0	3.880	-1.12	105.5	...	108.1	112.9	...	...	107.6	102.7	...	...	...
5213.790	26.0	3.940	-2.76	...	23.6	...	...	...	...	...	...	...	...	24.5
6187.990	26.0	3.940	-1.72	78.1	...	76.2	82.9	67.5	70.2	75.5	77.8	71.9	77.7	...
6027.060	26.0	4.080	-1.09	...	...	...	...	...	89.1	...	89.6	89.6	88.8	...
5677.670	26.0	4.100	-2.70	...	18.7	...	...	...	...	...	...	...	...	26.8
5293.960	26.0	4.140	-1.87	57.2	...	54.4	58.5	48.5	47.7	55.7	51.6	50.6	50.3	...
6127.910	26.0	4.140	-1.40	...	...	...	...	...	70.6	...	...	...	...	...
6165.360	26.0	4.140	-1.47	73.6	...	71.7	...	66.8	68.7	74.7	68.5	68.3	69.3	...
5608.980	26.0	4.210	-2.40	30.8	...	24.5	...	...	...	...	...	...	25.3	...
5618.630	26.0	4.210	-1.28	75.7	...	...	80.3	71.1	71.4	78.0	78.1	...	75.4	...
4969.890	26.0	4.220	-0.75	...	98.6	...	...	...	...	...	...	...	...	99.4

4986.210	26.0	4.220	-1.37	...	78.0	...	...	...	...	...	...	...	...	73.8
4991.830	26.0	4.220	-1.89	...	54.2	...	...	...	...	...	...	...	...	...
5074.730	26.0	4.220	-0.16	...	135.0	124.2	130.2	...	...	129.2	...	119.5	...	130.5
5195.450	26.0	4.220	-0.00	...	134.8	...	...	125.8	128.0	135.6	133.5	...	...	144.6
5638.270	26.0	4.220	-0.87	97.0	107.1	97.1	107.5	89.1	...	97.6	98.2	94.6	92.9	...
5738.230	26.0	4.220	-2.34	...	32.2	26.9	...	22.6	21.1	32.6	31.5	26.1	28.4	39.0
5579.340	26.0	4.230	-2.41	28.7	...	22.6	28.7	...	17.8	28.8	...	...	24.5	...
5243.770	26.0	4.260	-1.15	83.5	...	80.7	87.3	...	...	83.6	76.4	...	...	...
5308.680	26.0	4.260	-2.49	...	...	19.1	23.3	...	...	...	22.8	...	...	...
5646.690	26.0	4.260	-2.51	23.8	22.7	19.0	23.6	...	...	...	18.8	...	16.7	27.0
5652.310	26.0	4.260	-1.92	...	52.6	...	...	...	...	...	...	...	...	53.4
5731.770	26.0	4.260	-1.29	...	...	73.5	85.3	72.3	...	83.4	75.9	...	74.5	...
5717.840	26.0	4.280	-1.13	83.2	89.0	81.1	88.1	...	78.5	84.9	83.8	...	80.8	90.0
5814.800	26.0	4.280	-1.94	...	47.3	...	...	...	...	...	...	...	...	52.5
5861.100	26.0	4.280	-2.45	...	26.1	...	...	...	...	...	...	...	...	28.5
5007.710	26.0	4.290	-1.83	...	50.6	...	...	...	...	...	...	...	...	52.7
5383.360	26.0	4.310	0.64	...	...	...	...	...	...	...	...	...	...	191.3
5262.610	26.0	4.320	-2.28	...	24.5	...	...	...	...	...	...	...	...	25.3
6303.450	26.0	4.320	-2.66	...	17.3	...	...	...	...	...	...	...	...	16.7
5315.050	26.0	4.370	-1.55	...	63.2	...	...	...	...	...	...	...	...	...
5466.400	26.0	4.370	-0.63	101.5	...	99.4	105.3	93.2	95.1	103.9	97.3	95.8	98.3	...
5546.510	26.0	4.370	-1.31	69.5	75.6	65.8	77.0	...	60.9	73.4	70.2	...	...	79.2
5445.050	26.0	4.390	-0.01	128.4	...	131.2	137.8	118.9	126.1	133.0	127.7	124.5	...	...
5619.590	26.0	4.390	-1.70	...	52.4	...	...	...	...	...	...	...	...	58.6
8598.760	26.0	4.390	-1.09	...	...	...	...	...	...	...	...	...	...	100.1
5326.800	26.0	4.410	-2.10	...	35.2	...	...	...	...	...	...	...	...	...
5367.450	26.0	4.410	0.44	...	...	...	...	...	...	...	...	...	...	152.8
5295.320	26.0	4.420	-1.69	50.8	...	48.6	55.1	41.9	43.6	51.4	43.4	48.8	48.2	...
5285.110	26.0	4.430	-1.62	...	54.8	...	...	...	...	...	...	...	...	51.1
5435.190	26.0	4.430	-2.19	...	...	...	...	...	...	...	...	...	...	26.1
5463.280	26.0	4.430	0.11	...	...	...	...	123.1	124.3	...	...	...	...	...
5560.220	26.0	4.430	-1.19	71.4	...	72.4	77.7	65.0	64.8	75.0	67.9	71.0	70.8	...
5364.860	26.0	4.450	0.22	...	138.9	...	...	...	...	...	...	...	...	141.2
5462.970	26.0	4.470	-0.16	114.9	...	...	...	107.5	107.9	118.2	...	109.0	114.2	...
5651.460	26.0	4.470	-2.00	...	36.5	...	...	...	...	...	...	...	...	...
5720.890	26.0	4.550	-1.95	...	35.4	...	...	...	...	...	...	...	...	34.5
5679.030	26.0	4.650	-0.91	74.5	79.9	74.1	73.3	...	70.8	76.5	75.8	66.2	68.7	80.8
6007.960	26.0	4.650	-0.97	73.8	...	73.2	77.7	...	69.2	71.9	71.8	65.7	...	...
6253.840	26.0	4.730	-1.66	...	38.1	...	...	...	...	...	...	...	...	43.4

5552.680	26.0	4.960	-1.99	...	14.5	...	...	...	...	...	...	...	...	12.8
5549.640	26.0	4.990	-1.69	...	...	...	...	...	...	...	...	...	...	23.0
5559.640	26.0	4.990	-1.83	...	16.3	...	...	...	...	...	...	...	...	19.6
5633.950	26.0	4.990	-0.27	84.8	88.7	85.6	91.4	79.7	78.1	84.4	82.5	81.1	82.4	88.8
5577.030	26.0	5.030	-1.55	24.6	...	21.1	...	...	18.9	22.1	24.8	...	21.2	...
4520.210	26.1	2.810	-2.61	99.1	...	104.7	106.1	103.9	105.7	103.7	97.9	107.9	107.5	100.5
4993.340	26.1	2.810	-3.68	56.1	66.4	59.5	62.2	...	66.9	58.9	57.9	64.7	62.7	63.4
5256.930	26.1	2.890	-4.06	39.9	45.7	...	40.9	40.9	46.2	43.9	...	...	...	...
5284.100	26.1	2.890	-3.20	75.0	81.9	83.7	78.9	83.4	88.7	79.0	73.7	84.1	85.4	36.0
6369.450	26.1	2.890	-4.11	33.2	38.8	35.6	35.7	39.2	41.1	35.4	...	...	...	...
6084.110	26.1	3.200	-3.88	34.1	40.5	36.8	37.0	41.3	...	34.7	31.0	39.4	41.6	38.5
5234.630	26.1	3.220	-2.05	102.8	109.7	...	104.0	114.7	117.8	...	103.8	114.5	112.6	109.3
5414.060	26.1	3.220	-3.58	40.9	48.6	44.6	45.3	...	...	...	...	...	...	42.6
5264.800	26.1	3.230	-3.23	56.0	64.2	61.7	63.0	64.5	72.3	57.3	55.8	67.0	68.7	56.8
6149.250	26.1	3.890	-2.84	45.5	52.2	51.3	45.1	50.7	54.7	47.9	40.6	52.8	48.3	45.3
6247.560	26.1	3.890	-2.43	58.9	64.3	66.4	63.0	72.5	74.6	63.5	55.2	67.3	67.8	...
6416.930	26.1	3.890	-2.88	41.4	50.2	50.8	44.6	53.3	56.0	46.1	43.9	52.5	51.3	...
6456.380	26.1	3.900	-2.19	72.0	75.1	78.7	71.7	81.8	84.5	69.6	69.4	79.5	80.2	71.3
5301.030	27.0	1.710	-1.99	...	68.4	59.2	...	53.0	55.1	68.6	68.9	59.4	60.3	77.4
5530.770	27.0	1.710	-2.06	...	61.0	...	...	...	...	...	...	...	...	74.4
6116.990	27.0	1.780	-2.49	35.0	34.7	26.8	39.2	22.7	...	35.9	41.0	25.5	26.6	...
5647.240	27.0	2.280	-1.56	49.2	51.2	44.2	56.4	39.7	39.2	50.3	55.9	46.6	45.9	60.9
5212.690	27.0	3.510	-0.14	49.7	51.2	47.1	55.3	...	...	...	57.4	41.1	47.0	57.7
5280.610	27.0	3.630	-0.03	...	47.2	...	...	...	...	...	...	...	...	50.5
6455.000	27.0	3.630	-0.25	37.6	34.7	36.7	41.5	32.9	35.9	41.7	43.9	33.0	32.1	...
5342.700	27.0	4.020	0.69	54.7	...	51.0	59.5	47.1	54.7	55.1	58.4	51.3	57.6	59.9
5578.710	28.0	1.680	-2.64	...	109.2	97.8	108.9	94.5	...	108.8	96.8	...	101.9	...
5748.360	28.0	1.680	-3.26	76.5	...	72.3	81.3	...	65.8	80.9	68.6	71.4	73.4	...
6108.120	28.0	1.680	-2.45	115.0	...	111.4	119.8	...	...	...	107.8	...	109.5	...
6191.180	28.0	1.680	-2.35	121.1	...	119.0	132.2	112.6	114.5	126.8	121.1	118.0	119.5	...
6177.250	28.0	1.830	-3.50	...	...	...	...	...	42.1	53.6	49.8	47.4	50.4	...
4998.220	28.0	3.610	-0.78	76.8	...	75.7	82.9	72.7	71.7	78.5	...	78.4	75.0	...
4965.140	28.0	3.800	-1.14	...	60.5	...	...	...	...	...	...	...	...	60.0
4984.090	28.0	3.800	0.23	...	117.8	...	...	...	...	...	...	...	...	...
5452.840	28.0	3.800	-1.66	34.4	...	...	...	...	...	...	...	29.3	32.1	...
5462.500	28.0	3.850	-0.93	62.4	...	61.3	68.4	56.7	57.9	63.7	62.5	62.5	58.7	...
5468.120	28.0	3.850	-1.61	...	...	...	28.2	...	22.8	28.0	24.3	...	...	...
5589.360	28.0	3.900	-1.14	...	...	48.8	51.0	47.3	37.5	...	47.3	48.5	...	58.4

5593.720	28.0	3.900	-0.84	...	65.5	61.4	...	59.2	55.3	...	60.3	59.5	59.5	...
5638.750	28.0	3.900	-1.72	25.0	29.1	21.4	26.0	18.4	14.5	24.4	...	24.4	23.1	27.7
5453.250	28.0	4.090	-1.49	...	...	...	...	...	...	...	...	...	...	27.4
5625.320	28.0	4.090	-0.70	59.5	62.3	59.2	62.5	54.9	55.8	60.9	60.4	61.1	58.3	...
6111.070	28.0	4.090	-0.87	55.5	...	53.7	59.5	51.0	49.5	56.8	55.2	51.2	55.2	...
6133.960	28.0	4.090	-1.83	...	...	...	...	...	...	...	...	...	...	21.0
5641.880	28.0	4.100	-1.07	...	45.4	...	...	...	...	...	...	...	...	55.6
5682.200	28.0	4.110	-0.47	71.0	...	73.2	74.1	68.3	65.5	69.5	66.6	67.4	69.5	...
5760.840	28.0	4.110	-0.80	56.6	...	56.1	...	51.0	51.7	58.2	53.2	55.6	58.1	...
6186.720	28.0	4.110	-0.96	51.3	...	51.8	55.7	...	...	...	...	...	...	...
5392.320	28.0	4.150	-1.32	...	27.5	...	...	...	...	...	...	...	...	29.8
5643.070	28.0	4.170	-1.24	...	...	...	...	...	...	...	...	...	...	40.1
5805.210	28.0	4.170	-0.64	...	62.9	...	...	...	...	...	...	...	...	61.5
6130.140	28.0	4.270	-0.96	...	...	...	...	...	...	...	...	...	...	44.6
4722.150	30.0	4.030	-0.39	76.5	36.2	82.2	79.2	81.0	84.3	80.2	86.8	86.1	80.0	82.6
6362.360	30.0	5.790	0.27	...	...	...	...	...	41.5	...	...	...	...	...
4854.860	39.1	0.990	-0.38	...	...	...	...	79.6	...	...	...	...	...	...
5119.110	39.1	0.990	-1.36	...	...	...	...	...	...	47.8	...	...	...	...
5200.390	39.1	0.990	-0.57	...	79.0	76.4	78.7	81.3	77.3	82.6	76.0	79.4	79.0	88.1
4982.110	39.1	1.030	-1.29	42.2	42.9	41.1	43.4	47.0	39.4	44.9	43.0	42.7	38.6	51.3
5289.820	39.1	1.030	-1.85	19.9	22.7	17.9	21.1	...	...	...	22.0	22.5	20.6	26.6
5087.420	39.1	1.080	-0.17	...	...	...	...	86.5	87.4	...	...	...	...	...
5320.800	39.1	1.080	-1.95	14.9	17.1	13.6	15.8	...	...	...	...	...	15.4	24.3
5402.760	39.1	1.840	-0.62	...	36.9	...	...	...	39.0	36.4	...	39.3	...	41.4
6134.560	40.0	0.000	-1.28	24.4	20.5	16.0	24.3	...	8.2	21.6	21.0	...	14.3	34.5
6143.210	40.0	0.070	-1.10	29.6	24.7	18.4	28.3	...	...	...	26.3	18.3	16.0	42.2
6127.450	40.0	0.150	-1.06	26.8	22.6	16.4	26.0	11.6	11.2	26.3	23.7	16.7	14.1	41.7
4784.920	40.0	0.690	-0.49	...	...	...	17.0	...	...	...	...	...	...	...
4687.770	40.0	0.730	0.55	...	...	...	...	...	...	...	...	...	43.8	...
5853.690	56.1	0.600	-1.02	115.6	122.2	114.2	122.6	120.2	125.5	124.6	107.4	120.4	123.2	157.3
6496.900	56.1	0.600	-0.37	170.6	170.0	160.8	177.4	166.1	175.1	178.9	...	172.9	177.8	227.4
5482.260	57.1	0.000	-2.23	...	...	...	...	...	...	14.6	...	13.0	...	...
5805.790	57.1	0.130	-1.61	...	...	...	...	...	...	...	34.1	...	...	...
6774.230	57.1	0.130	-1.82	21.8	...	17.5	...	...	...	...	...	...	...	...
5303.540	57.1	0.320	-1.35	26.7	30.2	22.7	28.6	24.4	...	...	31.2	27.6	28.3	36.7
6390.480	57.1	0.320	-1.41	...	26.9	22.6	29.5	...	23.5	32.8	29.4	25.4	25.2	32.9
5274.210	58.1	1.040	0.13	...	39.9	12.2	39.0	35.1	...	39.6	...	37.1	...	40.0
6043.370	58.1	1.210	-0.48	11.4	14.9	...	...	...	...	...	...	11.4	...	...
5472.270	58.1	1.240	-0.18	16.7	...	15.8	17.1	18.8	...	20.6	...	17.2	14.0	15.8

5092.790	60.1	0.380	-0.61	40.7	43.6	34.9	45.0	41.1	43.7	43.3	...	40.6	...	48.0
5319.810	60.1	0.550	-0.14	52.8	58.6	49.5	...	53.4	56.9	55.2	...	49.6	48.8	...
5276.860	60.1	0.860	-0.61	17.3	19.0	13.8	18.5	15.1	18.7	21.4	...	...	...	...
5811.570	60.1	0.860	-0.86	...	11.9	...	...	...	...	...	...	...	...	...
4591.810	62.1	0.180	-1.12	21.0	...	17.1	22.8	19.7	...	24.7	...	20.6	23.7	...
4577.680	62.1	0.250	-0.65	34.3	...	29.4	35.1	...	36.2	36.9	41.6	38.5	35.8	49.6
4523.900	62.1	0.430	-0.39	40.3	...	38.6	...	38.3	...	...	...	45.9	44.1	...
4537.920	62.1	0.480	-0.48	33.5	...	31.8	...	33.6	...	35.3	31.1	37.5	...	...
4519.600	62.1	0.540	-0.35	36.8	...	32.3	39.1	35.9	...	38.2	39.5	37.5	...	48.0
4467.310	62.1	0.650	0.30	...	...	49.1	54.1	49.1	47.5	54.8	...	...	...	...
6645.110	63.1	1.380	0.12	25.3	23.5	23.1	23.8	20.6	...	22.0	18.5	18.7	19.9	27.7

Table 8.16: The atomic data used for the abundance analysis of stars in OC NGC 2506

Wavelength	Z^a	LEP^b	log gf		W_λ (mÅ)		Wavelength	Z^a	LEP^b	log gf		W_λ (mÅ)	
λ (Å)		(eV)		[#2212	#3231	#4138]	λ (Å)		(eV)		[#2212	#3231	#4138]
4668.530	11.0	2.100	-1.25	85.3	75.2	85.2	6122.220	20.0	1.900	-0.32	204.7	185.2	179.2
4982.790	11.0	2.100	-0.91	...	96.3	102.8	5581.970	20.0	2.520	-0.56	122.1	113.2	114.0
6154.230	11.0	2.100	-1.55	70.2	50.3	...	5590.120	20.0	2.520	-0.74	118.4	111.9	107.7
6160.760	11.0	2.100	-1.25	100.0	81.7	...	6166.440	20.0	2.520	-1.14	104.9	97.2	84.6
5711.090	12.0	4.340	-1.72	130.9	115.1	108.6	6169.560	20.0	2.520	-0.48	140.3	128.2	126.2
5528.410	12.0	4.350	-0.50	221.9	194.8	197.6	6455.600	20.0	2.520	-1.29	89.2	79.0	77.8
7835.220	13.0	4.020	-0.47	54.2	52.3	52.1	6499.650	20.0	2.520	-0.82	119.4	102.4	113.8
7836.040	13.0	4.020	-0.34	64.5	61.2	61.4	6471.650	20.0	2.530	-0.68	127.4	120.5	118.8
5665.570	14.0	4.920	-2.04	54.6	...	50.2	5686.840	21.0	1.440	0.38	52.2	24.8	19.6
5645.610	14.0	4.930	-2.14	51.9	...	42.8	6604.580	21.1	1.360	-1.31	84.2	68.0	67.6
5701.100	14.0	4.930	-2.05	48.9	48.9	52.4	5667.140	21.1	1.500	-1.21	76.9	65.2	64.5
5772.150	14.0	5.080	-1.75	67.2	53.0	61.9	5684.190	21.1	1.510	-1.25	65.5	60.4	...
5753.640	14.0	5.610	-1.30	54.9	45.4	52.8	6245.620	21.1	1.510	-1.03	80.0	83.0	80.2
6131.580	14.0	5.610	-1.71	25.6	...	...	5526.810	21.1	1.770	0.02	111.4	115.7	...
6131.840	14.0	5.610	-1.69	38.1	...	...	5039.950	22.0	0.020	-1.13	132.4	123.3	128.8
6237.310	14.0	5.610	-1.14	65.2	59.1	63.0	5460.500	22.0	0.050	-2.75	71.6	39.0	43.5
6243.810	14.0	5.610	-1.26	51.1	49.0	51.8	4999.500	22.0	0.830	0.31	159.4	145.7	...
6244.470	14.0	5.610	-1.36	43.1	54.1	50.2	5020.020	22.0	0.840	-0.36	125.7	117.8	117.2
6142.490	14.0	5.620	-1.54	37.3	...	31.2	5295.780	22.0	1.070	-1.58	62.8	...	...
6721.820	14.0	5.860	-1.06	50.1	42.6	45.4	6336.100	22.0	1.440	-1.69	...	17.6	19.8

Wavelength	Z^a	LEP^b	log gf		W_λ (mÅ)	
λ (Å)		(eV)		[#2212	#3231	#4138]
5474.230	22.0	1.460	-1.17	52.3	27.0	36.1
5490.150	22.0	1.460	-0.88	70.0	49.6	53.2
5222.670	22.0	2.080	-0.56	49.3	23.1	...
5739.990	22.0	2.240	-0.61	30.8	22.4	...
4708.650	22.1	1.240	-2.34	89.5	87.7	91.5
4764.510	22.1	1.240	-2.77	76.7	...	68.1
5005.170	22.1	1.570	-2.73	62.2	62.1	55.2
5381.030	22.1	1.570	-1.97	95.2	99.9	89.8
5336.780	22.1	1.580	-1.63	105.5	...	...
5396.240	22.1	1.580	-3.02	42.5	...	36.4
5418.770	22.1	1.580	-2.11	90.1	96.0	87.5
5492.880	22.1	1.580	-3.31	37.7	32.3	30.8
4911.190	22.1	3.120	-0.34	75.0	99.7	91.3
4577.150	23.0	0.000	-1.05	...	82.2	82.5
6251.830	23.0	0.290	-1.34	87.1	64.2	60.4
5626.020	23.0	1.040	-1.24	24.4	...	...
6111.650	23.0	1.040	-0.71	67.6	40.9	35.9
5727.660	23.0	1.050	-0.87	45.2	...	...
6135.370	23.0	1.050	-0.75	54.3	36.1	31.5
5737.070	23.0	1.060	-0.74	59.1	35.9	36.2
5668.370	23.0	1.080	-1.03	39.0	21.4	23.1
5670.850	23.0	1.080	-0.42	78.3	57.3	61.2
5727.050	23.0	1.080	-0.01	90.5	88.8	81.7
4545.940	24.0	0.940	-1.37	131.0	123.0	...
5296.700	24.0	0.980	-1.36	146.9	129.5	124.9
5300.750	24.0	0.980	-2.00	...	101.2	100.1
5345.800	24.0	1.000	-0.95	171.1	158.4	...
5238.960	24.0	2.710	-1.30	...	28.4	29.1
5329.140	24.0	2.910	-0.06	...	80.9	87.6
5783.070	24.0	3.320	-0.50	49.3	43.6	39.2
5784.970	24.0	3.320	-0.38	...	44.9	...
5214.130	24.0	3.370	-0.74	36.5	28.2	24.8
5287.150	24.0	3.440	-0.87	25.4	18.7	18.6
5312.860	24.0	3.450	-0.55	...	30.4	...
5304.190	24.0	3.460	-0.69	...	...	22.3
5237.310	24.1	4.070	-1.16	67.9	63.7	69.8
5279.870	24.1	4.070	-2.10	28.9	30.0	...
5308.430	24.1	4.070	-1.81	36.7	38.9	40.9
5313.580	24.1	4.070	-1.65	41.0	46.8	45.1
5334.850	24.1	4.070	-1.56	47.5	52.1	43.3
5502.070	24.1	4.170	-1.99	29.6	28.7	...
6013.490	25.0	3.070	-0.25	122.6	103.4	107.2
6016.640	25.0	3.070	-0.22	125.6	110.8	111.0
6021.800	25.0	3.080	-0.08	131.9	115.5	114.0
5377.610	25.0	3.850	-0.11	76.5	68.0	58.9
5399.470	25.0	3.850	-0.29	68.8	45.8	48.2
6710.310	26.0	1.490	-4.87	74.2	...	49.5
5307.360	26.0	1.610	-2.99	142.2	132.3	124.2
6137.000	26.0	2.200	-2.95	120.8	111.6	97.6
6335.340	26.0	2.200	-2.18	...	133.9	135.0
6392.540	26.0	2.280	-4.03	60.6	40.6	43.9
6608.020	26.0	2.280	-4.04	64.6	49.1	...
6252.560	26.0	2.400	-1.69	168.5	165.5	162.1
6136.630	26.0	2.450	-1.40	190.5	175.5	169.2
5701.550	26.0	2.560	-2.22	128.7	119.3	...
4683.540	26.0	2.830	-2.32	94.9	...	84.8
5570.030	26.0	2.850	-4.26	...	17.3	...
5215.190	26.0	3.270	-0.87	141.7	...	138.1
5569.630	26.0	3.420	-0.49	156.9	150.5	150.4
5576.100	26.0	3.430	-1.01	...	122.5	122.2
4547.830	26.0	3.550	-1.01	...	110.2	...
5242.490	26.0	3.630	-0.97	118.6	115.0	108.8
5294.550	26.0	3.640	-2.86	34.8	25.8	...
5539.280	26.0	3.640	-2.66	43.5	32.4	...
5636.700	26.0	3.640	-2.61	...	32.9	...
5760.350	26.0	3.640	-2.49	51.9	38.6	40.1
5466.990	26.0	3.650	-2.23	...	56.1	53.8
6411.650	26.0	3.650	-0.72	144.2	133.6	138.0
5379.580	26.0	3.690	-1.51	...	83.3	87.2
6336.840	26.0	3.690	-0.86	126.5	121.8	124.1
6003.020	26.0	3.880	-1.12	105.1	97.1	99.5
6187.990	26.0	3.940	-1.72	75.8	60.2	63.7

6027.060	26.0	4.080	-1.09	...	89.2	83.0
5293.960	26.0	4.140	-1.87	55.4	43.1	44.6
6165.360	26.0	4.140	-1.47	75.0	60.2	...
5074.730	26.0	4.220	-0.16	121.1	...	114.9
5195.450	26.0	4.220	-0.00	131.2	129.6	...
5638.270	26.0	4.220	-0.87	98.0	91.0	88.1
5738.230	26.0	4.220	-2.34	...	21.5	...
5243.770	26.0	4.260	-1.15	73.9	75.5	74.9
5731.770	26.0	4.260	-1.29	75.0	72.9	68.6
5717.840	26.0	4.280	-1.13	80.0	...	73.8
5466.400	26.0	4.370	-0.63	...	89.2	90.7
5546.510	26.0	4.370	-1.31	70.7	60.2	...
5445.050	26.0	4.390	-0.01	123.6	119.6	120.6
5295.320	26.0	4.420	-1.69	47.6	...	...
5560.220	26.0	4.430	-1.19	69.8	58.6	61.9
5462.970	26.0	4.470	-0.16	107.4	105.7	...
5679.030	26.0	4.650	-0.91	72.5	64.0	65.7
6007.960	26.0	4.650	-0.97	...	67.0	64.2
5633.950	26.0	4.990	-0.27	...	76.1	...
4520.210	26.1	2.810	-2.61	102.2	105.1	107.8
4993.340	26.1	2.810	-3.68	...	...	64.1
5256.930	26.1	2.890	-4.06	28.4	...	...
5284.100	26.1	2.890	-3.20	81.5	82.3	78.2
6084.110	26.1	3.200	-3.88	40.3	32.5	35.7
5234.630	26.1	3.220	-2.05	110.5	108.3	114.8
5264.800	26.1	3.230	-3.23	59.8	61.8	61.6
6247.560	26.1	3.890	-2.43	63.5	65.1	69.3
6416.930	26.1	3.890	-2.88	49.1	48.4	51.2
6456.380	26.1	3.900	-2.19	73.7	78.0	72.1
5301.030	27.0	1.710	-1.99	69.0	50.9	...
6116.990	27.0	1.780	-2.49	41.7	...	...
5647.240	27.0	2.280	-1.56	52.5	36.2	35.9
6455.000	27.0	3.630	-0.25	43.1	25.1	29.0
5342.700	27.0	4.020	0.69	54.1	42.0	47.4
5578.710	28.0	1.680	-2.64	...	93.3	89.2
5748.360	28.0	1.680	-3.26	77.6	...	...
6191.180	28.0	1.680	-2.35	124.4	...	111.3
6177.250	28.0	1.830	-3.50	59.7	39.9	36.1
4998.220	28.0	3.610	-0.78	77.4	62.9	...
5462.500	28.0	3.850	-0.93	56.8	52.2	50.2
5589.360	28.0	3.900	-1.14	51.6	30.8	36.2
5593.720	28.0	3.900	-0.84	57.8	54.4	54.1
5638.750	28.0	3.900	-1.72	24.4	...	11.7
5625.320	28.0	4.090	-0.70	60.5	50.6	49.8
6111.070	28.0	4.090	-0.87	50.9	45.3	45.3
5682.200	28.0	4.110	-0.47	69.9	63.4	62.4
5760.840	28.0	4.110	-0.80	49.2	45.6	39.5
4722.150	30.0	4.030	-0.39	80.1	83.4	82.3
5119.110	39.1	0.990	-1.36	...	70.5	32.6
5200.390	39.1	0.990	-0.57	84.0	77.0	69.4
4982.110	39.1	1.030	-1.29	45.6	...	...
5087.420	39.1	1.080	-0.17	90.2	...	84.1
5320.800	39.1	1.080	-1.95	22.1	...	...
5402.760	39.1	1.840	-0.62	39.2	...	25.1
6134.560	40.0	0.000	-1.28	22.8	...	...
6127.450	40.0	0.150	-1.06	21.0	10.6	...
5853.690	56.1	0.600	-1.02	126.3	123.5	123.2
6496.900	56.1	0.600	-0.37	167.9	...	...
5303.540	57.1	0.320	-1.35	42.2	29.5	27.7
6390.480	57.1	0.320	-1.41	40.2	28.9	...
5274.210	58.1	1.040	0.13	46.7	...	30.0
6043.370	58.1	1.210	-0.48	14.7	...	...
5472.270	58.1	1.240	-0.18	...	14.5	...
5092.790	60.1	0.380	-0.61	43.5	48.2	...
5319.810	60.1	0.550	-0.14	71.2	58.5	52.8
5276.860	60.1	0.860	-0.61	...	...	14.7
4577.680	62.1	0.250	-0.65	...	50.2	...
4523.900	62.1	0.430	-0.39	53.4	...	49.6
4537.920	62.1	0.480	-0.48	...	...	...
4519.600	62.1	0.540	-0.35	54.2	...	47.1
4467.310	62.1	0.650	0.30	67.0	63.0	...
6645.110	63.1	1.380	0.12	26.1	19.2	19.4

Table 8.17: The atomic data used for the abundance analysis of stars in OCs NGC 2548 and Collinder 350.

Wavelength	Z^a	LEP^b	log gf	W_λ (mÅ)		Wavelength	Z^a	LEP^b	log gf	W_λ (mÅ)	
				NGC 2548	Col 350					NGC 2548	Col 350
λ (Å)		(eV)		#1628	#47	λ (Å)		(eV)		#1628	#47
4668.530	11.0	2.100	-1.25	75.2	85.2	5460.500	22.0	0.050	-2.75	39.0	43.5
4982.790	11.0	2.100	-0.91	96.3	102.8	4999.500	22.0	0.830	0.31	145.7	...
6154.230	11.0	2.100	-1.55	50.3	...	5020.020	22.0	0.840	-0.36	117.8	117.2
6160.760	11.0	2.100	-1.25	81.7	...	6336.100	22.0	1.440	-1.69	17.6	19.8
5711.090	12.0	4.340	-1.72	115.1	108.6	5474.230	22.0	1.460	-1.17	27.0	36.1
5528.410	12.0	4.350	-0.50	194.8	197.6	5490.150	22.0	1.460	-0.88	49.6	53.2
7835.220	13.0	4.020	-0.47	52.3	52.1	5222.670	22.0	2.080	-0.56	23.1	...
7836.040	13.0	4.020	-0.34	61.2	61.4	5739.990	22.0	2.240	-0.61	22.4	...
5665.570	14.0	4.920	-2.04	...	50.2	4708.650	22.1	1.240	-2.34	87.7	91.5
5645.610	14.0	4.930	-2.14	...	42.8	4764.510	22.1	1.240	-2.77	...	68.1
5701.100	14.0	4.930	-2.05	48.9	52.4	5005.170	22.1	1.570	-2.73	62.1	55.2
5772.150	14.0	5.080	-1.75	53.0	61.9	5381.030	22.1	1.570	-1.97	99.9	89.8
5753.640	14.0	5.610	-1.30	45.4	52.8	5396.240	22.1	1.580	-3.02	...	36.4
6237.310	14.0	5.610	-1.14	59.1	63.0	5418.770	22.1	1.580	-2.11	96.0	87.5
6243.810	14.0	5.610	-1.26	49.0	51.8	5492.880	22.1	1.580	-3.31	32.3	30.8
6244.470	14.0	5.610	-1.36	54.1	50.2	4911.190	22.1	3.120	-0.34	99.7	91.3
6142.490	14.0	5.620	-1.54	...	31.2	4577.150	23.0	0.000	-1.05	82.2	82.5
6721.820	14.0	5.860	-1.06	42.6	45.4	6251.830	23.0	0.290	-1.34	64.2	60.4
6122.220	20.0	1.900	-0.32	185.2	179.2	6111.650	23.0	1.040	-0.71	40.9	35.9
5581.970	20.0	2.520	-0.56	113.2	114.0	6135.370	23.0	1.050	-0.75	36.1	31.5
5590.120	20.0	2.520	-0.74	111.9	107.7	5737.070	23.0	1.060	-0.74	35.9	36.2
6166.440	20.0	2.520	-1.14	97.2	84.6	5668.370	23.0	1.080	-1.03	21.4	23.1
6169.560	20.0	2.520	-0.48	128.2	126.2	5670.850	23.0	1.080	-0.42	57.3	61.2
6455.600	20.0	2.520	-1.29	79.0	77.8	5727.050	23.0	1.080	-0.01	88.8	81.7
6499.650	20.0	2.520	-0.82	102.4	113.8	4545.940	24.0	0.940	-1.37	123.0	...
6471.650	20.0	2.530	-0.68	120.5	118.8	5296.700	24.0	0.980	-1.36	129.5	124.9
5686.840	21.0	1.440	0.38	24.8	19.6	5300.750	24.0	0.980	-2.00	101.2	100.1
6604.580	21.1	1.360	-1.31	68.0	67.6	5345.800	24.0	1.000	-0.95	158.4	...
5667.140	21.1	1.500	-1.21	65.2	64.5	5238.960	24.0	2.710	-1.30	28.4	29.1
5684.190	21.1	1.510	-1.25	60.4	...	5329.140	24.0	2.910	-0.06	80.9	87.6
6245.620	21.1	1.510	-1.03	83.0	80.2	5783.070	24.0	3.320	-0.50	43.6	39.2
5526.810	21.1	1.770	0.02	115.7	...	5784.970	24.0	3.320	-0.38	44.9	...
5039.950	22.0	0.020	-1.13	123.3	128.8	5214.130	24.0	3.370	-0.74	28.2	24.8

Wavelength	Z^a	LEP^b	log gf	W_λ (mÅ)	
				NGC 2548	Col 350
λ (Å)		(eV)		#1628	#47
5287.150	24.0	3.440	-0.87	18.7	18.6
5312.860	24.0	3.450	-0.55	30.4	...
5304.190	24.0	3.460	-0.69	...	22.3
5237.310	24.1	4.070	-1.16	63.7	69.8
5279.870	24.1	4.070	-2.10	30.0	...
5308.430	24.1	4.070	-1.81	38.9	40.9
5313.580	24.1	4.070	-1.65	46.8	45.1
5334.850	24.1	4.070	-1.56	52.1	43.3
5502.070	24.1	4.170	-1.99	28.7	...
6013.490	25.0	3.070	-0.25	103.4	107.2
6016.640	25.0	3.070	-0.22	110.8	111.0
6021.800	25.0	3.080	-0.08	115.5	114.0
5377.610	25.0	3.850	-0.11	68.0	58.9
5399.470	25.0	3.850	-0.29	45.8	48.2
6710.310	26.0	1.490	-4.87	...	49.5
5307.360	26.0	1.610	-2.99	132.3	124.2
6137.000	26.0	2.200	-2.95	111.6	97.6
6335.340	26.0	2.200	-2.18	133.9	135.0
6392.540	26.0	2.280	-4.03	40.6	43.9
6608.020	26.0	2.280	-4.04	49.1	...
6252.560	26.0	2.400	-1.69	165.5	162.1
6136.630	26.0	2.450	-1.40	175.5	169.2
5701.550	26.0	2.560	-2.22	119.3	...
4683.540	26.0	2.830	-2.32	...	84.8
5570.030	26.0	2.850	-4.26	17.3	...
5215.190	26.0	3.270	-0.87	...	138.1
5569.630	26.0	3.420	-0.49	150.5	150.4
5576.100	26.0	3.430	-1.01	122.5	122.2
4547.830	26.0	3.550	-1.01	110.2	...
5242.490	26.0	3.630	-0.97	115.0	108.8
5294.550	26.0	3.640	-2.86	25.8	...
5539.280	26.0	3.640	-2.66	32.4	...
5636.700	26.0	3.640	-2.61	32.9	...
5760.350	26.0	3.640	-2.49	38.6	40.1
5466.990	26.0	3.650	-2.23	56.1	53.8
6411.650	26.0	3.650	-0.72	133.6	138.0
5379.580	26.0	3.690	-1.51	83.3	87.2
6336.840	26.0	3.690	-0.86	121.8	124.1
6003.020	26.0	3.880	-1.12	97.1	99.5
6187.990	26.0	3.940	-1.72	60.2	63.7
6027.060	26.0	4.080	-1.09	89.2	83.0
5293.960	26.0	4.140	-1.87	43.1	44.6
6165.360	26.0	4.140	-1.47	60.2	...
5074.730	26.0	4.220	-0.16	...	114.9
5195.450	26.0	4.220	-0.00	129.6	...
5638.270	26.0	4.220	-0.87	91.0	88.1
5738.230	26.0	4.220	-2.34	21.5	...
5243.770	26.0	4.260	-1.15	75.5	74.9
5731.770	26.0	4.260	-1.29	72.9	68.6
5717.840	26.0	4.280	-1.13	...	73.8
5466.400	26.0	4.370	-0.63	89.2	90.7
5546.510	26.0	4.370	-1.31	60.2	...
5445.050	26.0	4.390	-0.01	119.6	120.6
5560.220	26.0	4.430	-1.19	58.6	61.9
5462.970	26.0	4.470	-0.16	105.7	...
5679.030	26.0	4.650	-0.91	64.0	65.7
6007.960	26.0	4.650	-0.97	67.0	64.2
5633.950	26.0	4.990	-0.27	76.1	...
4520.210	26.1	2.810	-2.61	105.1	107.8
4993.340	26.1	2.810	-3.68	...	64.1
5284.100	26.1	2.890	-3.20	82.3	78.2
6084.110	26.1	3.200	-3.88	32.5	35.7
5234.630	26.1	3.220	-2.05	108.3	114.8
5264.800	26.1	3.230	-3.23	61.8	61.6
6247.560	26.1	3.890	-2.43	65.1	69.3
6416.930	26.1	3.890	-2.88	48.4	51.2
6456.380	26.1	3.900	-2.19	78.0	72.1
5301.030	27.0	1.710	-1.99	50.9	...
5647.240	27.0	2.280	-1.56	36.2	35.9
6455.000	27.0	3.630	-0.25	25.1	29.0
5342.700	27.0	4.020	0.69	42.0	47.4
5578.710	28.0	1.680	-2.64	93.3	89.2
6191.180	28.0	1.680	-2.35	...	111.3
6177.250	28.0	1.830	-3.50	39.9	36.1
4998.220	28.0	3.610	-0.78	62.9	...
5462.500	28.0	3.850	-0.93	52.2	50.2
5589.360	28.0	3.900	-1.14	30.8	36.2

Wavelength	Z[a]	LEP[b]	log gf	W_λ (mÅ)	
				NGC 2548	Col 350
λ (Å)		(eV)		#1628	#47
5593.720	28.0	3.900	-0.84	54.4	54.1
5638.750	28.0	3.900	-1.72	...	11.7
5625.320	28.0	4.090	-0.70	50.6	49.8
6111.070	28.0	4.090	-0.87	45.3	45.3
5682.200	28.0	4.110	-0.47	63.4	62.4
5760.840	28.0	4.110	-0.80	45.6	39.5
4722.150	30.0	4.030	-0.39	83.4	82.3
5119.110	39.1	0.990	-1.36	70.5	32.6
5200.390	39.1	0.990	-0.57	77.0	69.4
5087.420	39.1	1.080	-0.17	...	84.1
5402.760	39.1	1.840	-0.62	...	25.1
6127.450	40.0	0.150	-1.06	10.6	...
5853.690	56.1	0.600	-1.02	123.5	123.2
5303.540	57.1	0.320	-1.35	29.5	27.7
6390.480	57.1	0.320	-1.41	28.9	...
5274.210	58.1	1.040	0.13	...	30.0
5472.270	58.1	1.240	-0.18	14.5	...
5092.790	60.1	0.380	-0.61	48.2	...
5319.810	60.1	0.550	-0.14	58.5	52.8
5276.860	60.1	0.860	-0.61	...	14.7
4577.680	62.1	0.250	-0.65	50.2	...
4523.900	62.1	0.430	-0.39	...	49.6
4519.600	62.1	0.540	-0.35	...	47.1
4467.310	62.1	0.650	0.30	63.0	...
6645.110	63.1	1.380	0.12	19.2	19.4

Bibliography

[1] Abadi, M. G., Navarro, J. F., Steinmetz, M. & Eke, V. R. 2003, ApJ, 597, 21

[2] Allen D. M., Porto de Mello G. F., 2011, A&A, 525, 63

[3] Allende Prieto C., García López R. J., Lambert D. L., Gustafsson B., 1999, ApJ, 527, 879

[4] Alonso A., Arribas S., Martínez-Roger C., 1999, A&AS, 140, 261

[5] Amôres E. B., Lépine J. R. D., Mishurov Y. N. 2009, MNRAS, 400, 1768

[6] Andrievsky, S. M., Luck, R. E., Martin, P., Lepine, J. R. D. 2004, A&A, 413, 159

[7] Andrievsky, S. M., Kovtyukh, V. V., Luck, R. E., et al. 2002a, A&A, 381, 32

[8] Andrievsky, S. M., Bersier, D., Kovtyukh, V. V., et al. 2002b, A&A, 384, 140

[9] Andrievsky, S. M., Kovtyukh, V. V., Luck, R. E., et al. 2002c, A&A, 392, 491

[10] Anthony-Twarog, Barbara J.; Twarog, Bruce A., 2006, PASP, 118, 358

[11] Antoja, T., Helmi, A., Bienayme, O., Bland-Hawthorn, J. et al., 2012, MNRAS, 426, 1

[12] Asplund M., Grevesse N., Sauval A. J., Scott, P., 2009, ARA&A, 47, 481

[13] Balaguer-Núñez, L., Galadí-Enríquez, D., & Jordi, C. 2007, A&A, 470, 585

[14] Balaguer-Núñez, L., Jordi, C., Galadí-Enríquez, D., 2005, A&A, 437, 457

[15] Balaguer-Nú*ñ*ez L., jordi C., Galadí-Enríquez D., Masana E., 2004, A&A, 426, 827.

[16] Bartašiūtė S., Deveikis V., Straižys V., Bogdanovičius., 2007, BaltA, 16, 199.

[17] Becker, W. 1963, Z. Astrophys., 57, 117

[18] Bell E. F., et al., 2008, ApJ, 680, 295

[19] Belokurov, V., Zucker, D. B., Evans, N. W., Gilmore, G. et al., 2006, ApJ, 642, 137

[20] Bensby, T., 2013, arXiv:1312.4592

[21] Bensby, T., Alves-Brito, A., Oey, M. S., Yong, D., Meléndez, J., 2011, ApJ, 735, 46

[22] Bensby, T., Zenn, A. R., Oey, M. S., Feltzing, S., 2007, ApJ, 663, 13

[23] Bensby, T., Feltzing, S., Lundström, I., Ilyin, I., 2005, A&A, 433, 185

[24] Bensby, T., Feltzing, S., & Lundstrm, I., 2004b, A&A, 421, 969

[25] Bergond, G., Leon, S., & Guibert, J. 2001, A&A, 377, 462

[26] Bertelli, G., Girardi, L., Marigo, P., & Nasi, E. 2008, A&A, 484, 815

[27] Bica E., & Bonatto C., 2005, A&A, 431, 943

[28] Biémont E., Grevesse N., Hannaford P., Lowe R. M., 1981, ApJ, 248, 867

[29] Binney, J. & Merrifield, M., 1998, Galactic Astronomy, (Princeton: Princeton University Press)

[30] Bland-Hawthorn,J. & Freeman,K., 2004, PASA, 21, 110

[31] Bonatto, C. & Bica, E., 2005, A&A, 437, 483

[32] Bragaglia, A., Sestito, P., Villanova, S., Carretta, E., Randich, S., Tosi, M., 2008, A&A, 480, 79

[33] Burbidge, E. M., Burbidge, G. R., Fowler, W. A., & Hoyle F., 1957, RvMP, 29, 547

[34] Burris D. L., Pilachowski C. A., Armandroff T. E., Sneden C., Cowan J. J., Roe H., 2000, ApJ, 544, 302

[35] Busso M., Gallino R., Lambert D. L., Travaglio C., Smith V. V., 2001, ApJ, 557, 802

[36] Calura, F., & Matteucci, F., 2006, ApJ, 652, 889

[37] Cannon, R. D., Croke, B. F. W., Bell, R. A., Hesser, J. E., & Stathakis, R. A. 1998, MNRAS, 298, 601

[38] Caretta E., Bragaglia A., Gratton R. G., Tosi M., 2004, A&A, 422, 951

[39] Caretta E., Bragaglia A., Gratton R. G., 2007, A&A, 473, 129

[40] Carretta E., Bragaglia A., Gratton R. G., Tosi M., 2005, A&A, 441, 131

[41] Carney, B. W., Yong, D., Teixera de Almeida, M. L., & Seitzer, P. 2005b, AJ, 130, 1111

[42] Carollo D., et al., 2010, ApJ, 712, 692

[43] Carollo D., et al., 2007, Nature, 450, 1020

[44] Carpenter J. M., 2001, AJ, 121, 2851

[45] Carpenter, J. M. 2000, AJ, 120, 3139

[46] Carraro, G., Geisler, D., Villanova, S., Frinchaboy, P. M., & Majewski S. R., 2007, A&A, 476, 217

[47] Carraro, G., Bresolin, F., Villanova, S., Matteucci, F., Patat, F., & Romaniello, M., 2004, AJ, 128, 1676

[48] Carraro, G., Ng, Y. K., & Portinari, L., 1998, MNRAS, 296, 1045

[49] Carrera R., 2012, A&A, 544, 109

[50] Carrera, R.; Pancino, E., 2011, A&A. 535, 30

[51] Castelli, F., Kurucz, R. L., 2003, IAU Symposium 210, Modelling of Stellar Atmospheres, Uppsala, Sweden, eds. N.E. Piskunov, W.W. Weiss, and D. F. Gray, 2003, ASP-S210

[52] Chen, L., Hou, J. L., & Wang J. J., 2003, AJ, 125, 1397

[53] Cheng, Judy Y., Rockosi, Constance M. et al., 2012, ApJ, 752, 51

[54] Chiappini, C., 2001, AmSci, 89, 506

[55] Chiappini, C., Matteucci, F., & Gratton, R. 1997, ApJ, 477, 765

[56] Clariá J.J., Piatti A.E., Mermilliod J.-C., Palma T., 2008, AN, 329, 609

[57] Clariá, J. J., Piatti, A. E., Lapasset, E., & Parisi, M. C., 2005, BaltA, 14, 301

[58] Clariá, J. J., Mermilliod, J.-C., Piatti, A. E., 1999, A&AS, 134, 301

[59] Clariá, J. J., 1985, A&AS, 59, 195

[60] Clariá, J. J., 1973, A&AS, 9, 251

[61] Clarkson, W., Sahu, K., Anderson, J., et al. 2008, ApJ, 684, 1110

[62] Clegg R. E. S., Lambert D. L., Bell R. A., 1979, ApJ, 234, 188

[63] Cooper A. P. et al., 2010, MNRAS, 406, 744

[64] Cunha, K., Smith, V.V., Suntzeff, N., Lambert, D.L. 2010, ApJ, 717, 333

[65] Cutri R.M., Skrutskie M.F., Van Dyk S. et al., 2003, Vizier Online Data Catalogue, **II/246**

[66] Daflon, S. & Cunha, K. 2004, ApJ, 617, 1115

[67] David F. Gray, 1992, The Observation and Analysis of Stellar Photospheres (Cambridge Astrophysics Series)

[68] Deharveng, L., Peña, M., Caplan, J., Costero, R., 2000, MNRAS, 311, 329

[69] Dehnen W., & Binney J., 1998, MNRAS, 298, 387.

[70] de la Fuente Marcos R., & de la Fuente Marcos C., 2008, ApJ, 685, L125

[71] de la Fuente Marcos, R., de la Fuente Marcos, C., 2004, NewA, 9, 475

[72] De Silva, G. M., Freeman, K. C., Bland-Hawthorn, J., 2009, PASA, 26, 11

[73] De Silva G. M., Freeman K. C., Asplund M., Bland-Hawthorn, J., Bessell M. S., Collet, R. 2007, AJ, 133, 1161

[74] De Silva, G.M., Sneden, C., Paulson, D.B., Asplund, M., Bland-Hawthorn, J., Bessell, M.S., Freeman, K.C., 2006, AJ, 131, 455.

[75] de Vaucouleurs, G. 1964, in The Galaxy and the Magellanic Clouds, ed. F. J. Kerr, IAU Symp., 20, 195

[76] Dias W. S., & Lépine J. R. D., 2005, ApJ, 629, 825

[77] Dias W. S., Alessi B. S., Moitinho A., Lépine J. R. D., 2002, A&A, 389, 871

[78] Dodd, R. J., MacGillivray, H. T., & Hilditch, R. W., 1977, MNRAS, 181, 729

[79] D'Odorico, S., Ghigo, M., Ponz, D.: 1987, *An atlas of the thorium-argon spectrum for the ESO Echelle Spectrograph in the 3400-9000 Å region*, ESO Scientific Report, Garching: European Southern Observatory (ESO), 1987

[80] D'Orazi V. et al. 2009, ApJ, 693, 31

[81] Dürbeck, W., 1960, ZA, 49, 214

[82] Dwek E., et al., 1995, ApJ, 604, 93

[83] Eggen, O. J., 1983, AJ, 88, 184

[84] Eggen O. J., 1968, ApJ, 152, 83

[85] Eggen, O. J., Lynden-Bell, D., Sandage, A. R., 1962, ApJ 136, 747

[86] Edmonds, F. N., Jr., 1969, JQSRT, 9, 1427

[87] Edvardsson, B., Andersen, J., Gustafsson, B., Lambert, D. L., Nissen, P. E., & Tomkin, J., 1993, A&A, 275, 101

[88] Englmaier P., Pohl M., Bissantz N., 2008, arxiv: 0812.3491

[89] Friel, E. D., Jacobson, H. R., & Pilachowski, C. A. 2010, AJ, 139, 1942

[90] Friel E. D., 2006, in ESO Astrophysics Symposia 24, Chemical Abundances and Mixing in Stars in the Milky Way and its Satellites, ed. S. Randich, L. Pasquini (Heidelberg: Springer), 3

[91] Friel, E. D., & Janes, K. A. 1993, A&A, 267, 75

[92] Flynn C., Sommer-Larsen J., Christensen P. R., 1996, MNRAS, 281, 1027

[93] Flynn C., & Fuchs B., 1994, MNRAS, 270, 471

[94] Führ J.R., Wiese W.L., 2006, J. Phys. Chem. Ref. Data, 35, 1669

[95] Fuhrmann K., 1998, A&A, 338, 161

[96] Geisler D., Claria J. J., Minniti D., 1992, AJ, 104, 1892

[97] Ghez, A. M. et al. 2008, ApJ, 689, 1044

[98] Gilmore, G. & Reid, N., 1983, MNRAS, 202, 1025

[99] Glushkova, E. V. & Rastorguev, A. S., 1991, SvAL, 17, 13G

[100] Gratton, R., Sneden, C., & Carretta, E. 2004, ARA&A, 42, 385

[101] Gratton, R., 2000, ASPC, 198, 225

[102] Gustafsson, B., Edvardsson, B., Eriksson, K., Jørgensen, U. G., Nordlund, Å., Plez, B., 2008, A&A, 486, 951

[103] Hamdani S., North P., Mowlavi N., Raboud D., Mermilliod J.-C., 2000, A&A, 360, 509

[104] Hannaford P., Lowe R. M.,Grevesse N., Biémont E., Whaling W., 1982, ApJ, 261, 736

[105] Harris G. L. H., & Harris W. E., 1977, AJ, 82, 612.

[106] Heiter, U., Soubiran, C., Netopil, M. & Paunzen, E., 2014, A&A, 561, 93

[107] Helmi A., 2008, A&AR, 15, 145

[108] Herwig, F. 2005, ARA&A, 43, 435

[109] Hill, V., Lecureur, A., Gómez, A. et al., 2011, A&A, 534, 80

[110] Hill V., 2004, in McWilliam A., Rauch M., eds, Origin and Evolution of the Elements. Carnegie Observatories, Pasadena, p. 205

[111] Hills, J. G. 1975, AJ, 80, 1075

[112] Hinkle K., Wallace L., Valenti J., Harmer D., 2000, *Visible and Near Infrared Atlas of the Arcturus Spectrum 3727-9300 Å* (San Francisco: ASP)

[113] Hoag A.A., Johnson H.L., Iriarte B., Mitchell R.I., Hallam K.L., Sharpless S., 1961, Publ. Us. Nav. Obs. XVII part VII, 347

[114] Hobbs, L. M. & Thorburn, J. A., 1992, AJ, 104, 669

[115] Iben, I. 1968, Nature, 220, 143

[116] Ibata R. A., Wyse R. F. G., Gilmore G., Irwin M. J., Suntzeff N. B., 1997, AJ, 113, 634

[117] Iliadis, C. 2007, Nuclear Physics of Stars (Wiley-VCH)

[118] Jacobson, H. R., Pilachowski, C. A., Friel, Eileen D., 2011, AJ, 142, 59

[119] Jacobson, H. R., Friel, E. D., Pilachowski, C. A., 2009, AJ, 137, 4753

[120] Jacobson, H. R., Friel, E. D., Pilachowski, C. A., 2007, AJ, 134, 1216

[121] Janes K. A., 1979, ApJS, 39, 135

[122] Jappsen, A.-K., Klessen, R. S., Larson, R. B., Li, Y., Mac Low, M.-M. 2005, A&A, 435, 611

[123] Jílková, L., Carraro, G., Jungwiert, B., Minchev, I., 2012, A&A, 541, 64

[124] Johnson D. R. H., & Soderblom D. R., 1987, AJ, 93, 864

[125] Johnson, H. L. 1961, Lowell Obs. Bull., 5, N8

[126] Joshi U.C., & Sagar R., 1986, BASI, 14, 95

[127] Jurić M., Ivezić v. Ž., Brooks A., Lupton R. H., et al., 2008, ApJ, 673, 864

[128] Kaluzny, J. & Mazur, B., 1991, AcA, 41, 191

[129] Karakas, A. I., Lugaro, M., Gallino, R., 2007, ApJ, 656, 73

[130] Kazantzidis, S., Bullock, J. S., Zentner, A. R., Kravtsov, A. V., & Moustakas, L. A. 2008, ApJ, 688, 254

[131] Kerr F. J., & Lynden-Bell D., 1986, MNRAS, 221, 1023

[132] Kharchenko, N. V., et al. 2007, AN, 328,.889

[133] Kharchenko, N. V., Piskunov, A. E., Röser, S., Schilbach, E., & Scholz, R. D. 2005, A&A, 438, 1163

[134] Klement R. J., 2010, A&ARv, 18, 567

[135] Kuijken, K., Gilmore, G., 1989, MNRAS, 239, 651

[136] Kunder, A., Koch, A., Rich, R. M., et al., 2012, AJ, 143, 57

[137] Kurucz R. L., 1998, http://cfaku5.harvard.edu

[138] Kurucz R. L., Furenlid I., Brault J., & Testerman L. 1984, *Solar Flux Atlas from 296 to 1300 nm*, ed. R. L. Kurucz, I. Furenlid, J. Brault, & L. Testerman (Sunspot, NM: National Solar Observatory)

[139] Lada, C. J. & Lada, E. A., 2003, ARAA, 41, 57

[140] Lambert D. L., & Luck R. E., 1976, Observatory, 60, 100

[141] Lapasset, E., Clariá, J. J., & Mermilliod, J.-C., 2000, A&A, 361, 945

[142] Lawler J. E., Sneden C., Cowan J.J., Evans I.I., Den Hartog E.A., 2009, ApJ, 182, 51

[143] Lawler J. E., Den Hartog E. A., Sneden C., Cowan J. J., 2006, ApJS, 162, 227

[144] Lawler J. E., Bonvallet G., Sneden C., 2001, ApJ, 556, 452

[145] Lawler J. E., Wickliffe M. E., Den Hartog E. A., Sneden, C., 2001, AJ, 563, 1075.

[146] Lee, S. H.; Kang, Y.-W.; Ann, H. B., 2013, MNRAS, 432, 1672

[147] Lee, Y. S., et al. 2011, AJ, 141, 90

[148] Lépine, J. R. D., Cruz, P., Scarano, S., Jr., Barros, D. A., 2011, MNRAS, 417, 698

[149] Lépine, J. R. D., Roman-Lopes, A., Abraham, Z., Junqueira, T. C., Mishurov, Yu. N., 2011a, MNRAS, 414, 1607

[150] Lépine J. R. D., Mishurov Yu. N., Dedikov S. Yu., 2001, ApJ, 546, 234

[151] Lin C. C., Yuan C., Shu F. H., 1969, ApJ, 155, 721

[152] Lin C. C., & Shu F. H., 1964, ApJ, 140, 646

[153] Lindoff, U., 1973, A&AS, 9, 229

[154] Lodders K., 2003, ApJ, 591, 1220

[155] Loktin A., Gerasimenko T., Malisheva L., 2001, A&A, 20, 605

[156] Luck R. E., & Lambert D. L., 2011, AJ, 142, 136

[157] Luck R. E., Heiter U., 2007, AJ, 133, 2464

[158] Luck R. E., Heiter U., 2006, AJ, 131, 3069

[159] Maciejewski, G., Boeva, S., Georgiev, T., Mihov, B., Ovcharov, E., Valcheva, A., 2008, BaltA, 17, 51

[160] Maciel, W. J., Quireza, C., & Costa, R. D. D. 2007, A&A, 463, 13

[161] Maiorca, E., Randich, S., Busso, M., Magrini, L., Palmerini, S., 2011, ApJ, 736, 120

[162] Marigo, P., Girardi, L., Bressan, A., Groenewegen, M. A. T., Silva, L., Granato, G. L., 2008, A&A, 482, 883

[163] Mathieu R.D., Latham D.W., Griffin R.F., Gunn J.E., 1986, AJ, 92, 1100

[164] Magrini L., Randich S., Zoccali M., Jilkova L., Carraro G., Galli D., Maiorca E., Busso M., 2010, A&A, 523, 11

[165] Magrini L., Sestito P., Randich S., Galli D., 2009, A&A, 494, 95

[166] Martos M., Allen C., Franco J., Kurtz S., 1999, ApJ, 526, L89

[167] Matteucci, F., & Francois, P. 1989, MNRAS, 239, 885

[168] Matteucci, F., & Greggio, L. 1986, A&A, 154, 279

[169] McClure R.D., Twarog B.A., Forrester W.T., 1981, ApJ, 243, 841.

[170] McClure R.D., 1972, ApJ, 172, 615

[171] McKee, C. F. & Tan, J. C. 2002, Nature, 416, 59

[172] McWilliam A., 1998, ApJ, 115, 1640

[173] Meléndez J. & Barbuy B., 2009, A&A, 497, 611

[174] Meléndez, J., Asplund, M., Alves-Brito, A., et al., 2008, A&A, 484, 21

[175] Mermilliod J.-C., Mayor M., Udry S., 2008, A&A, 485, 303

[176] Mikolaitis, S.; Tautvaišienė, G., Gratton, R., Bragaglia, A., Carretta, E., 2011, MNRAS, 416, 1092

[177] Minchev, I., & Famaey, B. 2010, ApJ, 722, 112

[178] Minniti D. & Zoccali M., 2008, 245, 323

[179] Mishenina, T.V., Bienaymé, O., Gornaeva, T.I., Charbonnel, C., Soubiran, C., Korotin, S.A., Kovtyukh, V.V., 2006, A&A, 456, 1109

[180] Mishenina T. V., Soubiran C., Kovtyukh V. V., Korotin S. A., 2004, A&A, 418, 551

[181] Mishurov Yu N., Lepine J. R. D., Acharova I. A., 2002, ApJ, 571, 113

[182] Miyamoto M., & Nagai R., 1975, PASJ, 27, 533

[183] Moffat A.F.J., Vogt N. 1975, A&AS, 20, 85

[184] Möhler, S. 2004, in IAU Symposium, Vol. 224, The A-Star Puzzle, ed. J. Zverko, J. Ziznovsky, S. J. Adelman, & W. W. Weiss, 395-402

[185] Monroe, T. R., Pilachowski, C. A., 2010, AJ, 140, 2109

[186] Montgomery, K. A., Marschall, L. A., & Janes, K. A., 1993, AJ, 106, 181

[187] Moore C.E., Minnaert M. G. J., Houtgast J., 1966, *The Solar Spectrum 2935 Å to 8770 Å*, Second Revision of the Rowland's Preliminary Table of Solar Wavelengths. National Bureau of Standards Monograph 61

[188] Naoz Smadar, & Shaviv Nir J., 2007, New Astron., 12, 410

[189] Neese C. L., & Yoss K. M., 1988, Astron. J., 95, 463

[190] Nissen, P. E., & Schuster, W. J. 2010, A&A, 511, 10

[191] Nordström B. et al., 2004, A&A, 418, 989

[192] Pancino E., Carrera R., Rossetti E., Gallart C., 2010, A&A, 511, 56

[193] Parisi M. C., Claria J. J., Piatti A. E.,& Geisler D., 2005, MNRAS, 363, 1247

[194] Paulson, D.B., Sneden, C., Cochran, W.D., 2003, AJ, 125, 3185

[195] Peña, J. H., Peniche, R., Bravo, H., & Yam, O., 1994, RMxAA, 28, 7

[196] Peña, J. H. & Peniche, R., 1994, RMxAA, 28, 139

[197] Pesch P., 1961, ApJ, 134, 602

[198] Phelps, R. L., Janes, K. A., & Montgomery, K. A. 1994, AJ, 107, 1079

[199] Piatti, A. E., Claria, J. J., Abadi, M. G., 1995, AJ, 110, 2813

[200] Portinari, L., & Chiosi, C. 2000, A&A, 355, 929

[201] Prantzos, N., 2008, EAS, 32, 311

[202] Press W. H., Teukolsky S. A., Vetterling W. T., Flannery B. P., 1992, *Numerical Recipes in Fortran: The Art of Scientific Computing*, 2nd edn. Cambridge Univ. Press, Cambridge

[203] Prochaska J. X., McWilliam A., 2000, AJ, 537, 57

[204] Quinn, P. J., Hernquist, L., & Fullagar, D. P. 1993, ApJ, 403, 74

[205] Reddy A.B.S., Giridhar S., Lambert D. L., 2013, MNRAS, 431, 3338

[206] Reddy A.B.S., Giridhar S., Lambert D. L., 2012, MNRAS, 419, 1350

[207] Reddy, Bacham E., Lambert, David L., 2008, MNRAS, 391, 95

[208] Reddy B. E., Lambert D. L., Allende Prieto C., 2006, MNRAS, 367, 1329

[209] Reddy B.E., Tomkin, J., Lambert D.L., Allende Prieto C., 2003, MNRAS, 340, 304

[210] Robin A. C., Reylé C., Derriére S., Picaud S., 2003, A&A, 409, 523

[211] Rolfs, C. E. & Rodney, W. S. 1988, Cauldrons in the cosmos: Nuclear astrophysics (Chicago, IL: University of Chicago Press)

[212] Roškar, R., Debattista, V. P., Quinn, T. R., Stinson, G. S., & Wadsley, J., 2008, ApJ, 684, 79

[213] Rudolph, A. L., Fich, M., Bell, G. R., Norsen, T., et al., 2006, ApJS, 162, 346

[214] Ruphy S., Robin A. C., Epchtein N., Copet E., Bertin E., Fouque P., Guglielmo F., 1996, A&A, 313, 21

[215] Russeil, D. 2003 A&A, 397, 133

[216] Sanders W.L. 1977, A&AS, 27, 89

[217] Santos, N. C.; Lovis, C.; Melendez, J.; Montalto, M.; Naef, D.; Pace, G., 2012, A&A, 538, 151

[218] Santos N.C., Lovis C., Pace, G., Melendez, J., Naef D., 2009, A&A, 493, 309

[219] Scarano, S. Jr., & Lépine J. R. D., 2012, MNRAS, 428, 625

[220] Schlaufman, K. C., Rockosi, C. M., Allende Prieto, C., et al. 2009, ApJ, 703, 2177

[221] Schönrich, R., & Binney, J. 2009, MNRAS, 396, 203

[222] Searle, L. & Zinn, R., 1978, ApJ, 225, 357

[223] Sellwood, J. A., & Binney, J. J. 2002, MNRAS, 336, 785

[224] Sestito, P., Bragaglia, A., Randich, S., Pallavicini, R., Andrievsky, S. M., & Korotin, S. A. 2008, A&A, 488, 943

[225] Sestito, P., Randich, S., & Pallavicini, R. 2004, A&A, 426, 809

[226] Shaver, P. A., McGee, R. X., Newton, L. M., Danks, A. C., Pottasch, S. R., 1983, MNRAS, 204, 53

[227] Shetrone M., Venn K. A., Tolstoy E., Primas F., Hill V., Kaufer A., 2003, AJ, 125, 684

[228] Smiljanic R., Gauderon R., North P., Barbuy B., Charbonnel C., Mowlavi N., 2009, A&A, 502, 267

[229] Smith V. V., Suntzeff N. B., Cunha K., Gallino R., Busso B., Lambert D.L., & Straniero O., 2000, AJ, 119, 1239

[230] Smith V. V., & Lambert D. L., 1986, ApJ, 311, 843

[231] Sneden, C., Cowan, J. J., & Gallino, R. 2008, ARA&A, 46, 241

[232] Sneden C., 1973, PhD Thesis, Univ. of Texas, Austin

[233] Sobeck J.S., Lawler J.E., Sneden C., 2007, ApJ, 667, 1267

[234] Sofue Y., Honma M., Omodaka T., 2009, PASJ, 61, 227

[235] Soubiran, C., Bienaymé, O., Siebert, A., 2003, A&A, 398, 141

[236] Spitoni, E., & Matteucci, F., 2011, A&A, 531, A72

[237] Stanghellini L., & Haywood M., 2010, ApJ, 714, 1096

[238] Subramaniam, A., & Sagar, R. 1999, AJ, 117, 937

[239] Takeda, Y., Sato, B., Murata, D., 2008, PASJ, 60, 781

[240] Takeda Y., 2007, PASJ, 59, 335

[241] Tautvaišiene G., Edvardsson B., Tuominen I., Ilyin I., 2000, A&A, 360, 499

[242] Thorsett, S., & Chakrabarty, D., 1999, ApJ, 512, 288

[243] Tomkin J., & Lambert D. L., 1999, ApJ, 523, 324

[244] Tsujimoto, T., Nomoto, K., Yoshii, Y., Hashimoto, M., Yanagida, S., & Thielemann, F.-K., 1995, MN 277, 945

[245] Tull, R.G., MacQueen, P.J., Sneden, C., Lambert, D.L., 1995, PASP, 107, 251

[246] Twarog B.A., Ashman K.M., Anthony-Twarog B.J., 1997, AJ, 114, 2556

[247] Twarog, B. A., 1983, ApJ, 267, 207

[248] Vallee J. P., 2005, ApJ, 130, 569

[249] Vallee J. P., 2002, ApJ, 566, 261

[250] Venn, K. A., Irwin, M., Shetrone, M. D., et al., 2004, AJ, 128, 1177

[251] Villanova, S., Randich, S., Geisler, D., Carraro, G., Costa, E., 2010, A&A, 509, 102

[252] Wallerstein, G., Iben, I, Jr., Parker, P., et al., 1997, RvMP, 69, 995

[253] Wang, Y., & Zhao, G., 2013, arxiv: 1303.7436

[254] Wiese W. L., & Martin G. A., 1980, Wavelengths and Transition Probabilities for Atoms and Atomic Ions, NSRDS-NBS 68 (Washington, DC: USGPO)

[255] Woosley, S., & Heger, A., 2007, Phys. Rep., 442, 269

[256] Woosley S. E. & Weaver T. A., 1995, ApJS, 101, 181

[257] Wu, Zhen-Yu; Zhou Xu; Ma Jun; Du Cui-Hua., 2009, MNRAS, 399, 2146

[258] Wu, Zhen-Yu; Zhou, Xu; Ma, Jun; Jiang, Zhao-Ji; Chen, Jian-Sheng, 2005, PASP, 117, 32

[259] Wylie-de Boer, E., Freeman, K., Williams, M., 2010, AJ, 139, 636

[260] Wyse, R. F. G., Gilmore, G., Norris, J. E., Wilkinson, M. I., Kleyna, J. T., Koch, A., Evans, N. W., & Grebel, E. K., 2006, ApJ, 639, 13

[261] Yanny B. et al., 2003, ApJ, 588, 824

[262] Yong D., Carney B. W., Friel E. D., 2012, AJ, 144, 95

[263] Yong, D., Carney, B. W., Teixera de Almeida, M. L., & Pohl, B. L. 2006, AJ, 131, 2256

[264] Yong D., Carney B. W., Teixera de Almeida M. L., 2005, AJ, 130, 597

[265] Zacharias, N., Finch, C. T., Girard, T. M., et al., 2013, AJ, 145, 44

[266] Zoccali, M., Hill, V., Lecureur, A., et al. 2008, A&A, 486, 177

[267] Zoccali, M., Renzini, A., Ortolani, S., et al. 2003, A&A, 399, 931

[268] Zolotov A., Willman B., Brooks A. M., Governato F., Brook C. B., Hogg D. W., Quinn T., Stinson G., 2009, ApJ, 702, 1058